UCRL-53689-92
Distribution Category UC-700

Laboratory Directed Research and Development FY 1992

Lawrence Livermore National Laboratory

MASTER

DISTRIBUTION OF THIS DOCUMENT IS UNLIMIT

Acknowledgments

The Laboratory Directed Research and Development (LDRD) Program is directed by John F. Holzrichter, Assistant to the Director for LDRD. Gordon L. Struble is the Deputy Assistant to the Director for LDRD, Cynthia L. Gardner is the Resource Manager, and Stacey Sprague and Germaine Brassinga are the Administrative Specialists. The following people formed the publication staff for the FY 1992 LDRD report:

Scientific Editor
Gordon L. Struble
Publication Editor
Carolin Middleton
Editors
Susan Eldridge Anderson
Ginny Baldwin
Jay C. Cherniak
Cara W. Corey
Robert D. Kirvel
Lori A. McElroy
Designer
Ken Ball
Art and Production
Pam Allen
Ellen Baldwin
Alex Ballard
Irene Chan
Composition
Marion Capobianco
Cover Photograph
Don Gonzalez

We thank George F. Bing and Jane T. Staehle for careful reading of the entire manuscript.

Contents

Section 5. Energy Science and Technology 89

Section 6. Large-Scale Scientific Systems and Prototypes 103

Introduction

J. F. Holzrichter

The Laboratory Directed Research and Development (LDRD) Program at Lawrence Livermore National Laboratory (LLNL) funds projects that nurture and enrich the core competencies of the Laboratory. In choosing projects for funding, we select research in which we explore and demonstrate innovative concepts that prepare the Laboratory to solve problems of national importance. We support frontier research that expands the scientific and technical horizons of LLNL and that helps us attract an outstanding professional staff and maintain its excellence.

To obtain the highest-quality ideas from Laboratory personnel, we have developed several mechanisms for soliciting proposals. We promote pioneering work in the various scientific and technical areas by funding projects in the category Exploratory Research in the Directorates. Projects in this category are proposed by disciplinary scientists and are managed through the Laboratory's line organizations. These projects enhance LLNL's core competencies and bring new knowledge into the Laboratory. Some of the projects selected also encourage scientific collaboration among LLNL staff members and researchers at universities. As a result of the interactions fostered by these projects, Laboratory staff members gain contacts with the academic community and expertise in fields that are underrepresented at the national laboratories.

In a second category, the Laboratory Director selects a few larger projects to fund as Director's Initiatives. The Director uses this category to support projects that are proposed by an exceptional technical leader and are managed by an associate director. These projects have high technical merit, are generally multidisciplinary, and often provide new capabilities that allow the Laboratory to respond to initiatives of national importance.

LLNL investigators also may submit proposals in an open, Laboratory-Wide Competition, outside the usual management channels. In this category, the Laboratory awards small amounts of funding for new scientific and technological initiatives that are in a germinal stage. To select the projects funded in this competition, the members of the LDRD Research Committee, composed of approximately 20 LLNL scientists and engineers, evaluate proposals for their scientific excellence, long-term significance, and potential for enhancing the Laboratory's core competencies.

Each FY 1992 LDRD project was carefully peer reviewed before it was funded. Then the final portfolio of projects was selected by the Laboratory's LDRD Review Committee, which consists of LLNL senior managers and scientists, and it was approved by the Director. Thus, all projects are proposed by the Laboratory's most creative scientists and engineers, and except for those projects in the Laboratory-Wide Competition, they have strong management input from the directorates and the Director's Office.

The scientific and technical output from the FY 1992 LDRD Program has been significant. Highlights include

- Creating the first laser guide star to be coupled with adaptive optics, thus permitting ground-based telescopes to obtain the same resolution as smaller space-based instruments but with more light-gathering power.
- Significantly improving the limit on the mass of the electron antineutrino so that neutrinos now become a useful tool in diagnosing supernovae. In addition, we disproved the existence of a 17-keV neutrino.
- Developing a new class of organic aerogels that have robust mechanical properties and that have significantly lower thermal conductivity than inorganic aerogels.
- Developing a new heavy-ion accelerator concept, which may enable us to design heavy-ion experimental systems. This concept also markedly increases the possibility of using a heavy-ion driver for inertial fusion.
- Designing and demonstrating a high-power, diode-pumped, solid-state laser concept that will allow us

to pursue a variety of research projects, including laser material processing.

- Demonstrating that high-performance semiconductor arrays can be fabricated more efficiently, which will make this technology available to a broad range of applications such as inertial confinement fusion for civilian power.
- Developing a new type of fiber channel switch and new fiber channel standards for use in local- and wide-area networks, which will allow scientists and engineers to transfer data at gigabit rates.
- Developing the nation's only numerical model for high-technology air filtration systems. Filter designs that use this model will provide safer and cleaner environments in work areas where contamination with particulate hazardous materials is possible and will improve the methods for designing and manufacturing filters.

All FY 1992 projects are described in detail in this report. Other publications on LDRD projects are included in the publications list on page 235.

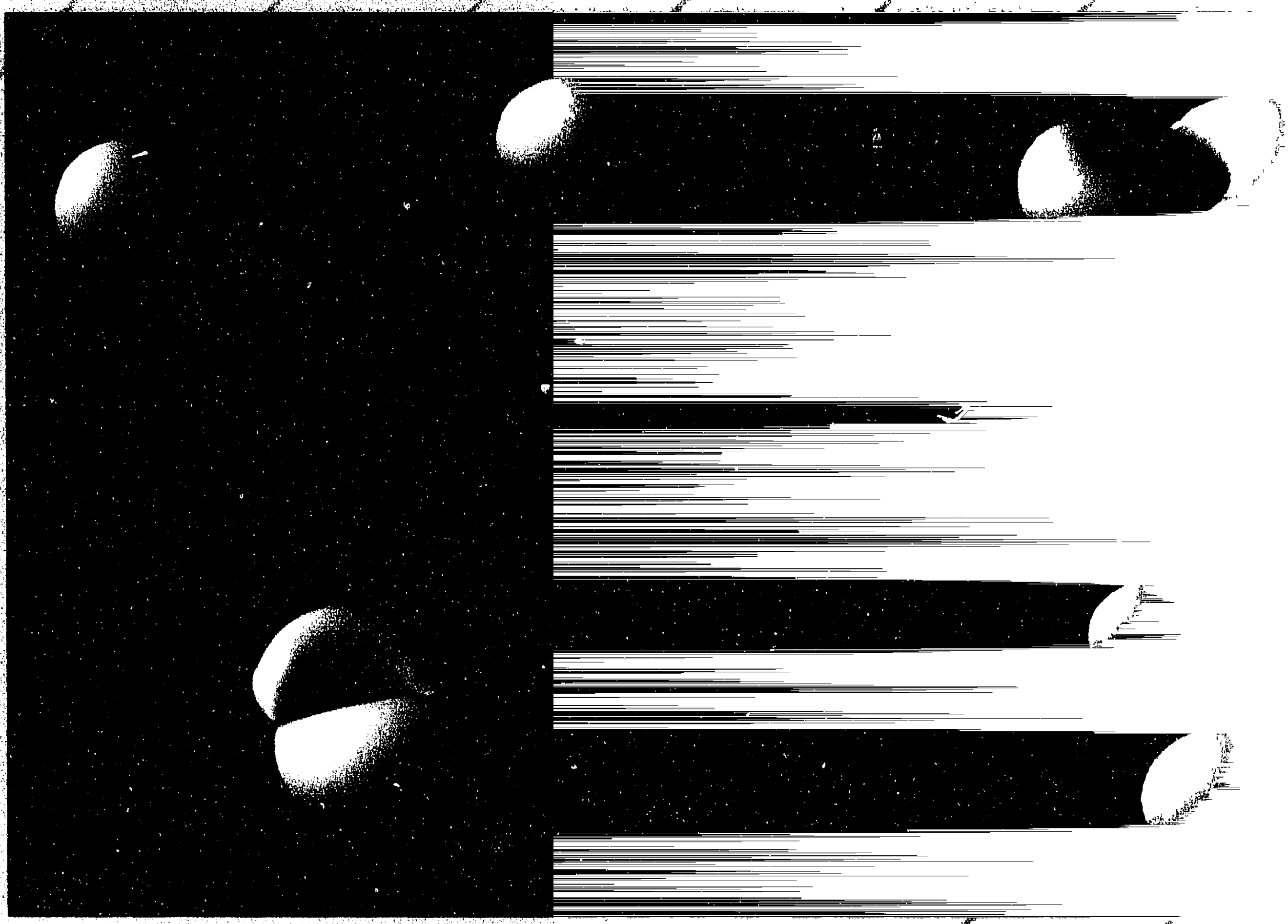

Nuclear and Atomic Science and Technology

Laboratory Directed Research
and Development FY 1992

On the previous page. A model calculation of the isosurface of energy density at four different times in the orbit of the deuteron. Nucleons start far apart, pass through an intermediate state with approximate toroidal symmetry, and separate at right angles.

New Concepts in Particle Transport

J. M. Ferguson, J. D. Rogers, and L. F. Carson

The transport equation (linear Boltzmann equation) is one of the key differential equations of physics. It is used in such diverse applications as nuclear reactor design, plasma physics studies, and theoretical astrophysics. While computer technology has made enormous strides in the past decades, the algorithms used for transport calculations are, for the most part, based on methods developed decades ago. The purpose of this study is to investigate new methods of solving the transport equation, exploiting modern computers and computer techniques.

Algorithm Analysis and Development

We are about two-thirds of the way through an analysis of the numerical errors generated by the various finite-element methods (FEMs) now in use within the transport community. In developing our methodology, we found a way to analyze the instability of the algorithms. Numerical instabilities have been at least as important an issue in choice of algorithms in this field as numerical accuracy. After developing this tool, we unexpectedly discovered a method that apparently combines high accuracy (fourth-order, for some cases) with high stability, at least in one dimension. In FY 1993, we will try to develop this method and apply it to solving multidimensional problems.

A successful parallel-processing algorithm that uses a method of domain decomposition was reported on in FY 1991 (Dorr and Ferguson, 1991). We are now upgrading this and related methods for the new generation of supercomputers. To study our computational techniques in all six dimensions of phase space, we have written a small Fortran code, which affords many opportunities for parallel processing. The code contains a relatively simple transport problem that was built into it for benchmark purposes. In the autumn of 1992, the code was used as a benchmark in choosing the first massively parallel supercomputer purchased by LLNL. We are using the code to apply our massively parallel processing methodology to the new generation of computers.

In developing the Fortran code, we made several discoveries regarding the efficient iterative solution of transport algorithms. For certain classes of problems, such as those of interest in nuclear reactor design, we found that a Jacobian iterative method, combined with overrelaxation techniques for acceleration, was as efficient as the widely used Gauss–Seidel method. Our technique affords a much better opportunity for using hundreds or thousands of processors in parallel.

In other work, we have incorporated a new algorithm into one of our busiest production codes. This algorithm is in daily use in LLNL's Applied Physics Program. We hope to improve the algorithm in FY 1993.

Nuclear Well-Logging Methods

We are developing new computational methods for solving the oil-well-logging problem. Nuclear well logging is a method of studying the materials surrounding exploratory boreholes. A tool consisting of a neutron or gamma-ray source and one or more detectors is lowered into the borehole, and the characteristics of the materials outside the borehole are inferred from the response of the detectors to neutrons and gamma rays returning from the material. Computation of this response has proven difficult. The current practice is to use the Monte Carlo method for the calculations.

We will use a finite-element solution to perform these calculations. Our method allows us to represent complicated geometry with an optimized grid. The density profiles of the different materials in the problem can be integrated directly with the functions used to represent the neutron or gamma-ray fluxes. Special methods will also be used to treat the relatively small sources and detectors in these problems. Our experience shows that by using a reasonable number of zones, we can obtain accurate solutions in this manner for complex geometries, even in three dimensions. ◆

References

Dorr, M., and J. M. Ferguson (1991), *A Killer Micro Attack on 3D Neutron Transport*, Lawrence Livermore National Laboratory, Livermore, CA, UCRL-JC-105427.

Search for and Characterization of Shape Isomers by Nuclear Spectroscopy

J. A. Becker, E. A. Henry, M. S. Weiss, S. J. Krieger, R. W. Hoff, C. R. Chinn, M. J. Brinkman, A. Kuhnert, D. R. Manatt, N. Roy, M. A. Stoyer, T. F. Wang, F. S. Stephens,* R. M. Diamond,* M. A. Deleplanque,* J. A. Cizewski,† Y. A. Akovali, ‡ J. L. Wood, C. R. Bingham,†† and H. K. Carter‡**

The atomic nucleus assumes many shapes in response to its collective and single-particle degrees of freedom. One is the superdeformed (SD) shape, where the nucleus is a prolate (football-like) spheroid with a major-to-minor axis ratio of about 2:1. Fission isomers in the actinide region, identified in the early 1960s, are examples of SD nuclei. These nuclei decay by fission (despite a fission barrier of several million electron volts) because gamma-ray decay to less-deformed normal states is inhibited by the large shape change required.

In 1986, researchers discovered high-spin SD states, with an axis ratio of 2:1, in ^{152}Dy. These states do not decay by fission (the fission barrier is substantially higher in this region than in the actinide region); they decay rapidly to states of normal deformation by gamma-ray emission. In 1988, shortly after the discovery of the high-spin SD states, Weiss predicted that SD low-spin shape isomers, with a well-developed second minimum in the nuclear potential, exist near ^{194}Hg. However, fission decay by these states is energetically forbidden, and they could have long lifetimes (Figure 1).

Weiss conjectured that shape isomers in nuclei could serve as energy storage media with an ultrahigh energy density. The energy density of a shape isomer at 5 MeV in a mercury nucleus is about 10^6 times larger than that of a conventional high-energy-density material like high explosives and only a factor of 40 less than that of a fissile nucleus like ^{235}U. At the same time, fission is forbidden for a shape isomer in nuclei near mercury, and only prompt gamma radiation would result on energy release—with no residual radioactivity. Thus, a shape isomer with a long lifetime that can be easily produced and triggered to release energy is a useful ultrahigh-energy-density material.

Our goal was to identify and characterize shape isomers to see if they have potential as an ultrahigh-density material. In our coordinated experimental and theoretical studies, we looked for shape isomeric nuclei, measured their nuclear properties, compared experimental results with theoretical calculations, and used theoretical predictions as a guide to further experiment. Prior to our work, nothing was known about SD nuclei near mass 194.

Techniques and Methods

Our experimental study of SD nuclei uses three spectroscopic approaches: heavy-ion reactions with the high-energy-resolution array (HERA) at Lawrence Berkeley Laboratory, beta-decay studies with the UNISOR online mass separator at Oak Ridge National Laboratory, and light-ion reactions with the tandem van de Graaff accelerator at LLNL. The HERA facility, a 20-germanium detector spectrometer, is sensitive to a principal signature of shape isomers, the cascade of 10 or more gamma rays (the SD band) that depopulates the

---

*Lawrence Berkeley Laboratory, Berkeley, CA.
†Rutgers University, New Brunswick, NJ.
‡Oak Ridge National Laboratory, Oak Ridge, TN.
**Georgia Institute of Technology, Atlanta.
††University of Tennessee, Knoxville.

rotational-level structure built on the isomer. We studied beta decay to see if it can populate shape isomers in nuclei near mass 194 as it does in actinide nuclei. The light-ion reactions necessarily populate the shape isomer directly because the rotational cascades decay to normal states before the shape isomer is reached.

The theoretical study of SD nuclei requires powerful computers, such as the Cray Y-MP, to perform three-dimensional microscopic calculations of nuclear potential energy surfaces using the Hartree–Fock method. These calculations identify groups of nuclei where shape isomerism at spin zero is predicted. We used the generator-coordinate method to extend the configuration-mixing formalism, thus incorporating both collective and single-particle nuclear dynamics in a coherent, quantum-mechanical formulation to study phenomena such as the depopulation of SD bands.

Experimental and Theoretical Progress

We searched for signatures of shape isomers in nuclei near mass 194, following the prediction of a low-spin shape isomer in ^{194}Hg by Weiss. In 1989, we observed an SD band in ^{192}Hg and have since identified 20 SD bands in nine nuclei using heavy-ion reactions. Presently, at least 34 SD bands in 15 nuclei are known near mass 194. We found no evidence for superdeformation in ^{190}Pb, ^{189,190}Au, and ^{188,189}Pt nuclei. These studies probably delineate the boundary of this superdeformation region in atomic number (Z) and neutron number (N). We also searched for superdeformation in the odd-mass ^{193,195,197}Pb nuclei; we do not understand why we did not observe superdeformation in these nuclei. In response to the experimentally observed extended region of SD nuclei, we performed additional calculations and defined a large region of nuclei with shape isomers (Figure 2). Comparison of calculations and experiment showed good agreement.

We experimentally characterized many important features of the SD bands built of the shape isomers, including several not observed in nuclei at normal deformation:

Decay out of the SD band. All SD bands identified so far in the mass 194 region decay to normal states by gamma-ray emission before the shape isomer is reached.

SD-band spin. We developed a method based on the nuclear rotational model to deduce the spin of SD bands. We deduced that the SD bands in ^{194}Pb and ^{196}Pb extend down to spin 6, the lowest spin SD state observed outside the actinide region.

Identical bands. Many SD bands in neighboring nuclei have energy values within 1 keV, an energy equality not obtained in normally deformed nuclear structures. The best examples of this phenomenon are the SD bands in ^{192}Hg, ^{194}Pb, and the excited SD bands in ^{194}Hg. When spins deduced in our analysis are included, the two ^{194}Hg excited bands have an alignment (relative angular momentum at a constant rotational frequency) of $i = 1\hbar$ relative to ^{192}Hg, another result not observed in normally deformed nuclei.

Linking transitions. We did not find the linking gamma rays that deexcite the SD band to normal levels in ^{194}Pb and ^{194}Hg. These transitions are necessary to establish experimentally the excitation energy and spin of the SD bands. We determined an upper limit of about 15% relative to the SD band full intensity for any single gamma ray linking the SD band with the normal states, which suggests that numerous, multiple gamma-ray cascades depopulate SD bands.

Population of SD bands by beta decay. In the actinide region, beta decay populates shape isomers. We studied the beta decay of ^{194}Bi to search for population of the known SD band in ^{194}Pb. We placed an upper limit of about 0.1% for population of this SD band by beta decay.

Oblate bands. Certain strong bands of levels identified in lead nuclei have a superficial resemblance to SD bands. We characterized these bands as belonging to nuclei with a small, oblate (doorknob-like) shape, not an SD shape.

Intraband lifetimes. We measured the SD band lifetimes in ^{194}Pb and deduced that the transition quadrupole moment is $Q_t \approx 20$ eb, which agrees well with Weiss's calculations.

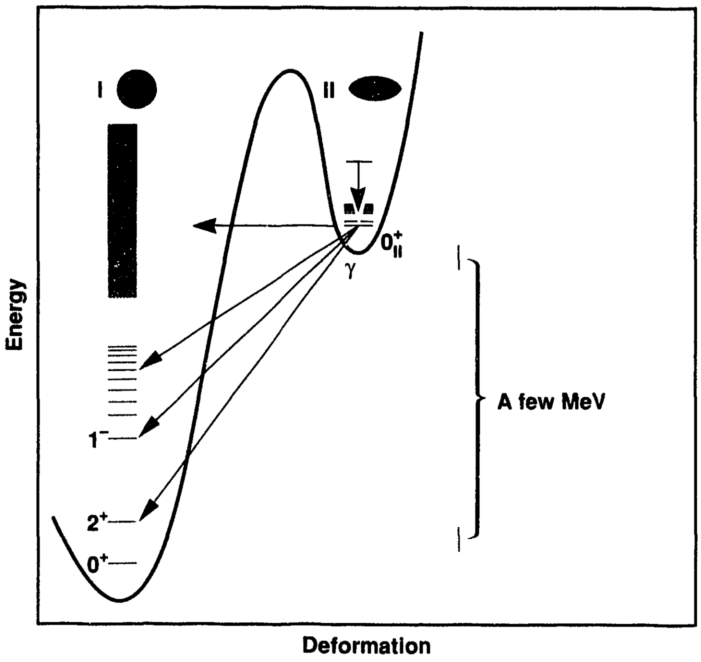

Figure 1. The nuclear potential-energy surface as a function of deformation showing the high fission barrier. The second minimum supports the shape isomer, with the rotational SD band built on it.

Our theoretical calculations have predicted or reproduced all experimentally observed characteristics:

Prediction of shape isomers in mercury, platinum, and osmium nuclei. Our initial calculations identified neutron-deficient mercury, platinum, and osmium nuclei as candidates for shape isomerism. The calculated quadrupole moment is verified by experiment for mercury and lead nuclei, and the excitation energy we estimate from our experiment on ^{194}Hg agrees with these calculations.

Expanded region of predicted shape isomerism. Calculations extended the region of predicted shape isomerism to 148 nuclei, from neutron-rich samarium to uranium.

Decay of SD bands to normal states. Calculations assuming E2 gamma-ray decay to normal states in competition with SD intraband transitions successfully reproduced the sharp depopulation of the SD bands, including the variation with neutron and proton number.

Octupole degree of freedom. We investigated the influence of the octupole (pear-like) shape on the stability and properties of SD shapes in ^{194}Pb.

Identical bands. We described identical bands in the Hartree–Fock model.

Lifetime of the shape isomer in ^{238}U. We calculated the absolute partial lifetime for E2 gamma-ray decay of the shape isomer in ^{238}U, reproducing the experimental value to within 2 orders of magnitude.

Highlights

We used the Doppler-shift attenuation method to measure the lifetimes of SD states in ^{194}Pb. The heavy-ion reaction ^{150}Sm(^{48}Ca,4n), at a beam energy of 205 MeV, populated the SD band. The target of 1.1-mg/cm^2-thick metal ^{150}Sm foil, on a 10-mg/cm^2 gold backing, produced the species of interest, slowed them rapidly, and resulted in spectra of shifted or broadened gamma-ray peaks. The forward element of HERA detected the gamma rays shifted to higher energies; the backward elements detected the gamma rays shifted to lower energies. We analyzed the distributions of the shifted gamma rays in the SD band and converted them to level lifetimes by using the slowing-down time of the recoiling nuclei in the target and gold backing. From these level lifetimes (0.1 to 0.3 ps), we calculated transition quadrupole moments Q_t using the rotational model expression. The Q_t values are all about 20 eb, in good agreement with Weiss's theoretical calculations. Constant Q_t values are not consistent with centrifugal stretching of the rotating nucleus.

We used the cranked (rotated) Hartree–Fock model to describe the phenomenon of identical bands. Our calculations show that the filling of specific orbitals can lead to SD bands with deexcitation gamma-ray energies differing by, at most, 2 keV in nuclei two mass units

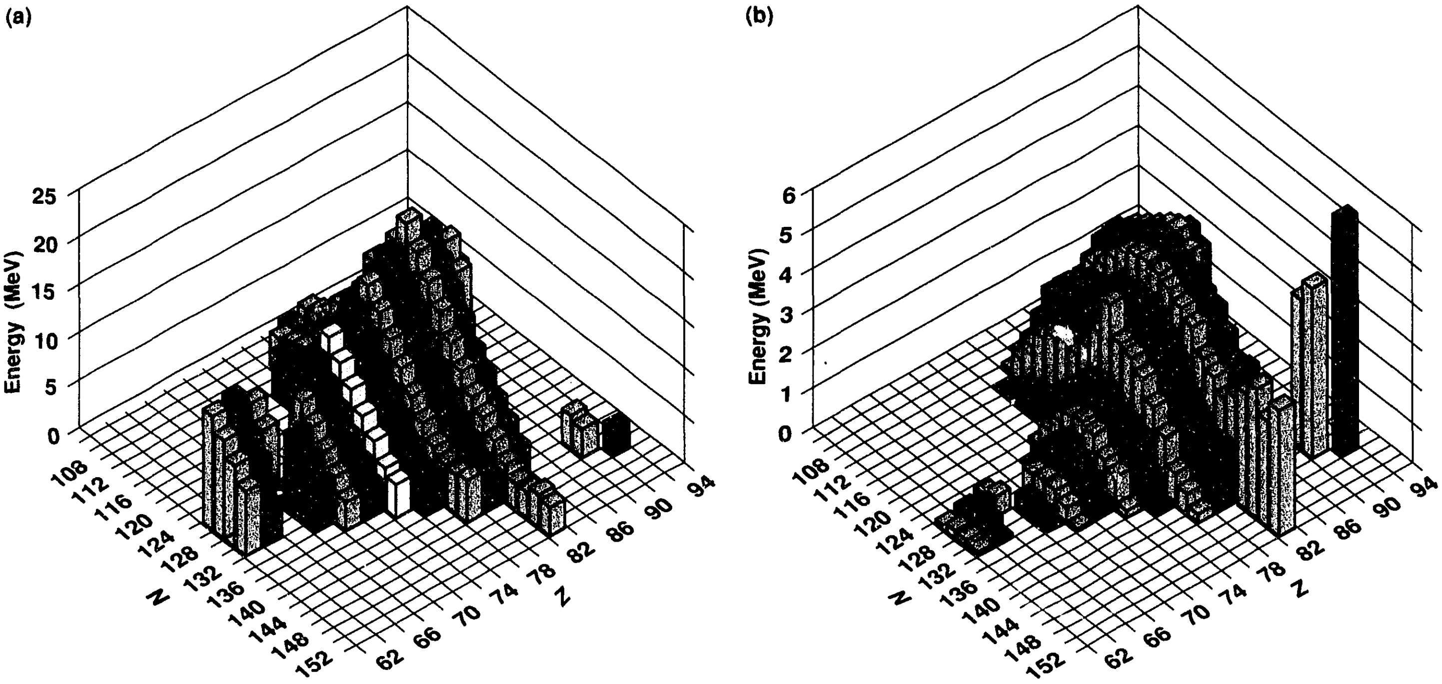

Figure 2. The calculated region of the nuclear chart showing nuclei that possess spin-zero shape isomers. Plotted as a function of proton and neutron number are (a) the excitation energy and (b) the depth of the second minimum.

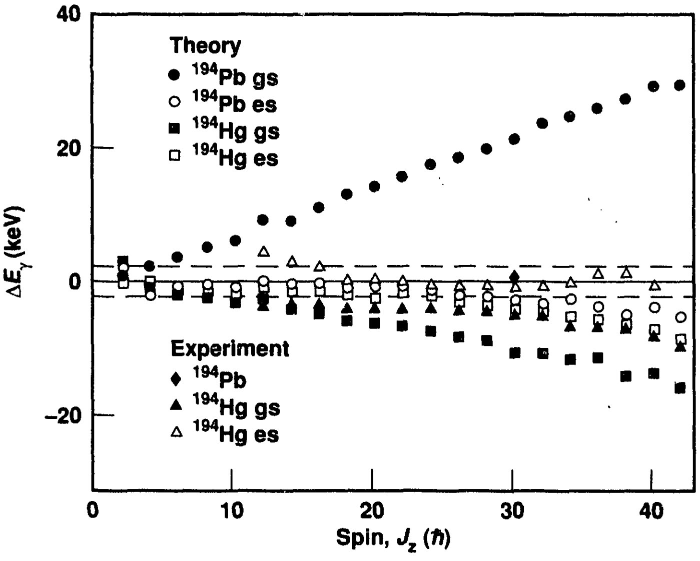

Figure 3. Experimental and theoretical results for identical bands in ^{194}Hg and ^{194}Pb relative to ^{192}Hg. Green data points refer to the lowest energy SD band; white data points refer to the excited SD band.

apart and over a range of angular momenta comparable to the experimental one. We demonstrated that the continuous change of the mean field with angular momentum is necessary for generating identical bands. The calculations (Figure 3) indicate that the SD excited bands of ^{194}Hg are identical to the SD ground band of ^{192}Hg, in agreement with experiment. However, the SD band in ^{194}Pb that is identical to the SD band in ^{192}Hg is also an excited band, contrary to the presumption by experimentalists that the observed SD band in ^{194}Pb is the SD ground-state band. Further investigation of this phenomenon is needed.

Conclusion

Our theory predicts the existence of spin-zero shape isomers in the mass 194 region. We identified experimentally the unmistakable signature of shape isomers—SD bands—in many nuclei in this mass region and characterized many of their properties. Two critical properties, the shape isomer excitation energy and lifetime, remain to be measured and compared with theory before we can identify shape isomers suitable for energy storage media. To measure and calculate these two properties, we must await more powerful spectrometers and parallel processors. ◆

Neutron–Proton Bremsstrahlung

D. Krofcheck, M. Blann, V. R. Brown, P. Anthony, B. Pohl, L. Hansen, T. C. Sangster,
S. Wender,[*] J. E. Koster,[*] R. O. Nelson,[*] M. Schillaci,[*] D. Mayo,[†] F. P. Brady,[†]
H. Nifenecker,[‡] J. A. Pinston,[‡] and H. LeBrun[‡]

Nuclei are held together by a nucleon–nucleon potential resulting largely from the exchange of mesons between nucleons. Microscopic nuclear reaction and structure calculations require knowledge of this potential as critical data. A sensitive probe of the nucleon–nucleon interaction is the electromagnetic radiation that is occasionally emitted when one nucleon scatters from another. By measuring this radiation as a function of the energy of the colliding nucleons, we probe both the nucleon–nucleon interaction as a function of internucleon separation and the role of the meson-exchange fields in determining the potential between nucleons. The neutron–proton (n,p) interaction in particular is expected to have strong contributions from the meson-exchange currents.

Measuring the n,pγ spectrum is difficult because no free neutron targets are available, and neutron beams of high intensity and with good energy resolution are generally not available. A unique opportunity exists at the Weapons Neutron Reactor at the Los Alamos Meson Physics Facility (LAMPF). There, a white-neutron source with a continuous energy distribution from a few million electron volts to more than 400 MeV with high intensity is available. We have taken advantage of this facility to measure the radiation from neutron–proton scattering processes for neutron energies up to 400 MeV.

A liquid-hydrogen target cell was designed, fabricated, and installed 18 m from a tungsten target at 15 deg to the proton beam. Protons incident on the target produced neutron pulses from the 800-MeV LAMPF beam. Two identical calorimeters were designed and fabricated (Figure 1). The calorimeters were preceded by two plastic, charged-particle veto detectors (20- × 40- × 0.4-cm^3) followed by six 9- × 18- × 1-cm^3 BaF$_2$ active gamma-ray converters, three 9- × 36- × 1-cm^3 Cherenkov detectors, and three 9- × 36- × 0.4-cm^3 energy-loss detectors. Each calorimeter was made up of 16 NaI crystals, each 10 × 10 × 40 cm^3. Signals from all elements were detected via 5-cm photomultiplier tubes.

When an n,p-scattering event took place with gamma radiation being emitted into the detector system, approximately 30% of the gamma rays were converted into e^+e^- showers in the BaF$_2$ elements. We recorded

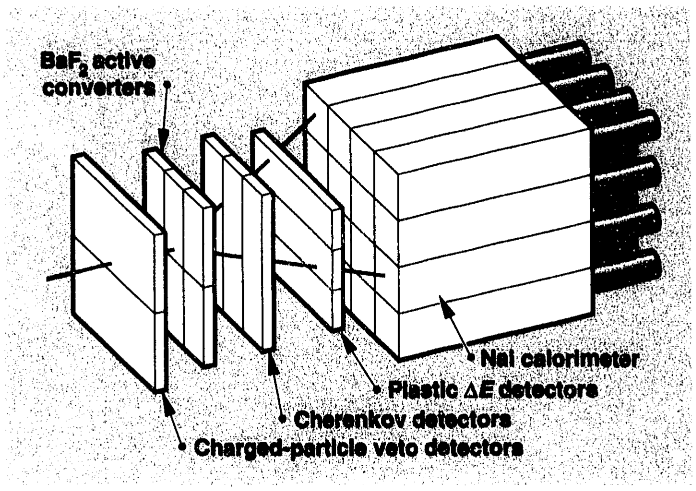

Figure 1. Schematic of a neutron–proton bremsstrahlung detector assembly. The function of each element is described in the text. The photomultiplier tubes and light pipes have been omitted for clarity.

---

[*] *Los Alamos National Laboratory, Los Alamos, NM.*
[†] *University of California at Davis.*
[‡] *Institut de Science Nucléaire, Grenoble, France.*

these signals and the delay time from the proton pulse that produced the neutron. Then we deduced the neutron energy from this "time of flight." The e^+e^- shower penetrated the Cherenkov counters, which rejected almost all events except electron showers. The e^+e^- shower then penetrated the energy-loss counter, further verifying that it was an electron shower, and finally penetrated the NaI calorimeters where the main energy was deposited. A time coincidence of a few nanoseconds was required between detector elements. Time and pulse-height information was recorded for all elements of the detector assemblies.

Beam time for this experiment ran from late June to early October 1992. Copious amounts of single-event-mode data were taken. Target-in data are considerably more intense than target-out data, verifying a favorable signal-to-noise ratio. Preliminary data sorts confirm a successful experiment in terms of statistics, time, and energy resolution of events. We believe that we will have met all objectives of our experiments when data analyses are completed and the results published. The results will be compared with quantal theories for the process, either verifying the theoretical predictions or providing guidance for further theoretical advances. ◆

High-Energy Physics Detectors at the Superconducting Super Collider

C. R. Wuest, E. Ables, R. M. Bionta, M. H. Capell, A. K. Chargin, G. A. Deis, O. D. Fackler, C. V. Johnson III, M. E. Lowry, K. G. McCammon, L. R. Pedrotti, R. H. Sawicki, K. M. Skulina, K. van Bibber, and T. J. Wenaus

LLNL is a founding member of the Gamma, Electron, and Muon (GEM) detector collaboration at the Superconducting Super Collider (SSC) Laboratory in Dallas, Texas. At this laboratory, protons will be accelerated in underground countercirculating rings 87 km in circumference and will be made to collide at an energy of 40 TeV inside special detector systems.

The GEM detector is one of two highly specialized detectors designed to track and measure the energies and electric charges of particles that emanate from these catastrophic collisions. New particles such as the top quark and the Higgs boson, from which quarks and leptons derive their masses, will likely be produced in large quantities at the SSC.

The GEM detector consists of five subsystems, all of which are dedicated detectors in their own right (Figure 1). These subsystems are

1. A large solenoidal superconducting magnet.
2. The central tracker, which pinpoints the location of the proton collisions and provides initial tracking information on particles.
3. The electromagnetic calorimeter, which tracks and measures the energy of electrons and gamma rays.
4. The hadron calorimeter, which tracks and measures the energy of pions, protons, neutrons, and other forms of hadronic matter.
5. The muon tracking chambers and muon trigger.

The last subsystem identifies and measures the momenta of the weakly interacting muons resulting from the decay of new fundamental particles. All of the instrumentation subsystems are located inside the large solenoidal superconducting magnet.

Contributions to GEM

LLNL's participation in GEM has involved physicists, engineers, and technologists from different areas of the Laboratory working together. In FY 1992, we continued to design new types of physics detectors for the calorimeter and muon subsystems of the GEM detector. Early in FY 1992, the superconducting magnet work, which was described in last year's annual report (Wuest et al., 1991), was transferred to SSC funding. This transfer was a successful example of a transition from LDRD to a completely funded outside program.

Our FY 1992 program has consisted of the following tasks:

Liquid-scintillator hadron calorimetry. LLNL continued its collaboration with Oak Ridge National Laboratory and the Institute for Theoretical and Experimental Physics (ITEP) on liquid-scintillator detectors for the GEM hadron calorimeter. This work culminated in LLNL's participation in a series of beam tests at the ITEP proton synchrotron in Moscow in December 1991.

Muon drift-chamber prototyping for the GEM detector. LLNL initiated a collaboration with physicists at the Massachusetts Institute of Technology to design and build resistive plate counters (RPCs) for the GEM muon trigger system. Our work has resulted in the identification of new materials that have improved key characteristics of RPCs by a factor of 100 over previous designs.

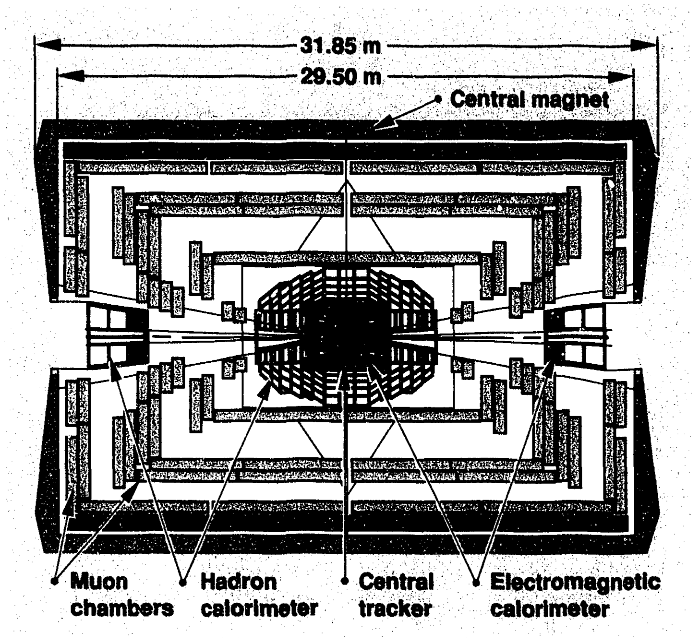

Figure 1. Side view of the GEM detector. This detector consists of five distinct subsystems arranged in concentric cylinders around the interaction point where protons will collide. All subsystems are located inside a large solenoidal superconducting magnet. The subsystems are the central tracker, the electromagnetic calorimeter, the hadron calorimeter, the muon system, and the superconducting magnet.

Research and development on electrooptics for GEM. Results obtained from the application of LLNL-developed electrooptic modulators include the effects of magnetic fields and high-energy, proton-beam irradiation of electrooptic systems.

Research and development on mechanical processing of barium fluoride scintillation crystals. Our work resulted in adaptation of the Laboratory's Nova optics technology to the precision machining and polishing of these crystals for the GEM electromagnetic calorimeter. We have also studied the application of ultraviolet-reflecting coatings to crystals to increase light-transport efficiency. This summer, LLNL physicists and engineers visited their counterparts in China to develop pilot plants for mass production of the calorimeter.

GEM detector alignment. We are developing a coupled engineering and physics effort for alignment of the GEM detector subsystems. A dedicated alignment group will develop alignment procedures and systems. We are taking advantage of our experience in aligning large complex systems at Nova and in the Nuclear Test Program to provide sensor systems and techniques that will allow precise determination of detector elements within GEM.

Collaboration with the L3 group at CERN. We continued to implement data-analysis and event-simulation computer codes on LLNL's massively parallel computer system, the BBN TC-2000. This work has significantly improved the processing capability of the L3 program. In addition, it has given us the experience necessary to develop advanced simulation and analysis systems for GEM. ◆

References

Wuest, C. R., et al. (1991), "High-Energy Physics Detectors at the Superconducting Super Collider," Laboratory Directed Research and Development FY91, Lawrence Livermore National Laboratory, Livermore, CA, UCRL-53689-91, pp. 93–97.

Design and Construction of a Pure-Positron Trap

T. E. Cowan, R. H. Howell, B. R. Beck, J. H. Hartley, J. L. McDonald, R. R. Rohatgi, and J. Fajans*

We designed and built an experiment to search for resonant states in positron–electron scattering in the energy range of 1 to 2 MeV. This energy range is chosen because of the anomalous positron–electron peaks emitted from superheavy ion–atom collisions, which appear to reflect the production and decay of a new family of neutral particle-like objects having mass of 1.6 to 1.8 MeV/c^2 (Cowan et al., 1986; Salabura et al., 1990).

Researchers have tried to detect these resonances through the time-reversed scattering channel using positron beams incident on thin foils (Tsertos et al., 1991; Wu et al., 1992). In each case, however, their experimental sensitivity has been limited by a broadening of the center-of-mass collision energy caused by the large momentum of the bound target electrons. Our experiment circumvents this limitation by using a high-resolution electron beam incident on a cold-positron gas target, which is confined in a Penning trap as a single-component, pure-positron plasma. We expect improvement in sensitivity by a factor of 100 over previous experiments.

Figure 1 shows the principal components of our experiment. A 60-cm-long Penning trap in a 60-kG solenoid magnetic field is used to capture and confine positrons, which are produced by the positron-production facility at the LLNL 100-MeV linear accelerator (linac). This facility provides the intense beams of low-energy positrons, and its unique short-pulse capability allows efficient trapping of the positrons by simple time-of-flight techniques. Once confined, the positrons cool by cyclotron radiation to the 4.2-K wall temperature of the trap. The resulting pure-positron plasma, with a density of 10^{10} e^+/cm^3, is used as a cold gas target through which a high-resolution electron beam (about 1 to 3 MeV) is injected.

---

*University of California at Berkeley.

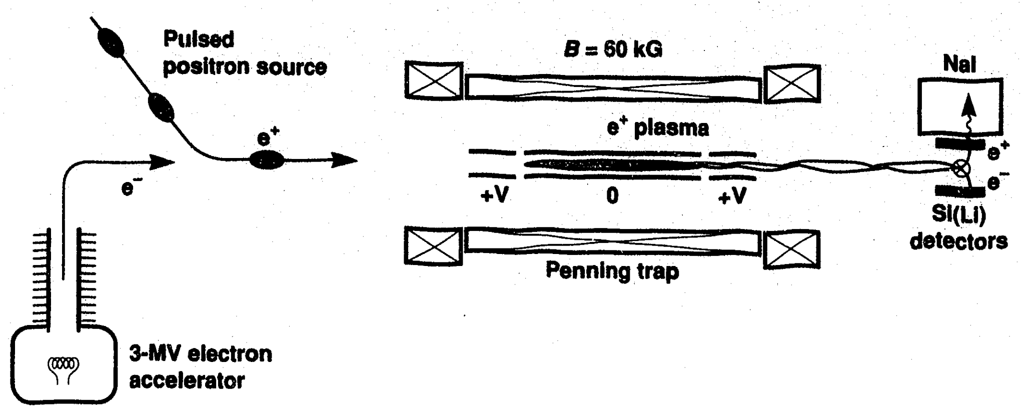

Figure 1. Schematic of the LLNL positron–electron scattering experiment. A positron plasma is formed by capturing positrons from the LLNL positron production facility. An electron beam is then injected, and scattered positrons and electrons are transported from the solenoid into a detector array.

The electron beam is produced by a 3-MV Pelletron accelerator. Scattered positrons and electrons are transported from the solenoid along magnetic-field lines to an array of solid-state detectors where their energies are measured. The positrons are distinguished from the electrons by both their orbital helicity and by the coincident detection of their characteristic 511-keV annihilation photons in sodium iodide scintillators. As we vary the electron-beam energy, we search for resonant enhancements in the positron–electron scattering rate. Such enhancements signal the formation and decay of new particle-like states having masses equal to the total center-of-mass energy in the positron–electron collisions.

Figure 2 compares the sensitivity expected in our experiment to that achieved in previous experiments. The relevant parameter range is plotted as the energy-integrated resonance signal vs the lifetime of the particle state. The green line denotes the "unitarity limit" (the maximum possible resonance intensity, assuming the particle can decay only to an e^+e^- pair), below which new particles may reside. The shaded area denotes the regions where new particles are excluded. The previous most sensitive experiments exclude the region above curves A and B. Our experiment should attain a sensitivity 100 times greater than previous experiments. We expect to detect any new resonances down to curves C, D, and E.

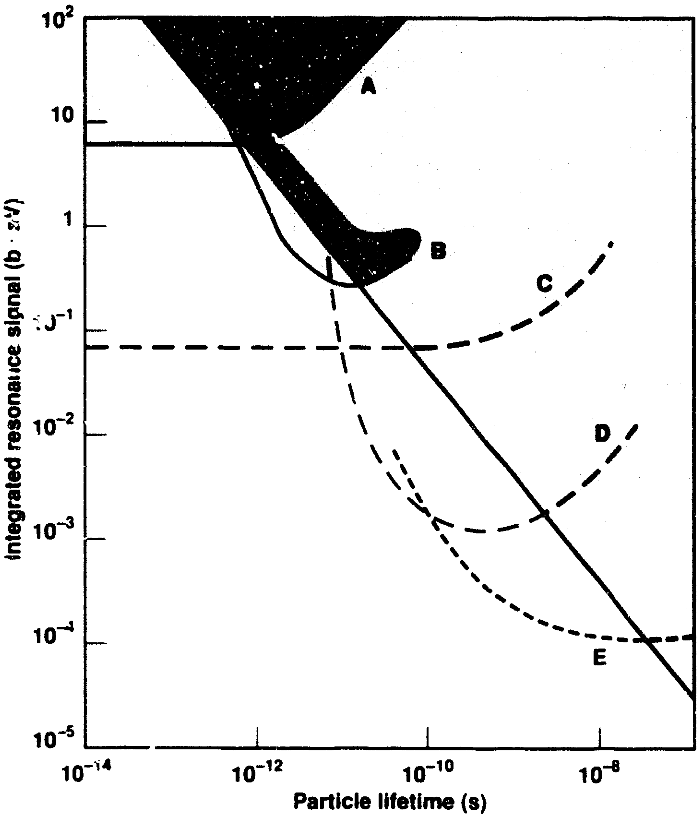

Figure 2. Experimental parameter space. Green line shows unitarity limit. Curves A and B show previous best experimental limits. Curves C, D, and E show expected limits for our experiment. Shading denotes excluded regions.

All major procurements and construction for this experiment have been completed. The solenoid specifications were unusual in that a high degree of magnetic uniformity was required over the 60-cm trap region to achieve usefully long positron plasma confinement times. The solenoid has achieved the required uniformity. Figure 3 shows the trap electrode structure. Long plasma confinement requires precision in the trapping electric fields. The precision gold-plated cylindrical copper electrodes are therefore mounted on a special ceramic V block, which is designed to maintain a 2.5-μm trap concentricity and straightness over the 60-cm length. We developed special low-thermal-conductivity, electrically shielded, cryogenic leads for operating the trap electrodes. A computer control system and a two-dimensional plasma-imaging system (using a microchannel-plate and charged-couple device camera) were also developed for the trap and have been in full operation for almost two years on a trap at UC Berkeley.

We used only nonmagnetic materials in and around the trap to maintain high magnetic uniformity. An aluminum, ultrahigh-vacuum chamber is used and is

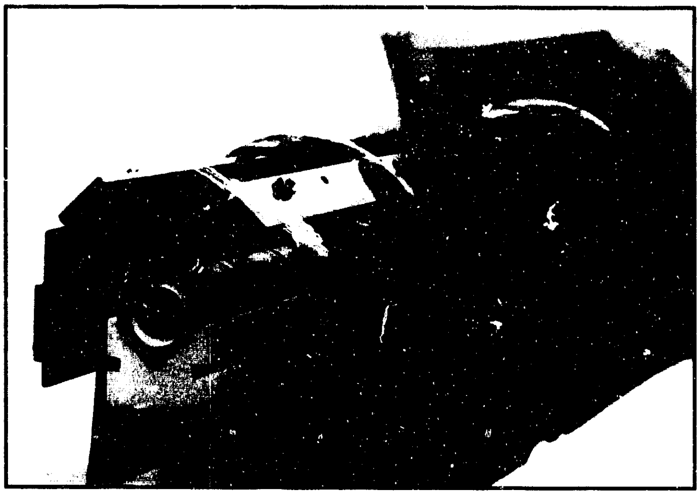

Figure 3. Electrode structure of the trap, showing cylindrical electrodes on precision ceramic V block.

shown attached to the end of the solenoid magnet in Figure 4. The figure also shows the incoming electron and positron beamline, with its "pancake" coils that form a solenoidal guide field for the low-energy positrons. Once the trap assembly is complete, we will begin trapping positrons from the linac positron production facility. Computer simulations of the positron beam and Penning trap suggest that a simple, passive time-of-flight technique has a high theoretical trapping efficiency. We therefore hope to quickly achieve the design density of the plasma of 10^{10} e^+/cm^3.

The 3-MV Pelletron accelerator has been installed and successfully tested. Its beam energy stability (<200 eV, peak-to-peak ripple at 2.7 MeV) exceeds the contract specifications, as does the operating energy range (up to 3.2 MeV) and maximum beam current capability. Figure 5 shows the Pelletron accelerator, 90-deg analyzing magnet, and beamline for the electron beam.

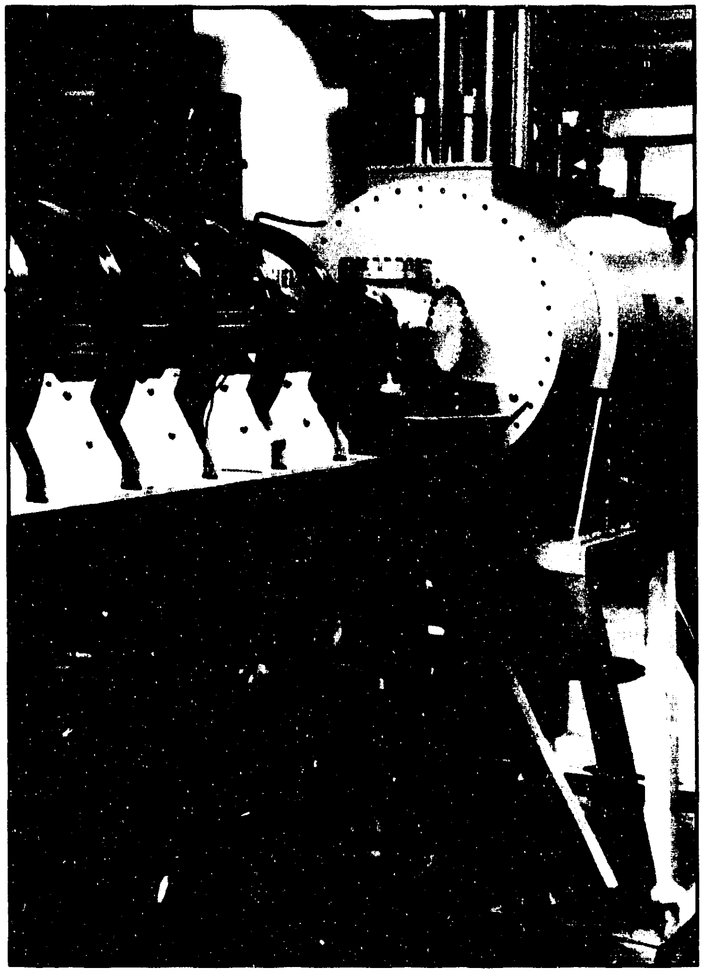

Figure 4. Solenoid magnet in experimental area. The aluminum vacuum chamber and beamline for injecting positrons and electrons into the trap are visible in foreground.

A prototype of the coincident positron–electron detection system designed for this experiment has been built and tested using a smaller superconducting solenoid. Its high detection efficiency proved immediately applicable to attack many remaining questions of the original heavy-ion positron–electron experiments. A dedicated system, the High-Efficiency Coincident Lepton Spectrometer (HECLS), has been built and is operational at Texas A&M University's K500 superconducting cyclotron. In a series of experiments, funded independently by the DOE Office of Energy Research, Division of High Energy and Nuclear Physics, the HECLS is being used to explore the production of correlated e^+e^- peaks in lighter collision systems than studied previously (Cowan et al., 1991).

The unique technology afforded by the pure-positron plasma trap enables a variety of new research possibilities. In addition to the positron–electron scattering experiment, we anticipate that the trap will foster important new research programs in pure-positron and electron plasma physics, electron and positron spin-polarization physics, and production of antihydrogren beams for fundamental tests of how established physical laws apply to antimatter (Cowan et al., 1992). ◆

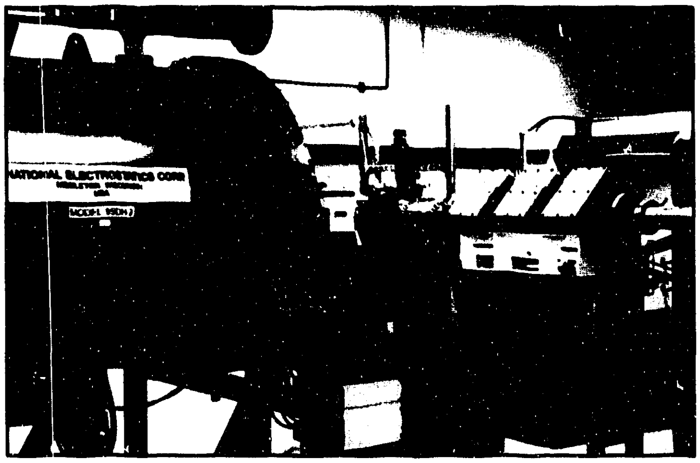

Figure 5. Pelletron accelerator and electron beamline.

References

Cowan, T. E., H. Backe, H. Bokemeyer, H. Folger, J. S. Greenberg, K. Sakaguchi, D. Schwalm, J. Schweppe, K. E. Stiebing, and P. Vincent (1986), "Observation of Correlated Narrow Peak Structures in Positron and Electron Spectra from Superheavy Collision Systems," *Phys. Rev. Lett.* **56**, 444.

Cowan, T. E., B. R. Beck, J. H. Hartley, R. H. Howell, R. R. Rohatgi, J. Fajans, and R. Gopalan (in press), "Development of a Pure Cryogenic Positron Plasma Using a Linac Positron Source," in *Proc. Antihydrogen Workshop* (CERU and Max Planck Institute for Quantum Optics, Garching, Munich, Germany).

Cowan, T. E., M. W. Clark, J. H. Hartley, J. L. McDonald, J. W. McDonald, R. R. Rohatgi, D. H. G. Schneider, R. L. Watson, V. Horvat, and W. H. Trazaska (1991), *Search for Correlated Positron–Electron Peaks in Xe + Au Collisions*, Lawrence Livermore National Laboratory, Livermore, CA, UCRL-JC-110841.

Salabura, P., H. Backe, K. Bethge, H. Bokemeyer, T. E. Cowan, H. Folger, J. S. Greenberg, K. Sakaguchi, D. Schwalm, J. Schweppe, and K. E. Stiebing (1990), "Correlated e^+e^- Peaks Observed in Heavy-Ion Collisions," *Phys. Lett. B* **245**, 153.

Tsertos, H., P. Kienle, S. M. Judge, and K. Schreckenbach (1991), "Experimental Exclusion of Neutral Resonances in Bhabha Scattering at MeV Energies," *Phys. Lett. B* **266**, 259.

Wu, X. Y., P. Asoka-Kumar, J. S. Greenberg, S. D. Henderson, H. Huomo, K. G. Lynn, M. S. Lubell, R. Mayer, J. McDonough, B. F. Phlips, and A. Vehanen (1992), "A Search for Low-Mass States in Elastic e^+e^- Scattering," *Phys. Rev. Lett.* **69**, 1729.

A Large-Scale, Dark-Matter Axion Search

K. van Bibber, P. Anthony, W. Stoeffl, R. L. Patrick, S. S. Shen, D. S. Slack, P. Sikivie,[*]
N. S. Sullivan,[*] D. B. Tanner,[*] N. A. Golubev,[†] O. V. Kazachenko,[†] V. Kuzmin,[†] A. Pashenkov,[†]
I. V. Sekachev,[†] L. J. Rosenberg,[‡] C. A. Hagmann,[**] D. M. Moltz,[††] F. Villa,[‡‡] and F. A. Nezrick[***]

What constitutes the dark matter of the universe is still a mystery. One of the best candidates, however, is a very light elementary particle called the axion, which has been predicted to exist but is as yet undiscovered. The mass of the axion has been constrained to be between about 1 μeV and 1 meV. Paradoxically, the lighter the mass of the axion, the greater the total fraction of the mass of the universe that axions would compose. If our galactic dark-matter halo were made up of axions, their local density would be truly prodigious, about 100 trillion in the volume of a sugar cube.

Axions, however, are believed to interact extremely weakly with ordinary matter (quarks, gluons, and leptons) and radiation (photons), so little hope was held that the axion would ever be found. But Pierre Sikivie of the University of Florida showed in 1983 that dark-matter axions might be detected by their conversion into microwave photons.

The experimental realization of Sikivie's method has three essential components. The first is a very large high-field magnet, ideally a superconducting solenoid; the second is one or more microwave cavities of high Q, or quality factor; and the third is state-of-the-art, ultralow-noise microwave amplifiers. The cavity is tuned slowly, and when the frequency of the cavity (times Planck's constant) equals the mass of the axion (times the speed of light squared), the strong magnetic field stimulates the axion to decay into a microwave photon in a standing wave of the microwave cavity. The extremely weak signal is amplified and detected as a sharp line in the power spectrum. Two pilot experiments were performed in the late 1980s, one at the

---

[*] University of Florida, Gainesville.
[†] Institute for Nuclear Research of the Russian Academy of Sciences, Moscow.
[‡] Massachusetts Institute of Technology, Cambridge.
[**] University of California at Berkeley.
[††] Lawrence Berkeley Laboratory, Berkeley, CA.
[‡‡] Stanford Linear Accelerator Center, Stanford, CA.
[***] Fermi National Accelerator Center, Batavia, IL.

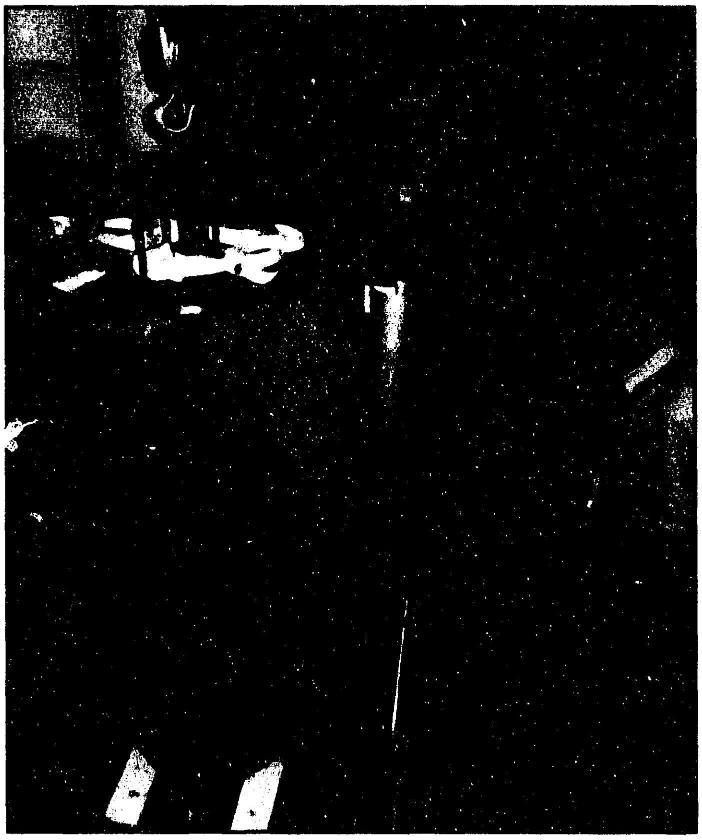

Figure 1. The INR four-cavity array at LLNL. Also shown are members of the project team, Christian Hagmann (left) from UC Berkeley and Nikolai Golubev from the INR of the Russian Academy of Sciences, Moscow.

University of Florida and the other at Brookhaven National Laboratory, but they fell short of the power sensitivity thought to be required to detect the axion by a factor of 10 to 1000.

During FY 1992, we concluded engineering and conceptual-design studies toward a large-scale search for dark-matter axions. Our principal achievement was a joint microwave-cavity prototyping exercise between LLNL, the Institute for Nuclear Research (INR) of the Russian Academy of Sciences, and the University of Florida. An array of four microwave cavities was fabricated by INR at its laboratories in Troitsk and shipped to LLNL for evaluation at 4 K in a large liquid-helium dewar in the Magnetic Fusion Energy complex (see Figure 1). Three Russian scientists visited LLNL in September 1992 to participate in the tests.

The cavities are made of high-purity copper electroplated onto stainless steel. Each is 180 mm in diameter and 800 mm long. They can be tuned up or down by about 25% from their central frequency by the radial displacement of copper or sapphire rods inside. The quality factors of the cavities at 300 K have been measured to be 18,000, about 40% of the theoretical maximum expected at room temperature.

It is now realistic to propose a next-generation axion search that may be sensitive enough to detect cosmological axions. Such a search is feasible in view of recent advances in ultralow-noise microwave amplifiers, the compact and efficient high-field magnets now available, and ongoing cavity studies. ◆

Search for 17-keV Neutrino Emission in the Beta Decay of Gaseous Tritium

W. Stoeffl

In 1985, Simpson interpreted a distortion in the low-energy end of the tritium beta spectrum as evidence for a 3% neutrino mixing with a heavy neutrino mass of 17 keV (Simpson, 1985). If the 17-keV anomaly in tritium and other isotopes represents a true particle and not just a kink in an experimental spectrum, it would have profound implications for the field of particle physics and cosmology. Several recent measurements have confirmed the 17-keV neutrino in other isotopes besides tritium.

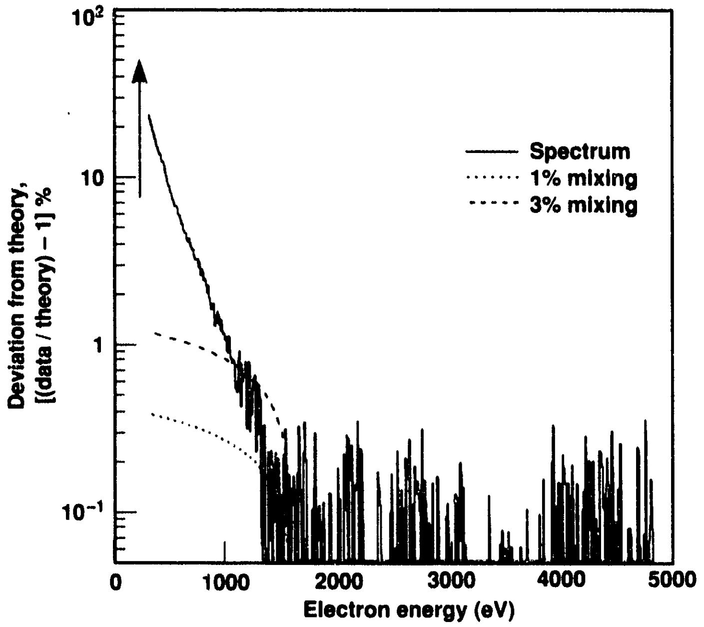

Figure 1. Deviation of the tritium beta-decay spectrum from beta-decay theory. Also shown are the predicted deviations caused by a 17-keV neutrino with 1% and 3% mixing. Shakeoff and autoionization electrons produce a peak that is 25,000% higher in intensity. This peak is indicated by the arrow.

Spectrometric Analysis of Tritium

The LLNL Nuclear Chemistry Division possesses a unique spectrometer for testing the electron spectrum of gaseous tritium. The low-density gas source and very high resolution of our spectrometer enable us to avoid the many pitfalls associated with tritium embedded in solids.

The sudden but small increase in the spectrum of tritium happens at a low energy of just 1.6 keV. Although the 17-keV neutrino has been seen in several more-energetic nuclear decays, tritium is unique because of its simplicity and because the original hint for the 17-keV neutrino came from it.

We spent FY 1992 calibrating the wide-range efficiency of our spectrometer. To see the tiny effect of the 17-keV neutrino, we need a precision of 0.1% efficiency over a wide energy range. This value is about a factor of 20 more precise than that at which standard nuclear physics germanium detectors are calibrated. The efficiency linearity of our system could only be calibrated with the tritium spectrum itself. We relied on the precision of the instrument and the fact that the tritium spectrum should always look the same regardless of the analyzing energy and the setting of the magnets. The tuning required many thousands of tritium spectra. We now believe that we know the response of our spectrometer with sufficient precision.

An Unexpected Outcome

The first full-scale runs of the tritium spectrum revealed a surprising result, as shown in Figure 1. The tritium spectra from Simpson had the correct shape, but the interpretation of the shape is not consistent with a 17-keV neutrino. It is intriguing and a conspiracy of nature that the onset of the increased rate agrees to about 50 eV for the two experiments. We excluded scattering effects as the cause of the rate increase. Since we can measure the tritium spectrum from the endpoint at 18.6 keV down to an actual energy of 0 eV, we can follow the shape of this tiny kink over a much longer range than Simpson could. His silicon and germanium detectors have an intrinsic noise threshold of about 800, rather close to the kink at 1.6 keV.

The shape of the low-energy increase looks like a perfect exponential rise toward zero energy. We assume that those electrons may be partly caused by energetic shakeoff in the tritium decay process itself. But there is no substantial theory to allow for such a high-energy transfer. Since Simpson saw the kink in a "calorimetric" detector, which counts all released energy, shakeoff alone cannot be the cause for his effect. But small corrections to the actual beta-decay strength, caused by the interaction between the nucleus and the orbiting electrons, may be the explanation.

This field of physics has not been explored well, mostly because of the lack of adequate instruments for probing this part of beta spectra. We plan to investigate our finding in more detail and with different spectrometer settings to ensure that the observed effect is not an artifact of our experimental apparatus. ◆

References

Simpson, J. J. (1985), "Evidence of Heavy-Neutrino Emission in Beta Decay," *Phys. Rev. Lett.* **54**, 1891.

Nuclear Matter at Extreme Temperatures and Densities

J. Thomas and T. C. Sangster

According to theory, in the first few microseconds following the big bang, the universe consisted only of a bubbly plasma of quarks and gluons. The physics of relativistic heavy-ion collision allows us to study the hypothesis of this elementary drama and has been declared by the National Academy of Sciences to be the number one nuclear science priority of the 20th century. In 1997, when the Relativistic Heavy Ion Collider (RHIC), located in Brookhaven, New York, is completed, a new and powerful tool will be available to study heavy-ion collision. RHIC will accelerate heavy-ion beams in countercirculating rings, causing them to collide violently and re-creating, for the first time, the original conditions of the universe. The resulting dense matter is expected to exceed 10 times the density of normal nuclei. The temperatures will range from 200 to 400 MeV.

Quark and Gluon Plasma

LLNL is leading the magnet subsystem design for one of the RHIC particle detectors. We are working with Brookhaven, Los Alamos, and Oak Ridge national laboratories, and 50 other universities and institutions worldwide in this effort. Our detector, PHENIX, will observe photons, hadrons, electrons, muons, and other particles emitted by the heavy-ion collisions.

PHENIX will measure particle energies and correlations with great precision over a wide dynamic range. We hope to observe the quark and gluon plasma and to study its dimensions, its temperature, and the properties of exotic particles produced by the plasma. For example, we will measure the kaon spectra to determine if there is an excess production of matter derived from strange quarks, which do not ordinarily occur in nature.

In FY 1992, we conducted an extensive series of studies to optimize the performance of PHENIX and designed specific subsystems to identity particles. We have increased the detector's sensitivity to the ϕ meson by studying its decay into π mesons. Changes in the ϕ meson are important because they indicate the presence of quark and gluon plasma. We have completed a systematic study of the theoretical computer codes that predict the properties of the plasma and that have been key in developing an integrated simulation program, PISA, for the computer-aided design of the detector.

We are designing the single largest piece of the PHENIX detector: the 800-ton magnet. During FY 1992, we completed an extensive study of two options for the magnet: a cryogenic superconducting magnet and a conventional warm magnet. We chose the warm magnet because it is less expensive to manufacture. We are refining the design of the magnetic coils as well as our cost estimates for the coil construction, magnet, and support steel. To better understand construction techniques, we built a 0.25-scale model of the magnet in FY 1992. ◆

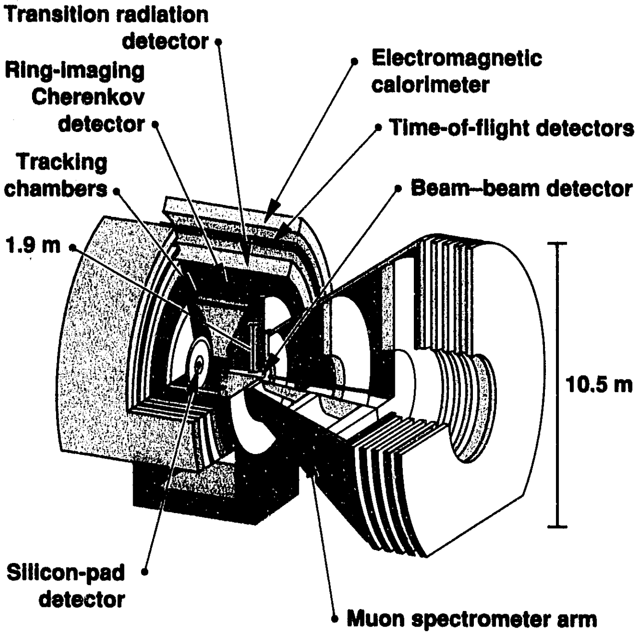

Figure 1. Cross section of PHENIX detector. The 15-m-tall, 20-m-long detector will observe the quark and gluon plasma produced by violent ion-beam collisions. The beam–beam detector catches the fragments resulting from the collisions, and the central magnet has several other particle-tracking detectors.

Mass Measurements in Ion Traps

P. Beiersdorfer, R. E. Marrs, B. R. Beck, and L. Schweikhard*

Precise measurements of highly charged ions are of great interest for testing the predictions of quantum electrodynamics in superhigh fields and constructing accurate relativistic wave functions. LLNL has been unsurpassed in its ability to study highly charged ions. This leadership role was reaffirmed with the advent of LLNL's Super-EBIT, an electron-beam ion trap that allows production and trapping of ions with a charge as high as U^{90+}, as well as with the RETRAP system for cooling and storing highly charged ions in precision trap configurations (Knapp and Marrs, 1991).

Our New Mass-Spectrometry System

Building on these resources, we are developing a portable mass-spectrometry system for use on ion traps to measure fundamental atomic constants that have eluded measurement with existing techniques. This

---

*Institut für Physik, Johannes Gutenberg Universität Mainz, Mainz, FRG.

system is designed to (1) measure absolute electron–ion interaction cross sections, (2) "weigh" the energy fraction associated with quantum electrodynamics, and (3) detect the decay products of a form of nuclear decay that can take place only when an ion is stripped bare of its atomic electrons.

Mass-spectrometry systems employ radiofrequency waves that resonate with the motion of an ion in a magnetic field. The frequency of this so-called ion-cyclotron motion is proportional to the ratio of the ion's charge and mass, Q/M. As a result, ions with different charges or masses resonate at different frequencies with the radio waves and can thus be distinguished from one another. Ion-cyclotron mass spectrometers are an established tool in the chemical sciences and materials research (Marshall and Grosshans, 1991).

The challenge in developing a system for highly charged ion research is twofold. First, we require the proper facility for producing and trapping highly charged ions. Second, because of the high charge states involved, the mass spectrometer must handle frequencies much higher than those used for studying chemical reactions.

We have successfully addressed both issues. By applying exciter fields to ions in the Super-EBIT device, we have shown that we can couple to the motion of highly charged ions and manipulate the ions in the trap. Furthermore, we have developed a high-frequency system that enables us to excite and detect ion motion with frequencies as high as 100 MHz (Schweikhard et al., in press). The system was tested on He^+ in a 7-T field by our collaborators at Ohio State University (Alber et al., in press), and very good mass resolution was achieved (Figure 1).

Our efforts now focus on building an interface between the high-resolution, high-frequency system and Super-EBIT. Two experiments are planned for the near future: manipulation of ions of different ionization stages in the trap, and measurements of absolute electron–ion interaction cross sections. The experience gained from these experiments will be crucial for achieving our ultimate goal: weighing the energy fraction in bare uranium arising from quantum electrodynamics. ◆

References

Alber, G., A. G. Marshall, N. C. Hill, L. Schweikhard, and T. L. Ricca (in press), "Ultrahigh-Resolution Fourier Transform Ion Cyclotron Resonance Mass Spectrometer," *Rev. Sci. Instrum.*

Knapp, D., and R. Marrs (1991), "Super-EBIT: A Trap for Very Highly Charged Ions," *Laboratory Directed Research and Development FY91,* Lawrence Livermore National Laboratory, Livermore, CA, UCRL-53689-91, p. 60.

Marshall, A. G., and P. B. Grosshans (1991), "General Theory of Excitation in Ion Cyclotron Resonance Mass Spectrometry," *Anal. Chem.* **63**, 215.

Schweikhard, L., G. M. Alber, and A. G. Marshall (in press), "High Frequency Fourier Transform Ion Cyclotron Resonance," *J. Am. Soc. Mass Spectrom.*

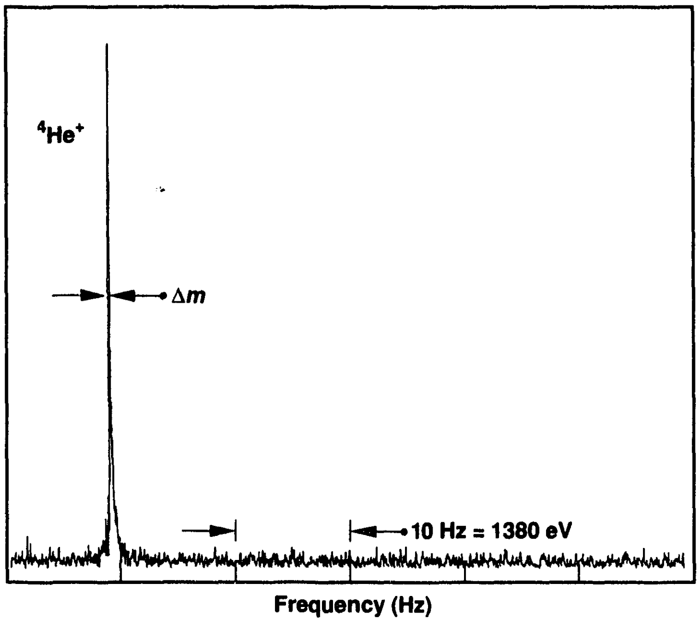

Figure 1. Mass spectrum of He^+ in a 7-T magnetic field. The mass resolution is 5 ppb or 18.2 eV.

The IMPACT Project

J. H. Hammer, M. S. DiCapua, J. L. Eddleman, C. W. Hartman, H. S. McLean, and A. W. Molvik

Accelerated, compact torus (CT) plasma rings are of interest for a number of applications. These include weapons effects testing, weapons physics, high-power current switching, and high-density fusion. Interaction with magnetized plasma from accelerated compact toroids (IMPACT) is an experimental and computational physics program that studies the basic principles of CT acceleration and compression. Our most recent emphasis has been improving the performance and output power density of the device.

The CT is a toroidal, or doughnut-shaped, plasma configuration. The plasma in the CT is an electrically conducting, ionized gas (usually hydrogen) heated to about 100,000 K. A magnetic field that confines the plasma and gives the CT structural integrity is produced by currents flowing within the plasma itself. The entire CT structure is movable; no magnetic field coils are needed. Therefore, it can be used as a container to hold plasma during acceleration.

Figure 1 shows the accelerator, which has four phases of operation: CT formation, precompression of the rings prior to acceleration, acceleration, and focusing of the rings. The accelerating force is provided by the Lorentz ($J \times B$) force of an azimuthal magnetic field injected behind the CT. In our experiments, we have observed that a large-diameter CT (50 cm) can be accelerated to high, directed kinetic energy and that

Figure 1. The IMPACT apparatus, consisting of a formation gun, precompression cone, and acceleration/focusing stage.

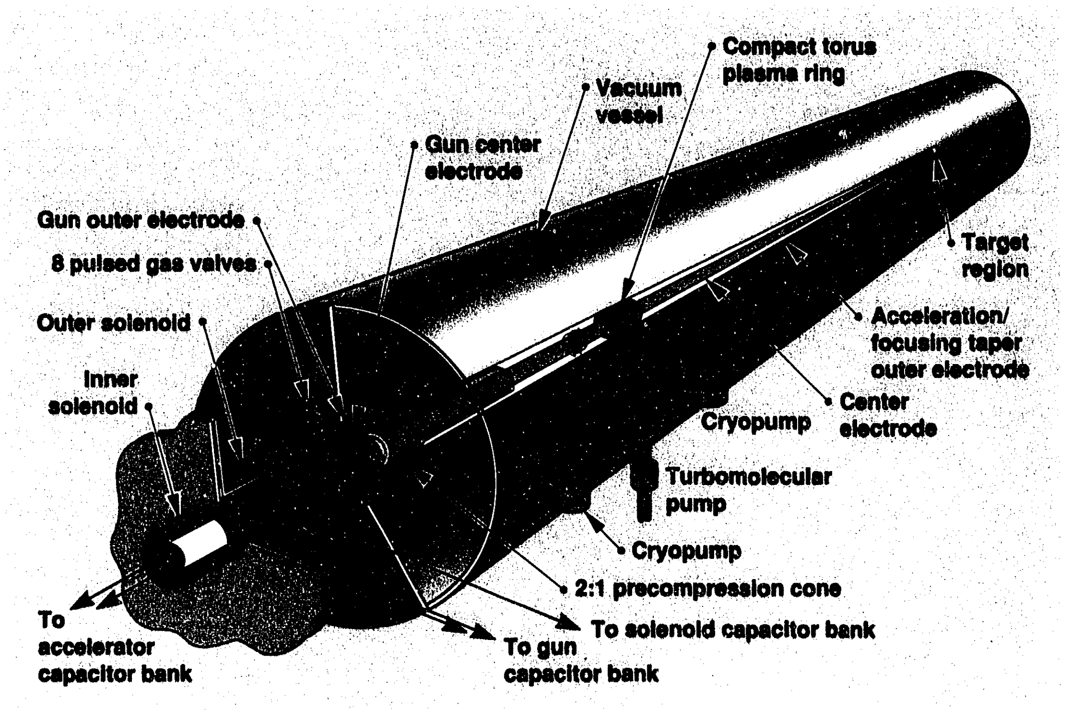

the precompression of CTs agrees closely with our computational models.

Our recent experiments to accelerate and focus the CT at small diameters (<16 cm) and over a large distance (740 cm) worked well at low energy levels. Our results showed the expected increase in magnetic field and decrease in CT length during focusing. Experiments at higher energy levels, however, have been limited by the interaction of the CT with gas desorbed from electrode surface, or "wall-evolved gases." The gas causes a drag force on the CT and reduces delivery of the accelerating current. We are working to solve the wall-evolution problem by improving conditioning of plasma-facing, electrode surfaces. We are also improving diagnostics, data analysis, and modeling to find out in detail what is happening.

During FY 1992, we tested several conditioning techniques, including tantalum lining of the accelerator center conductor; chromium gettering in the precompressor to reduce oxygen and other impurities; perforated gold-plated electrodes to improve pumping from the inter-electrode region of the accelerator; low-pressure, glow-discharge cleaning in the perforated system; and titanium gettering of the vacuum tank to lower the base pressure. We observed some benefits, such as improved CT lifetime and density control with chromium gettering.

We also found we could more rapidly recover our best operation after an up-to-air cycle if we used glow-discharge cleaning. The performance limitations of the accelerator were not significantly altered, however. Our most recent improvement is a high-temperature (~500°C), bakable, electrode section of the accelerator that should drive off weakly bound gases. Tests of this system are in progress and will continue in FY 1993.

Our diagnostic improvements have increased our understanding of the causes of drag. In particular, time-resolved optical spectroscopy has shown the evolution of impurities, especially oxygen, ahead of the CT. The oxygen is swept up and successively ionized by the moving CT. We included the effect of wall-evolved gas in our models and found drag effects similar to what is seen experimentally.

Success of the concept will depend on solving the wall-evolution problem. Experience in magnetic fusion experiments with similar problems suggests that good vacuum practice and surface conditioning can ultimately be effective. ◆

Actinide Electronic-Structure Calculations

J. Sytsma, E. Tamura, N. Edelstein,* and A. Gonis

In this project, we seek to better understand the electronic structure of actinide surfaces and ions. To accomplish this, we have initiated a theoretical and computational study of the surface properties of actinide elements and an experimental study of the electronic structure of curium and americium ions.

The physical properties of the interface between a vacuum and a bulk material are of fundamental interest. In addition, an understanding of surface electronic structure allows us to take advantage of such properties as crystal structure and lattice spacing when synthesizing new and interesting materials. We can use well-established surface-spectroscopy techniques (e.g., low-energy electron diffraction [LEED], ultraviolet photoemission spectroscopy [UPS], and near-edge x-ray absorption fine structure [NEXAFS]) to study these materials. We want to extend existing, nonrelativistic, surface-spectroscopy theories to include relativistic effects so that we can study materials that consist of heavy elements such as actinides and use spectroscopies where relativistic effects are important.

---

*Lawrence Berkeley Laboratory, Berkeley, CA.

In principle, any physical quantity observed experimentally with these spectroscopic techniques can be described by the surface Green's function. The advantage of the Green's function formalism is not only that the perturbation can be handled systematically but also that the spectral weight function (the density of states) of the quasiparticles (the ground-state electrons) can be obtained easily through the diagonal terms of the Green's function.

Figure 1 shows the results of our initial calculation of uranium absorbed on a Pt(111) surface. The figure shows the density of states (DOS) for the uranium monolayer on the Pt(111) surface. The calculation is based on the assumption that uranium can be grown epitaxially on the Pt(111) substrate. Above the Fermi level, indicated by zero on the energy axis (in the platinum-substrate bandgap), we see several uranium-layer–induced surface states. We have reported the corresponding theoretical LEED and USP spectra and are awaiting experimental verification.

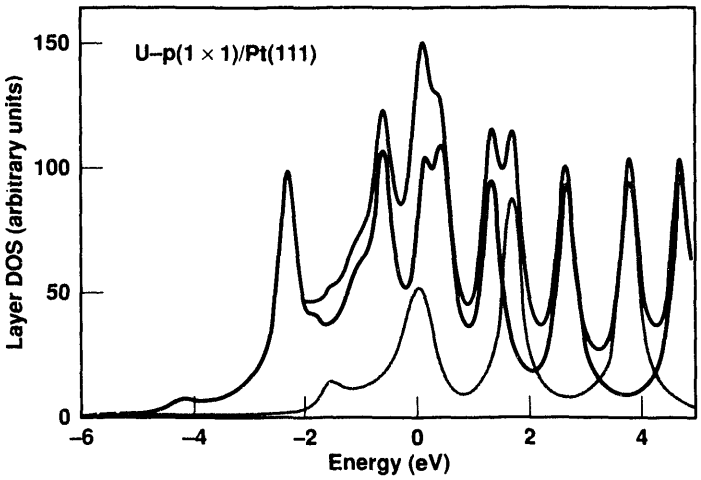

Figure 1. The momentum- and symmetry-resolved layer DOS of a uranium layer on the Pt(111) surface, which has threefold axial rotation symmetry and three mirror (reflection) planes (C_{3v}): total (green line), Λ_6 (black line), and Λ_{4+5} (gray line) in the normal (Λ) direction to the surface. The subscripts correspond to two different rotation/reflection symmetry types.

In FY 1993, we will further generalize the theory and the associated computer codes to magnetically polarized systems where the full-potential approach (no potential-form assumption) is desired. We also will extend the code to other spectroscopies, such as NEXAFS and electron holography.

In our experimental work, we have used two-photon spectroscopy (TPS) to study the electronic structure of Cm^{3+} and Am^{2+}. In TPS, the energy of the excitation light is not resonant with the transition; instead, two photons provide the energy matching. Recent advances in TPS studies of rare earths (4f elements) suggest application to their actinide analogs (5f elements). Important differences in the electronic structures of the actinides should test new theories that have arisen from TPS studies of the rare-earth ions.

We tested the cryogenic part of the experimental system on Ce^{3+} in $LuPO_4$ before measuring Cm^{3+} and Am^{2+} in fluorite-type lattices. Our goal was to investigate the first 5d level of Ce^{3+}, which will be split into five components by the crystal field and spin-orbit coupling. We directly observed four of five zero-phonon lines and determined the corresponding symmetries using two-photon excitation. Because the single-photon transitions for Ce^{3+} are in the ultraviolet, two-photon excitation requires visible light. Therefore, we used a Nd:YAG pumped-dye laser, which gives tunable, vertically polarized light. A Soleil–Babinet compensator allows us to change the polarization with respect to the crystal axes so that we can measure the polarization dependency of the two-photon transition. The polarization dependency yields direct information about the symmetry of the final 5d component. With the experience gained in the study of chemically similar lanthanides, we can begin experiments to determine the electronic structure of the highly radioactive Cm^{3+} and Am^{2+} ions. ◆

Investigating the Particle Selectivity of a Traveling Potential Wave

R. S. Lowder, R. F. Post, W. L. Barr, and L. A. Schwager

In FY 1992, we developed an isotope-separation method that may solve the U.S. light-isotope shortage (Post, 1992). We call our method the Solitron process and believe that it may also have applications for accelerator-beam processing and gas analysis. We separate isotopes by electronically driving a soliton-like electrostatic-potential wave through a monoenergetic beam of ions. We "tune" the strength and speed of the wave to make the wave–ion interaction isotopically selective with respect to the resulting ion energy and subsequent ion collection.

The Solitron Process

The device that demonstrates the Solitron process directs a beam of ions though a wave-interaction region to a collector with a bias voltage C that serves as an energy analyzer. The demonstration device is approximately 4 m long with a 0.5-m vacuum-chamber diameter. It has an ion source at one end, a center section with electrodes connected to external electronics to produce the traveling potential wave, and a collection section at the other end. We produce the wave by sequentially pulsing an array of 200 electrodes with an inner aperture of 4 × 20 cm and a total length of 264 cm. The wave velocity and length depend on the pulse length and the sequencing frequency. Figure 1 shows that the ion beam was neon (91% ^{20}Ne, 9% ^{22}Ne) at 400 eV, and the wave velocity was 78 km/s (about 25% faster than the ions). The half-sinusoidal wave had a length of about 20 cm. We varied the wave potential Φ from 0 to 100 V and measured the resulting ion exit energies. Figure 1 also shows the theoretical exit energies for ^{20}Ne and ^{22}Ne.

Our theory and experiment agreed. The first energy jump (at $\Phi = 30$ V) occurs when the wave potential equals the ^{20}Ne energy in the moving wave frame, resulting in a final ^{20}Ne energy of nearly 1 keV. Similarly, the second energy jump (at $\Phi = 45$ V) corresponds to accelerated ^{22}Ne. Figure 1 shows the energy jumps that define the behavior of most of the ions. However, a significant number (on the order of 10%) of the ions are only partially processed by the wave, and Figure 1 also demonstrates their presence. The linear rise

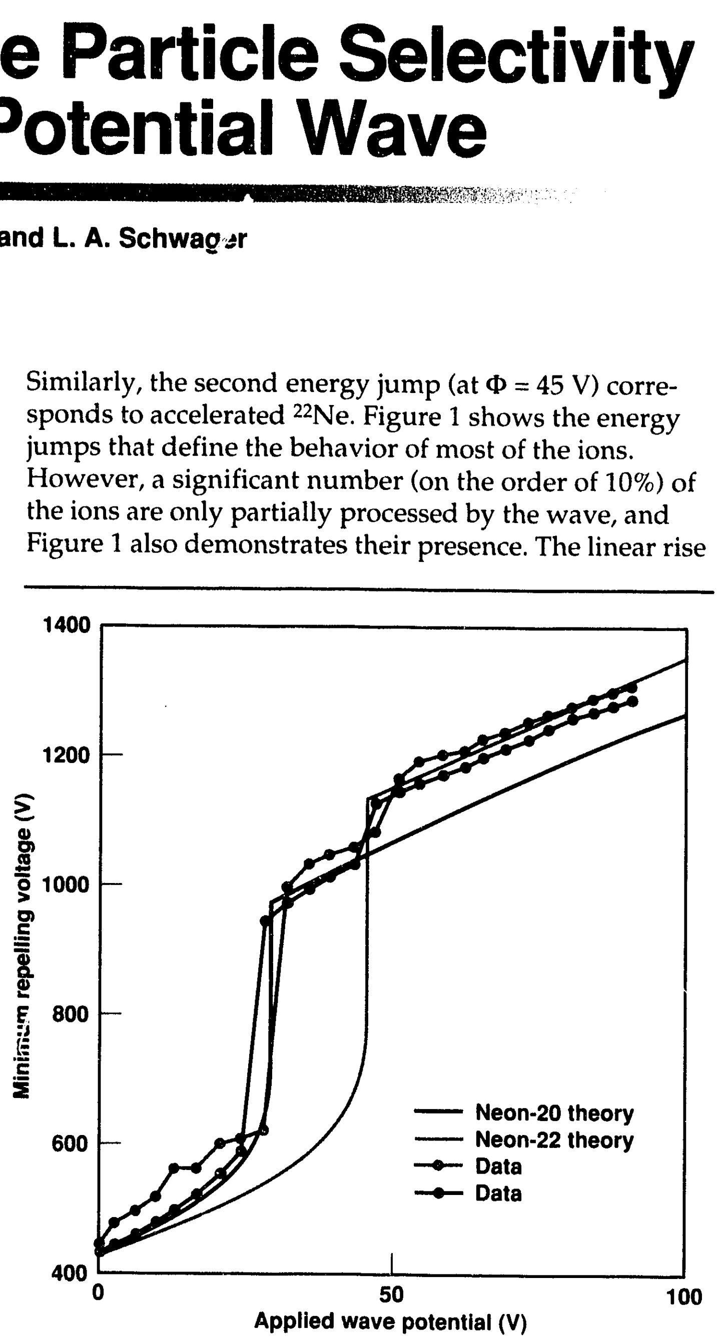

Figure 1. Dependence of maximum ion energy on wave potential. The beam energy is 400 eV. The wave velocity is 78 km/s. The theory results are for an isotopically pure beam. The experiment agreed with our theory.

in exit energy beyond these jumps represents ions entering the processing region coincidentally with the wave. Energy values below these jumps correspond to partially processed ions exiting coincidentally with the wave.

Thus, to collect only ^{20}Ne, we would choose $\Phi = 35$ V and C between 650 and 900 V; to collect only ^{22}Ne, $\Phi = 50$ V and $C = 1125$ V. The isotopic variation in exit energy adds versatility; that is, if a ^{24}Ne isotope existed, then the same parameters for ^{22}Ne could be used to isolate ^{22}Ne as a middle isotope. In FY 1993, we will explore separating gases other than neon, and particularly our ability to separate individual isotopes. ◆

References

Post, R. F. (1992), *A Method for Discriminative Particle Selection*, U.S. Patent 5140158 (August 18).

Pair Plasma Formation, Propagation, and Interactions

P. C. Wheeler, P. W. Rambo, and S. T. Brandon

Pair plasmas are neutral ensembles of electrons and positrons. They can be generated in a thin gamma-ray converter or in certain astrophysical phenomena, such as supernova explosions. Pair plasmas can be produced in the form of a broad plasma front (e.g., a spherical shell expanding from a gamma-ray source) or in narrow plasmoids having relativistic velocity and significant directed kinetic energy.

Project Goals

The goals of our analytical and calculational study are to better understand the detailed physical processes that occur in the formation and emission of relativistic pair plasmas, in plasmoid propagation across a vacuum or through a tenuous gas, and in the interaction of energetic pair plasmas with matter and electromagnetic (EM) fields. A broad pair plasma front can amplify preestablished magnetostatic fields or electromagnetic radiation, producing an intense electromagnetic pulse (EMP). Understanding these phenomena will contribute to our knowledge of high-power microwave propagation in the upper atmosphere and EMP generation.

Achievements

We have analyzed the stability of the interface between a relativistic pair plasma piston and a reflecting electromagnetic wave. We are now investigating the amplification and radiation processes occurring in the interaction with a magnetostatic field. Our investigation of pair plasmoid propagation has yielded several interesting results.

We formulated a generalized, fully relativistic analytical model for a long, narrow positron beam propagating through a background plasma and found a radial equilibrium state. This model provided useful guidance for numerical simulations of plasmoid propagation.

Our two-dimensional (2D) and three-dimensional (3D) simulations using the particle-in-cell (PIC) code show that whereas positrons are magnetically confined, electrons tend to leave the plasmoid quickly. The positron beam remains nearly charge and current neutralized by continuously pulling in electrons from the background plasma. The net energy loss from this process causes beam erosion. We found that the best stability and lowest erosion occur for intense, high-energy beams.

Simulations of wakefields and kink instabilities, referred to as $m = 0$ and $m = 1$ instabilities, respectively, showed that wakefields are excited in the background plasma and induce axial energy gradients, which accelerate the erosion process. However, a transverse external magnetic field (e.g., the earth's) dephases this mode and actually lowers the erosion rate.

We found no kink ($m = 1$) instability in our 3D PIC simulations. These results are in contrast to electron-beam propagation, where $m = 1$ instabilities are a major limitation. We are formulating quantitative scaling relations for erosion and instabilities.

Plans for FY 1993

We plan to expand our investigations across the broad spectrum of issues in pair plasmoid formation, propagation, and interactions, including the issues of magnetic snowplow and attendant shocks, heating, head erosion, and filamentation. We will try to define the limits of propagation efficiency and determine parameters for optimum propagation. We will also continue to explore the processes involved in pair plasma interactions with EM fields, including relativistic shock formation, instabilities in the shock and interface, and EM radiation losses. ◆

Plutonium Melting Measurements Using the Diamond Anvil Cell

B. Goodwin, J. Akella, and C.-S. Yoo

The diamond anvil cell (DAC) is a versatile experimental tool for studying the properties of materials at very high pressures (>300 GPa) and high temperatures (~6000 K). The DAC apparatus is well suited for investigating hazardous toxic materials because the samples required are very small (milligrams) and are easily contained. Thus, we have an excellent tool for studying the melting of toxic metals at very high pressures.

We measured the melting curve of plutonium with a laser-heated DAC apparatus. The plutonium melting curve is of great interest in nuclear design because the subtle interplay of material strength and its loss due to melting solves a long-standing problem in calculating implosion devices. Precise measurements of the melting curve will enable more accurate calculations of the distribution of solids and liquids in implosion systems and so strongly influence the final implosion configuration. The distribution of material phases also controls the initial conditions for hydrodynamic instabilities and hence controls device performance.

The melting curve places constraints on our calculations that influence the entire implosion process. These constraints have already influenced work on plutonium equations of state. As a result, we have improved our understanding of the implosion process. The techniques developed here are already being applied to nonnuclear materials research and may prove useful in manufacturing new synthetic materials.

Diamonds are transparent to electromagnetic radiation and have high thermal conductivity. These features were used to develop a laser-heating technique in the DAC. This laser-heating technique was used by a group at UC Berkeley to investigate the melting curve of lead and was used earlier to study silicate minerals melting. In collaboration with the group at Berkeley, we are investigating the melting of uranium up to 1 Mbar (100 GPa) pressure. To heat the sample, we use micro-laser optics to focus a continuous wave or pulsed Nd:YAG laser (wavelength of 1.064 mm) on the sample in the DAC. The radius of the focal spot could vary from 5 to 20 mm, depending on the optics used and the focusing conditions. For a good absorbing sample, the input laser power corresponds to a heating rate of about 104 K/s in the DAC. With this heating rate, a thermal steady state can be achieved in a few seconds, melting can be observed visually under a microscope, and the light emitted from the sample can be used to determine the temperature. Temperatures can be measured to about 100 K with an S-2 type photomultiplier tube.

This technique can be improved using an electronic camera with a two-dimensional array detector. Time-dependent sample temperature is determined by fitting thermal emission spectra to a thermal radiation equation. This latter technique has been incorporated into the laser-heating system being set up at LLNL. Sample pressure is determined by the chrome-doped ruby chip technique. Diamonds are extremely good thermal conductors, so there is no thermal effect on the pressure calibration because of heating the samples when they are separated by a few micrometers. With the tailored diamond anvils and modified DAC, higher pressures (>100 GPa) can be obtained and temperatures measured more accurately.

In FY 1992, we debugged the DAC system, performed temperature calibrations, and began to investigate melting of nontoxic material iron. So far, we have measured melting of iron to 40 GPa. We also have loaded samples of uranium under argon and hydrostatically measured 15 points on the uranium melting curve up to a pressure of 42 GPa. In FY 1993, we will attain our goal of collecting plutonium melting data to at least 40 GPa.

Future plans for this remarkable capability we have developed include combining the laser-heated DAC with x-ray crystallographic techniques. By placing the DAC in an x-ray beam, we will be able to determine the sample density and temperature simultaneously at ultrahigh pressures. We will then be able to determine the equation of state and the melting properties of metals and other materials. We will be able to do this in regimes that previously could only be fleetingly reached during chemical or nuclear-explosion–driven experiments.

In addition, we are measuring the high-pressure and high-temperature properties of exotic new materials, such as Buckminster fullerenes. We will also use this capability to synthesize new materials, such as materials that hypothetically are harder than diamonds.

The laser-heated DAC is an extremely powerful and unique capability that exists at only one or two other places in the world. This world-class facility, developed for weapons physics research, places LLNL at the cutting edge of materials research. ◆

A Study of Opacities in the NLTE Model

S. Dalhed

The light emitted in the explosions of supernovae enables scientists to understand the evolution and composition of these important objects. In addition to being the site where all heavy elements in the universe are probably generated, supernovae may also serve as "standard candles," or cosmological distance indicators.

To understand the dynamics of supernovae, we use complex computer codes to model the temperature and densities of the matter and radiation fields, which are intimately connected. The radiation field, along with fast electrons created by nuclear reactions, determines the ionization state of the matter in the outer envelope of the star. At the same time, the radiation field is determined by the deexcitation and recombination of the matter. Since each atomic transition is not, in general, balanced by its own inverse process, we must use the nonlocal thermodynamic equilibrium (NLTE) model to describe the stellar evolution. The Doppler-shifted energies of lines, the widths of the lines, and the ratios of various lines in the emission spectrum provide valuable clues about the evolution of the star.

The Need for Atomic Data

Astronomers possess a large set of supernova spectra that have not been fully analyzed. The evolution codes being developed include state-of-the-art physics for hydrodynamics, thermodynamics, and radiative transfer. What is most urgently needed at this time is accurate, self-consistent atomic data.

The purpose of our research is to extend the atomic-modeling capability developed at LLNL and elsewhere to the ions of iron, cobalt, and nickel. Although many other atoms and their ions are present in supernovae, we have concentrated on those three. Line emission from iron, cobalt, and nickel and their first several ionization stages dominates the late-time spectrum of supernovae and provides a sensitive gauge of matter conditions in the emission region. The best available atomic model consists of (1) energy levels listed in tables generated by the National Institute of Standards and Technology, and (2) a plethora of radiative and collisional rates from many sources, which were obtained using a variety of approximations. While for some features, computed spectra compare surprisingly well with measured spectra, there are numerous areas of discrepancy.

In connection with soft–x-ray laser research at LLNL, a collection of atomic-physics codes has been developed locally and assembled from other institutions to provide self-consistent data sets, or models, for atoms and their ionization stages. These models include the energy levels and the atomic rates that connect them. The basis of the set of codes is a set of fully relativistic, single-configuration Dirac–Fock wave functions for the bound orbitals. We calculate the Hamiltonian matrix and include (1) Breit corrections to the Coulomb interactions between the electrons, and (2) quantum electrodynamic corrections such as electron self-energy and vacuum polarization. We diagonalize the Hamiltonian to give the full multiconfigurational wave functions in intermediate coupling. Racah algebra is used to compute the angular-momentum part of the matrix elements.

Producing New Atomic Data

For highly ionized ions, the method and package of codes described above are ideally suited for generating large manifolds of atomic-state functions at one time. Unfortunately, for neutral and near-neutral ions such as those considered here, several code modifications were needed because of the strong correlation between wave functions, which results in sensitive term dependence of the energy levels. This dependence means that the correct correlation energy can only be obtained by calculating small subsets of energy levels independently, one set at a time, with different sets of orbitals for each calculation. No codifiable rules govern which orbitals are necessary for the various terms, so the generation of atomic data is nearly an art form.

Nonetheless, atomic data are being produced that include multipole radiative-transition oscillator strengths, distorted-wave collisional cross sections, and photoionization cross sections. These data are internally self-consistent and obey sum rules. Hence, they represent a significant improvement over existing data. We have nearly completed the evolution codes that will use the data. Together with the new atomic data, these codes will represent a considerable advance in our ability to understand supernova evolution. ◆

Studying Solid-Density, High-Temperature Plasma

D. R. Slaughter, D. F. Price, W. E. White, R. L. Shepherd, P. R. Bolton, R. E. Stewart, R. S. Walling, and G. Guethlein

Our project goals are twofold. First, we want to develop a chirp-pulse–amplified, small-scale laser with a 100-fs pulse length that can heat high-energy, solid-density plasmas to kilovolt temperatures before hydrodynamic decompression can take place. Second, we want to use this laser to experimentally determine the properties of these plasmas, such as opacity and equation of state, that are important for inertial confinement fusion and astrophysical and weapons physics applications.

We have successfully developed a Ti:sapphire laser that produces 0.04-J pulses with 100-fs pulse widths at a repetition rate of 10 Hz. If we focus the beam with an offaxis parabolic mirror, we can produce a spot that is 1.8 times diffraction limited on a target of 5 µm (full width at half-maximum) at a peak power of 1.3×10^{18} W/cm^2. We tested a dye-converted, flashlamp-pumped, Ti:sapphire amplifier that will increase pulse energies to at least 0.25 J/pulse. We added a vacuum compressor housing to the laser to prevent self-phase modulation and breakup of the beam in air before it hits the target. In addition, we designed a 100-TW, Ti:sapphire, high-power laser system that may provide 10-J pulses at a lower repetition rate.

At these high intensities, small-scale wings or prepulses in the beam can produce, at the interface of a solid target and a vacuum, low-density plasmas that absorb the energy of the principal high-intensity pulse and prevent the heating of the solid-density portion of the target. To reduce or prevent this effect, we identified prepulses in the pulse and reduced them by adding active switching in the regenerative amplifier and a passive, flowing dye-cell absorber that allowed us to achieve prepulse contrast of about 10^{-10}. We traced the other major source of poor contrast, in the pulse stretcher, at picosecond timescales to uncorrected third- and fourth-order terms that deviate from a pure Gaussian pulse shape at 10% of the peak intensity. We developed a new lens design that promises to correct this problem in our compressor and to significantly reduce prepulses and wings in the compressed pulse.

Our first plasma-production experiments explored the coupling of a low-prepulse, high-intensity laser with a solid plasma at a sharp vacuum interface. At a smooth surface, our high-intensity pulses appear to produce decompressed plasma material that improved compressors and frequency doubling should correct. We achieved nearly 80% absorption on a porous, black aluminum target. Spectroscopic measurements of the density of this target indicated no decompression of the porous, foam-like target, and we achieved temperatures of 200 to 300 eV. The conversion efficiency to x rays with a low, prepulse beam is between 2 and 0.2%, with a component of hard–x-ray generation in a spectrum of 120 keV at a conversion efficiency of 10^{-6} of the incident light.

We performed hydrodynamic simulations of these targets with the LASNEX computer code to predict the state of the heated targets and to determine the importance of pulse width and pulse contrast on plasma conditions. Our simulations show that, with about 10^{18} W/cm^2 absorbed energy on a solid target, solid-density plasmas with temperatures of 500 to 3000 eV may be achievable. Plasma temperatures depend on the superthermal electron generation, electron conduction, and thermal transport models used. These models are highly uncertain in the high-intensity regime of interest and must be understood and explored experimentally before reliable predictions can be made.

From the results achieved in FY 1992, we are optimistic that we can couple laser light in solid-density material on a subpicosecond timescale. In FY 1993, we will increase the energy of our pulses to 0.25 J, test our 10-J design, and build an improved compressor to eliminate prepulse effects. Using interferometry and reflectometry, we will measure the scale length of the plasma created with our short-pulse system, determine the absorption and hot-electron production mechanisms in our targets, and optimize target geometry for maximum laser coupling. We also will develop a subpicosecond, x-ray streak camera to study the dynamics of the heated targets. ◆

Measurements of Field Emission with Electron Counters

P. J. Ebert and F. J. James*

The purpose of our research is to study electron field-emission statistics, i.e., how many electrons are emitted simultaneously in a single field-emission event. This work was prompted by our earlier, unpublished results of experiments that revealed multiple energy peaks in the detection of electrons emitted from a field-emission source (Figure 1). The earlier experiments led to the development of x-ray diagnostics for the Nuclear Test Program. Figure 1a shows eight clearly resolved electron peaks measured with a Si(Li) detector in 1972. The accelerating voltage was 40 kV, and the field-emitted electrons show energies that are integral multiples of 40 keV. This result could only have occurred if the source emitted several electrons simultaneously in a single field-emission event.

One objective of our study was to verify our earlier, unpublished results with a different source. We accomplished this objective in the summer of FY 1992, when we again measured multiple energy peaks. We extended the range from 9 keV, the lower limit of our detector resolution, to 40 keV, the upper limit of accelerating voltage. Figure 1b shows a 20-keV electron spectrum obtained with a gas-flow proportional counter. The spectrum has six clearly resolved peaks. Currently, no field-emission theory can explain these novel observations.

We will make two major improvements in future experiments that will be conducted at Jackson State University. First, we will modify the electron source to measure emission from a single, isolated field-emission tip under various experimental conditions. Second, we will replace the gas proportional counter with a high-resolution Si(Li) detector. The knowledge gained from this study will improve our understanding of electron tunneling and its effects. If multiple emission can be controlled, it holds promise for the development of table-top sources of coherent electrons and coherent vacuum ultraviolet and soft–x-ray radiation. ◆

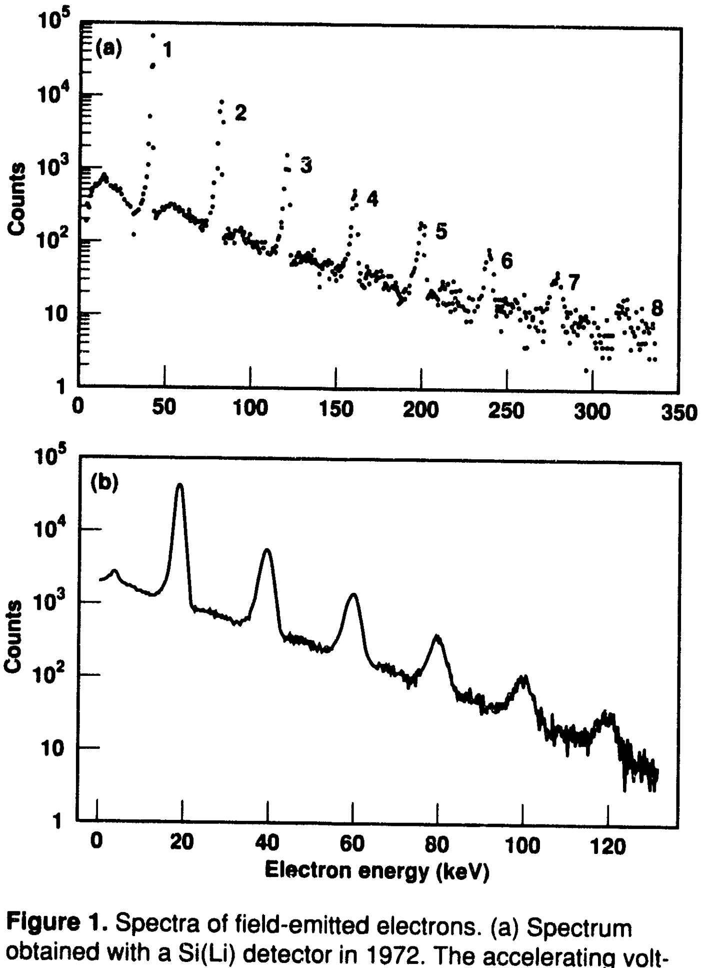

Figure 1. Spectra of field-emitted electrons. (a) Spectrum obtained with a Si(Li) detector in 1972. The accelerating voltage is 40 kV. (b) Spectrum obtained with a wire proportional counter in August 1992. The accelerating voltage is 20 kV. The spectrum shown in (b) verifies the earlier results with a different source and detector.

Jackson State University, Jackson, MS.

Unattributed Nuclear Explosions

J. C. Davis, C. H. Poppe, D. A. Leich, and H. Vantine

The unattributed use of a nuclear weapon or dispersal device by a rogue country or terrorist group represents a growing risk to the physical security of the United States and to the emerging reduction of tension worldwide. Should such an event take place, national leaders must have the best information possible to make decisions quickly and accurately on appropriate political and military responses. To do so, we must rapidly collect and analyze the data required to determine, if possible, the origin of the device, its materials, and its design provenance.

We are developing a systematic methodology to engineer a nuclear device in reverse—back to its origin—using the signals and debris from an explosion. First, we conducted a crude trial run of the methodology without any detailed computer calculations. From our experience with nuclear tests, we estimated debris compositions for three scenarios, including the environmental factors that would affect the debris. A separate, independent analysis, working backward from the estimated debris composition, correctly concluded the basic materials and design features of each device.

Next, we formulated a series of computer-modeled problems that contained a progression of increasing detail. Using our weapons-design explosion codes, we calculated the first set of problems through the nuclear explosion to determine the postdetonation residual actinides and fission products. (In the future, our model problems will also incorporate activation products from the device structural material and surrounding medium, stable isotopes, electromagnetic radiation, and seismic energy.)

We gave the data for these calculated residuals to two independent teams of experts in nuclear test diagnostics and forensic reconstruction. They had no prior knowledge of the models and tried to determine the device designs and materials from the given data. According to preliminary interpretations, both teams made accurate conclusions, and they are proceeding with independent computer modeling to refine their results. We will compare their results to the actual properties of the model to study discrimination, sensitivity, and errors; to validate the technical assumptions made in the reverse engineering; and to identify persistent signatures.

Using the results of the initial phase, we will refine our baseline methodology to consider in detail how the detonation environment would affect the measurement of key debris components. We will study several scenarios, including ground bursts and underwater detonations. On the basis of the best available scientific information and experience with atmospheric, underwater, and underground nuclear testing, we will estimate the effects of mixing, dispersal, and background on the signals and samples. We will use this information to assess which data are most important to quickly provide useful information on the characteristics and origin of the device. ◆

Using Supernovae to Probe the Fundamental Physics of Weak Interactions

R. W. Mayle, J. R. Wilson, and G. Fuller*

Supernovae explosions occur when the core of an evolved massive star exhausts its energy supply (from nuclear fusion reactions) and collapses to a volume about 1 trillion times smaller than its original size. This catastrophe (supernova) expels the stellar envelope and releases a tremendous amount of energy in a burst of neutrinos. All of the four fundamental interactions of physics—gravitational, electromagnetic, nuclear, and weak—are involved in the evolution of the supernovae. However, because of the large amount of energy released in neutrinos, the weak interaction plays a pivotal role in the dynamics of these objects. Our project uses the numerical modeling of supernovae to study various theories of the weak interaction. Neutrinos were detected on Earth from a supernova event in 1987, and we use these neutrino measurements to constrain the physics of the weak interaction.

We studied the effect of neutrino mass oscillations on the dynamics of the supernovae evolution. Neutrino mass oscillations are a manifestation of the quantum-mechanical prediction that closely related massive elementary particles can exchange identities (oscillate) as they travel through space. There are at least three types or "flavors" of neutrinos (electron, muon, and tauon) as inferred from earthly laboratory experiments. These flavors of neutrinos can oscillate among themselves as they travel from their creation (for our purposes in a supernova) to their destruction (possibly in a neutrino detector on Earth). We found that the maximum mass of a neutrino that oscillates is 1/5000 the mass of an electron and that a neutrino with a larger mass will not reproduce the same neutrino events as those observed from the supernova event in 1987.

We also finished work on the possible existence of massive neutrinos (about 1/25 the mass of an electron) assuming that mass oscillations did not occur. For this work, we were motivated by some land-based experiments that indicated such a neutrino existed. We found that the most massive neutrino consistent with the observed neutrinos is about 1/50 the size of an electron.

In FY 1993, we will study the effect of the weak interaction on the creation of the heavy elements (e.g., uranium). It is still unclear where the astrophysical site for the syntheses of these elements is, and we hope to determine a more definite site for their formation, possibly in supernovae. ◆

University of California at San Diego.

Numerical Simulations of Soliton Dynamics to Study Light Nuclei

W. Y. Crutchfield, N. J. Snyderman, and V. R. Brown

Quantum chromodynamics (QCD), the dynamical theory of the strong interactions, has successfully predicted the high-energy behavior of nucleons. However, QCD has had little direct effect on low-energy nuclear physics, the study of the low-energy behavior of nucleons, because QCD is difficult to calculate at low energies. However, a remarkable suggestion by Witten (1979, 1983) may allow QCD calculations of nuclear phenomena. In this concept of QCD, baryons and nuclei arise as topological solitons in a theory of meson dynamics. This concept of nuclear physics was conceived more than 30 years ago in the visionary work of Skyrme. It could lead to a simple, fundamental description of low-energy nuclear physics.

The Skyrme–Witten theory has received intense but preliminary investigation and has displayed a number of successes. The Skyrme–Witten model correctly predicts π–meson dynamics, the properties of baryons, and baryon resonances. Prior to our work, researchers using this model treated light nuclei with a static approximation. Their work produced the correct ground-state quantum numbers and correctly predicted the alpha particle to be the most tightly bound (Braaten and Carson, 1988). However, their work did not produce reasonable sizes for the nuclei.

Within this framework, we took the first steps toward calculating the properties of light nuclei from QCD. We carried out the semiclassical quantization of the $B = 2$ soliton sector of the Skyrme model. We based our analysis on time-varying solutions to the classical Skyrme equations. We found time-varying solutions through numerical simulations of soliton dynamics in three dimensions on a finite lattice.

Although we are not the first to simulate soliton dynamics (Allder et al., 1987; Verbaarschot et al., 1987), we have improved the speed of these calculations by 1 or 2 orders of magnitude using the finite-difference modeling expertise of LLNL's Applied Mathematics Group. We are the first to find bound-state solutions in three dimensions (Crutchfield et al., 1992). Figure 1 shows a three-dimensional rendering of an energy isosurface in the bound dinucleon system at different times in its orbit. At the moment of closest approach, the energy isosurface is approximately toroidal. The previously discovered static solution is also toroidal.

We simulate the dynamics of the $B = 2$ system inside a box of finite size L with a computational grid of finite resolution dx. For the physical problem, we extrapolate to an infinite L and an infinitesimal dx by performing sequences of experiments on grids with different values of L and dx. Figure 2 shows results from four of these experiments. The black line is the extrapolation to infinite L and infinitesimal dx.

For given grid parameters L and dx, we perform many simulations with varying amounts of energy. In each simulation, we observe the motions of the baryons as they interact with each other. From our observations, we can calculate many physically important properties. Figure 2 shows the most important of these properties, the Bohr–Sommerfeld quantization function. The curve covers energies from the static soliton, a toroidal field configuration, to two unbound skyrmions. From our extrapolation, we can determine the approximate bound states of the $B = 2$ system using the quantization condition $W = (2n + 1)\pi e^2$, where e^2 is the dimensionless coupling constant of the Skyrme model and n is the principal quantum number. Other researchers have estimated e^2 to be about 30. Figure 2 shows how we use the quantization condition to find the energy of the lowest quantized state ($n = 0$).

We can calculate other physical parameters from each computational experiment. We measure moments of inertia, baryon moments, and magnetic moments as a function of time. We use these measurements, extrapolated to $L = \infty$ and $dx = 0$, to determine the static properties of the deuteron. If we examine the classical solutions that contribute to the quantized solution, we find that the baryons are usually well separated, leading to a small energy splitting between the spin–isospin states. This result was inaccessible with the time-independent solutions used in previous work. We also find that the quadrupole moment of the deuteron is much larger than the quadrupole moment of its constituent nucleons. These observations are physically correct and validate our approach.

With this project, we have achieved several technical firsts. We are the first to semiclassically quantize a time-varying solution in three dimensions and to use numerical solutions in quantizing a nonlinear field theory. Our work validates the Skyrme–Witten approach to the low-energy limit of QCD. The inclusion of time-dependent solutions in the semiclassical quantization improves the agreement of the Skyrme–Witten model with experiment, which suggests that the Skyrme–Witten model can provide a first-principles understanding of low-energy nuclear phenomena. ◆

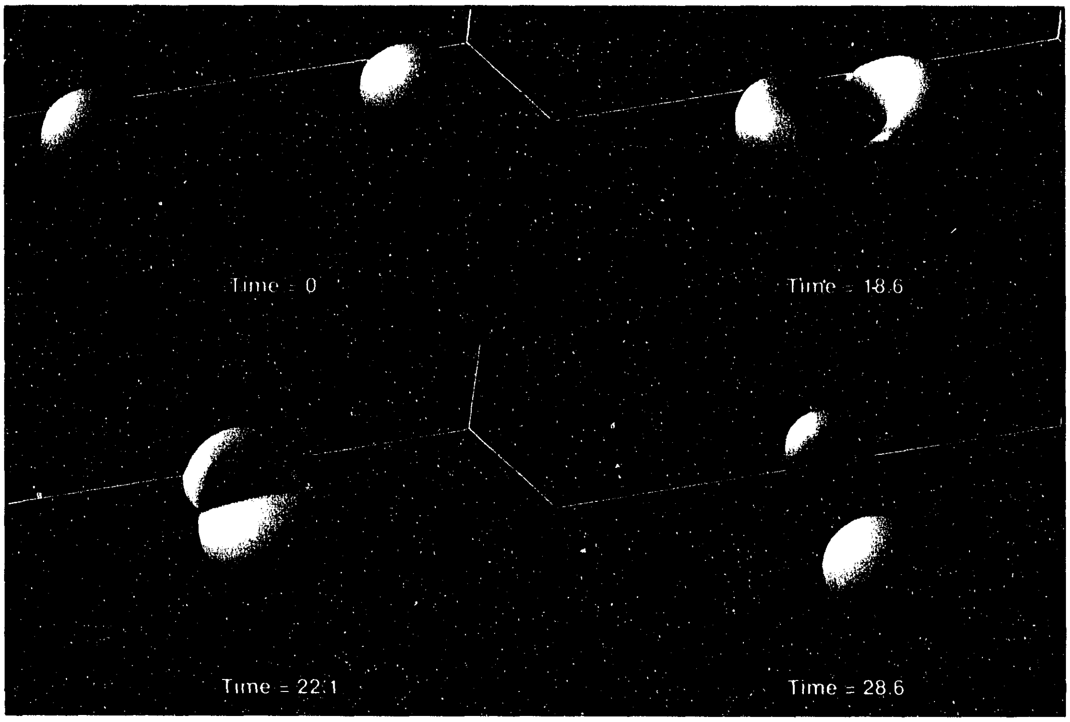

Figure 1. Isosurface of energy density at four different times (measured in normalized Skyrmion units) in the orbit of the deuteron. Nucleons start far apart, pass through an intermediate state with approximate toroidal symmetry, and separate at right angles.

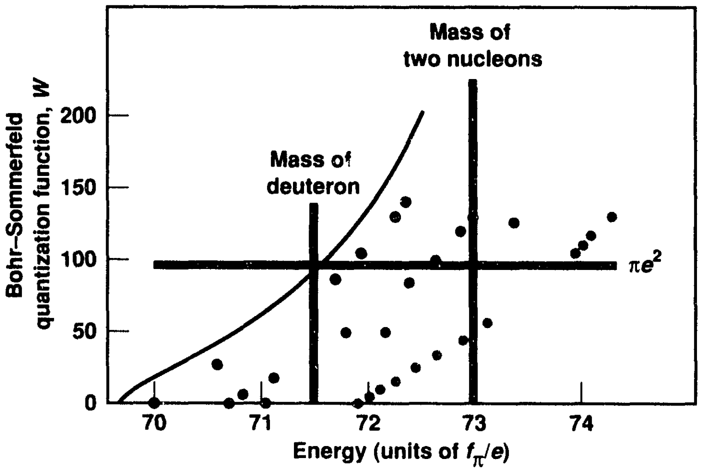

Figure 2. Bohr–Sommerfeld quantization function. Each dot represents a single computation experiment. Four series of experiments are shown for varying values of L and dx. Black line is the extrapolation to $L = \infty$ and $dx = 0$.

References

Allder, A., S. Koonin, R. Seki, and H. Sommermann (1987), "Dynamics of Skyrmion Collisions in 3+1 Dimensions," *Phys. Rev. Lett.* **59**, 2836.

Braaten, E., and L. Carson (1988), "Deuteron as a Toroidal Skyrmion," *Phys. Rev. D* **38**, 3525.

Crutchfield, W. Y., N. J. Snyderman, and V. R. Brown (1992), "Deuteron in the Skyrme Model," *Phys. Rev. Lett.* **68**, 1660.

Verbaarschot, J., T. Walhout, J. Wambach, and H. Wyld (1987), "Scattering of Skyrmions in an Axially Symmetric System," *Nucl. Phys. A* **461**, 603.

Witten, E. (1979), "Baryons in the 1/*N* Expansion," *Nucl. Phys. B* **160**, 57.

Witten, E. (1983), "Current Algebra, Baryons, and Quark Confinement," *Nucl. Phys. B* **223**, 433.

Heavy-Ion Physics at the Brookhaven Alternating Gradient Synchrotron

T. C. Sangster and J. Thomas

The Alternating Gradient Synchrotron (AGS) at Brookhaven National Laboratory (BNL) accelerates silicon nuclei to energies of 14 GeV/A. At these energies, it is possible to create very dense nuclear matter (three to five times normal) in violent collisions with another heavy nucleus. At such extreme densities, nuclear matter may undergo a phase transition from purely hadronic matter (bound states of quarks) to a new state of deconfined quarks and gluons called quark–gluon plasma (QGP). We now have a unique opportunity at the AGS to search for and identify signals from the QGP in high-density nuclear matter.

Our heavy-ion group is working on two experiments at the AGS. The silicon-beam experimental program was completed during the spring of FY 1992. The analysis of the silicon-beam data has just begun, and final results are still one to two years away. Preliminary results do not show any indication of quark–gluon plasma formation. However, a new booster accelerator, which was commissioned at BNL in FY 1992, will allow the AGS to accelerate much heavier gold beams to 11.5 GeV/A. We are working to establish a new experimental program at the AGS to study the higher densities and much larger overlap volumes expected with the gold beams.

Silicon-Beam Experiment

Our contribution to the silicon-beam experiment was an array of phoswich, or phosphor-sandwich, detectors for measuring the protons emitted at large laboratory angles. Studying the emission of particles at large angles is important in establishing possible production mechanisms such as rescattering, which may mimic QGP formation. In Figure 1, we plot the proton-production probability as a function of the laboratory angle measurement. The three sets of points are for constraints on the overlap of the two colliding nuclei. More central collisions sample larger overlaps and consequently higher densities. Many more protons are emitted in central than in peripheral collisions.

Gold-Beam Experiments

We are fabricating three new detector systems for the gold-beam experiment. The first system is a high-multiplicity tracking chamber that will be crucial in identifying particles that pass through the large-angle spectrometer. The chamber must simultaneously measure the location of up to 10 charged particles. Second, we will upgrade the current phoswich array to handle the more numerous protons expected in the gold–gold collisions. This upgrade should make it possible to study multiparticle correlations where subtle changes

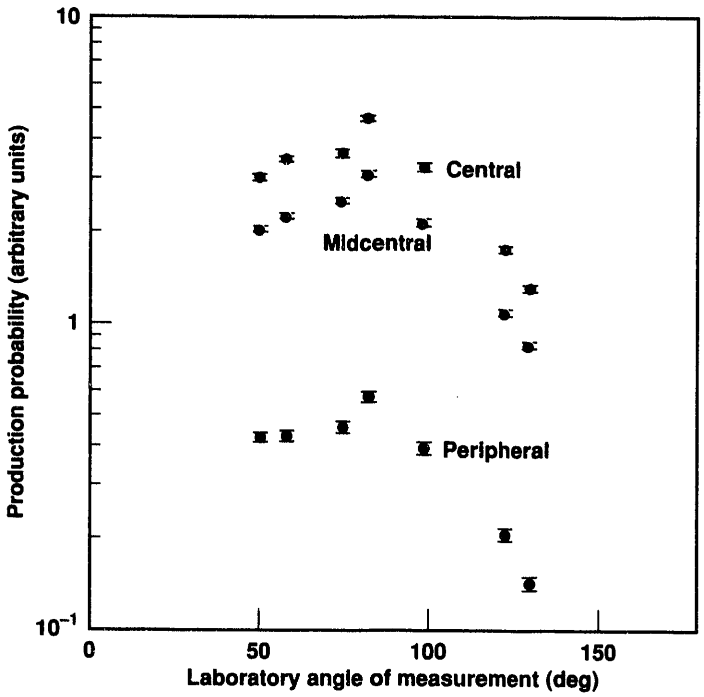

Figure 1. Proton-production probability measured by the phoswich array for central, midcentral, and peripheral silicon–gold collisions. Data points represent locations of detectors. More protons are emitted in central than in peripheral collisions.

may offer important clues for QGP formation. Third, our projectile hodoscope will add a new dimension to the event-characterization information by providing an event-by-event reaction plane. Such a measurement opens entirely new physics possibilities at the AGS, such as collective phenomena and pion shadowing.

We tested prototypes of both the tracking chamber and the projectile hodoscope during FY 1992. We are analyzing the results of these tests before we begin final construction of the detector systems in early FY 1993. We plan to install the new detectors at the AGS in early FY 1993 and to run the first full gold-beam experiment later in the year. ◆

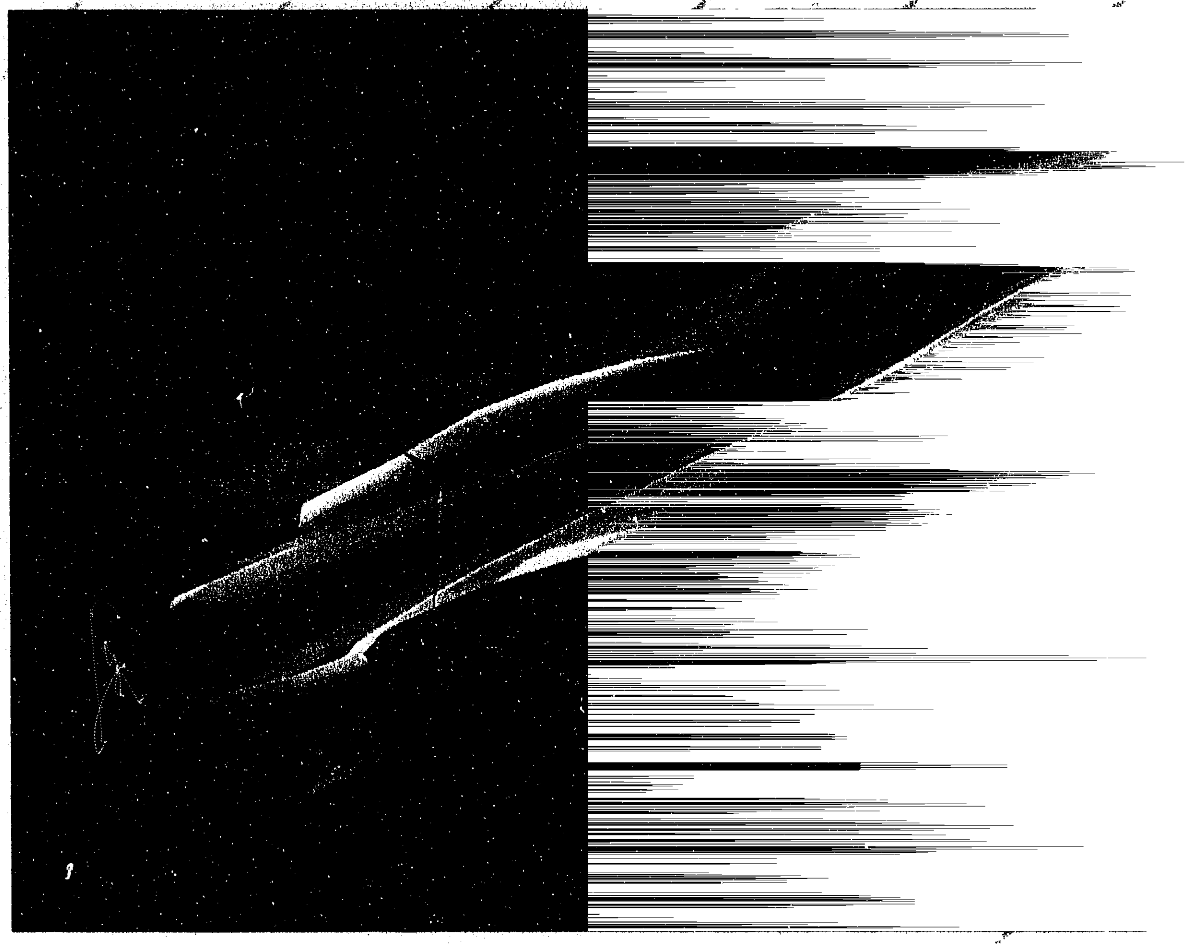

High-Performance Computation and Communication

Laboratory Directed Research
and Development FY 1992

On the previous page. Contour plot of a snapshot of the electric potential for a three-dimensional gyrokinetic simulation of an ion-temperature–gradient instability partially stabilized by shear in an applied electric field $E \times$ magnetic field B induced drift.

Generation of Full-Scale Computational Physics Programs from a Natural Description

G. O. Cook, Jr., S. A. Brown, J. F. Painter, R. Rainsberger, and J. Uejio

As scientific computation has grown in importance over the last several years, so have the demands placed on it. Each year, scientists want computer programs to model more physical phenomena at one time, model them more completely, and provide better numerical accuracy. Although computer speed has increased, we have not been able to change the way we write computer programs. Increasing demands for greater complexity will soon overwhelm what has always been a labor-intensive, time-consuming task.

However, most of the time spent writing and rewriting programs for scientific simulations is not spent on the challenging work of modeling the scientific problem or choosing good numerical methods for simulating it. Instead, this time is spent on mechanically rewriting the ideas in the form required by the computer languages available. These languages are close enough to natural languages for small simple mathematical expressions, but they are inadequate for the complexity of even part of a modern scientific simulation code.

We solved this problem with ALPAL, a program that automatically generates programs or portions of programs for large-scale scientific computation. To develop a code with ALPAL, programmers must only specify the mathematical model to be solved, in a language similar to the familiar language of scientific journals and textbooks. ALPAL automates the mechanical 95% of the work spent developing scientific simulation programs, thus greatly increasing productivity. Although ALPAL is still a research code, we have tested it on enough practical problems to prove that it can solve models too complicated for traditional methods of writing scientific simulation programs.

Large Scientific Simulation Codes

The large scientific simulation programs at the Laboratory are too big and complicated for one person to write, understand, or maintain. As a consequence, each program, or code, is organized as a collection of separate "modules," each of which can be treated almost as an independent program. The modules share data, and a part of the main program controls the sequence in which the modules run, among other functions. We are interested in those modules that directly relate to the scientific problem.

When code developers write a module, they decide which physical phenomena the module should simulate and model these phenomena as a system of mathematical equations, usually partial differential equations. Then they decide how to approximate the equations numerically and express the approximation in a computer language such as Fortran. Next, they debug the program by running the simulation code. If the results are wrong, they change the mathematical model, numerical approximation, or computer code. Thus, they must perform similar tasks repeatedly, which requires an enormous amount of time. For example, a code developer may spend a year developing an initial version of a physics module and a significant amount of time thereafter maintaining it.

We designed ALPAL to automate the routine aspects of code development. The automation increases the speed, efficiency, and reliability of developing the module. Scientists then have more time for experiments that improve the quality of their physical models. ALPAL also makes available important numerical methods (e.g., implicit methods for tracking changes in time) that are too difficult to implement by traditional methods.

Specifying a Scientific Model for ALPAL

ALPAL automates only the most time-consuming and least challenging of the tasks of scientific code developers: the actual writing of the computer program. If scientists are relieved of the routine parts of code development, they can concentrate on the mathematical models and their numerical approximations. Neither ALPAL nor any other computer program can substitute for scientists' expertise and judgment in these areas.

With ALPAL, scientists can describe their models in a high-level language similar to the familiar language of scientific journals (Figure 1). For example, they can describe algebraic equations, finite-difference operators, finite-element basis functions, and interfaces to other code modules in the usual mathematical language.

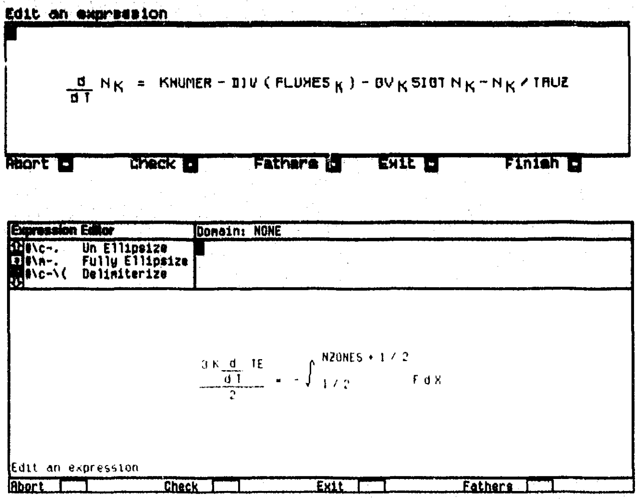

$$\frac{d}{dT} N_K = KNUMER - DIV(FLUXES_K) - DV_K SIGT N_K - N_K / TAUE$$

$$\frac{3K \frac{d}{dT} TE}{2} = -\int_{1/2}^{NZONES+1/2} F\,dX$$

Figure 1. Sample input to ALPAL. These examples are equations that ALPAL users have entered on the computer screen. With the mouse and keyboard, the user can edit the equations in this natural two-dimensional form.

After the code developers enter a description of their solution to a problem, ALPAL analyzes the problem, reorganizes it, and makes extensive symbolic computations implied by the problem specification. For example, ALPAL will perform symbolic differentiations and deduce exactly where the resulting expressions are defined. Then ALPAL generates a code module, in the Fortran or C computer languages, that can be included in the large simulation code.

The amount of time this saves the code developer can be measured by the fact that ALPAL generates a code module about 20 times larger than the code developer's specifications. Also, the code is generally more efficient and more compact than that written by traditional means.

Applications

To demonstrate ALPAL's viability, we constructed various physics models for which ALPAL has generated code modules. To simulate laser-plasma interactions, we constructed four modules: a one-dimensional laser propagation model, an implicit one-dimensional hydrodynamics model, an implicit two-temperature diffusion model, and an implicit atomic kinetics model. With ALPAL, we also generated code modules for a complicated charged particle transport model, a nonlinear flux-limited temperature diffusion model, and Fokker–Planck equations. We developed these code modules with less effort than it takes with traditional methods and found it easy and quick to make changes.

Conclusion

ALPAL is still a research code despite our frequent improvements. Nevertheless, it is sufficiently powerful that we have already used it to develop large scientific simulation codes. We plan to use ALPAL for various other projects at LLNL. ◆

Massively Parallel Computing Initiative

E. D. Brooks III

We have developed and tested a new supercomputing concept in which hundreds to thousands of high-performance microprocessors work in parallel to solve complex computational problems. This approach to building supercomputers represents a fundamental change in computer architecture that will provide unprecedented computing power for LLNL scientists and engineers.

The transition to massively parallel systems is driven by the performance revolution in microprocessor technology. In the early 1980s, microprocessors were simple computing devices; they were slow and could only handle 8-bit character quantities. These microprocessors sparked the personal computer revolution but were useful only for text-processing and control applications.

In the past decade, microprocessor technology has improved rapidly; the performance of microprocessor-powered equipment now rivals supercomputer performance for 64-bit, scalar floating-point operations. We expect that the vector-processing speed of the microprocessor-powered devices will soon rival the vector-processing speed of supercomputers.

Because microprocessors are evolving rapidly to provide supercomputer performance for a fraction of the cost of the supercomputer and because the performance development of conventional supercomputer technology has remained relatively stagnant, we believe microprocessor technology will soon displace supercomputing technology. The goal of the Massively Parallel Computing Initiative (MPCI) is to learn how to exploit the potential of massively parallel computing so that LLNL can achieve higher levels of performance in its critical mission applications. We want to ensure that LLNL can take advantage of new parallel systems as they are developed.

In the MPCI, we had several specific objectives:

- To evaluate the potential of highly parallel microprocessor-based machines for production computing.
- To determine the best scalable algorithms and programming models for massively parallel machines.
- To collaborate with the U.S. supercomputer industry to achieve practical massively parallel machines.
- To create technical strategies to facilitate LLNL's transition to massively parallel production computing.

We have met these objectives and are beginning the era of routine use of massively parallel machines at LLNL's Livermore Computer Center (LCC) and National Energy Research Supercomputer Center (NERSC). Through our efforts, we have helped create a substantial base of computational scientists, engineers, and systems programmers literate in the techniques of massively parallel computing. These people and their expertise are our most valuable contribution to the LLNL computing effort.

We have developed and tested parallel-scaling paradigms for a wide range of applications, including:

- Neutron transport.
- Hydrodynamics.
- Structural analysis.
- Applied mathematics.
- Plasma physics.
- Simulation of computer systems.
- Electromagnetics.
- Climate modeling.
- High-energy physics.
- Quantum mechanics.
- Molecular dynamics.
- Radiation transport.
- Parallelized computer graphics.
- Game theory.
- Nuclear physics.

Given this range of application development within the MPCI, we cannot provide complete documentation in this paper. For more information, however, the reader may refer to Brooks and Warren (1991) and to Brooks et al. (1992).

As examples of the two ends of the application performance spectrum, consider Monte Carlo photon transport and adaptive mesh hydrodynamics. Using a single processor of the BBN TC-2000, we found that a symbolic implicit Monte Carlo (SIMC) transport algorithm ran at 35% of the speed of the Cray Research Y-MP processor. Our 128-processor BBN TC-2000 offers a performance potential of 44.8 times the single central processing unit (CPU) speed of the conventional supercomputer if the application can be efficiently parallelized. To date, we have obtained 30.5 times the single CPU speed of the Cray Y-MP using 118 processors on the BBN TC-2000. Figure 1 shows the increase in speed, as a function of the number of processors, for the SIMC algorithm. Massively parallel systems clearly provide a new computational capability to process Monte Carlo transport algorithms using larger numbers of relatively faster processors. Indeed, a single microprocessor can now outperform conventional supercomputer CPUs for this algorithm.

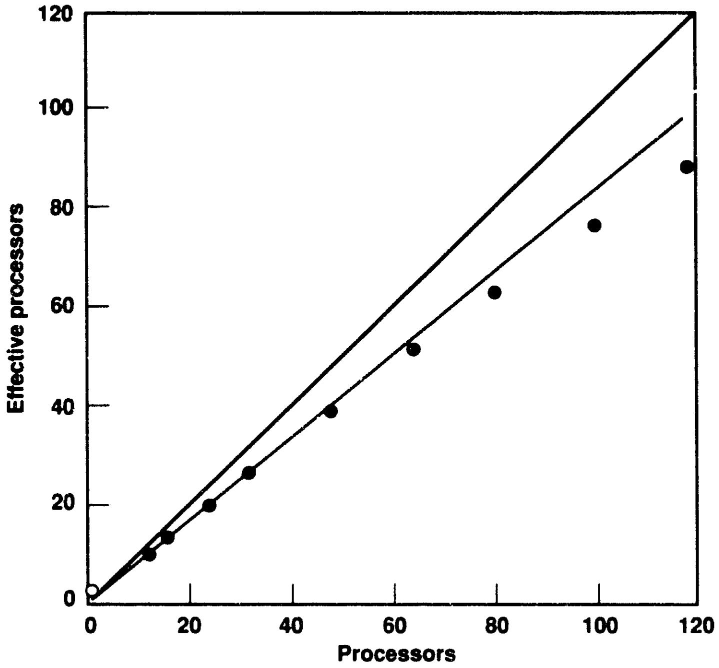

Figure 1. The effective performance of the parallel SIMC algorithm on the BBN TC-2000 as a function of the number of processors. Dark-green line is the idealized linear increase in speed that would occur if we do not include the parallelization overhead of the code used to control the processors. Light-green line is the possible increase in speed if the parallelization overhead of the code is included. Closed circles show the measured increase in speed on the BBN TC-2000. Open circle shows the single-processor performance of the Cray Y-MP CPU.

Hydrodynamics codes are usually highly vectorized on conventional supercomputers and, as a result, run with a high degree of efficiency. These codes tend to require a very high bandwidth to main memory, which puts cache-dependent microprocessors at a distinct disadvantage. For example, the vector floating-point performance for the Motorola 88000 microprocessor is particularly poor, obtaining only one-fiftieth the speed of a Cray X-MP on a typical well-vectorized hydrodynamics code.

We do not suggest that this speed loss be made up through the use of massive parallelism. However, we expect that by implementing highly vectorized codes on massively parallel systems, we will provide a new computational capability when the basic vector speed of the microprocessor is closer to that of the conventional supercomputer. We expect that this performance gap will close in the next few years.

We have learned important lessons from the MPCI. We have learned that a mixed programming model environment that offers data-parallel, message-passing, and remote-memory reference capabilities is important to the success of parallel computing at LLNL. LLNL applications are often complex combinations of algorithms, each of which may require a different programming model. We must have massively parallel systems that support mixed programming models to provide efficient overall performance.

We have developed the notion of capacity and capability use of massively parallel computing systems. In the past, supercomputers were the most powerful and cost-effective machines for scientific computation. However, parallel machines are now more cost-effective and have displaced much of the capacity workload from our supercomputer centers. Unfortunately, the capacity workload at our supercomputer centers comprises about 90% of the workload, and the remaining capability workload is insufficient to support a viable supercomputer center. Unless massively parallel platforms offer both capacity and capability service, they will not be financially viable.

Many scientists and engineers from LLNL and from several university and corporate research groups have participated in the MPCI. Records from our BBN TC-2000 accounts indicate that more than 250 LLNL researchers used the machine during the three-year initiative. Researchers from 17 other institutions, inside and outside the United States, also participated.

The MPCI has positioned the Laboratory to take advantage of massively parallel computing platforms as they are developed. Massively parallel systems have supplanted conventional supercomputers for Monte

Carlo and other scalar-dominated applications and will eventually supplant conventional supercomputers for highly vectorized applications.

The MPCI has greatly affected LLNL's computer centers. Before the MPCI, neither the LCC nor the NERSC considered massively parallel computing platforms as potential production supercomputers. Now, however, the LCC is soliciting competitive bids for a production massively parallel computing platform, and the NERSC is planning to acquire a massively parallel system for production work in FY 1993. ◆

References

Brooks, E. D., III, and K. H. Warren (1991), *The 1991 MPCI Yearly Report: The Attack of the Killer Micros*, Lawrence Livermore National Laboratory, Livermore, CA, UCRL-ID-107022.

Brooks, E. D., III, et al. (1992), *The 1992 MPCI Yearly Report: Harnessing the Killer Micros*, Lawrence Livermore National Laboratory, Livermore, CA, UCRL-ID-107022-92.

The Multicomputer Toolbox

A. Skjellum, S. G. Smith, C. H. Still, and R. D. Falgout

The Multicomputer Toolbox is the first general-purpose collection of communication, mathematical, and support libraries for parallel computers. Because these computers can carry out more than one computation at the same time on different central processing units, they are more powerful than individual computers.

The Toolbox operates on the nCUBE hypercube, the Symult S2010 and Intel Delta meshes, the BBN TC-2000 Butterfly (the LLNL parallel computer), and the Thinking Machines CM-5 system (Figure 1). It also supports networks of workstations with identical architectures, although they are not strict parallel computers, and will support new parallel processors as they become available. Although the Toolbox supports various applications, we are specifically developing simulations of groundwater remediation, chemical-process dynamic flow, and power systems. We also developed a neutron-transport code called ARDRA, based on the Toolbox.

Programming Features

The Toolbox has two features that distinguish it from other parallel libraries and make it the state of the art in parallel library development. First, a user can program an abstract model of computer architecture rather than program directly to the machine architecture. This ability means that the application writer can easily move codes between computers with different architectures.

Second, each mathematical or scientific calculation in the Toolbox supports user-specified data layouts. This feature is important because in parallel computers, calculations are divided between processors and different parts of a calculation might have different optimal layouts. In some cases, the Toolbox supports different ways of calculating one mathematical procedure. Thus, the user can tune the entire application, instead of only a single step of a calculation, for better overall performance.

To be worthwhile, software for parallel processors must apply to many generations of machines. Therefore, the Toolbox is made applicable to many types of computers and flexible enough to be used in new generations. The flexibility shows in the high-level communications interface, where complex data structures can be communicated effortlessly between computers.

Mathematical Code Update

In FY 1992, we added a package of iterative linear-system solvers to the Toolbox. We also researched and developed a set of concurrent basic linear algebra subprograms so that applications that use sequential basic linear algebra subprograms can be used on a parallel computer. As in other Toolbox technology, we designed the algorithms to support user-defined data layouts rather than specifying layouts within the algorithm. We added a Fortran interface to the standard C message-passing layer so that the Toolbox can be applied to applications and numerical methods that use Fortran. We also extended the existing communication layer so that parallel computers having different architectures can use the Toolbox in the future.

We will continue developing the Toolbox in FY 1993 with outside funding. We plan to make the Toolbox a deliverable product and develop a user manual and program documentation. By providing free Toolbox technology, we plan to encourage Toolbox use throughout DOE, academia, and industry, thus enriching parallel processing and promoting a market in parallel libraries. ◆

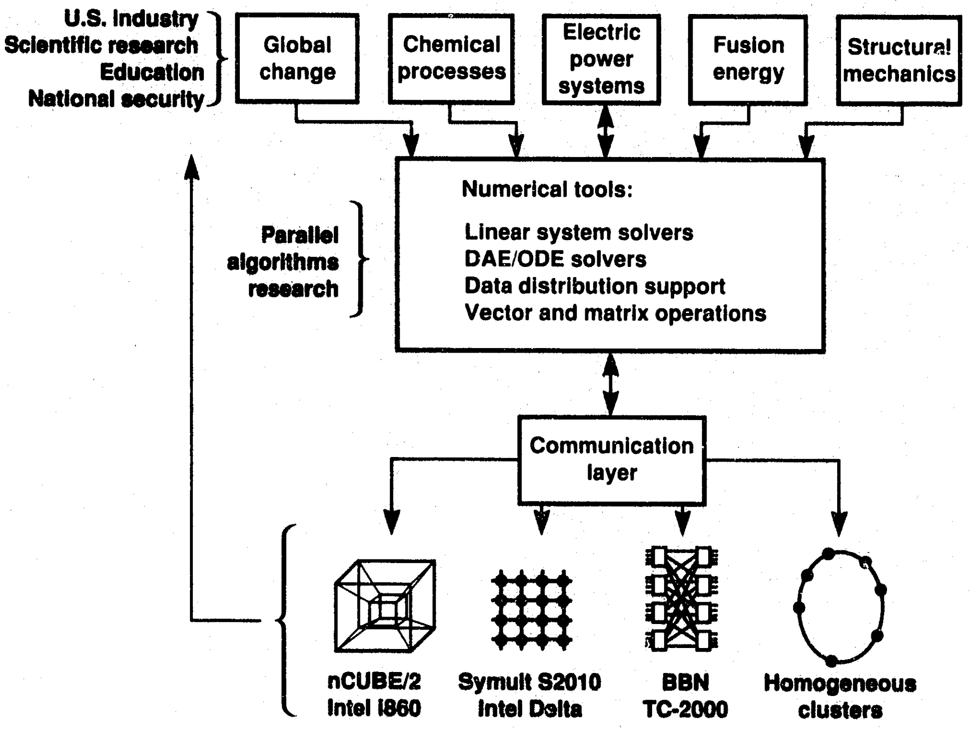

Figure 1. Four multicomputers (bottom) and some users they support (top). The Toolbox provides a synergy between applications, algorithm developers, and real computers.

Evolution of a Vortex Wake and Interaction with a Free Surface

J. B. Bell and D. L. Marcus

The vortex-wake system behind submerged bodies leaves a characteristic signature on the free surface, e.g., the wake behind a boat. Although small in amplitude, such disturbances are visible because the particle motions induced by the wake flow create a straining field at the surface that modifies its physical characteristics, including reflection, refraction, and scattering of visible and infrared light. These disturbances can be seen clearly in photographs taken of the sea surface from aircraft and satellites, using both passive and active sensors. Consequently, we are studying the interaction between a vortex pair and a free surface.

Vortex-wake signatures occur at a relatively late stage in the lifetime of the trailing vortex system. The motion is complicated by the onset of various demise mechanisms, such as Crow instability, vortex reconnection, vortex breakdown, and turbulent diffusion. Furthermore, in passing through thermoclines on its way to the surface, the existing vortical flow interacts with the baroclinic vorticity generated when pressure and density gradients become nonparallel, so further distortion is created. The effect of these interactions on the ultimate form of the surface signatures is unknown.

Our goal is to develop a numerical model for complex, three-dimensional (3D), incompressible, stratified flows. We are using these methods to understand and predict the effect that passage of the vortex system through a sharply stratified medium has on the existing vorticity and on the ultimate form of the surface signatures.

Computations that are developed to study vortex-surface interactions have applications that extend far beyond the context of naval hydrodynamics. Many problems in astrophysics, atmospheric science, defense science, oceanography, and engineering can be modeled by the incompressible, variable-density Navier–Stokes equations. This technology will permit study of flow regimes in areas that previously have been inaccessible. The fine structure and wide range of length scales that this methodology can resolve will also make it a useful tool in the direct numerical simulation of turbulence.

We have developed a numerical method for the incompressible, Navier–Stokes equations in stratified media and have used it to model problems in vortex-surface interaction. This method is based on a second-order, fractional-step scheme in which diffusion-convection terms are advanced without enforcing the incompressibility condition. The resulting intermediate-velocity field is then projected onto the space of discretely divergence-free vector fields. The nonlinear convection terms are treated using a higher-order upwind procedure. The procedure is second order for smooth flows and remains stable and nonoscillatory for nonsmooth flows with low fluid viscosities. With this approach, we can resolve the fine vortical structure of stratified flows.

In developing the numerical tools needed to model the interaction of a vortex wake with a free surface, we extended the variable-density projection to three dimensions, first for a fluid in which the density jump is modeled by a Boussinesq (small-amplitude) approximation, then for a finite-amplitude density jump. Next, we developed a front-tracking method to accurately model the motion of the free surface and to incorporate the effect of properties dependent on interfacial conditions (i.e., contaminants). Our volume-of-fluid method is similar to shock-tracking algorithms for gas dynamics that treat selected discontinuities as free boundaries moving through the finite-difference mesh. We carried out 3D simulations of the dynamics of vortex rings and pairs interacting with a free surface, particularly vortex reconnection. Additionally, we studied the interaction of coherent structures in turbulent shear flows with a free surface.

Ongoing work in this area includes developing incompressible, adaptive, mesh-refinement technology; developing a method for incorporating surface-tension effects in interface calculations; and conducting parametric studies of free-surface vorticity dynamics, in particular comparing our numerical investigations with the experimental literature. ◆

References

Marcus, D. L., and S. A. Berger (1989), "The Interaction between a Counter-Rotating Vortex Pair in Vertical Ascent and a Free Surface," *Phys. Fluids A* **1**, 1988.

Developing the Remote Experimental Site Concept

T. A. Casper, W. H. Meyer, and D. N. Butner

We are developing the remote experimental site (RES) concept to provide a mechanism for LLNL to interact with remotely located facilities over ESNET, the energy sciences wide-area computer network (WAN) that links all energy research laboratories and universities. This concept uses a WAN extension of a distributed computer system previously used to acquire data and to control instruments in use on magnetic fusion experiments at LLNL. The fundamental mechanism that we use to synchronize and control experimental events relies on the principle of remote procedure calls (RPCs), which we implement through our interprocess communications system (IPCS) software. IPCS provides a seamless and transparent method for process-to-process interaction between multiple workstations in a heterogeneous computer network. This network involves workstations from various vendors, using both Unix and VMS operating systems.

In FY 1992, we extended this IPCS concept to provide synchronization and communication between processes running on computers at LLNL and those at the DIII-D tokamak fusion experiment operated by General Atomics (GA) in San Diego, California. We installed a Unix workstation and associated data-acquisition hardware modules in the DIII-D control room to provide LLNL researchers with a real-time connection to their experimental operations. Using IPCS and this hardware connection to the DIII-D experiment, we fully synchronized LLNL's computer network to that at GA, subject only to the roundtrip network delay time, which is typically about 100 ms. We thereby extended the online computational resources available to the experiment.

Any computers, whether at or remote to the GA facility, that run our IPCS and other synchronization and monitoring software can be used for real-time experimental operations, which is the essence of a distributed computing model. We implemented this system using the RPC concept that forms much of the basis for the now emerging technology of the distributed computing environment (DCE).

By employing "daemon" processes that run in the background on computers at LLNL and at GA, we provide user-transparent access to the DIII-D database from our own analysis software and from commercially available packages such as PV-WAVE (from Precision Visuals, Inc.) and Interactive Data Language (IDL, from Research Systems, Inc.). This client–server model for data access provides both interactive and automated intershot analysis and display capabilities that take advantage of the computational power at both institutions, even though they are separated by some 800 km. These newly developed capabilities are now supporting operations for experimenters located at LLNL on the DIII-D experiment under our experimental collaboration program with GA.

To extend this interaction, we are developing techniques to use the National Storage Laboratory—a prototype, terabyte-capacity, data-storage facility located at the National Energy Research Supercomputer Center—to store network-accessible experimental data. Initially, we are using the network file system protocols to provide connectivity to this storage facility. With future funding, we intend to pursue use of this mass storage system and may convert to a distributed file system, which is consistent with the present directions for DCE.

In addition, we plan to extend our RES implementation to accommodate both multiple databases and to allow for data storage from different experiments. Using diagnostic instruments, we will begin to implement the WAN remote control associated with the RES concept. Further applications of data analysis and display using distributed computing concepts will improve the efficiency of our computational resources. We will continue to develop prototypical applications within the real experimental physics environment under our collaboration on the DIII-D tokamak fusion experiment at GA. ◆

Algorithmic Strategies for High-Performance Computing

G. McNamara and N. G. Smiriga

During FY 1992, we continued work on the lattice Boltzmann method of simulating hydrodynamics. Our primary aim was to improve the fundamental lattice Boltzmann methodology, but we also explored extending the method to a wider range of hydrodynamic problems.

The lattice Boltzmann method simulates fluid dynamics by modeling, in a simplified manner, the molecular collisions that occur in real fluids. The model assumes a collection of particles on a regular two- or three-dimensional lattice. These particles travel along the links connecting neighboring lattice sites and collide at the sites. The lattice Boltzmann simulation records, for each site, variables that describe the density of particles arriving from neighboring sites. It models the collision process with a mathematical collision operator that redistributes the incoming particle densities among the outgoing lattice links. The collision operator tends to distribute the particles in a local equilibrium distribution, which is a function of the total mass, momentum, and energy of the particles at that site. The model requires proper lattice geometry, local equilibrium distribution, and a collision operator to mimic the Navier–Stokes hydrodynamics of real fluids.

The lattice Boltzmann method has successfully modeled fluid flow that involves complicated boundary conditions, such as flow through porous media and simulations of colloidal suspensions. However, existing lattice Boltzmann models are limited and inefficient in ways our work seeks to remedy.

As part of our study, we examined the Chapman–Enskog expansion used to derive the hydrodynamic equations that govern the macroscopic evolution of a lattice Boltzmann system. Our work demonstrates that proper hydrodynamic behavior is obtained only if the low-order velocity moments of the local equilibrium distribution match those of the Maxwell–Boltzmann distribution. This realization leads to a simple, mechanical means of first recognizing lattice geometry that can support the correct lattice Boltzmann model and then generating the appropriate local equilibrium for that geometry.

Using this methodology, we produced the first lattice Boltzmann model to correctly simulate thermal hydrodynamics in two or three dimensions. Previous lattice Boltzmann models incorporated only mass and momentum conservation in their microscopic collision operators and thus could not simulate thermal behavior. Our model adds energy conservation to the collision operator and correctly accounts for thermal conductivity and viscous heating.

Unfortunately, this model becomes linearly unstable when the transport coefficients are reduced to near zero to produce turbulent flow. The model is thus limited to simulations of low Reynolds- and Rayleigh-number, nonturbulent flows. Accordingly, we modified the local equilibrium distribution to maximize its entropy. This technique has improved the stability in nonthermal lattice Boltzmann systems, but it has not yet resulted in a stable thermal model.

We are also investigating lattice Boltzmann systems for modeling immiscible fluids. We produced a three-dimensional immiscible fluid model with variable surface tension and different viscosities in the two phases. In the future, this model may usefully simulate viscous segregation and thermal transport in immiscible fluid systems. ◆

Sisal Scientific Computing Project

D. C. Cann and J. T. Feo

Although multiprocessor computer systems have been commercially available for a decade, the number of scientific programming groups effectively using the capability of these machines is discouragingly small. Today, hundreds of parallel programming machines are run as capacity machines (i.e., multiple single-processor systems). Scientific research, work in the control of complex systems, and the development of commercial products will be delayed if we do not effectively use parallel architectures.

The greatest obstacles to using parallel architectures are imperative languages (languages in which programs largely consist of a series of commands to assign values to objects), which fail to provide a suitable environment for parallel program development and restrict the formulation of parallel algorithms. Writing correct, determinant programs in imperative languages is difficult and expensive (four to five times the cost of sequential programming).

To transcend the imperative programming model, LLNL has developed a high-level functional programming language, Sisal, that achieves the performance of imperative languages on conventional multiprocessor systems, reduces the cost of parallel programming, facilitates algorithm development, and simplifies compilation. In Sisal, programmers express their algorithm as pure mathematical functions, which allows them to write correct, determinant code faster and in fewer lines than in imperative languages. Functional programs are also machine-independent, so they can be ported to a variety of computer systems—including the next generation of machines—without rewriting.

The objectives of our project are to make the Sisal software available to the general scientific community, educate the scientific community in functional programming, and work with programming groups to write Sisal programs. Although Sisal is based on mathematical principles, the model is sufficiently different from conventional programming methodologies to require some retraining of programmers and redesigning of algorithms.

To attract scientific users, we offered free computer time to groups willing to write their applications in Sisal. During FY 1992, we received 45 proposals from interested groups outside LLNL. The proposals covered a broad spectrum of scientific fields including biology, chemistry, computer science, engineering, geology, medicine, numerical analysis, and physics. We opened accounts for outside participants on our four-processor SGI Iris 430, and the Cray 2, X-MP, and Y-MP machines at the National Energy Research Supercomputer Center. In addition to the proposals, we received more than 200 requests for information. Sisal is now installed at more than 70 sites worldwide, including three supercomputer centers.

Two important applications resulted from our project: a Sisal code to compute the Fourier transform for a symmetric group of size N, S_N*, and a Sisal code to simulate material dislocation in metal-class materials. Non-Abelian fast Fourier transforms (FFTs) appear in connection with the statistical analysis of ranked data. Researchers have proposed fast algorithms for computing such FFTs based upon a generalization of common FFT techniques; however, no vector or parallel implementation can be derived naturally by manipulating the non-Abelian FFT mathematical formulas. This study derived a parallel algorithm based on an almost direct translation of the mathematical expression of an FFT on the symmetric group S_N. The algorithm was easy to express in Sisal, and the researchers are optimizing the code for the Cray Y-MP.

The objective of the second study was to write a new code to simulate the movement of dislocations in metal-class materials undergoing high-temperature deformation. The code handles more dislocations than extent codes and will eventually model curved dislocation lines in three-dimensional space. The model tracks the motion of the dislocations by solving a system of coupled ordinary differential equations, which are solved by a Runge–Kutta–Fehlberg integrator. Again, the system's mathematics were easy to express in Sisal. Sisal's mixed language interface was used to interface with input and output routines (including a graphics package) written in Fortran and C. The researchers were particularly impressed with the portability of Sisal. They developed the code on Sun workstations but executed production runs on the Cray machines without any reprogramming.

To educate the scientific community in functional programming, we conducted a series of workshops and tutorials and published a set of manuals and programming guides. We taught a tutorial and sponsored a research exhibit at Supercomputing '91 in Albuquerque, New Mexico, and taught Sisal workshops at the University of Puerto Rico and the Ohio Supercomputer Center. We also participated in the Parallel Systems Fair at the International Parallel Processing Symposium in Beverly Hills, California. Additionally, we taught a two-day class for the National Technology University. We released manuals for the compiler and debugger and published two programming tutorials.

Our project culminated in the Second Sisal User Conference held October 5–6, 1992, in San Diego, California. The conference included a keynote speech and 21 presented papers. Sisal users from the United States, Puerto Rico, Australia, and Switzerland attended. ◆

Computational Algorithm Project

D. W. Hewett, G. DiPeso, and D. Larson

Our goal was to investigate new applications of our recently developed procedure for solving strongly coupled, partial differential equations. This procedure has enabled an exciting array of long-timescale plasma simulation models. The new method, coupled-equation, dynamic, alternating direction implicit (CEDADI), is a generalization of the alternating direction implicit (ADI) technique that has the advantages of requiring small storage and converging rapidly when "properly" implemented.

CEDADI starts with the finite difference of the equations on an orthogonal mesh. A fictitious time derivative is added with the intent to "timestep" the system of equations to the time-asymptotic state. A dynamic timestep selector is added that aggressively attempts to increase the timestep as quickly as stability—determined by comparisons between norms from single and double steps—will allow. This dynamic extension, termed DADI, still follows the traditional ADI method that splits the highest derivatives into their components along each of the coordinate directions. The components are in turn solved implicitly along each coordinate direction.

We also applied this method to systems of strongly coupled equations. Our interest in such systems of equations follows from years of difficulty in dealing with various versions of the electromagnetic field equations known as Maxwell's equations. Solved *explicitly*, these equations are amenable to simple leapfrog integration at the cost of small timesteps to avoid instability caused by waves moving more than a grid cell in one timestep. For *implicit* time integration for larger timesteps, more complex "curl–curl" operator equations often arise when Maxwell's equations are combined. It is these equations that our new method solves so well.

What makes our method appropriate for curl–curl equations is that they require vector decomposition into an electromagnetic part that has a rotational (solenoidal) character and another part that is electrostatic or irrotational. Such decomposition can be visualized as the rotational and irrotational parts of the vector field shown in Figure 1. Previous attempts to solve these operators used such decompositions but required expensive vigilance to avoid generating spurious components that invalidate the vector decomposition. Our CEDADI method reduces the expense by simultaneously solving the constraint equation that controls the spurious fields with the original equations.

In this project, we have exploited and extended our CEDADI procedure by incorporating into each coordinate-direction solution an implicit block-tridiagonal method that further increases the 2-order-of-magnitude speed advantage already achieved in certain cases by another factor of 6. Incorporating this additional advantage, we are confident that our latest simulation model (a new quasi-neutral version of our radiation-free, Darwin approximation to Maxwell's equations) can be made into an efficient computer algorithm. We are now implementing this algorithm and expect it to be useful in modeling plasma processing and other high-density, low-frequency plasma behavior. ◆

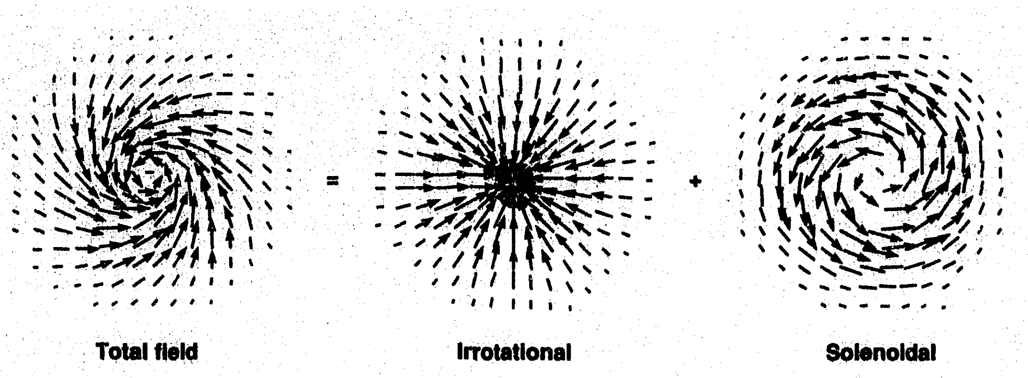

Figure 1. Example of vector decomposition. General vector fields (e.g., the total electric field) can be represented by an irrotational (electrostatic) part and a solenoidal (inductive) part.

The Amoeba Project: Automated Planning for the Tactical Battlefield

C. Cunningham and E. Powell

In the Amoeba project, we are developing techniques to intelligently control military units in an interactive combat simulation. These techniques should allow fewer than 100 people to direct corps-level engagements (up to 10,000 decision-making units).

In FY 1992, we focused on planning and controlling movement in a command hierarchy, which allows a few decision makers to control the movement of many units. This hierarchy is similar to the military command structure, of which each element has only a few immediate dependents. We first considered the movement of units through the terrain because movement is fundamental to other types of maneuvers and because accomplishing this step dramatically reduces the workload for the players.

We based our scheme on the A* algorithm, which minimizes path length and has been used for determining routes in other combat simulations. We developed procedures that provide a balance between reducing path length and preserving the formation of a small number of units. To respond to unexpected events, we keep performance estimates for each unit, which give the unit criteria to detect trouble, notify its superior, and invoke replanning. As a result, our model of the mechanized company readily negotiates perceived terrain, which changes as information is gathered about it (Figure 1).

Because the enemy's behavior will influence the goal of the company, we investigated adaptive goal selection by planning bounding overwatch maneuvers, in which one tank platoon watches for the enemy from an observation post while another changes position. We determined the value of an observation post by such factors as the platoon's view of the terrain, its proximity to the approaching unit, and the movement plans of both units. Our planning procedure gives sensible behaviors for the platoons. We believe that our techniques will also be effective in planning positions from which to engage the enemy.

Our bounding overwatch study showed that balancing different goals by a rigid rule sometimes led to poor global behavior, such as the refusal of an overwatching platoon to leave a particularly good vantage point—a problem that would become more severe in the face of the enemy. Thus, a mechanism will be needed to adapt the rules of engagement to changing situations.

We further developed the cooperative behavior of units, as in the bounding overwatch, in a simulation of logistics operations in a rocket artillery platoon. Here, several mobile rocket launchers and supply vehicles work together to allow the launchers to perform efficiently and avoid counter-battery fire.

We implemented these model problems on an interactive graphics testbed that we produced during FY 1992. This testbed runs on the Computer Simulation Laboratory's VAX machine at LLNL and has several features in common with the Janus combat simulation, such as its terrain representation.

In FY 1993, we will move to an open-system environment on a distributed-simulation network being developed for the Janus 2000. We are implementing a polygonal terrain model that will be compatible with the terrain representations of combat simulations such as UCCATS and SimNet. The planning of simple fire and movement engagements will be our major technical focus. ◆

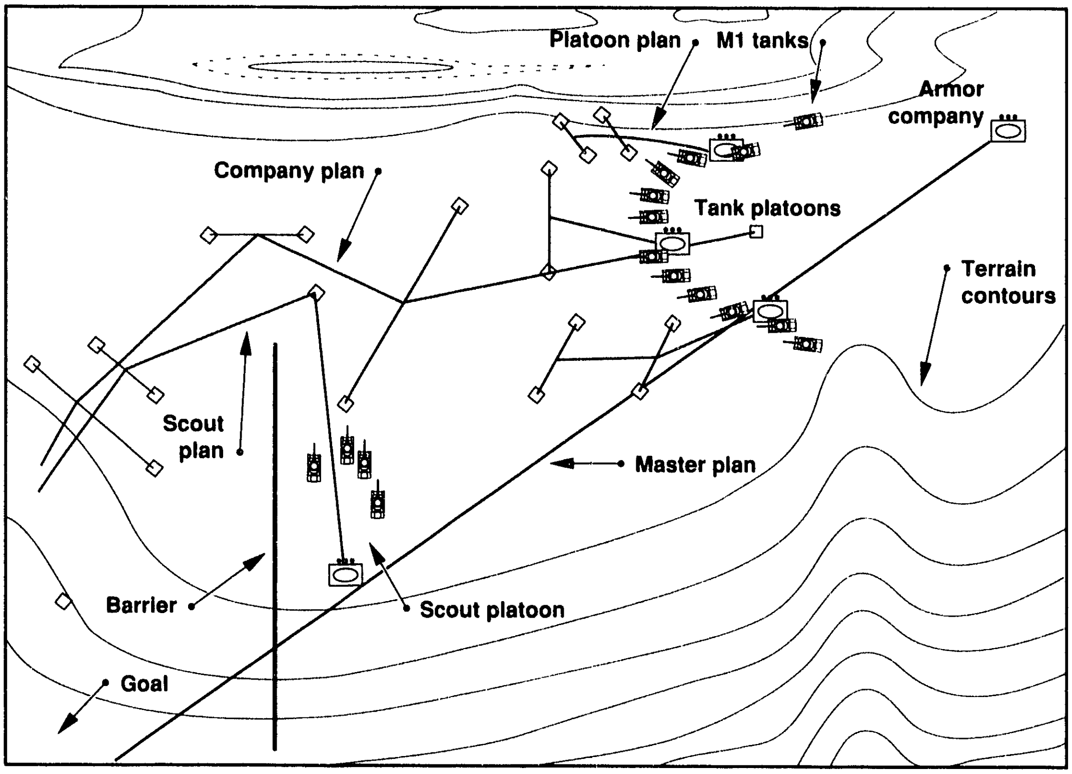

Figure 1. Computer simulation of a battlefield, developed with our modeling scheme. An armor company prepares to negotiate a barrier, discovered and investigated by its scout platoon. Plans show anticipated future positions for the units, derived by the elaboration of the company's master plan.

Research in the Effective Use of Circuit Switches in Data Communications

W. J. Lennon and P. R. Rupert

Emerging, large-scale energy and weapons research applications require communication rates of gigabits per second. Attaining such rates with a traditional shared-bus approach like Ethernet would require high-speed electronics considerably beyond the state of the art. The required rates can be achieved, however, with an inherently parallel, circuit-switch–based local area network (LAN).

LLNL's High-Performance Switching System (HPSS) project has developed, in collaboration with private industry, a novel, circuit-switch–based LAN that will be capable of more than 1024 simultaneous, 1-Gbit/s connections between office workstations, support facilities, and onsite supercomputers. Each port may establish more than 1000 connections/s or send up to thirty 1000 × 1000, 24-bit displays/s. A 266-Mbit/s switch and adapters are being tested. A 32-port prototype switch is scheduled for Defense Systems application testing during FY 1993, first at a rate of 266 Mbit/s per port and later at 1 Gbit/s.

This project has been designed to complement and leverage the results of the HPSS project to support a broader community. We have two underlying goals: to foster outside access to LLNL resources and expertise, and to advance LLNL's capabilities in gigabit-per-second network technology.

Our current focus is on developing a gigabit-per-second product testbed, implementing the BLANCA–XUNET gigabit-per-second wide area network (WAN) and defining a metropolitan area network (MAN), the last in cooperation with 11 other San Francisco area government, university, and private-sector laboratories. We have reduced or deferred work in several task areas: circuit-switch parametric studies, American National Standards Institute (ANSI) standards activities, and development of a "lightweight" network protocol.

We had five significant achievements in FY 1992:

1. LLNL has become a full research partner in the AT&T-led gigabit-per-second experimental university network consortium, XUNET. We have successfully proposed Fibre Channel as its high-performance connection standard. XUNET hosts BLANCA, one of five national gigabit-per-second WAN testbeds sponsored as part of the High Performance Computing and Communication Program.
2. LLNL and others in the region are forming a Bay Area gigabit-per-second network, BAGnet.
3. Pacific Bell will contribute fiber-optic resources to collaborate with us on these and a third gigabit-per-second network linking LLNL, Lawrence Berkeley Laboratory, and Sandia National Laboratories, California.
4. We have conducted several major tests in our gigabit-per-second technology testbed.
5. We have established ties with LLNL's National Storage Laboratory.

In FY 1993, we will foster gigabit-per-second scientific-application collaborations between LLNL and UC Berkeley in two research areas: surface physics and combustion research. Scientists at the two facilities will have very-high-speed access to codes on each others' workstations as well as access to unique resources at the two sites. A similar experiment will support collaborations between scientists at LLNL and the California Institute of Technology, who are studying inertial instabilities. We will also develop a plan with scientists at LLNL's Magnetic Fusion Energy Program and General Atomic to conduct a remote experiment-siting demonstration for the DIII-D tokamak in San Diego, California. All of these experiments require collaboration with common carriers like Pacific Bell and MCI.

Upon delivery of the first commercially available Fibre Channel LAN at LLNL, we will begin our circuit-switch–based LAN research. We will develop discrete event simulation models, performance-analysis procedures, and LAN test suites. Finally, we will continue gigabit-per-second communication product testing and begin to test Fibre Channel products. ◆

Section
3

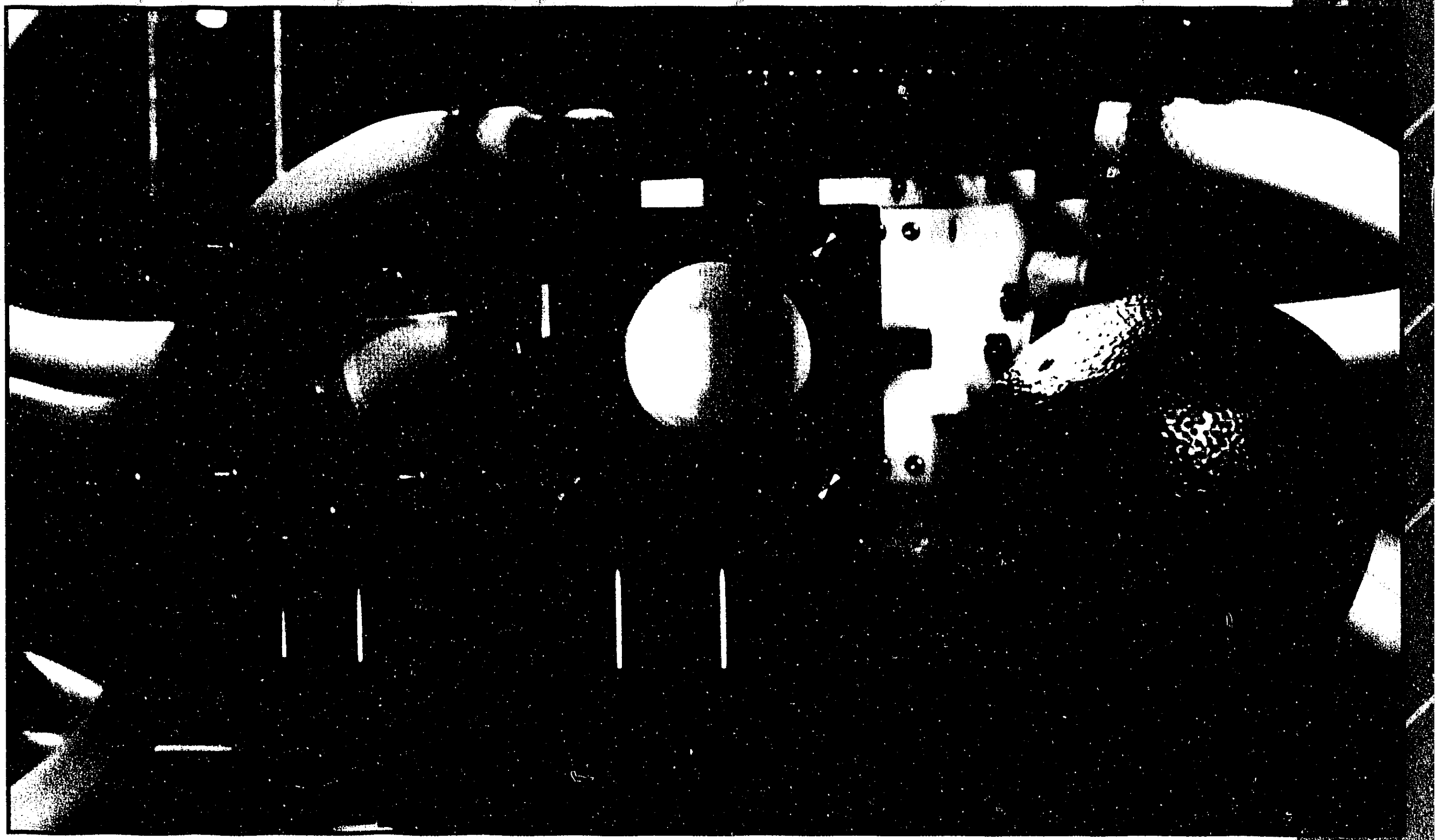

High-Performance Lasers and Beams

Laboratory Directed Research
and Development FY 1992

On the previous page. First kilowatt-level, diode-pumped machining laser. The laser head is about the size of a lunch box. For size reference, note the orange and the 5-cm-diam optics through which the beam is emitted.

Laser Guide Stars and Adaptive Optics for Large Astronomical Telescopes

C. Max, H. Friedman, J. Brase, K. Avicola, H. Bissinger, D. Gavel, E. Johansson, R. Kiefer, J. Morris, S. Olivier, D. Rapp, J. T. Salmon, K. Waltjen, L. W. Bradford,* and S. Flatte*

The Laser Guide Star Project aims to develop technology for high-resolution imaging on large ground-based telescopes by compensating for the deleterious effects of atmospheric turbulence. We are pursuing the laser guide star technique to create a reference wavefront for an adaptive optics system. Using this technique, we will perform a feasibility demonstration to achieve high-order wavefront corrections. We will also investigate the utility of these corrections for large telescope systems. If this technology proves feasible, it would improve the imaging resolution of present telescopes by a factor of 10 to 100.

To create a guide star, we use the LLNL Atomic Vapor Laser Isotope Separation (AVLIS) lasers tuned to the sodium D line to resonantly excite an atmospheric sodium layer 90 km above the earth's surface. This excitation makes an artificial star, which we use as a wavefront reference. Two nearby telescopes observe the artificial star: One monitors the star's properties, and the other corrects the image of a nearby astronomical object by using special deformable mirror technology developed within the AVLIS program.

In FY 1992, we installed the laser guide star optical site at LLNL and began broadcasting our laser into the atmosphere. We used two telescopes to characterize the brightness, size, and shape of the laser guide star and to measure the atmospheric distortions using the guide star as a reference. We also developed and fielded a new high-speed wavefront sensor to measure the atmospheric turbulence in detail.

Figure 1 shows an image of the round laser guide star at the 90-km altitude of the sodium layer. The atmospheric compensation system places an aperture around the laser guide star to block out the Rayleigh scattered light.

Figure 2 shows the brightness of the laser guide star as a function of the power of the upgoing laser beam. The data points are our measurements made using a charge-coupled-device (CCD) camera, and the green line is our theoretical prediction using a detailed model for the atomic physics of the sodium layer. When we broadcast 1100 W from the AVLIS laser beam, the guide star is about fifth magnitude and is visible with the naked eye.

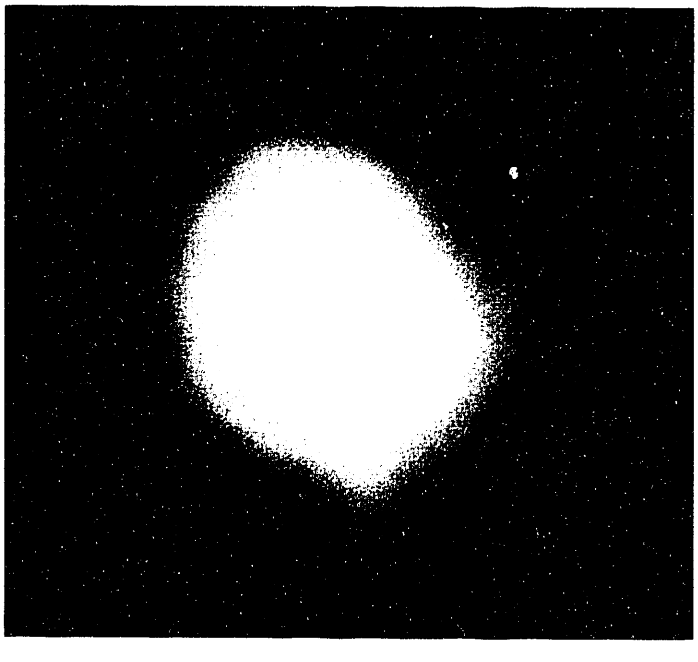

Figure 1. Image of the laser guide star. To create this guide star, we use the LLNL AVLIS laser to excite the sodium layer 90 km above the earth's surface.

---

*University of California at Santa Cruz.

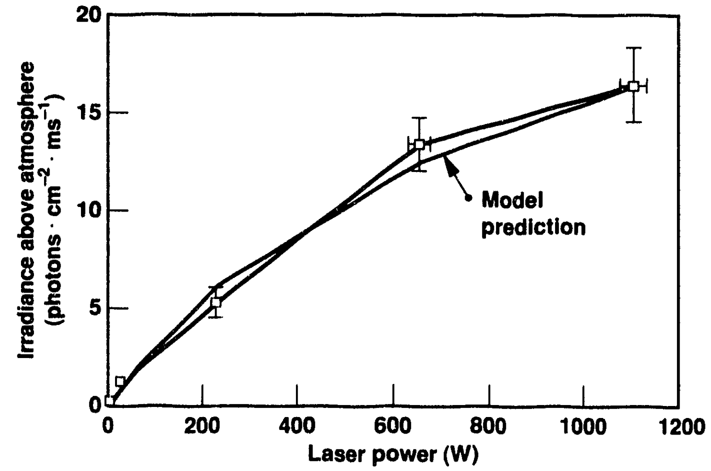

During FY 1993, we plan to turn on an optical pulse stretcher, which will lengthen the laser pulse by a factor of 16 and make the laser guide star considerably brighter. We will integrate our deformable mirror and control computer into our adaptive optics system and perform closed-loop atmospheric compensation. We will also continue our design studies for laser guide star adaptive optics systems on large astronomical telescopes. ◆

Figure 2. Brightness of the laser guide star as a function of laser power. Black line connects data points measured using a Photometrics CCD camera; green line is our theoretical prediction. Brightness is referred to its value above the atmosphere.

Coupling Physics in Ultra-Intense, Laser-Plasma Interactions

C. Darrow, W. L. Kruer, M. Tabak, E. M. Campbell, D. Klem, S. Lane, and S. Wilks

We investigated the coupling of intense, subpicosecond laser pulses with plasmas that were preformed on solid targets. Our goal was to produce directed bursts of megavolt electrons traveling in the original laser-propagation direction. Specifically, we investigated production of energetic electrons and hard x rays and absorption of laser light. To accommodate these tasks, we upgraded our laser and target facilities.

Coupling Physics Issues

Producing energetic electrons with high efficiency and with highly directed motion requires ultra-intense laser pulses. The normalized momentum of an electron quivering in the field of the laser is given by $\alpha = p_{osc}/mc = 8.53 \times 10^{-10}\ \mathrm{W} \cdot \mu\mathrm{m}^2/\mathrm{cm}^2$.

When spatial gradients in α^2 are present, a net nonoscillatory, nonlinear force (the ponderomotive force) can accelerate electrons. As α approaches or exceeds unity, the longitudinal component of the ponderomotive force can dominate. In extremely sharp gradients, electrons can be accelerated in the *forward* direction to energies equal to the peak quiver energy on the order of 1 MeV, as in our experiments.

Relativistic considerations alter this simple physical picture. For example, simulations by Wilks et al. (1992) predict electron energies several times the peak quiver energy with an effective distribution temperature, approximately equal to the ponderomotive potential $\Phi_p = 0.5(1 + \alpha^2)^{1/2}$ MeV.

Fast Electron Measurements

We detected electrons directly using a magnetic monochromator designed for high collection efficiency, electrical and x-ray noise immunity, and accurate absolute calibration. We obtained the energy distribution of electrons escaping the target by taking shots for various values of the monochromator magnetic field. We observed electron energies up to 4 MeV with distribution temperatures of about 1 MeV. (The maximum observable energy was limited by the maximum magnetic field strength obtainable in our magnet; we expect that electrons with energies in excess of 7 MeV will be observed in the near future with a reconfigured magnet.)

The typical electron yield of 3% (into 4π steradians) fell dramatically when the laser energy was reduced from 4 to 3 J. The maximum electron yields were obtained with best focus 0.5 to 1.0 mm in front of the target.

Hard–X-Ray Experiments

We measured hard x rays to provide independent information on the distribution of fast electrons produced in the laser-plasma interaction. Hard x rays are produced when energetic electrons collide with solid density material in the immediate vicinity of the target. Various models predict the relationship between the x-ray and electron distributions. In our first experiments, a single-channel NaI crystal was used to detect hard x rays produced with relatively low intensity irradiation of 10^{17} W · μm²/cm². Various thicknesses of lead, copper, and aluminum filters were placed over the crystal on many shots to estimate the x-ray spectral distribution. As expected, the data have a great deal of scatter. Nevertheless, assuming an exponential distribution, the data imply a temperature of 10 to 100 kV with an energy yield of about 0.003%.

A second nine-channel, x-ray detector array has since been fabricated. A limited number of test shots were taken and show the presence of multimegavolt x rays.

Absorption Experiments

We measured absorption to determine the efficiency with which laser energy couples to the target. Our measurements are the first with both subpicosecond pulse widths and relativistic α's. In these experiments, the target was surrounded with a highly reflective sphere with holes cut to allow light to enter and exit at the proper angles. Energy meters outside the sphere monitored the incident, backscattered, and specular light energies (E_{inc}, E_{back}, and E_{spec}, respectively), while diodes inside the sphere monitored the diffuse scatter (E_{diff}). Absorption is determined using

$$A = \frac{E_{\text{inc}} - E_{\text{diff}} - E_{\text{spec}}}{E_{\text{inc}}} . \tag{1}$$

Absorption was approximately 50% at 2×10^{16} W · μm²/cm² and fell with increasing intensity to about 25% at 10^{17} W/cm². The measured absorptions were similar for the targets of carbon–hydrogen (plastic), aluminum, and tantalum. The data give some indication of increasing absorption at the highest intensities, but more data are needed to improve the statistics. The latter is precisely the intensity range over which the electron quiver motion becomes relativistic. Although preliminary in nature, these results suggest the importance of the new absorption physics associated with relativistic effects in plasmas. ◆

References

Wilks, S. C., W. L. Kruer, M. Tabak, and A. B. Langdon (1992), "Absorption of Ultra-Intense Laser Pulses," *Phys. Rev. Lett.* **69**, 1383.

Design of a Charge-Exchange X-Ray Laser

B. Ritchie and B. Elza

Our project involved modeling using crude charge-exchange cross sections and calculating accurate charge-exchange cross sections using state-of-the-art collision theory. We researched extending an innovative collision method to reactive collisions (Ritchie, 1992). We extended the method to molecular systems and evaluated the theory against standard results for electron-molecule scattering (Elza and Ritchie, in press).

We chose hydrogen as our target system because it shares features with more-complicated molecular systems and has been well studied. We obtained an interaction potential that describes this system from chemical structure codes and correctly reproduced various experimentally measured quantities, including the quadrapole moment. Molecular hydrogen's homonuclear diatomic nature made it ideal for our purposes. We evaluated our results against those obtained by other methods. This allowed us to explore the relatively low-energy, electron-molecule-scattering regime and to obtain useful insights into requirements for converging our results.

A Gaussian wave packet with a larger width corresponds to a better-resolved, more monoenergetic calculation. Figure 1 shows the results of our calculations for three widths: 10, 12, and 20 a.u. The figure also shows how quickly our results converge to the benchmark results. A wave-packet width of 15 a.u. yields results that are within a few percent of the highly converged 20-a.u.-width results. Also, the relatively low energy (E = 13.6 eV or k = 1) of this calculation is much lower than comparable methods presently in the literature for solving the time-dependent Schroedinger equation (TDSE). Noncentral, explicitly time-dependent processes can be accurately studied by solving the TDSE on a grid. Since time is explicitly included in the formula, the target system and scattering projectile can be allowed to evolve in time while being affected by the presence of a time-dependent field.

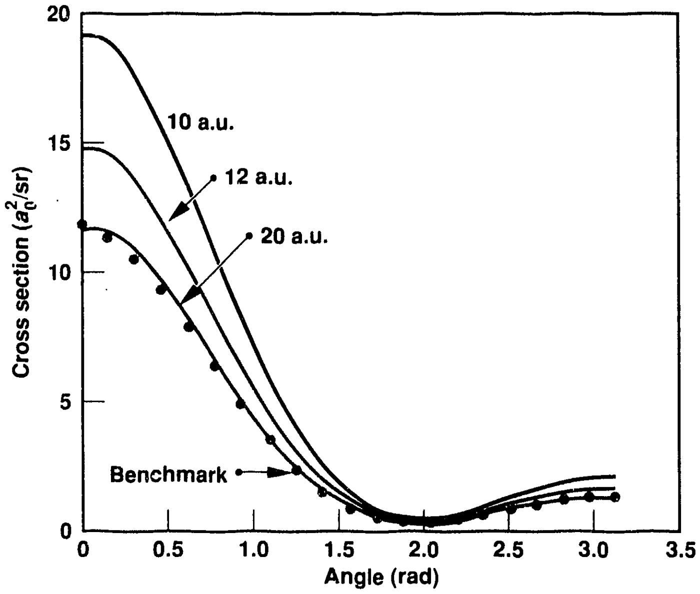

Figure 1. Differential cross section for electron-molecule scattering.

Because of limitations on our benchmark calculations, we have concentrated on relatively simple target systems rather than on our method for solving the TDSE. Indeed, we could obtain similarly accurate results for systems that are too complicated for all but a few time-independent methods. However, this would take a great deal more development time than our simple test calculations and would not provide extra insight on the applicability of our method.

The next phase of this project will allow the target system and scattering projectile to evolve in time. This extension will be compared to experimental results because no comparable theoretical calculations are available in the literature. We have selected an experiment based on positron-atom scattering for these comparisons, which allows us to study reactive processes. ◆

References

Elza, B., and B. Ritchie (1992), *Use of Time-Dependent Wave-Packet Theory in Electron-Molecule Scattering*, Lawrence Livermore National Laboratory, Livermore, CA, UCRL-JC-112736.

Ritchie, B. (1992), "Time-Dependent Wave-Packet Theory for Electron Scattering," *Phys. Rev. A* **45**, R4207.

Ultralow-Cost Diode Arrays

R. W. Solarz, M. A. Emanuel, R. J. Beach, W. J. Benett, and W. J. Freitas

Semiconductor laser diodes are reliable and highly efficient light sources. They are also very compact; a conventional device has about the same dimensions as a 1-cm-long human hair. However, applications that require many laser diodes assembled into a single system, such as laser welding or generating electric power with laser fusion, are extremely expensive because of the many fabrication steps and the costs associated with handling numerous small, delicate components. We estimate that the cost of conventional laser diodes will drop no lower than $0.50/W, but laser fusion would require a price below $0.10/W to be economical. We have determined that the best way to meet this goal is to adopt a different device structure that is more amenable to cheap mass production—the "monolithic" laser diode.

In the monolithic structure, many laser diodes are created on the surface of a single wafer by sophisticated chemical micromachining processes, and the completed wafer is handled as a single light source, thus requiring far less handling and giving far better yield than conventional structures. Monolithic laser diodes demonstrated thus far have shown efficiencies of about half of those found in conventional structures because their fabrication technology is less evolved. The technology must be developed to reduce this gap to near zero.

Monolithic Laser-Diode Development

In FY 1992, we began establishing a facility to research and develop monolithic laser diodes. We installed and activated a metal-organic chemical-vapor-deposition crystal-growth reactor and optimized growth processes to produce extremely high-quality laser-diode wafers for both conventional and monolithic lasers. We also installed and activated device-fabrication equipment for wafer patterning, dielectric and metal deposition, heat treatment, and wet-chemical processing, and we optimized the processes. We began conventional laser-diode fabrication to aid in process optimization for the monolithic structures to follow; the resulting diodes have near-record performance in power-conversion efficiency (>53%), which is the primary figure of merit for high-power devices.

Because effective cooling of high-power devices is required to push them to their operational limits, we

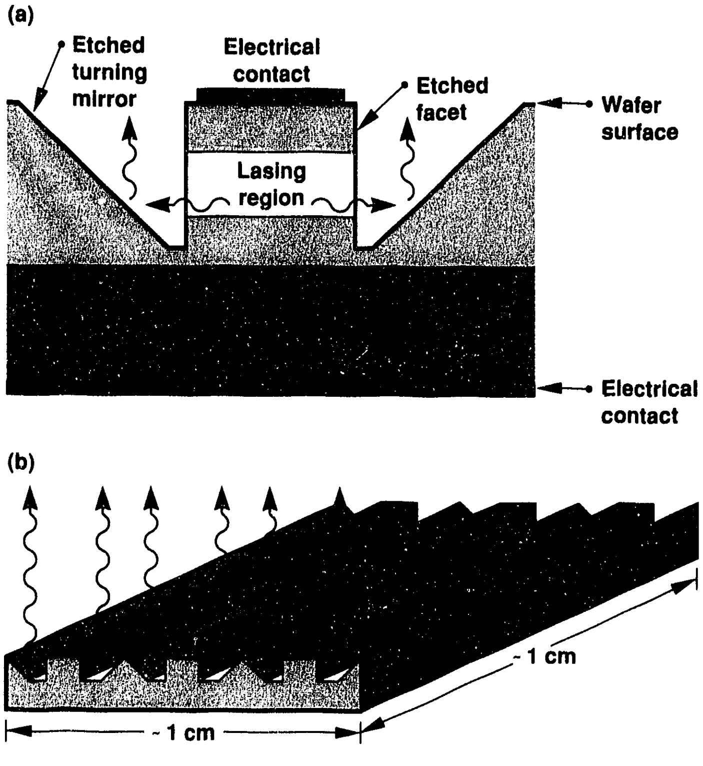

Figure 1. Monolithic laser-diode array with turning mirrors showing (a) cross section and (b) large-area array. This approach promises the performance of conventional devices with the cost effectiveness of monolithic fabrication.

began to design microchannel heatsinks for the monolithic structures using a high-performance cooling technology developed at LLNL for cooling conventional diodes.

Design Approach and Fabrication Techniques

During FY 1992, we evaluated various approaches to the design and fabrication of monolithic structures. Through literature searches, discussions with independent consultants, and in-house analysis, we identified a design approach and fabrication technique. Using the chosen design approach, we will fabricate 45-deg turning mirrors to direct the light perpendicular to the wafer surface (Figure 1). The approach promises the performance of conventional devices with the cost effectiveness of monolithic fabrication.

The fabrication technique, a chemical micromachining process known as chemically assisted ion-beam etching, requires highly specialized equipment. We are beginning to establish the facility to house this system. In addition, we added new professional staff experienced in such processes. In FY 1993, we will begin fabricating and packaging these devices to evaluate their performance. ◆

Tactical-Laser-Weapons Technology

R. W. Solarz, G. F. Albrecht, S. B. Sutton, S. P. Velsko, B. J. Comaskey, and R. J. Beach

Effective tactical-laser-weapons operations make stringent demands on beam quality, peak power, total delivered energy, system thermal recovery, compactness, and system efficiency. Our goal is to research concepts that satisfy these requirements and prove new technologies for producing large-scale laser weapons.

High-pulse energy and high-average-power solid-state lasers are conventionally driven by lamp pumping. However, our new laser weapons concepts are based on diode pumping. Laser systems are improved by diode pumping in the same way that radio technology was improved by replacing vacuum tubes with transistors.

Diode-Pumping Package

In FY 1992, we completed specifications for the first-generation weapons-grade version of our diode package. In our new configuration, we stack diode bars closer together than our present research diode packaging and make them more compatible with mass production. Because the advanced stacks will be twice as dense as our present diode-pumped modules, the diode arrays will be twice as bright, operating at 1200 W/cm^2 instead of 600 W/cm^2.

We are also studying how we might make heat-capacity–based laser weapons. In the heat-capacity operation, no cooling is applied to the gain media (crystal or glass disks) during diode pumping. We minimize the thermal-optical distortions from heat flow by limiting the heat flow. The nearly uniform temperature distribution in the gain media removes stress-fracture limitations on the pumping. Our diode-pumped slab testbed is ready to demonstrate heat-capacity operation. We are fabricating the actual slab and will begin tests in FY 1993.

Repetitive Rearming

In our most aggressive new laser concept, we segment the gain media into disks similar to Nova laser amplifiers to permit rapid cooling after lasing. Rapid cooling allows repetitive rearming of the laser weapon within the engagement time, an advance similar to replacing a single-shot rifle with a machine gun. Our studies indicate that the pumping uniformity needed for good wavefront control can be obtained with this configuration. In FY 1992, we made extensive optical tests of Nova 10-cm disk amplifiers under intense flashlamp pumping. We demonstrated that with careful disk selection and mounting, the double-passed optical quality of a 6-cm, central, clear aperture remains near diffraction limited throughout the pump pulse.

We are investigating mist-cooling to thermally recondition laser-disk gain media. Our modeling results indicate that we can achieve 30-W/cm^2 peak cooling rates and that thermal reconditioning in our megajoule-class lasers is possible. We will continue detailed boundary-layer simulations in FY 1993 to understand the dynamics of this cooling process.

Many antisensor weapons require light with a wavelength that lies within the 3- to 5-µm atmospheric transmission bands. We constructed a long-pulse surrogate laser and a heat-capacity-operation nonlinear crystal for anharmonic wavelength conversion. In FY 1993, we will use this system to provide basic data to verify the theoretical models that we used and thus to optimize conversion-efficiency designs and test the nonlinear-crystal heat-capacity-operation concept. ◆

High-Power Diode-Pumped Machining Laser

R. W. Solarz, G. F. Albrecht, R. J. Beach, B. J. Comaskey, M. A. Emanuel, W. J. Benett, B. L. Freitas, and S. C. Mitchell

Developing kilowatt-level, diode-pumped, solid-state lasers for industrial use has been a goal of materials-processing researchers. Diode-pumped, solid-state lasers offer higher reliability and lower energy consumption at an improved potential for good beam quality. In FY 1992, we demonstrated the first operation of a diode-pumped, solid-state laser with kilowatt power. We achieved the kilowatt power level by progressively increasing the diode-pumped power to the 300-W/cm^2 level by step-by-step advances in diode cooling and packaging technology.

The laser was a Nd:YAG zigzag slab oscillator with flat tips. The crystal, 8 cm long by 2 cm high by 0.5 cm thick, was pumped from two sides by 80 diode packages. Each diode package contained a microchannel cooler and carried a 1.8-cm AlGaAs diode bar that was operated at 2500 Hz with pulses about 150 µs long. We obtained the 1 kW at 2500 Hz with the laser operating in a free-running mode. This laser power is more than an order of magnitude higher than has been reported by other researchers. Figure 1 shows the laser in operation.

We are building a laser with about 2-kW output power for delivery to the Laser Material Processing Group in FY 1993. We also plan to use these lasers in our testbed setting for industrial cutting and welding projects. The laser head will be a straightforward extension of our 1-kW unit, and the oscillator crystal will be 14 cm in length. ◆

References

Beach, R., W. J. Benett, B. L. Freitas, D. Mundinger, B. J. Comaskey, R. W. Solarz, and M. A. Emanuel (1992), "Modular Microchannel Cooled Heatsinks for High Average Power Laser Diode Arrays," *IEEE J. Quant. Electron.* **28**, 966.

Comaskey, B. J., R. Beach, G. Albrecht, W. J. Benett, B. L. Freitas, C. Petty, D. VanLue, D. Mundinger, and R. W. Solarz (1992), "High Average Power Diode-Pumped Slab Laser," *IEEE J. Quant. Electron.* **28**, 992.

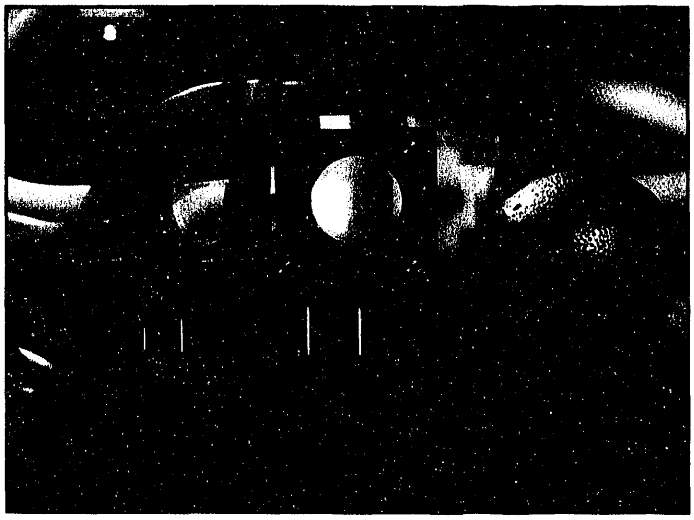

Figure 1. First kilowatt-level, diode-pumped machining laser. The laser head is about the size of a lunch box. For size reference, note the orange and the 5-cm-diam optics through which the beam is emitted.

Developing Heavy-Ion Fusion Technology

A. Friedman, J. Barnard, H. Kirbie, and M. Newton

DOE's Fusion Policy Advisory Committee has identified heavy-ion beam-driven inertial fusion (HIF) as a promising alternative for generating fusion power. Historically, two accelerators, the linear induction accelerator in the United States and the radiofrequency (rf) linear accelerator (linac) in Europe, have been used as heavy-ion drivers. However, the recirculating induction accelerator, the "recirculator" shown in Figure 1, is potentially less expensive than either the induction or the rf linac.

The principle of acceleration is the same in the recirculator and in the induction linac, but the recirculator reuses accelerator components by bending the beam in a closed path. The recirculator configuration introduces new physics and engineering issues not present in existing heavy-ion accelerator technologies. Our objective was to evaluate these physics and engineering issues by focusing on three areas: system studies of recirculators, physics of recirculators, and initial validation and development of new recirculator technologies.

System Studies

Cost effectiveness was the principal motivation for evaluating the recirculator as a driver for inertial fusion. We developed a system model in a spreadsheet format to estimate the cost and efficiency of a complete recirculator-driver system.

We evaluated several recirculator systems that have a total driver output energy of 4 MJ and an ion mass of 200 (Barnard et al., 1991). Of the systems evaluated, the most attractive recirculated the ion beam 100 times through three acceleration rings. This configuration used advanced pulsed-power technologies, cost less than $500 million, and delivered the beam with an estimated efficiency of 35%.

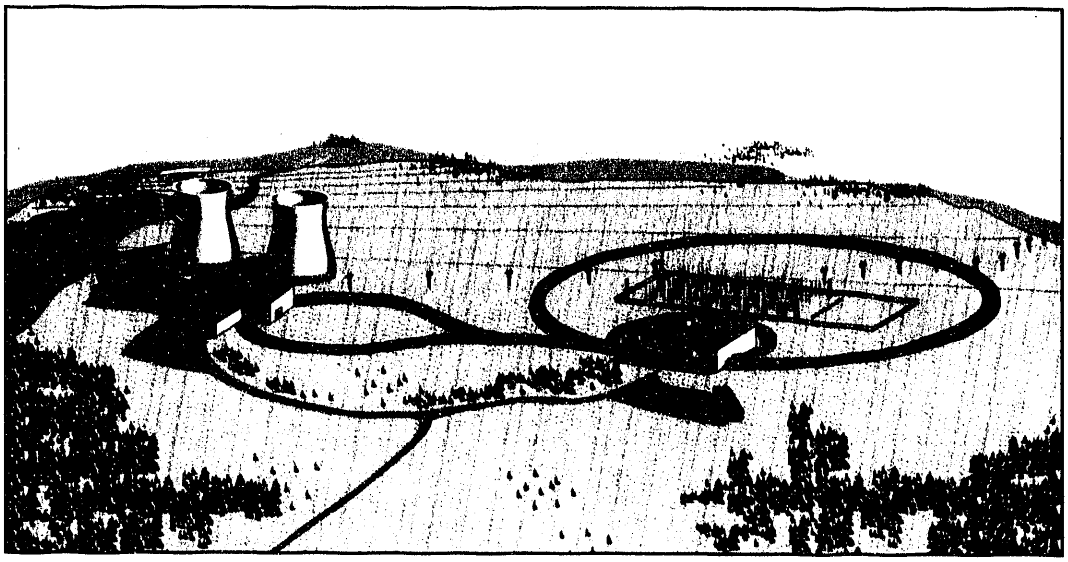

Figure 1. Conceptual design of a recirculator-driven, heavy-ion fusion power plant.

We compared the design of our recirculator with that of a similar linear accelerator and found that the recirculator cost almost a factor of 3 less.

Physics and Modeling

Several critical issues concerning the transport of high-current ion beams over the several hundred kilometer path from injector to target were identified. To transport adequate energy onto a sufficiently small spot at the target, the beam at the final optic must have high current and low emittance. Stripping by the residual gas and charge exchange between heavy ions are major sources of loss of heavy ions in the beam. In addition, several processes affect the location of the beam centroid or increase the beam emittance. Among these are distortion due to bends, "beam breakup" instability, longitudinal module-impedance instability, betatron-orbit resonances, and misalignment effects.

We developed the recirculator design program CIRCE, which is an envelope code in the transverse direction and a Lagrangian fluid code in the longitudinal direction. We used CIRCE to model transport in the high-energy ring of the recirculator and to study design issues. We studied extraction from a recirculator lattice, the design of transition lattices at the ends of the extraction section, the sensitivity of beam transport to magnet-strength errors, algorithms for steering the beam centroid, and methods for controlling the longitudinal dynamics of the beam.

We simulated emittance growth in a small, oval recirculator on the scale of Lawrence Berkeley Laboratory's (LBL's) proposed induction linac systems experiments (ILSE) facility using the three-dimensional, particle-in-cell code WARP (Friedman et al., 1992). Our results indicate that transitions from bends to straight sections may be a source of beam mismatch, which can thermalize into a larger emittance. The predicted emittance growth is acceptable for a driver-scale recirculator.

New Recirculator Technologies

A recirculating induction accelerator requires an extraordinary modulator to drive the induction cells. The modulator must generate acceleration pulses at a variable repetition rate consistent with the ion recirculation time and must reset the magnetic core material in the induction cell between acceleration pulses. Some recirculator drivers require repetition rates as high as 100 kHz; recirculator experiments on the proposed ILSE accelerator at LBL may require repetition rates in excess of 200 kHz. The pulse duration delivered by the modulator must also vary from pulse to pulse because of beam compression. Standard modulator technologies cannot provide the pulse-to-pulse variability.

Consequently, we are investigating new modulator concepts for near-term recirculator experiments. Such experiments would require a modulator that can generate 5-kV, 0.5- to 1-μs pulses at 70 to 200 kHz with a 100-pulse burst duration. We focused on field-effect transistor technology with fiber-optic–isolated gate drives for the modulator development work. We built a small modulator and generated a pair of 1-kV pulses onto an induction core at 200 kHz. The modulator resets the induction core between pulses.

Conclusions

We have made significant progress toward our goal of evaluating and developing a new, less expensive heavy-ion driver. Because of our research, the recirculator has become the favored concept for ongoing LLNL HIF reactor studies. HIF itself has become the favored approach for inertial fusion energy in the United States; the acceptance of HIF is due in part to the potential cost effectiveness of advance heavy-ion drivers.

LLNL and LBL researchers are working together to design and develop the proposed ILSE facility and associated experiments. We will seek to confirm the recirculator concept through experiments on ILSE and have reserved space on the end of ILSE's beamline for a recirculator ring. ◆

References

Barnard, J., et al. (1992), *Study of Recirculating Induction Accelerators as Drivers for Heavy Ion Fusion*, Lawrence Livermore National Laboratory, Livermore, CA, UCRL-LR-108095.

Friedman, A., D. P. Grote, and I. Haber (1992), "Three Dimensional Particle Simulation of Heavy-Ion Fusion Beams," *Phys. Fluids B* **4**, 2203.

Designing a Compact, 1-kJ-Class Glass Laser

J. T. Hunt, K. R. Manes, and J. B. Trenholme

We designed a 1-kJ, 1-ns laser that produces x-ray flashes for general research and medical use. Our goal was to develop an inexpensive, well-engineered, and easy-to-operate glass laser that would incorporate the latest miniaturized components and integrated optics technologies. Our design is small enough to fit comfortably on a 1.5- × 10-m table in a university or medical center laboratory.

Our design extends recent LLNL laser-system development with two power-amplification stages: a six-bounce zigzag slab, which is used as a preamplifier, and a final amplification stage that employs Brewster-angle slabs. Both amplifiers use a platinum-free phosphate glass like that used in LLNL's Nova laser (i.e., LG 750 or LHG-8) and store 250 to 300 J/L with an electrical efficiency exceeding 3%. The anamorphic relay filter shown in Figure 1 not only controls the beam's quality but also reshapes the rectangular spatial profile. The beam's intensity modulation would be controlled with two filtering slits located at the line foci of the anamorphic relay filter. The system could be fired every 20 min.

We focused our LDRD effort on one key component—the zigzag slab amplifier—because the slab amplifier potentially can deliver, at the same cost, significantly more power than the more traditional rod amplifier. The slab amplifier architecture looks promising because it can supply 20 times the power of the rod architecture and is 10 times more efficient. However, we are concerned about the degraded performance that might result from competing nonlinear processes: self-focusing–induced beam breakup, intensity-dependent polarization rotation, and the nonlinear grating created by the beam overlap caused by the zigzag path.

We have extended the theory of nonlinear optical propagation to include these processes, and we have generated specific predictions for laser-beam propagation in our proposed geometry. In FY 1993, we hope to test our hypotheses.

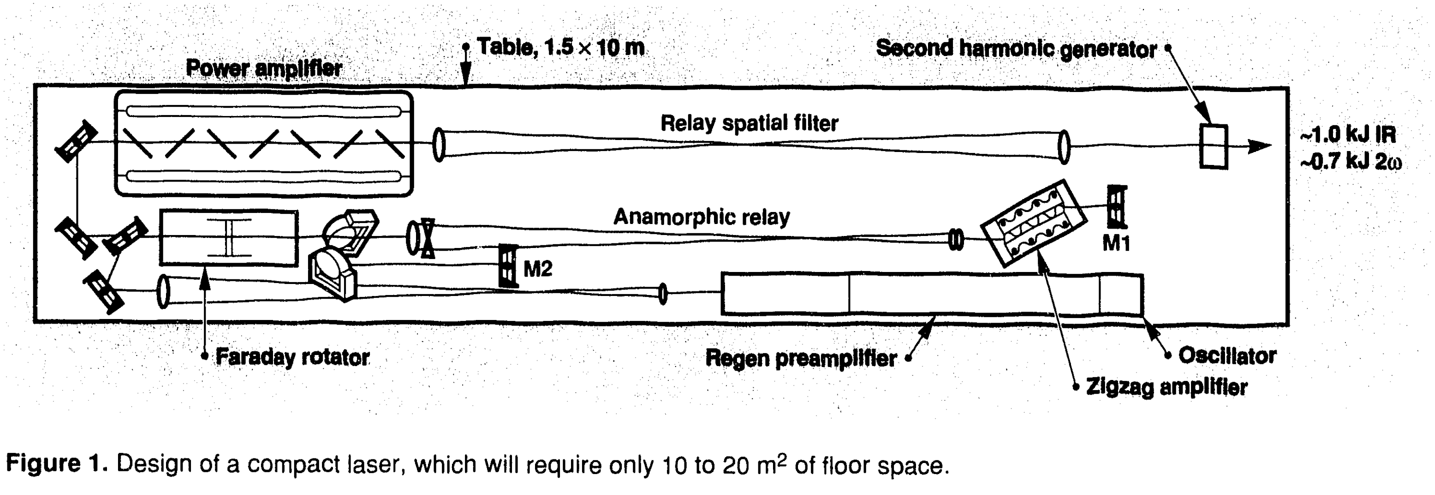

Figure 1. Design of a compact laser, which will require only 10 to 20 m^2 of floor space.

Recent research at LLNL has shown that this kind of laser system can meet or exceed performance parameters needed for a compact, 1-kJ glass laser with superb beam uniformity (peak-to-average ratio of less than 1% in a 10 J/3-ns pulse). By adding our active Fresnel rhomb zigzag slab amplifier, we believe we can build a compact, efficient, glass-laser system that provides excellent beam quality at a fraction of the cost of the Nova-style lasers now in laboratory use. ◆

A Micro–Storage-Ring, X-Ray Source

M. J. Moran

We studied the feasibility of designing a low-energy, electron-storage ring to produce coherent x rays using the Smith–Purcell (S-P) effect. The S-P effect is the production of radiation by electrons as they pass close to, without actually striking, the surface of a grating (Figure 1). Preliminary calculations suggested that such a system could be feasible with a 1- to 5-MeV, electron-storage ring that used novel, electrostatic, electron-beam cooling devices. Our study focused on S-P x-ray production and storage-ring design.

A new storage-ring design was anticipated because efficient S-P x-ray production requires extremely low emittance electron beams. Emittance (beam diameter times divergence angle) is a measure of electron-beam quality, and lower emittances represent higher-quality beams. The S-P effect produces narrow spectral bands of coherent photons, but short wavelengths may require microscopic electron-beam diameters. A new mathematical model made possible detailed studies of S-P emission distributions and their dependence on the "impact parameter" (the height of the electron beam above the grating surface). For electrons with energies below 5 MeV, the S-P intensity declines rapidly as the impact parameter becomes greater than the photon wavelength.

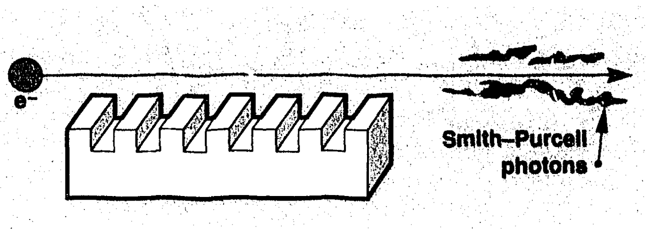

Figure 1. The Smith–Purcell effect. Electromagnetic interactions can produce coherent radiation in the forward direction as an electron grazes the surface of a grating-like structure.

The computer calculations suggested that for efficient x-ray generation, the S-P effect may require electron-beam emittances that violate the Heisenberg uncertainty principle, which establishes an ultimate limit on the emittances that be achieved. For the process to be feasible, the overall length of the grating must be considered (shorter gratings are easier to accommodate), and electron-beam energies greater than 10 MeV will be required (Moran, 1992). Thus, this result precludes using a low-energy storage ring. For energies greater than 10 MeV, each electron randomly emits more than 1 eV of synchrotron radiation during each circuit of its orbit. This level of synchrotron radiation introduces substantial perturbations to the electron orbits and makes the desired emittances unfeasible.

The theoretical study was complemented by an experiment to measure details of S-P emissions with an arrangement similar to that needed for x-ray generation. The 1.5-MeV High-Energy Electron-Beam Microscope (HEEBM) at the National Center for Electron Microscopy at Berkeley produced a 200-nm-diam electron beam for the experiment. The S-P gratings used were microstructures etched into the surface of a silicon wafer with microlithographic techniques. These microstructures, with periods of 8.75 and 17.5 μm, were designed to produce visible S-P radiation in the forward direction. A movable, optical-fiber probe sampled the angular distribution of the S-P radiation and transmitted the light to a spectral analyzer for measurements of the absolute spectral intensity.

This experiment was unprecedented both as a basic physics experiment on the HEEBM and for the detailed control of parameters in measuring the S-P effect. The basic experiment worked well; unfortunately, S-P radiation was not detected. The overall experimental sensitivity appears to be about a factor of 10 too low to measure S-P radiation from the approximately 0.5-nA electron beam.

Although use of storage rings as x-ray sources has been eliminated, linear acceleration of the electrons may still be a useful approach because it avoids the emittance broadening associated with synchrotron radiation in storage rings. Linear acceleration is supported further by reports of single-atom, field-emission, electron sources that produce extremely small electron beams with the emittances needed for S-P x-ray generation (Fink, 1988). If the electron beams produced by such sources can be accelerated without appreciable emittance growth, it may be possible to generate useful fluxes of coherent S-P x rays for applications such as microscopy or holography. ◆

References

Fink, H. W. (1988), "Point Source for Ions and Electrons," *Phys. Scripta* **38**, 260.

Moran, M. J. (1992), "X-Ray Production by the Smith–Purcell Effect," *Phys. Rev. Lett.* **69**, 2523.

Super-Emissive, Hollow-Cathode Electron Gun

B. M. Penetrante, R. E. Marrs, J. N. Bardsley, M. A. Gundersen,* and G. F. Kirkman-Amemiya†

The purpose of this project is to develop a compact and rugged low-emittance, high-current electron gun that can operate in both pulsed and dc modes. The design parameters for this gun suggest that it would increase the extracted ion rate and x-ray flux of the LLNL electron-beam ion trap (EBIT) by a factor of 250. This increased performance of EBIT would allow us to observe new atomic, nuclear, and surface physics phenomena involving very highly charged ions.

In pulsed mode, this gun can achieve emission densities 2 orders of magnitude higher than those currently used in advanced accelerators for the same pulse length. It can operate with a higher duty factor and simpler electron optics, and it does not have the vacuum problems that limit cathode performance in present systems. Successful demonstration of this gun would be an important advance for many high-power electron-beam devices, including EBIT, electron-beam–pumped lasers and ion sources, plasma-based microwave generators, and high-brightness accelerators.

Electron-Gun Design

The device employs a low-voltage, hollow-cathode arc discharge as the source of electrons (see Figure 1). The discharge is triggered by an ultraviolet flashlamp behind the hollow-cathode region. A high-voltage, pulsed discharge circuit is used to initiate the transformation of the discharge into a high-current arc. The space-charge field causes partial plasma trapping within the hollow-cathode region, and ion bombardment of the cathode induces cathode heating and secondary electron emission. After initial heating of the cathode through capacitive discharge, a low-voltage dc power supply

---

*University of Southern California, Los Angeles.

†Integrated Applied Physics, Inc., Waltham, MA.

sustains the high-current arc. The arc cathode emits electrons as a result of thermionic, field, and thermionic–field emission processes. These emission mechanisms supply an electron current from the cathode nearly equal to the total discharge current.

The electron gun offers many advantages. It is rugged because no delicate heater elements are required. The device is insensitive to contamination because high-temperature, low-work-function surfaces are not required. The gun is suitable for large-area beam production because it can be scaled to any size without constraints imposed by heater-element design. Its simple design promises substantial cost savings compared with other high-perveance cathodes.

Electron-Gun Operation

During FY 1992, we developed the simulation codes to provide computer-aided design specifications for the gun, and we fabricated and tested several prototypes of the electron source. Progress was made in demonstrating short-pulse (100-ns), long-pulse (100-ms), and dc (10-s) operation of the gun. We demonstrated dc operation of the electron source sustained at 80 V dc and 10 A current. The dc arc discharge was sustained for at least 10 s before power dissipation on the air-cooled cathode–anode structure became unacceptable. With proper water cooling of the electrode structure and differential pumping, we expect our new gun to provide a true dc, low-emittance, high-current electron beam for an intense EBIT. ◆

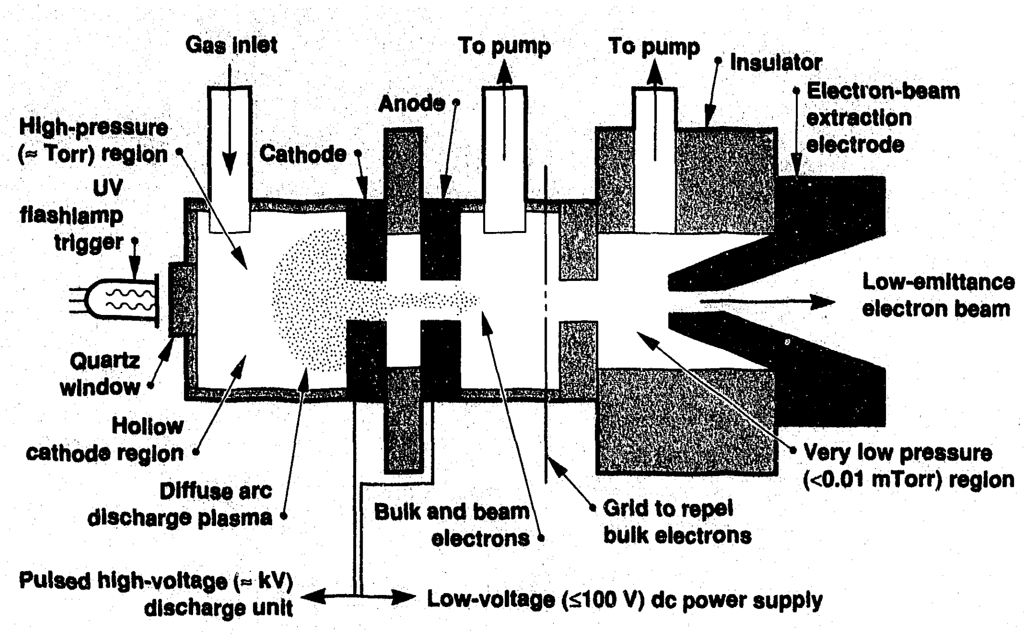

Figure 1. Schematic of the super-emissive, hollow-cathode electron gun. The design parameters of the gun suggest that it would increase the performance of EBIT and thereby allow us to observe new phenomena involving very highly charged ions.

Section 4

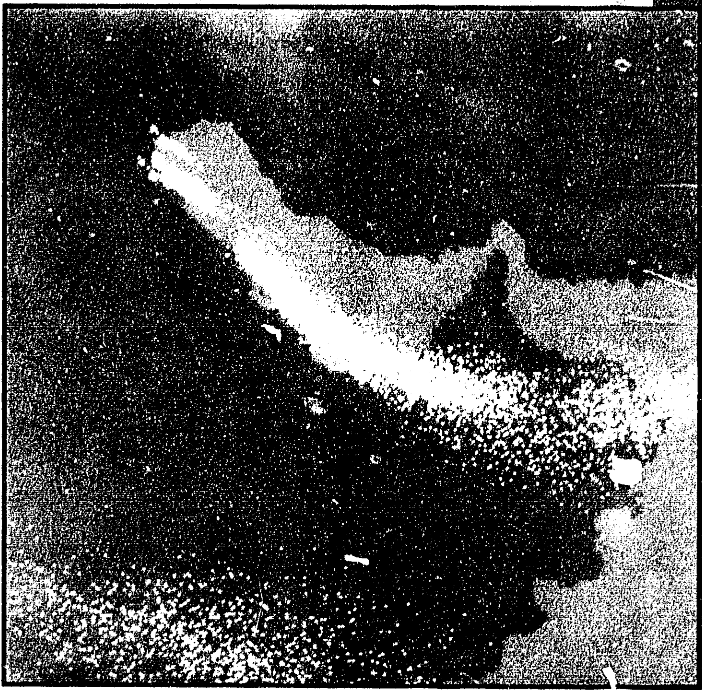

Environmental Science and Technology

Laboratory Directed Research
and Development FY 1992

On the previous page. Observed and simulated smoke plume from the oil fires in Kuwait. The left panel, a photograph of the plume, was taken by a weather satellite. The right panel is a simulated forecast of the plume's structure and location. The photograph, which was taken at the approximate time of the forecast, shows considerable agreement with the model calculations.

Integrating Organic and Inorganic Geochemistry to Study Oil Formation and Toxic Cleanup

K. G. Knauss and A. K. Burnham

By understanding porosity generation and maintenance and the influence of pressure and temperature on oil formation, we can more easily find, recover, and maintain our petroleum resources. Traditionally, organic and inorganic geochemists explore different aspects of these systems. By combining the expertise of LLNL's Organic and Inorganic Geochemistry groups, we hope to significantly increase our knowledge of both processes. In FY 1992, we researched the behavior of organic chemical species in aqueous environments and the influence of aqueous organic chemical species on mineral dissolution and precipitation and on element transport to better understand how oil forms and where it can be found. We are applying the knowledge we gained from these experiments to developing remedial technology for contaminated soil and groundwater.

Porosity Generation and Maintenance

During FY 1992, we completed dissolution kinetics experiments that examined the effect of malonate dicarboxylic acid anion, as a function of pH and temperature, on oil reservoir porosity. We found that under mildly acidic to neutral pH conditions, malonate in high concentrations can increase the rate of mineral dissolution. We also completed hydrous pyrolysis experiments designed to examine the effects of temperature and pressure on kerogen pyrolysis kinetics and products. Our results explained the apparent discrepancy between calculated activation energies obtained using hydrous and anhydrous experimental approaches. We observed that pressure has no effect on pyrolysis kinetics under relevant geologic conditions; therefore, it is primarily temperature that determines the rate of pyrolysis (Figure 1). Note that data for the pyrolysis products, acetate and propionate, are coincident at the two pressures examined. This finding constrains models for the pyrolysis process. We made substantial progress in developing the interface between the Inorganic and Organic Geochemistry groups.

Environmental Cleanup

We also began developing innovative soil and groundwater remedial technologies, using one problem site as an analog for similar sites. Through laboratory experiments and geochemical modeling, we hope, in FY 1993, to determine the fundamental behavior of nonaqueous-phase liquid contaminants and their

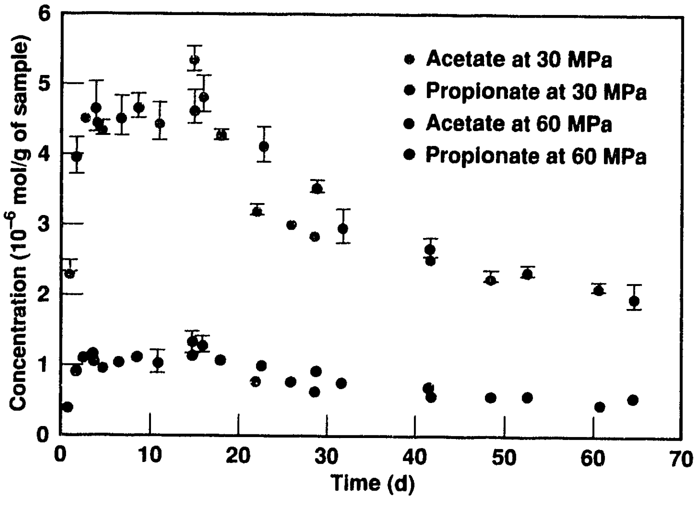

Figure 1. Effect of pressure on carboxylic acid anion pyrolysis kinetics. In tracking the concentration of acetate and propionate in New Albany Slate, we found that both 30 and 60 MPa are geologically relevant. Therefore, temperature, not pressure, affects oil formation rate in this range.

interaction with the inorganic system. We will then evaluate site response to various recovery techniques, focusing initially on dynamic stripping with steam. We hope to optimize the chemical and physical conditions of the stripping process to maximize the effectiveness of the cleanup and mitigate any potential problems. The key component of this proposal is the integral link between experiment and theory. ◆

Chemical and Nuclear Properties of the Heavy Transactinium Elements

P. Baisden and D. Hoffman

We study single atoms of short-lived isotopes produced in heavy-ion bombardments of rare, heavy-actinide targets. We conduct these experiments both on- and offline at accelerators such as the 88-in. cyclotron at Lawrence Berkeley Laboratory and the Unilac at GSI in Darmstadt, Germany. In these experiments, we investigate

- Relativistic effects on chemical properties.
- The rapid change of spontaneous fission properties in the region of the fermium isotopes.
- The limits of nuclear stability.
- The production of new isotopes.

In previous studies, we compared the results of liquid–liquid extractions of rutherfordium (element 104) with those of its lighter, Group IV homologs and with those of thorium and plutonium (IV). We found that rutherfordium behaves like thorium under some conditions and like plutonium (IV) under others. Rutherfordium's properties, therefore, cannot be predicted by simple extrapolation from those of the lighter, Group IV homologs zirconium and hafnium.

We prepared new targets of ^{249}Bk and, at GSI, bombarded them with ^{18}O to produce isotopes of hahnium (element 105) so that we could study its aqueous- and

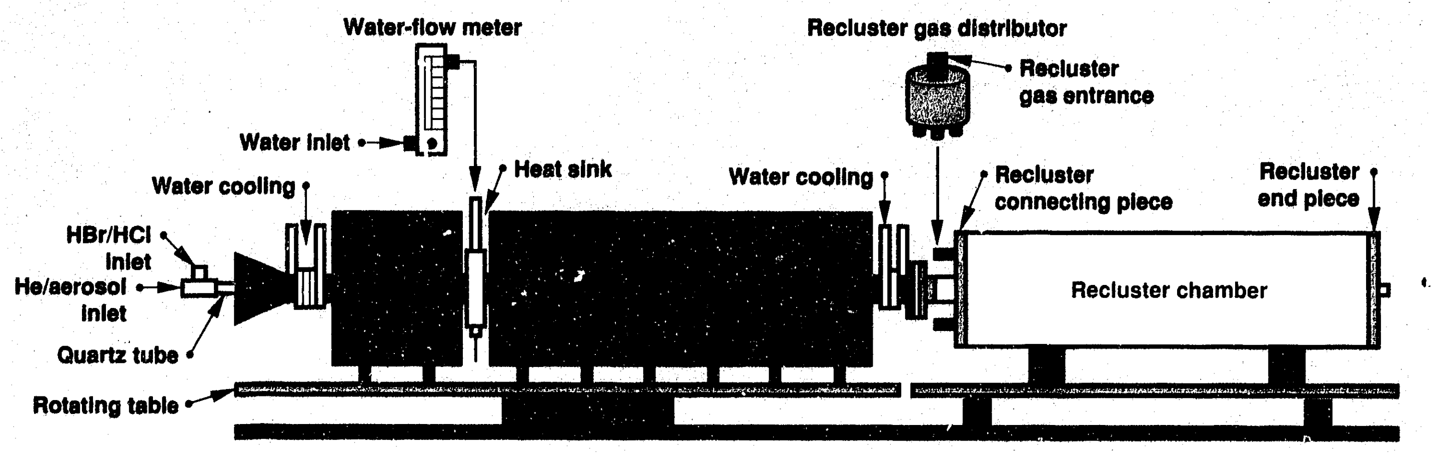

Figure 1. A side view of the chromatographic and recluster segments of the heavy-element volatility instrument. Ovens are shown in green; the Inconel jacket that surrounds the column is shown in black.

gas-phase properties. In our initial experiments, we investigated the volatility of the chloride complexes of hahnium using our heavy-element volatility instrument (HEVI). A helium gas-jet system carried the reaction products recoiling from the ^{249}Bk target on MoO_3 aerosol clusters from the target chamber to the inlet of HEVI.

HEVI, shown in Figure 1, is an isothermal, gas chromatography system consisting of a quartz column surrounded by a series of ovens. The column can be operated isothermally at temperatures between 200 and 1000°C. Hahnium chloride complexes that are not volatile at the column temperature will condense on the inner wall of the column. However, those complexes that are volatile at temperatures above the column temperature will exit the column, where they will be reclustered on KCl aerosols and transported to the counters for detection. Thus, we can determine relative volatility by varying the column temperature.

In FY 1993, we will compare the results of the current experiments with measurements of other halides and with theoretical predictions from multiconfigurational Dirac–Fock calculations. ◆

Solution Chemistry of the Transactinium Elements

M. Neu,* N. Hannink,* K. Czerwinski,* R. Russo,* R. Silva, R. Torres, P. Baisden, and D. Hoffman

In this project, we studied the behavior of actinides in aqueous solution. We measured the solubility-limited speciation of ^{242}Pu as a function of time in near-neutral carbonate solutions to better understand the chemical behavior of plutonium in groundwater. We constructed a remote, laser-induced, photoacoustic spectroscopy (LIPAS) apparatus, placed it in a glove box, and linked it via fiber optics to the laser laboratory (Figure 1). LIPAS is a relatively new, sensitive, and noninvasive technique that uses many principles of absorption spectroscopy. Using the remote LIPAS, we avoid the risk of human exposure and contamination of the laser laboratory, and we use a small-volume cuvette to reduce the amount of plutonium. A computer-linked, solution control and monitoring system controls atmospheric CO_2, temperature, and pH.

In these experiments, we electrochemically prepared a solution that contained plutonium in a single oxidation state and then mixed the plutonium solution with a preequilibrated carbonate solution. We scanned and recorded spectral absorption regions for Pu^{4+}, PuO_2^{+}, and PuO_2^{2+} with the LIPAS system and measured aliquots of the plutonium carbonate solutions with a

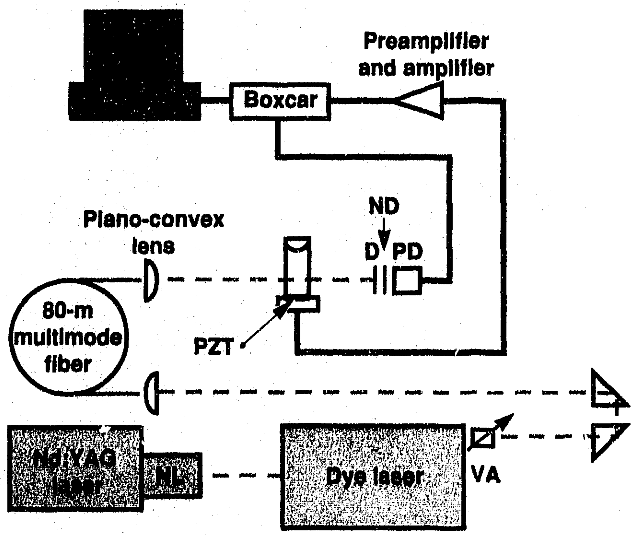

Figure 1. Schematic of the remote, laser-induced, photoacoustic spectrometer (LIPAS), where NL is the nonlinear optics, VA is the variable attenuator, PZT is the piezoelectric transducer, D is the diffuser, ND is the neutral density filter, and PD is the photodiode.

**Lawrence Berkeley Laboratory, Berkeley, CA.*

liquid scintillation counter at regular time intervals. A three-week-long Pu(IV) experiment is complete, and the data indicate that Pu(IV) is less soluble in simple carbonate solution than in natural groundwater. Spectral data show that the major species in solution was Pu(IV) polymer; concentrations of other species were below the spectroscopic detection limit. A Pu(V) experiment is in progress, and we will compare spectroscopic results with those obtained using chemical extractions.

We are investigating actinyl(V) cation–cation complexes. Complexes of plutonyl(V) with other actinides have been little studied. Our goal is to measure the equilibrium constant (K_{eq}) for two such cation–cation complexes, $PuO_2^+ \cdot UO_2^{2+}$ and $PuO_2^+ \cdot NpO_2^+$. Because both complexes are expected to have a small K_{eq} (~1), we will use LIPAS to monitor their formation. We will quantify the K_{eq} with the computer program Stability Quotients from Absorbance Data (SQUAD). We are testing the entire LIPAS system using stable lanthanides to ensure proper response. We will first study a known cation–cation complex, $NpO_2^+ \cdot UO_2^{2+}$, to verify that LIPAS can detect a complex with the expected K_{eq} and that SQUAD can determine the K_{eq}. Then we will study the $PuO_2^+ \cdot UO_2^{2+}$ and $PuO_2^+ \cdot NpO_2^+$ complexes.

We are measuring the thermodynamic equilibrium constants for the formation of Pu(IV) complexes with several ligands. (K. Raymond's group at UC Berkeley provided the ligands.) Because Fe(III) and Pu(IV) are chemically similar, we are investigating the Pu(IV) complexing of compounds that are known to form stable complexes with the ferric ion. We use desferrioxamine (DFO). In our initial work, we determined the Pu^{4+}/DFO stoichiometry to be L:M = 3:2 at low pH and L:M = 1:1 above pH 6. We have calculated a formation constant for the 3:2 species of 10^{60} from spectroscopic and pH data (obtained from experiments in which ethylenediaminetetraacetic acid [EDTA] was a competing ligand).

We have completed experiments with a catecholamide synthetic analog of DFO that contains two additional binding groups that can interact with metal ions. The compound forms an extremely stable complex with Pu(IV). The formation constant of the 1:1 complex is $10^{43.3}$. We will continue our DFO experiments to better understand the coordination chemistry of this natural product with plutonium, and we will investigate the binding ability of three other analogs that we have synthesized. ◆

Incorporating Toxics Capabilities into ARAC

D. L. Ermak

We have developed a dense-gas version of the advection-diffusion, particle-in-cell (ADPIC) model to simulate the atmospheric dispersion of denser-than-air toxic and combustible releases under realistic conditions of terrain and varying meteorological conditions. This model was developed to meet our objective of having a dense-gas dispersion model that can be used operationally within our Atmospheric Release Advisory Capability (ARAC) emergency response system.

Prior to this effort, we reviewed the existing dense-gas dispersion models, but none were suitable for this application. The three-dimensional, primitive-equation models can simulate dense-gas dispersion under complex conditions but require large amounts of computer time, which are not available in operational applications. The simpler plume and puff models are computationally fast but are limited to situations with flat terrain and constant winds. In the absence of a suitable model, we considered modifying ADPIC, our existing operational dispersion model, for trace-gas releases. Our intention was to add the major effects of dense-gas dispersion to the model while retaining its high computational speed and its ability to simulate atmospheric dispersion under realistic conditions.

Characteristics of Dense-Gas Clouds

The atmospheric dispersion of denser-than-air gases requires a somewhat different approach to modeling than the conventional one used for the dispersion of trace gases. In a trace-gas release, the quantity of material released to the atmosphere is too small to have any significant effect on the atmospheric flow into which it is mixing. Consequently, trace-gas dispersion is controlled solely by the advective and diffusive properties of the ambient atmosphere. On the other hand, a dense-gas release behaves more like an independent, continuous cloud. Physical properties, including density, temperature, and turbulence level, differ significantly from those of the ambient atmosphere. The dispersion of a dense-gas cloud is controlled as much, if not more, by these properties as by the conditions in the ambient atmosphere.

Several major effects observed in the dispersion of dense-gas clouds released at ground level are not observed in the dispersion of trace emissions. One is a reduction of turbulent mixing in the vertical direction of the vapor cloud with the ambient atmosphere due to stable density stratification of the cloud relative to the above-lying ambient air. Another is the generation of gravity-spreading flow due to density gradients in the horizontal direction. These two effects result in a lower and wider cloud than that observed with a trace or neutral-density gas release. In addition, dense-gas clouds tend to follow the downhill slope independent of wind direction and can become "trapped" in valleys or low spots. When the release is a cold, dense gas, such as liquefied natural gas (LNG), the ground-surface heat flux into the cloud may affect cloud dispersion.

Although advection-diffusion models like ADPIC have been widely used and validated against numerous field tests of trace-gas releases, they do not contain the necessary physics to simulate atmospheric dispersion of denser-than-air releases. Specifically, they do not include descriptions of phenomena such as gravity flow, turbulence damping, and thermal effects of ground heating. Indeed, advection-diffusion models do not even account for density variations within the cloud and surrounding atmosphere, which are the source of all dense-gas dispersion effects.

Modifying ADPIC to Simulate Dense-Gas Releases

In developing the new version of ADPIC, we assumed that the dense-gas effects could be described by the vertically averaged thermodynamic properties of the cloud and the local cloud height. This simplification has been successfully used in one-dimensional, dense-gas dispersion models and assumes that the dense-gas cloud is relatively thin in comparison to its horizontal dimensions. We treated the dense-gas effects as a perturbation to the ambient thermodynamic properties (density and temperature), ground-level heat flux, turbulence level (diffusivity), and wind field (gravity flow) within the local region of the dense-gas cloud. These perturbations were calculated from (1) conservation of mass, momentum, and energy principles; (2) the ideal gas law equation of state; and (3) the defined mass and energy properties associated with the individual Lagrangian marker particles used to describe the distribution (cloud structure) of the dispersing dense gas.

ADPIC Simulations of Dense-Gas Dispersion

We used the new dense-gas ADPIC to simulate the dispersion of ground-level, colder-than-ambient, denser-than-air releases. The results compared well with those of field-scale experiments. Here we compare simulations of LNG vapor dispersion observed in two field-scale experiments, Burro 8 and Burro 9, conducted by LLNL in 1980 at China Lake, California. The composition of LNG is mainly methane, whose molecular weight is half that of air. However, LNG is formed by cooling the gas to 112 K, so the source temperature is about one-third that of ambient air (~300 K). Compared with ambient air, LNG vapor is about 65% denser and much cooler.

In the Burro 8 and Burro 9 experiments, about 25 m^3 of LNG (~6000 m^3 of LNG vapor) was released at a nearly constant rate for about 1.5 min. Although the LNG was released onto water (in the form of a small pond), most of the dispersion occurred over land. The main difference between these two experiments was the meteorological conditions. The Burro 8 test occurred under lower wind speed (1.8 vs 5.7 m/s) and more stable ambient atmospheric conditions (class E vs D stability) than the Burro 9 test.

Figure 1 shows the simulated clouds at comparable times for the two tests. The dispersing clouds are represented by "dot-plots," where each dot is the location of an individual marker particle projected onto the plane of interest. The wind is blowing from left to right in all views.

Although the gravity-flow rates are similar in both simulations (~0.5 m/s), the effect on cloud shape is more pronounced at the low wind speed of Burro 8. Viewed from above, the simulated Burro 8 cloud is rounder or pancake-shaped, whereas the Burro 9

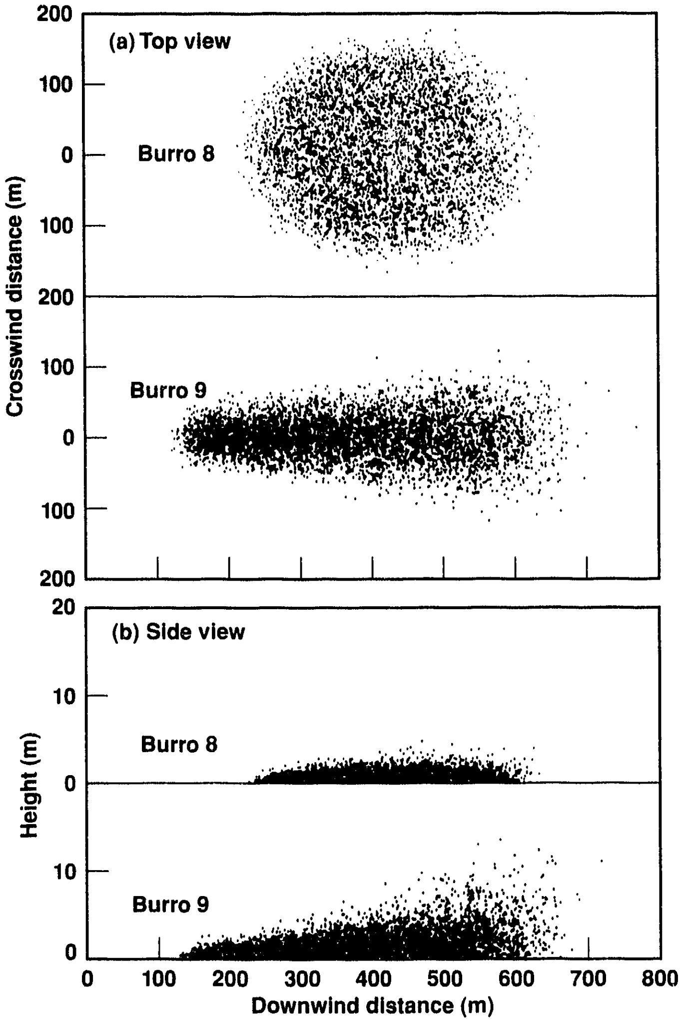

Figure 1. Simulation of dense-cloud dispersion for two field-scale experiments, Burro 8 and Burro 9. Dot-plot projections of the marker-particle locations are shown on (a) horizontal and (b) vertical inwind planes. Wind direction is from left to right in both views. Top and side views of the Burro 8 simulation are shown at 4 min; those of the Burro 9 simulation are shown at 1.5 min. Gravity-flow effects are greater in Burro 8, during which the wind speed was lower, as shown by the rounder shape in top view.

cloud has the more typical cigar shape. In addition, the Burro 8 cloud is wider and lower than the Burro 9 cloud. Under the low-wind-speed conditions of Burro 8, gravity flow has more time to widen the cloud before it travels downwind and dissipates to where the density is essentially equal to the ambient value. The dense-gas effect on cloud height is also greater in the simulated Burro 8 test, resulting in a lower cloud in the Burro 8 simulation.

Versatility of the New ADPIC Model

ADPIC is generally run in conjunction with a mass-conserving wind-flow model to provide the ambient wind field. All of the dense-gas modifications are contained within the ADPIC code, including those that affect wind-flow pattern. Consequently, the new dense-gas version of ADPIC is not restricted to a single wind-flow model; rather, it can be run with alternative wind-flow models to provide the ambient wind field. These models include the fully conservative (mass, momentum, and energy) prognostic wind-flow models, as well as the more commonly used data-interpolating, mass-conserving diagnostic models. This versatility of the dense-gas version of ADPIC allows it to be coupled with a diagnostic wind-flow model for emergency-response purposes. Then when time constraints are reduced, it can be used with a physically more complete, yet computationally slower prognostic model. ◆

Risk Analysis of DOE Sites

L. R. Anspaugh, D. W. Layton, T. Straume, and D. Hsieh*

Many DOE facilities have soils, groundwater, and even biota that are contaminated with organic compounds, heavy elements, or radionuclides. An important part of the process of cleaning up such contamination is to analyze the potential health risks posed by human contact with toxic substances in environmental media. Risk assessments at DOE sites can be particularly complex because the toxic and radioactive substances (e.g., volatile organic compounds vs nonvolatile radionuclides) have physicochemical properties that are vastly different from one another. Hence, the exposure pathways of concern can also differ markedly. Unfortunately, there are no commonly accepted approaches for quantifying concurrent, multipathway exposures to metals, radionuclides, and organic substances that take into account variations in chemical and landscape properties.

Evaluating Compartmental Models

We have taken an initial step in developing improved exposure-assessment models for use in risk assessments of hazardous substances at DOE waste sites. Our research during FY 1992 focused on evaluating multicompartmental environmental models for predicting the movement of contaminants in surficial soils. Compartmental models represent the environment as a series of distinct, interconnected volumes (e.g., atmosphere, soil layers, surface water, groundwater, and biota). They account for the simultaneous movement of substances between those compartments and the biotic or abiotic transformation within compartments (Mackay et al., 1992). The structure of such models facilitates greatly the analysis of multiple pathways of exposure as well as the parameters that affect the magnitude of exposures (McKone and Layton, 1986).

Simulating Trichloroethylene Concentrations

Our collaborations with faculty and students in the Department of Environmental Toxicology at UC Davis include intercomparisons among different compartmental models and comparisons between model results and actual environmental measurements. For example, we have compared the depth-dependent concentrations of trichloroethylene (TCE) in soil predicted from an analytical transport model (Jury et al., 1983) with those predicted using a three-compartment representation of a soil column. Figure 1 shows the extent of overprediction and underprediction of TCE concentrations arising from the use of separate soil compartments. These simulations indicate that the two sets of predicted concentrations converge at a depth of about 30 cm. Our analyses also show that the leaching of TCE from contaminated

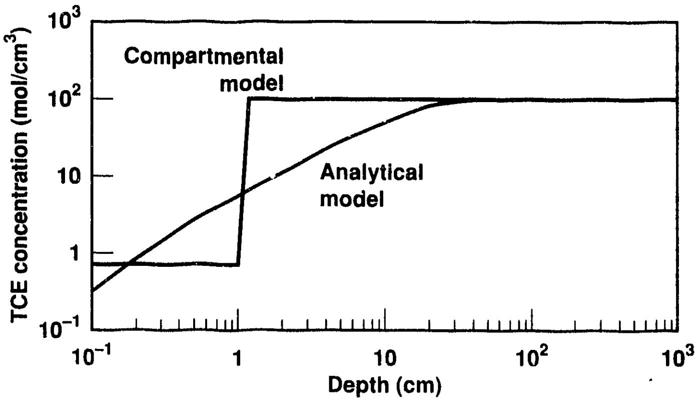

Figure 1. Concentration of TCE as a function of depth in the soil one year after incorporation into surface soil. Predicted concentrations from a compartmental model converge with those from the analytical transport model at a depth of ~30 cm.

---

*University of California at Davis.

soils can result in human exposures that are dominated by inhaling TCE volatilized from well water used as a domestic supply, ingesting that water, and dermal uptake while bathing.

Next, we will compare model predictions with environmental monitoring data collected at LLNL and elsewhere, compare selected compartmental models, analyze the sensitivity of the exposure estimates, and apply these models to one or more DOE sites containing mixed wastes. ◆

References

Jury, W., W. Spencer, and W. Farmer (1983), "Behavior Assessment Model for Trace Organics in Soil: I. Model Description," *J. Environ. Qual.* **12**, 558–564.

Mackay, D., S. Paterson, and W. Y. Shiu (1992), "Generic Models for Evaluating the Regional Fate of Chemicals," *Chemosphere* **24**, 695–717.

McKone, T. E., and D. W. Layton (1986), "Screening the Potential Risks of Toxic Substances Using a Multi-Media Compartment Model: Estimation of Human Exposure," *Regul. Toxicol. Pharmacol.* **6**, 359–380.

Pulsed-Plasma Processing of Effluent Pollutants and Hazardous Chemicals

G. E. Vogtlin, J. N. Bardsley, and P. H. Wallman

The Clean Air Act of 1990 introduced new regulations restricting the emission of pollutants to the atmosphere. LLNL is engaged in research to help industry and government meet these new regulations. Our approach is to use an electrical discharge to change the pollutants into either useful or harmless chemicals. We call the action of this discharge pulsed-plasma processing. Our primary goal has been to efficiently remove nitric oxide (NO), which is created by combustion processes. Nitric oxide is an essential ingredient in the formation of lower atmospheric ozone and contributes to about half of the acid rain.

In pulsed-plasma processing, the radicals are created by electrons from an electrical discharge. The discharge must be from a small, positive, high-stressed electrode to a large, low-stressed electrode. The discharge is driven by a high-power, high-repetition-rate, pulsed modulator. The addition of ammonia converts nitric and sulfur oxides to ammonium sulfate and nitrate, which can be used as fertilizers.

The principal experimental apparatus used in this effort is a closed-loop gas system (Figure 1). This system permits the introduction of various gas combinations prior to testing. Analysis can be conducted during or after these tests. This processor accommodates electrode geometries up to 50 mm in diameter. The recirculated gas can be heated up to 200°C. Heating is important to determine the effect on electrical discharges, chemical reactions, and water content.

During FY 1992, we significantly improved the efficiency of NO removal by adding the hydrocarbon, n-octane. We believe that any hydrocarbon can improve the efficiency through a reaction with the hydroxyl radical (OH) and subsequent oxidation. The end result of these reactions is the oxidation of NO and formation of OH, which can then be reused to oxidize NO. This process generates low levels of pollutants, such as carbon monoxide and nitrous oxide. Nitrogen dioxide (NO_2) is formed by the oxidation of NO and can be removed by adding a carbonate or ammonia. It appears that NO_2 can also be removed by pulsed-plasma processing.

Through modeling and experiments, we want to optimize the efficiency of this process and to explore its potential for use in large systems. We are investigating the optimum pulse length, shape, and amplitude of the voltage drive pulse and the maximum pulse repetition rate. We will measure the energy efficiency of pollutant cleanup for various compounds and acid-gas-removal techniques and determine those pollutants not removed by this process. We will also investigate the possible creation of new pollutants from the pulsed-plasma process.

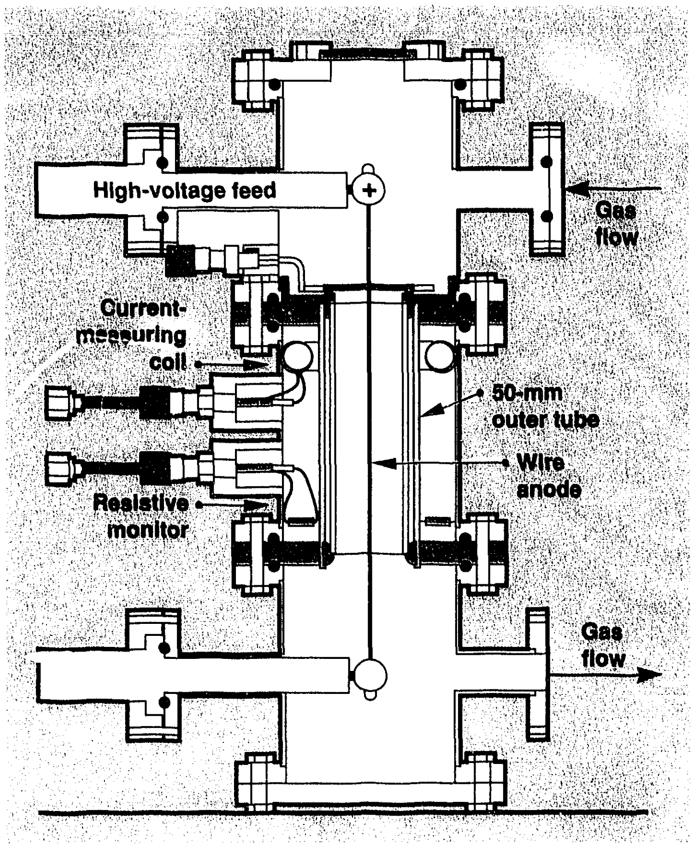

Figure 1. Pulsed-plasma processor, which can accommodate many electrode shapes and temperatures up to 200°C.

Combustion of Toxic Chemicals

C. K. Westbrook and W. J. Pitz

Our project concerned emissions of a variety of toxic chemical species from many types of combustion systems. The chemicals are primarily those for which the 1990 Clean Air Act prescribes strict emission limits and range from volatile organic compounds (VOCs) to chlorinated hydrocarbons (CHCs) and toxic metals. Our research consists of numerical modeling of the production and destruction of these chemicals under practical combustion conditions, using detailed chemical kinetic modeling techniques developed originally for modeling of purely hydrocarbon chemical systems.

We carried out several independent studies within this project, each in collaboration with a different experimental group and each addressing a different set of chemicals identified by the Clean Air Act. In the first study, we examined the production and emission primarily of VOCs from refineries, especially formaldehyde, 1,3-butadiene, carbon monoxide, and small aromatic species. The fuels used in U.S. refinery processes have not been well characterized in the past. If their emissions cannot be brought within levels specified by the Clean Air Act, the additional refinery costs to replace the fuels with "cleaner" fuels would be excessive. We used a kinetic model designed to simulate a stirred reactor as a good representation of an industrial burner. This work indicated the major chemical paths and rates of the most significant pollutant emissions.

We developed kinetic-reaction mechanisms for oxidation of CHCs, which can be best understood as conventional hydrocarbons in which some or all of the hydrogen atoms have been replaced by chlorine atoms. Because the C–H bond strength is greater than the C–Cl bond strength and the thermochemistry of the chlorinated species is different from that of conventional hydrocarbons, the reaction rates for the two systems will differ. However, a great deal of insight can be provided from experience dealing with the hydrocarbon systems. We developed reaction mechanisms for such toxic chemicals as carbon tetrachloride; methyl, ethyl, and vinyl chloride; trichloroethylene; and various related chemicals. Our current work involves using these models under practical conditions to understand the differences between CHC and conventional hydrocarbon systems.

In collaboration with experimental programs at Sandia National Laboratories, California, and the University of Iowa, we carried out numerical modeling studies of the potential of supercritical water oxidation (SCWO) for destruction of toxic chemicals. Although SCWO has shown promise for this application, modeling is needed to predict conditions for optimal performance and monitoring production of unwanted minor chemical constituents. In particular, our project addressed the limitations that the very high pressures and temperatures typical of SCWO place on extensions of conventional techniques for gas-phase, chemical kinetic modeling. It appears that the most important modifications involve corrections to reaction rates that ordinarily are pressure-dependent but eventually lose that dependence.

Further refinements dealing with collective effects, activation volumes, and other factors are being developed for FY 1993. Presently, our kinetic models offer significant promise as predictive and diagnostic tools for SCWO. ◆

A Real-Time, In-Field Impact Assessment System

J. M. Sims, B. Lawver, and T. Sullivan

Impacts on the environment and on public health must be assessed accurately and swiftly during emergencies involving releases of contaminants. When such emergencies occur in heavily populated regions, regulatory and public concern increases regarding public exposure. Environmental managers in charge of cleanup operations and restoration projects must assess the potential impacts of cleanup technologies and decide which technology should be used and when to apply it.

We have been working on several projects to assist decision makers and to supply needed information to regulators and the public. We have integrated the proven technologies of atmospheric dispersion modeling by the Atmospheric Release Advisory Capability (ARAC), real-time acoustic meteorological data acquisition, and real-time pollutant monitoring to help managers estimate exposure while an operation is occurring. Our transportable system uses readily available computer workstation hardware and acoustic meteorological stations. Most pollutant monitoring equipment that is designed for field use and is computer compatible, such as gas chromatography units or radiation detectors, can be integrated into the system.

Transport and Dispersion Models

Figure 1 shows the individual components of the system we use for real-time dispersion predictions on regional scales. This figure also shows the path in which collected data flow. We have acquired state-of-the-art, phased-array sound detecting and ranging (SODAR) for obtaining upper-level wind profiles to supplement data collected from surface wind stations. The instruments for measuring the wind and pollutant release rate are interfaced to and controlled by data loggers. A standalone, scientific color workstation accesses the data loggers by a communication modem connected to local phone lines. We use the meteorological and source information as input to a version of the ARAC models (Rodrigues et al., 1992) that are resident on the workstation and are executed in sequence to provide dispersion results for 1 km or beyond. The results can be displayed instantaneously on a computer monitor, or they can be directed to a laser printer connected to the workstation via an Ethernet link. This procedure is repeated each time a new set of wind data is collected.

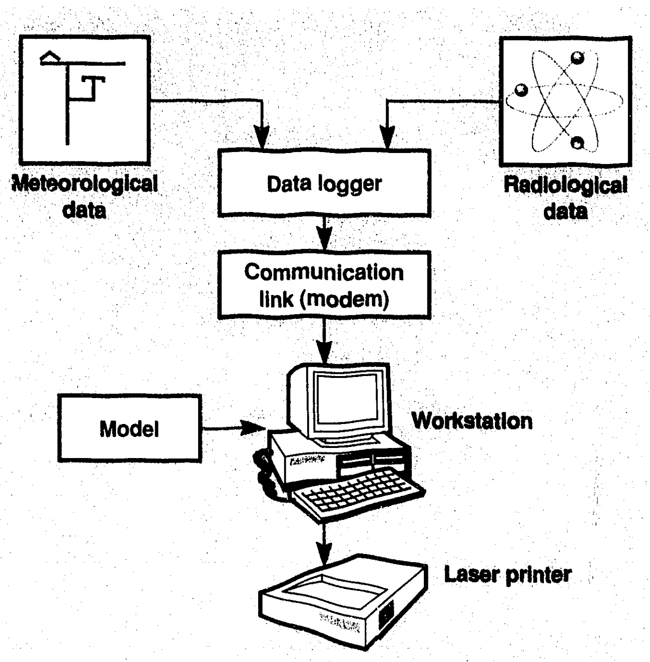

Figure 1. Schematic of system components and setup for real-time dispersion predictions on a regional scale.

Predicting Transport and Dispersion of Airborne Pollutants

Figure 2 shows an example of dispersion calculations for 15,000 m around the LLNL site using the emergency system. The wind fields we used for this example were generated by the ARAC model MATHEW using meteorological data from onsite and offsite towers. The system produces contour and cloud-volume plots in real time. ◆

References

Rodrigues, D. J., G. D. Greenly, R. Lange, L. A. Lawson, P. Gresho, B. S. Lawver, and H. Walker (1992), *User's Guide to the MATHEW/ADPIC Models*, Lawrence Livermore National Laboratory, Livermore, CA, UCRL-MA-103581, 2nd ed.

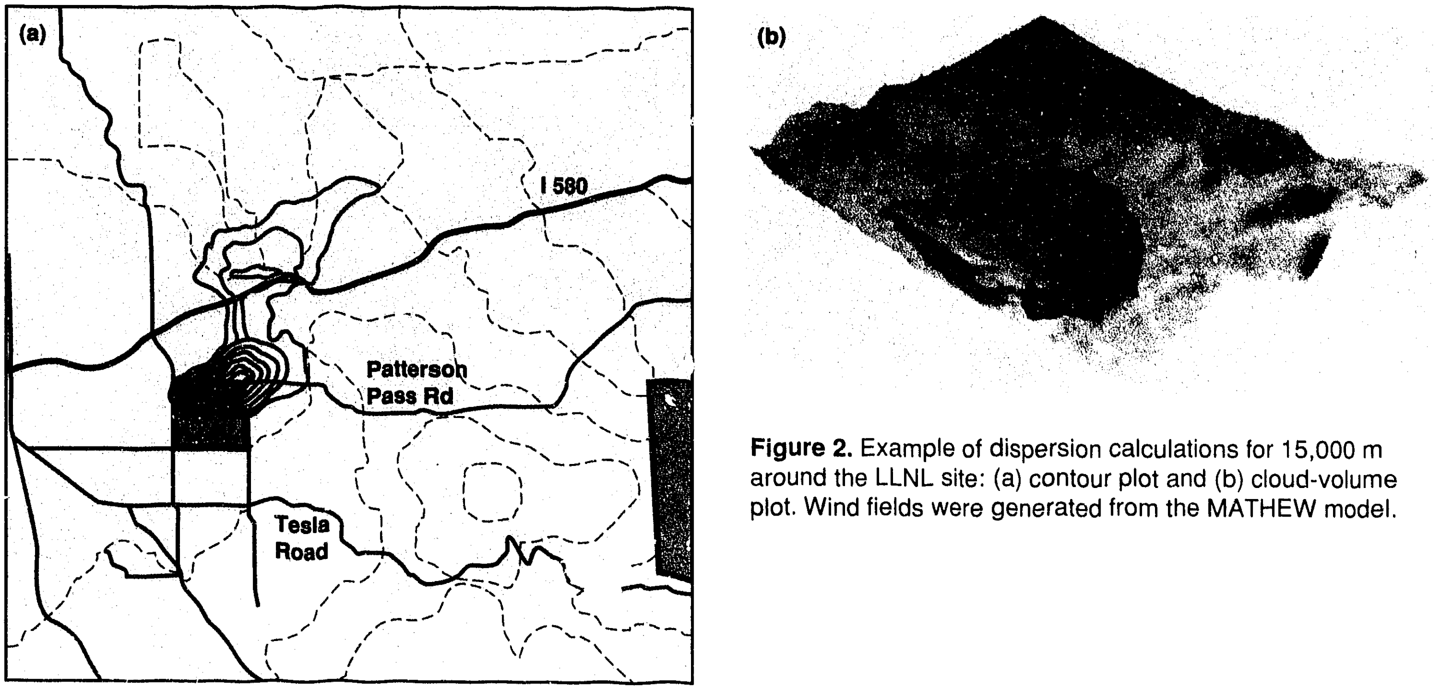

Figure 2. Example of dispersion calculations for 15,000 m around the LLNL site: (a) contour plot and (b) cloud-volume plot. Wind fields were generated from the MATHEW model.

Passivating Mixed-Waste Residues

R. Hickman

In this project, we developed a method for separating the radioactive and hazardous components of mixed wastes consisting of diluted cutting oil contaminated with trichloroethylene (TCE) and depleted uranium turnings. Our goal was to separate the mixed waste into an all-radioactive stream and an all-hazardous stream and to develop a technique to passivate the chemically reactive radioactive component. The radioactive component is contained in the solids stream; the hazardous components are contained in the liquids stream. We would vacuum-dry the turnings from the solids stream and cast them into billets with low surface-to-volume ratios, thus rendering the billets adequately chemically passive and therefore nonpyrophoric.

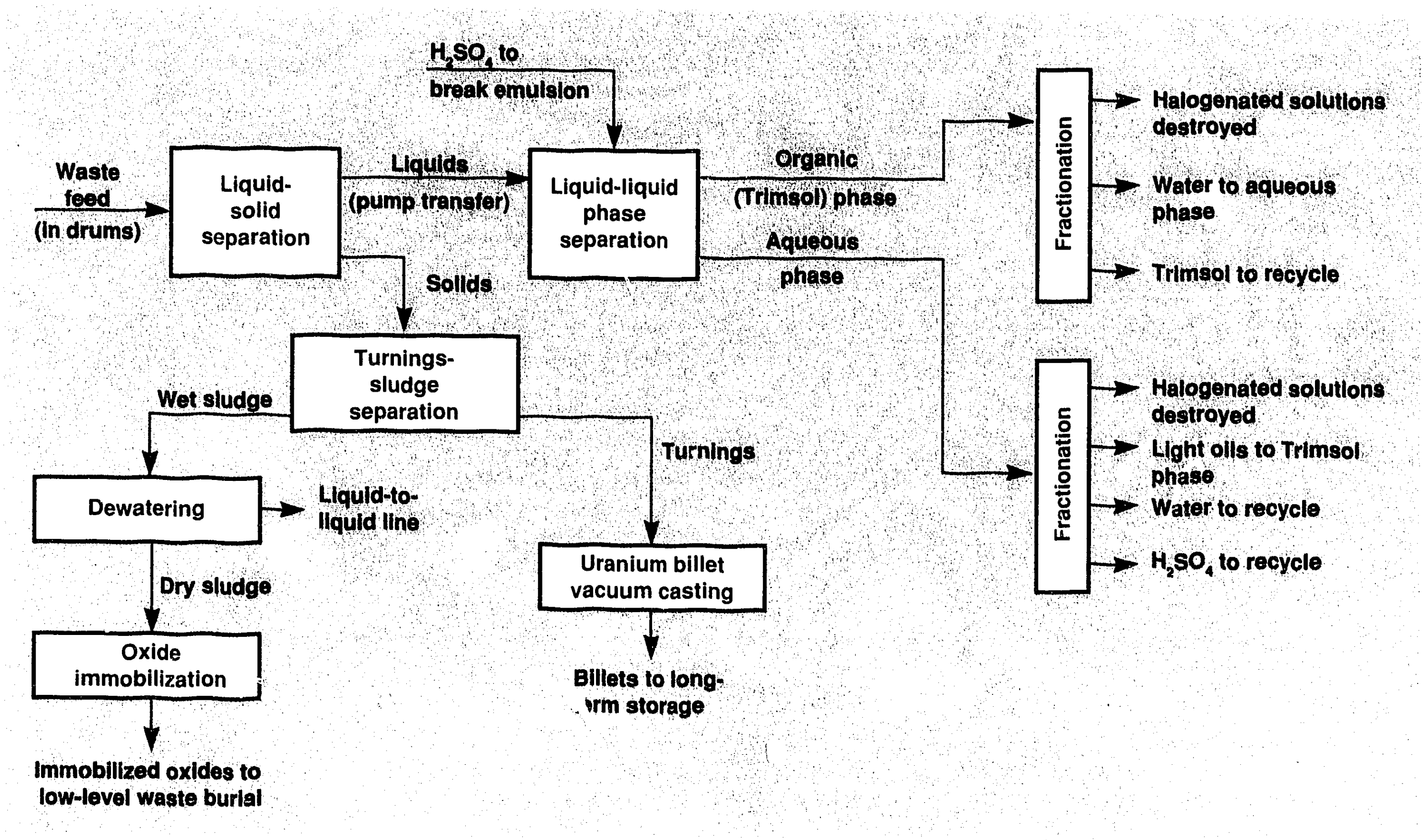

Figure 1. Schematic diagram of our method to consolidate uranium turnings originally mixed with water, cutting oil, and halogenated solvents. Our method recycles most of the liquid waste.

The liquid phase consists of a suspension of Trimsol cutting oil in water and contaminated with TCE. We evaluated the liquid phase for a multistage distillation operation that would recycle the cutting oil to the mechanical shops for onsite use or, at the least, reduce the volume of the liquid waste 75% by removing water.

In FY 1992, we achieved the following milestones:

- Designed a method to separate the liquids from the solids. First, we pump most of the liquid from the drums containing the mixed waste. The device then dumps the solids onto a coarse screen. We separate the remaining liquids by dewatering the oxide sludge. Solids left on the screen are cast in billets.
- Purchased the remaining parts of a fractionation column that would allow us to distill the liquid waste.
- Investigated the most appropriate inert atmospheric melting apparatus and planned modifications to the existing apparatus.

Our method consolidates the uranium turnings in billets suitable for long-term storage. Much of the liquid waste—light oils, water, and Trimsol—can be recycled. ◆

Technology for New Air-Cleaning Systems

W. Bergman, I. R. Corey, and D. Speck

We are developing air-filtration models that will accelerate the design of new air-cleaning systems. Our models will be used to conduct fast and inexpensive theoretical evaluations of new air-cleaning concepts prior to time-consuming and expensive experimental studies and will reduce the number of prototypes and tests needed to design and optimize air-cleaning systems.

In FY 1992, we defined the overall system architecture and compiled various fluid-flow models to compute theoretical air-flow resistance and filter efficiency. Air-flow resistance is derived from the streamlines, the theoretical points that move in the velocity-vector field. Air-filter efficiency can be computed by superimposing particle trajectories on the streamlines. We incorporated various analytical flow models like the Kuwabara model and numerical models based on Navier–Stokes equations into our computer code to represent the air flow.

We evaluated more than 10 numerical fluid codes for analyzing two- and three-dimensional flow fields in the model's filter-fiber matrix. Because filter-fiber geometries are irregular and complex, we were interested in user friendliness and ease in specifying geometry and mesh generation. After consulting with fluid-flow experts and conducting sample calculations using these fluid codes, we selected a commercially available fluid-dynamics code called Nekton from Fluent, Inc. Nekton has superior setup and solution times. It uses a novel solution method based on the spectral method and is well suited for the low Reynolds-number flow regime that applies to most high-efficiency air filters.

Figure 1 shows an example calculation using the Nekton code to determine the velocity-vector field through a matrix of parallel fibers. The circles represent cross sections of the fibers, and the arrows represent the velocity vectors at different points within the flow field. The magnitude of the vectors is proportional to the velocity. The air-flow resistance across the filter-fiber matrix is determined directly from the flow streamlines that are derived from velocity vectors.

In FY 1993, we will enhance this code by adding particle-transport and filter-clogging codes. The particle-transport code will track the trajectories of particles that are superimposed on the velocity-flow field for a given fiber matrix. We will take the filter-clogging code from models that we reviewed in FY 1992.

Our filter-clogging study confirmed that depth filtration using fibrous and granular media to retain particles from fluid–particle suspensions is inherently nonsteady. Filter efficiency and air-flow resistance increase over time, and the filter media structure changes continuously. Because particle deposits vary throughout a filter, this structural change is local and time-dependent. The filter efficiency and air-flow resistance increase over time because the particle deposits offer additional sites for capturing other particles but make the filter structure less porous.

We also examined the new silica aerogel developed at LLNL in FY 1991 to determine if it might function as a filter medium. The aerogel sample had a very high air-flow resistance; it disintegrated when exposed to oil mists and crumbled easily. In FY 1993, we will examine aerogels of greater permeability. ◆

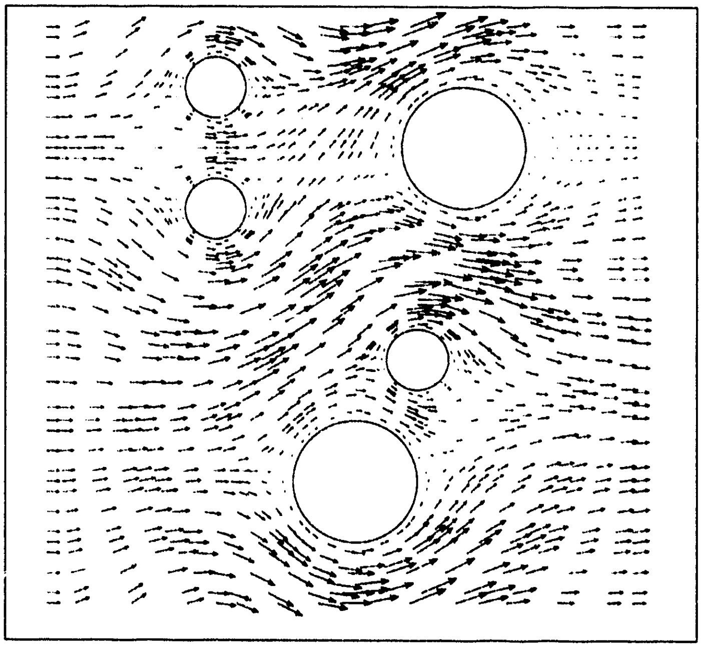

Figure 1. Example calculation of the velocity-vector field for air flow past a matrix of fibers that represents a portion of an air filter. Circles represent cross sections of the fibers; arrows represent the velocity vectors at different points within the flow field.

Energy Science and Technology

Laboratory Directed Research and Development FY 1992

On the previous page. A computer-generated model of the International Thermonuclear Experimental Reactor (ITER) device, which will be about 30 m high—as tall as a nine-story building. ITER is being designed to have a nominal fusion power of 1000 MW or more and to operate with pulses that have flat-top duration of about 1000 s.

Short-Pulse Laser Techniques for Plasma-Instability Studies

R. P. Drake,[*] J. F. Camacho,[*] S. M. Cameron,[*] C. Coverdale,[*] C. Darrow,[*] and T. W. Johnston[†]

Lasers with pulses on the order of 1 ps will make it possible to conduct experiments of unprecedented quality and precision. These short-pulse lasers will permit studies of several basic phenomena in plasma physics, including the onset of laser-plasma instabilities, competition among two or more instabilities, and development of relativistic effects as laser intensity increases. The use of multiple laser pulses allows a well-characterized plasma to be irradiated with a very-well-characterized electromagnetic wave. We have worked to identify and evaluate techniques of employing such lasers for these studies.

Plasma Instabilities

Two important processes in optical media including plasmas are stimulated Raman scattering (SRS) and stimulated Brillouin scattering (SBS). In both processes, an electromagnetic wave is scattered from the medium by a sound-like wave with some shift in its frequency. For SRS in plasmas, the sound-like wave is an electron-plasma wave, whereas for SBS, it is an ion acoustic wave. These two instabilities compete, and it is not clear why one or the other dominates in experimental data or how to predict which one will dominate.

We have completed the quantitative design of an experiment to address the basic physics that underlies the impact of SBS on SRS (Figure 1). In this experiment, we will replace SBS and its associated ion wave, which as an instability can be difficult to control, with a density ripple that is controllably driven by the beating of two laser beams. A total of five laser beams will be used, three of which will be obtained by splitting and frequency-converting or Raman-shifting a single input beam. One of the laser beams will produce a plasma large enough for SRS to be driven in it. Three other laser beams will be injected; two of them will beat together to drive the density ripple in the plasma, and the other will be used to diagnose the ion-wave amplitude and other plasma parameters through Thomson scattering enhanced by four-wave mixing (FWM).

The final laser beam will drive SRS in the presence of the density ripple. Measurements of the scattered SRS light and the Thomson-scattered light will allow us to test predictions of how the threshold of SRS and the frequency of scattered light waves from SRS depend on the degree of mode coupling between the ion waves associated with the density ripple and the electron-plasma waves associated with SRS.

Filamentation of Laser Beams

In the regime of relativistic effects, a laser beam is predicted to break up into filaments if it reaches sufficient intensity because the relativistic response of the plasma causes the light to focus. We considered methods of diagnosing the relativistic filamentation of a laser beam. It has been suggested that the imaging of harmonic emission might reveal filamentary structures in plasmas and allow one to detect relativistic self-focusing. However, the structure of the plasma can alter the phase of the emitted light and destroy the capability of obtaining an accurate image.

We examined the results of a filamentation model developed by T. W. Johnston and collaborators to assess the implications of this effect for possible experiments. We concluded that such measurements would not provide useful data. We have begun exploring other possibilities, including a suggestion by Chan Joshi of UC Los Angeles to image the x-ray emission from partially ionized gases, whose degree of ionization is sensitive to laser intensity. ◆

---

[*] *LLNL and University of California at Davis.*

[†] *INRS Energie, Varennes, Quebec, Canada.*

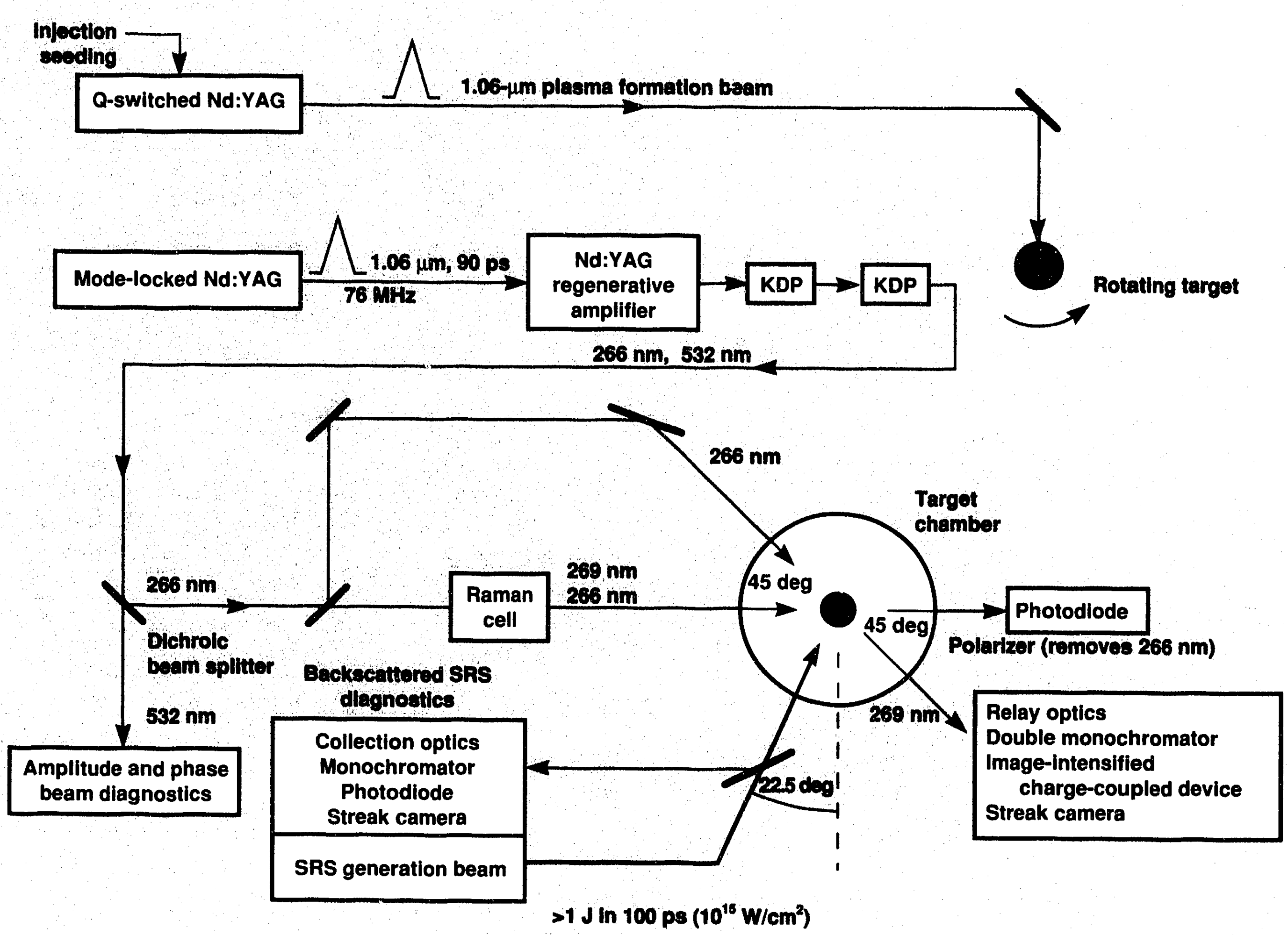

Figure 1. Schematic of our proposed four-wave mixing (FWM), mode-coupling experiment. This experiment addresses the basic physics underlying the impact of SBS on SRS.

Thomson-Scattering Studies of Stimulated Raman Scattering

**R. P. Drake,[*] K. L. Baker,[*] K. Mizuno,[*] B. W. Sleaford,[*] K. G. Estabrook,[*]
D. M. Villeneuve,[†] and B. La Fontaine[‡]**

Stimulated Raman scattering (SRS) is an important nonlinear process in optical media, including plasmas. In this process, an incident light wave decays into a scattered light wave and a sound-like wave whose frequency is characteristic of the medium. When SRS occurs in plasmas, this sound-like wave is an electron-plasma wave.

Once a plasma wave is driven to large amplitude, significant nonlinear behavior may be observed. Plasma waves and their saturation are of interest for two reasons. First, several distinct mechanisms can couple the wave energy into other waves or into plasma particles. Second, the consequences of electron-plasma wave saturation are of concern in laser fusion, short-pulse x-ray lasers, and accelerator schemes. In FY 1992, we obtained the first simultaneous measurements of the spectrum of wave frequency and wave number of SRS-driven plasma waves, using Thomson scattering. These measurements provide evidence that directly addresses saturation dynamics.

Producing and Detecting SRS-Driven Plasma Waves

We used a laser beam to explode a CH target that was 0.2 to 0.5 μm thick. The beam had a wavelength of 1.064 μm, an energy of about 100 J, and a duration of 3 ns. The density of the plasma produced by the explosion decreased through the range of densities over which SRS can be driven during the laser pulse. We used a splitter to sample scattered light reflected through the focusing lens by SRS and analyzed it with a spectrometer. A small fraction of the incident laser beam was converted to three times its initial frequency and injected through a different focusing lens to probe the driven plasma waves by Thomson scattering, a process similar to scattering from a diffraction grating. The signal was collected using a large lens and analyzed in angle and in frequency before being detected by a gated imager and a charge-coupled-device (CCD) camera.

Observed SRS Instabilities

Because the laser intensity was a few times 10^{13} W/cm^2, the SRS instability was only slightly above the threshold owing to collisional damping of the waves. The range of scattered-light wavelengths was typically small, as shown in Figure 1. The distance above the abscissa increases with plasma-wave frequency, and the horizontal position depends on wave number. Stray light at the probe frequency is also shown in Figure 1. Thicker targets systematically produced emission at longer wavelengths, which originated from higher densities.

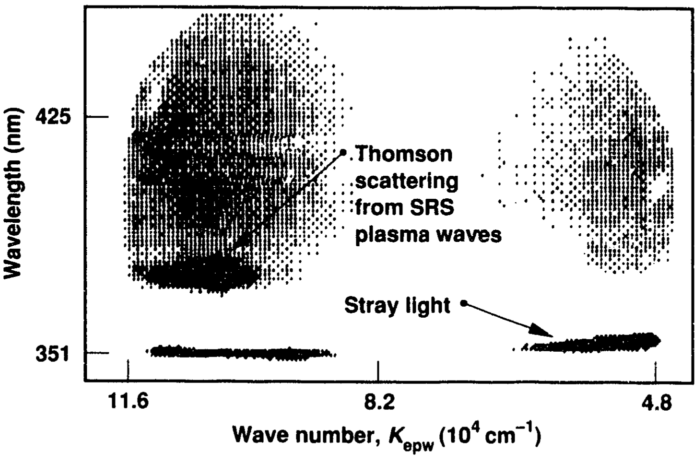

Figure 1. Observed wavelength of Thomson-scattered light and wave number, K_{epw}, of electron-plasma waves driven by SRS.

---

[*] *LLNL and University of California at Davis.*

[†] *National Research Council, Ottawa, Ontario, Canada.*

[‡] *INRS Energie, Varennes, Quebec, Canada.*

Both the frequency and wave number of the plasma waves are consistent with values inferred from the observed scattered light using the theory of SRS. In addition, to within instrument resolution, plasma waves driven by SRS under these conditions did not broaden in wave number or drive other plasma waves of detectable intensity. We are comparing these observations with predictions made using nonlinear theory. ◆

Ion Acoustic Decay

R. P. Drake,* B. S. Bauer,* K. L. Baker,* K. Mizuno,* B. W. Sleaford,* A. V. Rubenchik,* K. G. Estabrook,* C. Labaune,† S. Baton,† T. Jalinaud,† E. Schifano,† M. V. Goldman,‡ and D. Newman‡

The ion acoustic-decay instability (IADI) involves the decay of a laser-light wave in a plasma into two sound-like waves: an ion acoustic wave and an electron-plasma wave. This instability occurs in laser plasmas, in other laboratory plasmas driven by intense radiation, in ionospheric-modification experiments, and probably in the plasma environment surrounding compact astrophysical sources. The electron-plasma waves emit radiation at the second harmonic of the laser frequency. We used this radiation to study the nonlinear evolution of the sound-like turbulence driven by acoustic decay.

Results of Electron-Plasma Wave Studies

We made the first observations of time-resolved, second-harmonic emission at several angles simultaneously and emission both parallel and perpendicular to the electric field of the laser light. To make these observations, we used from 1 to 80 J of 1.053-μm light to irradiate CH targets in 550-ps pulses, producing characteristic intensities in the range of 10^{13} to 10^{14} W/cm^2. A random-phase plate was used to scramble the structure in the laser beam and produce more uniform irradiation of the plasma.

These conditions drove the IADI well above threshold, producing red-shifted Stokes emission that was well separated from the emission spike at the second harmonic of the laser frequency, as shown in Figure 1. These data, obtained using an average laser intensity of 2×10^{14} W/cm^2, show that the spectrum was broadened toward longer wavelengths from the exact second-harmonic wavelength of 526.5 nm and was not strongly dependent on observation angle. The spectral structure of the Stokes emission was qualitatively similar for all intensities and angles of observation. The duration of the signals showed trends anticipated from the instability thresholds. The scaling of the signal strength, the spectral width, and the angular dependence of the emission depend on the nature of the sound-like turbulence that is driven in the plasma by the instability. These data will be used to test state-of-the-art nonlinear simulations of the development of sound-like turbulence. ◆

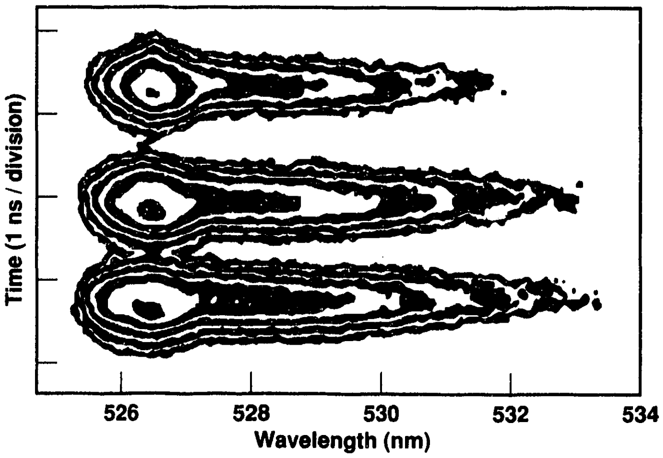

Figure 1. Spectrum of the second-harmonic emission at angles of 148 deg (top), 135 deg (middle), and 122 deg (bottom) relative to the direction of laser propagation. The contours are spaced by a factor of 2 in spectral intensity and have a width of a factor of 1.4.

---

*LLNL and University of California at Davis.
†Ecole Polytechnique, Palaiseau, France.
‡University of Colorado, Boulder.

Microbial Methane-Conversion Enzymes

B. E. Watkins, R. T. Taylor, M. L. Carman, N. N. Shaw, M. Himmelsbach, J. H. Satcher, N. W. Winter, R. D. Sanner, C. W. Morris, R. A. Reibold, M. W. Droege, J. R. Weakely,[*] L. Chauffe,[†] and A. L. Balch[‡]

Transportation fuels are a critical energy commodity that affect nearly every sector of the United States. Currently, they account for 27% of the total U.S. energy consumption and 63% of all U.S. oil needs. Consequently, government and industry seek to economically convert domestic fossil energy resources other than crude oil to liquid hydrocarbons that can be used as transportation fuels.

Worldwide, natural gas is very abundant, with about 110 billion m^3 of proven reserves. Estimators predict that if these reserves could be processed into a liquid hydrocarbon, they would provide enough transportation fuel worldwide to last 100 years.

Methane is the primary hydrocarbon in natural gas. However, to convert methane directly into liquid fuels requires developing new catalysts. The most promising of the known catalysts requires very high operating temperatures (700 to 800°C), which result in an unacceptably low product yield because of the uncontrolled overoxidation of methane to CO and CO_2. To convert methane into liquid fuels, we must control the catalytic activation of the methane C–H bond at a lower temperature, which could prevent overoxidation. Efforts to synthesize catalysts chemically can benefit from studying the biological catalysts that can partially and efficiently oxidize methane into methanol.

A naturally occurring biocatalyst—the enzyme methane monooxygenase (MMO)—exists in a select group of aerobic soil and water bacteria called methanotrophs. These bacteria can efficiently and selectively use methane as their sole source of energy and carbon for cellular growth. MMO partially oxidizes methane to form methanol, a product that can be easily converted to liquid hydrocarbon transportation fuels, used directly as a liquid fuel or fuel additive, or serve as a feed stock for chemicals production. Currently, there is no analogous nonbiological process to accomplish this conversion.

We seek to characterize the active site of MMO so that we can develop synthetic, bioinorganic complexes that mimic the process of this enzyme but will be more robust and have higher catalytic density than the enzyme. Our work has centered on the methanotroph *Methylosinus trichosporium* OB3b because it is easy to grow and because its enzymatic activity is high in both intact cells and broken cells, which allows us to study the enzyme separate from the cells. We examined in detail the influence of the culture conditions on this methanotroph because they affect the cell growth rate and yield and the amount, location, activity, and form of the MMO enzyme that the cells produce.

Two distinct forms of MMO occur, depending on the ratio of copper to cell mass in the culture medium. Under nitrate-excess, oxygen-limited, and high $CuSO_4$ concentrations, this methanotroph contains many internal membranes and synthesizes mostly a particulate form of MMO. In contrast, under nitrate-limited, low $CuSO_4$ concentrations, this same methanotroph exhibits fewer internal membranes and produces exclusively a soluble form of MMO.

We chose to study the particulate form of MMO for several reasons. First, particulate MMO is approximately an order of magnitude more catalytically active with methane than soluble MMO. Second, far less is known about particulate MMO than the soluble form. Third, as we varied the concentration of $CuSO_4$ in the cells, the level of enzymatic activity correlated linearly and directly with the measured copper and iron content of the enzyme. These results suggest that copper

---

[*] University of Oregon, Eugene.
[†] California State University, Hayward.
[‡] University of California at Davis.

and iron (or a membrane-bound, iron-dependent reductase) may play a role at the active site of particulate MMO (Figure 1).

In contrast, only iron has been found to be an active site metal-cofactor of soluble MMO. In addition, unlike particulate MMO, the soluble form of MMO is very active with a variety of substrates (e.g., chloroform, isobutane, and toluene), which suggests that fundamental differences exist between the active site structures of these two forms of MMO.

To determine more accurately the location of soluble MMO's active site, we studied the proteins and their subunits that facilitate the partial oxidation of methane to methanol. The binuclear iron-containing soluble MMO contains a large hydroxylase protein (molecular weight of 240,000 amu) within which the addition of an –OH group onto a methyl radical appears to occur. This suggests that the protein is the site of the partial oxidation. Also, acetylene appears to be a suicide substrate for soluble MMO. A suicide substrate behaves like a normal substrate, except that midway through the catalytic process, it irreversibly inactivates the enzyme by forming a covalent link with one or more amino acids in the active site pocket. After adding (1,2-^{14}C)acetylene to the enzyme, two molecules of this substrate became covalently bonded to the hydroxylase protein, which indicates that the enzyme has two active sites per molecule.

We separated the C-labeled hydroxylase subunits by urea-ion-exchange chromatography, followed by slab gel electrophoresis (Figure 2). We found that 72% of the radioactivity was in the alpha subunit and 26% in the beta subunit. This result suggests that the active-site pockets are located at the interface of these two subunits. Our research has allowed us to label the active-site pockets and thereby begin to identify the amino acids that comprise them.

We synthesized a series of copper complexes, one of which mimics the active-site structure of the binuclear, oxygen-bridged center of MMO, and others that possess a single copper ion. Neither unchelated Cu(II) nor the mononuclear complex can oxidize cyclohexane (a hydrocarbon) in the presence of hydrogen peroxide. However, the binuclear Cu(II) complex can oxidize cyclohexane to a mixture of cyclohexanol and cyclohexanone. These data show the proof of principle that the coordinately asymmetric complexes will function as biomimetic catalysts

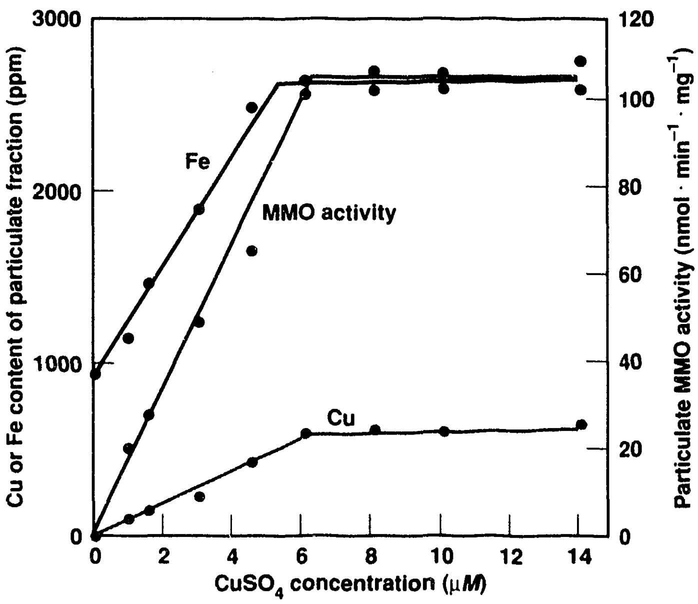

Figure 1. Effect of the growth medium CuSO$_4$ concentration on the particulate MMO catalytic activity, and copper and iron content of the particulate fraction. For nine growth experiments, the average copper content was 28 ppm (range of 22 to 39 ppm), and the average iron content was 951 ppm (range of 698 to 1273 ppm).

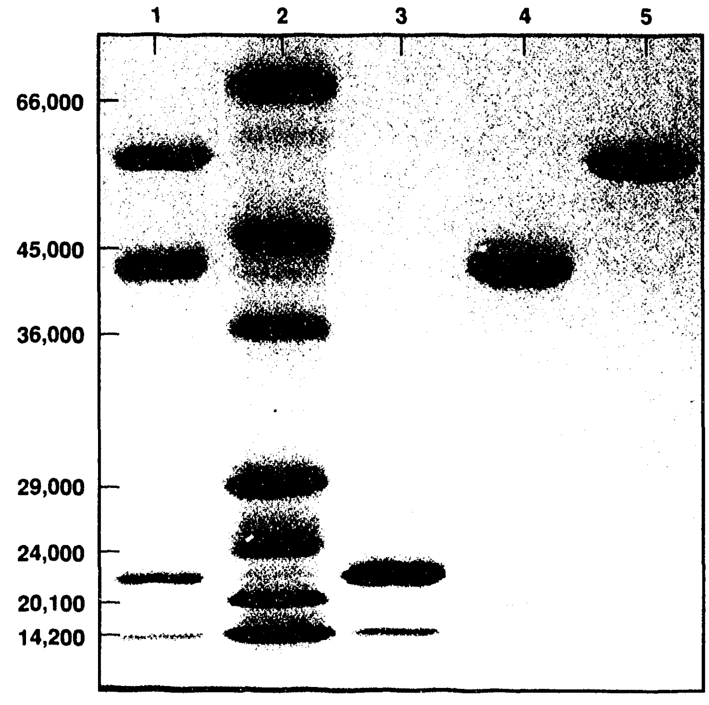

Figure 2. Polyacrylamide gel electrophoresis of the ^{14}C-labeled polypeptide subunits from (1,2-^{14}C)acetylene-inactivated soluble MMO hydroxylase. Lane 1: ^{14}C-labeled hydroxylase protein; lane 2: molecular weight protein standards; lane 3: gamma subunit; lane 4: beta subunit; and lane 5: alpha subunit.

and that they have the ability to oxidize hydrocarbons. We are using this ligand as a starting point to synthesize new catalysts and ligands. Specifically, we are preparing complexes with other metals (e.g., iron, zinc, and manganese) and complexes with additional ligand groups and with varying oxygen-to-nitrogen contact atoms. ◆

Energy Economics Modeling Project

A. D. Lamont and R. Koopman

We have developed models and modeling capabilities to evaluate the long-term effect of several proposed energy policies. The project has focused on "network" modeling, which divides the energy system into basic processes represented by nodes in a network. Each node represents an energy resource, a conversion process, a market, or an energy end use. The connections between the nodes represent actual flows of energy commodities, such as crude oil flowing from oil wells (a resource) to an oil refinery (a conversion process). At each node the model computes the quantities of inputs required to meet the demands for its output and passes these demands to the nodes that supply it. Simultaneously, at each node, the model computes the prices that it requires to operate and passes that information to the nodes that use its output. Through an iterative algorithm, the model computes the equilibrium prices and quantities demanded for each time period in the model scenario. The network approach is formally equivalent to a market equilibrium.

With the network approach, each node is a model of a portion of the energy system and can simulate the response of part of the energy industry to changes in demand, price, and government policy. Thus, the model can evaluate the long-term effect of government policies on investment and operating decisions in the energy industry and can project the long-term structural effect of the proposed policies.

Accomplishments

We have developed a new model of the U.S. energy system and a prototype software tool for structuring energy economics models as networks. In collaboration with Lawrence Berkeley Laboratory, we have developed the Lawrence Laboratories Energy Model (LLEM). LLEM is a single-region model of the United States; each technology and end use represents that technology or end use for the entire country. LLEM includes 85 energy-conversion technologies, 27 end uses, and 13 energy resources. We can add other energy technologies later on.

LLEM simulates the effect of proposed policies for controlling environmental emissions. The model estimates the emissions from each process and incorporates the cost of emissions permits in the financial calculations for each node. To check the model and to develop an initial baseline calibration, we compared LLEM's projections to long-term projections made by DOE's Energy Information Administration (EIA).

We also have developed a prototype software system for building and running network models. A modeling system for network models provides the user with a library of standard nodes, a language for describing how nodes are linked to form a model, and a database for storing the parameters and current state of each node during a model run. The system also implements the solution algorithm.

The usefulness of the approach is determined by the ease with which a user can structure a network from existing nodes or create new kinds of nodes and modify existing ones. Current modeling systems are written in Fortran, and the interactions between the nodes require complex programming structures that are difficult to modify. We have developed a new system, ProtoNet, based on an object-oriented programming language (object Pascal). ProtoNet simplifies the job of modifying existing node models or developing new ones by insulating the user from the complexity of the interactions, which are handled by the system through a set of standard procedures. We are preparing a version of ProtoNet that can be distributed to potential users.

In FY 1992, we completed a study for the EIA that demonstrated ProtoNet's ability to address new energy policies and the ease with which ProtoNet can be modified. The study demonstrated ProtoNet's ability to model new natural-gas marketing regulations and the sulfur emissions allowance market provided for in the 1990 Federal Clean Air Act Amendments, which grant electric utilities allowances to emit sulfur. However, each utility is also allowed to buy or sell permits in the marketplace. Utilities that can inexpensively reduce emissions by burning more natural gas, retrofitting with scrubbers, or burning low-sulfur coal can sell excess allowances to another utility. Such flexibility is expected to reduce the cost of meeting sulfur emissions limits.

Conclusions

We have developed a significant capability for analyzing the economics of energy systems. Our capabilities include a modeling system that can build large and complex models on a mainframe computer; a smaller, more flexible modeling system that runs on microcomputers; and a complete model of the U.S. energy system that includes all major processes and energy commodities and has been calibrated against existing energy models. ◆

Refuelable Zinc–Air Electric Vehicle Battery with Onboard Zinc Recovery

J. F. Cooper, J. E. Noring, and A. Maimoni

We are designing a battery that will give electric vehicles (EVs) some of the competitive features of gas-driven cars: long range (400 km), rapid refueling (10 min), and highway-safe acceleration. In our battery, zinc particles react with air to generate zinc oxide and electricity. The zinc fuel can be generated at home and needs only a modest commercial infrastructure to support it.

Two-Phase Strategy

Nightly, owners would use household power to reduce the battery-reaction products (zinc oxide) onto 5 to 10 metallic slabs suspended in an onboard electrolyte tank with power cells (Figure 1). The slabs would be removed at local service stations about every 400 km and shredded to 1-mm particles that would be returned to the vehicle as fuel. If the vehicles were driven more than 400 km in a single day (only 10% of annual travel), the station would replace the exhausted electrolyte and add new zinc fuel.

Because 90% of the battery's zinc would be produced at home and the cost of shredding would be small, a fleet of EVs could be introduced with little commercial investment beyond the existing gasoline-station infrastructure. Onboard zinc reduction also would allow recovery of braking energy (with use of a suitable buffer) and means that EVs could use base-load utility power during off-peak hours.

In the long run, commercial zinc-recovery plants would gradually replace onboard recovery, taking advantage of large-scale, regional production. Unlike homeowners, commercial producers could use carbothermal energy to reduce zinc oxide to zinc, which would use a fraction of the energy of electric recharge. Carbothermal reduction also might give zinc–air batteries an overall energy balance more favorable than that of automobiles using petroleum-based fuels.

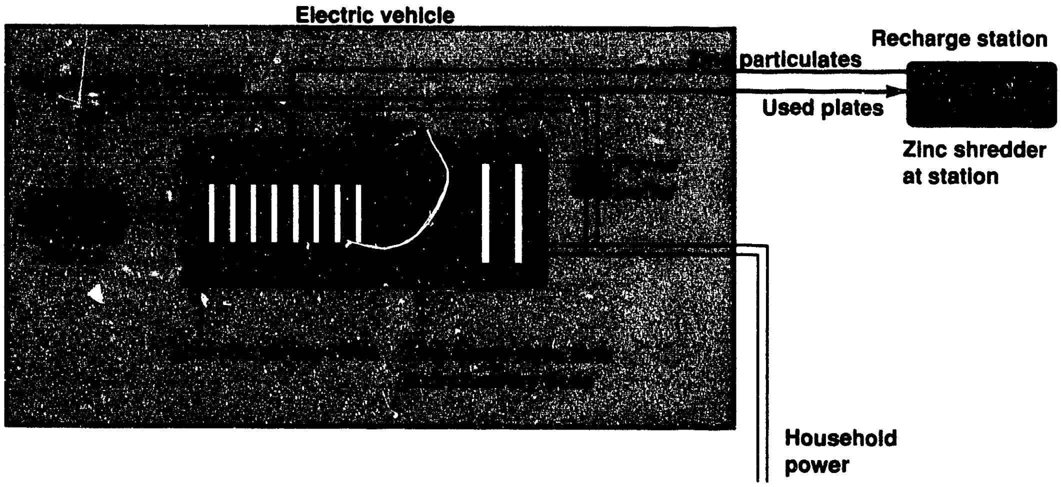

Figure 1. Refuelable zinc–air electric battery with onboard zinc recovery. Zinc usage is estimated to be about 200 g/km ($0.03/km for electricity).

Cell Configurations

In FY 1992, we tested a promising power-cell configuration under 90-km/h cruise conditions (115 mA/cm^2, 60 to 70°C). In this configuration, we intermittently added zinc particles (0.5 to 1 mm) to the battery, which fully discharged them with about 95% coulomb efficiency. The cell maintained stable discharge characteristics under constant load during a 16-hour test. We maintained self-feeding and stable particle-size distributions through a novel mechanism that slowly inverts the natural size stratification to prevent clogging. To simulate road conditions, we used a vibration table in some of these tests.

We integrated other candidate cell designs with vehicle models so that we could estimate relations between zinc consumption, electricity cost, weight, and range for modestly powered vehicles. Zinc usage was estimated to be about 200 g/km ($0.03/km for electricity) for a 1.6-tonne, conventionally designed five-passenger sedan requiring zinc additions every 400 km.

In FY 1993, we will test multiple cells integrated with a complete zinc-recovery cycle. We will use specific thermal and electrochemical technologies to evaluate the battery's energy use and economy. ◆

Three-Dimensional Gyrokinetic Particle-in-Cell Simulation of Plasmas on a Massively Parallel Computer

B. I. Cohen, T. J. Williams, and J. A. Byers

The goal of our project is to use massively parallel computing to improve our gyrokinetic particle-in-cell (GPIC) simulation of fusion-plasma microturbulence. The following list briefly describes our FY 1992 goals and the progress made toward achieving them.

Begin working on the Intel Delta machine. LLNL's time allocation on the Delta machine at the California Institute of Technology was not realized. Nevertheless, we vigorously pursued the goal of writing a new code for purely distributed-memory parallel processors like the Delta.

Conduct a study of a plasma instability on the CM2 massively parallel computer at Los Alamos National Laboratory. We made several physics test runs that followed a documented plasma instability, but our programmatic runs on the Cray showed that the signal-to-noise problem with fully nonlinear gyrokinetic codes made well-resolved simulations prohibitively expensive, even with the faster CM2 version of the code. We therefore decided to implement the much quieter δf method (Dimits and Lee, 1990) in the CM2 code rather than run large, fully nonlinear simulations.

Develop data diagnostics to handle results from any computer. We rewrote our code output functions using the netCDF library, which is a system for writing machine-independent, portable, self-describing data files. Our locally developed graphics postprocessing software now reads these files. In addition, we learned how to use the commercial visualization systems IDL and AVS. Forthcoming releases of these systems promise to read the netCDF files, freeing us from writing postprocessing codes.

Develop more-efficient numerical physics methods for our simulations. In addition to our δf work, we tested our semi-implicit, orbit-averaged algorithm. This technique improves efficiency by allowing larger timesteps and fewer simulation electrons. We implemented quasi-ballooning coordinates to obtain more useful resolution from a given number of grid points, and we introduced additional toroidal physics effects into our model.

Improvements to the GPIC Codes

We fully parallelized the three-dimensional GPIC codes on the TC2000 and the CM2. Our new parallel fast Fourier transform for the TC2000, together with restructured memory usage, made the code faster by a factor of about 50. Surprisingly, the TC2000 code is now the fastest of our codes—faster than the CM2 code, which is in turn faster than the Cray 2 code. The parametric dependence of the codes' speed ratios is so complicated that it is misleading to make a single statement about those ratios. Broadly speaking, the TC2000 code is two to four times faster than the Cray 2 code. Detailed measurements of timings and scalings with processor count are given by Williams and Matsuda (1992); Figure 1 is an example. On both the CM2 and the TC2000, the parallel efficiency bottleneck is communication between the field-grid data arrays and the particle data arrays (*gathers* and *scatters*). Because the particles move chaotically, traversing grid cells at random, the communication pattern between the grid and particle arrays changes randomly—the worst possible case for interprocessor communication when array elements are finely distributed across the processors' memories.

This inefficiency spurred the faster development of a new code, which distributes the arrays in blocks across processor memories in an intelligent manner that is tied to spatial decomposition of the simulation domain. Particle data are stored in the memory of the processor that owns the associated grid data, eliminating interprocessor communication in gathers and scatters between its own subarrays. Particles that cross the coarse subdomain boundaries are collected and passed to the appropriate neighbor processor as a single message. Grid data on the subdomain borders are likewise passed to neighbor processors; each processor keeps a small number of *guard cells* around its borders for storing the grid data from neighbor subdomains that are needed for operations on its own data. This generic domain-decomposition, message-passing (DDMP) version of the code is nearly complete enough for testing to begin. It is inherently portable among machines like the CM5 and the Intel Paragon.

Our goals for FY 1993 are to:

- Complete development and shakedown of the DDMP code.
- Make scaling studies of this code and compare them with an analytical performance model for computation and communication.

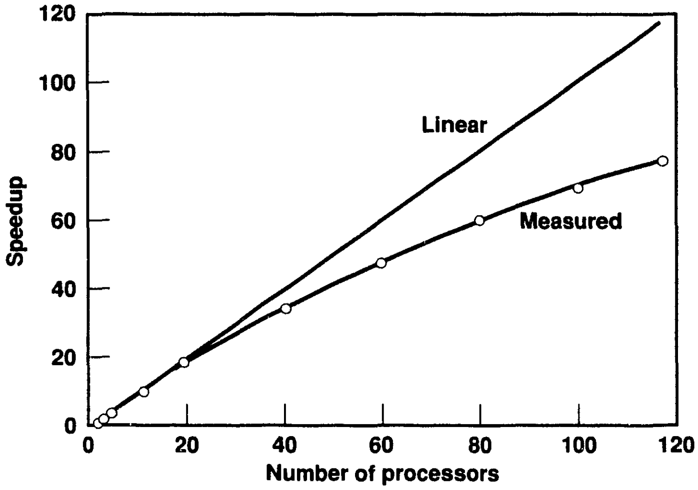

Figure 1. Measured speedups of a simulation code on the TC2000 machine. The code used is an older, non-message-passing code. Green curve is the theoretical ideal linear speedup. Run parameters are 115,351 particles and 32,768 grid cells.

- Install the netCDF input/output system into all of our GPIC codes.
- Replace our locally developed graphics postprocessing software with the commercial software pair IDL/AVS.
- Push toward using the parallel code in previously intractable simulations. ◆

References

Dimits, A. M., and W. W. Lee (1990), *Partially Linearized Algorithms in Gyrokinetic Particle Simulations*, Princeton Plasma Physics Laboratory, Princeton, NJ, PPPL-2718.

Williams, T. J., and Y. Matsuda (1992), "3D Gyrokinetic Particle-In-Cell Codes on the TC2000 and CM2," in *The 1992 MPCI Yearly Report: Harnessing the Killer Micros*, E. D. Brooks III, Ed., Lawrence Livermore National Laboratory, Livermore, CA, UCRL-ID-107022-92, pp. 303–311.

An Improved Tokamak Divertor for Steady-State Operation: The Radiative Slot Divertor

S. L. Allen, K. Thomassen, B. G. Logan, G. Porter, and M. Rensink

One potential source of energy for the future is fusion. The sun is fueled by fusion reactions; the large solar mass confines the plasma that sustains the reactions. One approach to confine plasma for fusion on earth uses magnetic fields in a doughnut-shaped device called a tokamak. Research has shown that noncircular (e.g., D-shaped) plasma cross sections result in better plasma confinement and hence more energy output. At the top and bottom of this plasma is a specially shaped set of magnetic field lines called a divertor. Although only a small amount of power leaks into the divertor region, the power can be very highly localized spatially. Current estimates for future tokamaks indicate that the localized heat flux caused by this leakage is greater than can be tolerated with existing materials.

We researched the design of a new tokamak divertor that radiates the power in the divertor region, spreading out the heat flux and thereby reducing the peak heat load. Proof-of-principle experiments have been performed on the DIII-D tokamak at General Atomics as part of its collaboration with LLNL. Using gas injection in the divertor region, the heat flux to the divertor plate was reduced by a factor of up to 5. Our LDRD design effort was twofold:

- Develop a computer code for modeling radiative divertor experiments with nitrogen injection on the DIII-D tokamak.
- Design improved radiative divertor structures.

Development of benchmark computer codes is perhaps the most useful tool for predicting performance of future divertor designs. Existing computer modeling codes cannot self-consistently calculate arbitrary impurity densities in the plasma because of difficulties in numerical convergence and limitations on code size and execution speed. LEDGE, a two-dimensional fluid code being developed by the Magnetic Fusion Theory Group at LLNL, should be more stable numerically and will be used to calculate impurities in the future. In the mean time, we used a simplified calculation to estimate the radiated power in the DIII-D experiments. An early version of the LEDGE code is used to calculate the core and edge physics parameters. A postprocessor code was developed under the LDRD contract to calculate the radiation from a particular impurity. We found that a small impurity density, <3% of nitrogen, was needed to explain the experimental results.

An important feature of the impurity calculation is that substantial deviations from "coronal" equilibrium were included in the atomic physics. In coronal equilibrium, ionization of an impurity ion (removal of an electron) by electron impact is balanced by recombination (dielectronic plus radiative), i.e., the ion gains an electron. For the divertor, recombination by energetic hydrogenic neutrals and the impurity ion confinement are equally important in the ionization balance. The result is that the mean charge of the impurity ion is lower than expected at a particular electron temperature, and the radiation is much higher (in some cases, several orders of magnitude). The impurity calculations are completely general, and we have estimated impurity radiation for several elements, such as argon and molybdenum. Argon and the other noble gases are important in that they do not adhere to the walls of the tokamak and can be readily recycled.

Several divertor configurations were also examined, particularly a slot design that concentrates the neutral atoms and molecules in channels within the divertor. In most tokamaks, the divertor plates are constructed of a low-Z material, such as carbon or beryllium. These slots would extend from the plate toward the core of the plasma. Several preliminary designs were developed for the existing DIII-D tokamak (Allen et al., in press) and the new steady-state advanced tokamak being developed as a collaborative effort in the United States. The five-year plan for the DIII-D tokamak outlines installation of a radiative divertor in the next two to three years. ◆

References

Allen, S. L., M. E. Rensink, D. N. Hill, R. Wood, D. Nilson, B. G. Logan, R. Stambaugh, T. W. Petrie, G. M. Staebler, M. A. Mahdavi, R. Hulse, and R. B. Campbell (in press), "A Design Study for an Advanced Divertor for DIII-D and ITER: The Radiative Slot Divertor," *J. Nucl. Mater.*

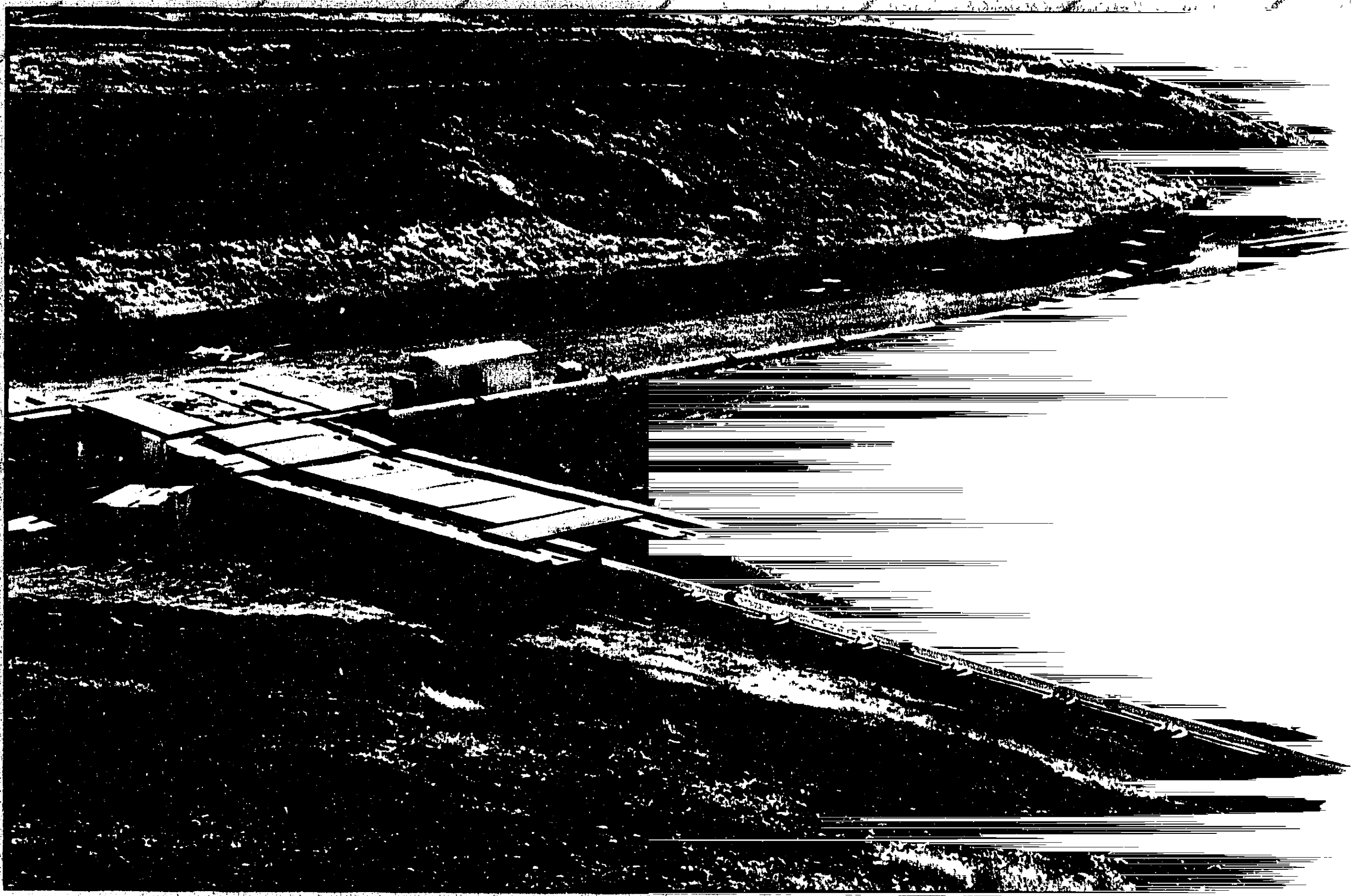

Large-Scale Scientific Systems and Prototypes

Laboratory Directed Research
and Development FY 1992

On the previous page. The SHARP launcher, located at Site 300. When it is located at Vandenberg Air Force Base, the device will be able to launch a 5-kg vehicle to an apogee beyond 400 km. The launch would demonstrate that a projectile can enter space with muzzle velocities above 3 km/s.

SHARP Suborbital Launches

F. Rienecker, J. W. Hunter, L. R. Bertolini, D. W. Hughes, C. H. Jackson, W. N. Massey, P. Heston, D. Hargiss, K. J. Haney, T. R. Metz, S. G. Gemberling, M. R. Hall, C. S. Patel, L. Valle, R. G. Dong, S. R. Trettenero, R. Lopez, L. A. Nattrass, R. F. Perret, and K. B. Pedersen

The Super-High-Altitude Research Project (SHARP) is a large gas gun that is under construction. When completed, SHARP should be capable of launching 1- to 10-kg vehicles at velocities of 3 to 6 km/s. Figure 1 shows the launcher on October 1, 1992.

This project has two milestones. Milestone 1 is to launch a 5-kg plastic projectile at a velocity of 4 km/s. The launch will take place at Site 300, which is located 24 km southeast of LLNL. Milestone 2 is to launch a 5-kg vehicle to an apogee beyond 400 km. This launch will take place at Vandenberg Air Force Base.

The results achieved for SHARP in FY 1992 have been significant. During that time, we obtained the environmental assessment, which took almost two years. We carried out the civil engineering design and construction of the launcher supports and concrete pad, and we installed all major parts of the launcher. We also designed and installed the diagnostics and controls. In addition, we presented five design reviews and started the mechanical safety notes and operating safety procedure.

Potential applications for SHARP include the following.

Launching supplies to low-Earth orbit or lunar orbit. SHARP is the forerunner of a larger-mass delivery system. A successful milestone 2 would demonstrate that projectiles can be sent into space with muzzle velocities above 3 km/s. It would also show the utility of hydrogen as a driving fluid in larger launchers. Using a larger

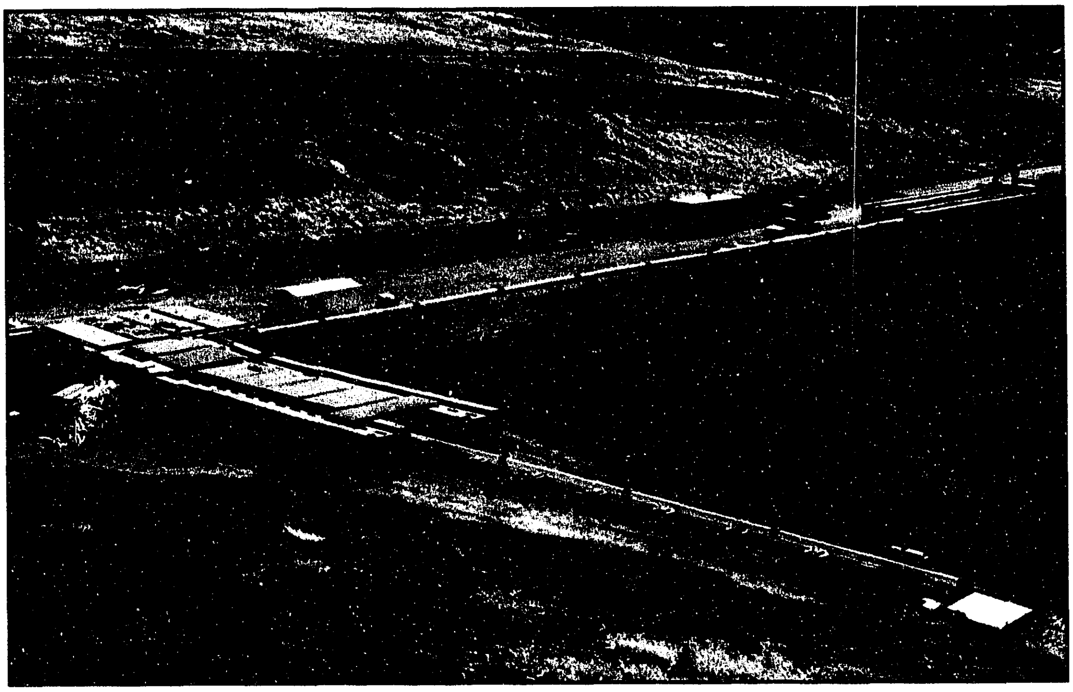

Figure 1. The SHARP launcher at Site 300. One of our milestones is to launch a 5-kg vehicle (from Vandenberg Air Force Base) to an apogee beyond 400 km. The launch would demonstrate that a projectile can enter space with muzzle velocities above 3 km/s.

launcher would greatly reduce the cost of delivering supplies to space. Follow-on launchers could be several kilometers long and deliver 10-ton payloads into space for a fraction of the current delivery cost. Furthermore, they could run in the side-injected mode, which would eliminate the long pump tube. This capability is the kind of breakthrough the United States needs to make space exploration and utilization economical.

Hypersonic testing. Owing to the size of the vehicle that SHARP should be capable of launching, it is expected to attain full National Aerospace Plane Reynolds numbers and Mach numbers simultaneously. No other ground test facility promises this capability. In addition, launching a hypersonic vehicle from SHARP would eliminate the turbulence and partially dissociated oxygen normally seen in shock tunnels. These features would enable SHARP to provide data that were previously unobtainable.

Lethality testbed. SHARP could be used to launch full-scale, armor-penetrating projectiles at armored targets. It could also be used to perform lethality tests on Scud-type warheads. No other launcher will have nearly as great a kinetic energy at velocities above 3 km/s. ◆

Active Acoustic Underwater Surveillance

T. Donich, G. L. Goudreau, J. Jones-Olivera, M. A. Christon, C. S. Landram, C. E. Rosenkilde, S. Govindjee, K. Lewis, and S. W. McAllister

The new submarines are much quieter and do not radiate as much acoustic energy into the water from internal sources as did older models. Thus, the passive technique of using hydrophones to listen for acoustic signatures is no longer useful at long ranges. We have developed an active system known as the Odin transmitter, which is a high-power projector for long-range active acoustic surveillance.

We are also investigating the use of time-domain code to solve the problem of the so-called target strength (acoustic cross section) of submerged structures, such as submarines. Active pulse systems are relatively new, and submarine designs using the older frequency-domain methods are not providing answers that are comparable with experimental data.

Odin: High-Power, Underwater, Acoustic Transmitter

Split-ring projectors (SRPs) are acoustic transmitters used underwater in active sonar systems to detect submarines. In FY 1990, LLNL began using the combustion of chemical fuels to drive an SRP element. When a chemical fuel combusts inside the cylinder, the resulting pressure pulse drives the shell outward, loading strain energy into the split-ring shell. The split-ring shell rings down, converting the strain energy to acoustic energy (Figure 1); this is known as an impulse-driven SRP.

We assessed the feasibility of scaling the impulse-driven SRP to a ship-towed, surveillance system (Figure 2). We hypothesized that impulse-driven SRP technology could create the acoustic power needed for

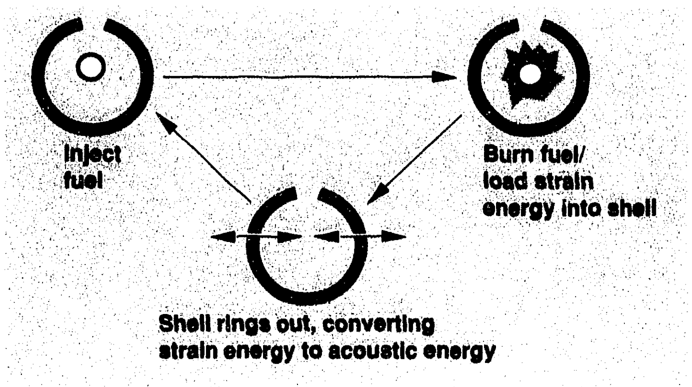

Figure 1. Cycle for a chemical-fuel driven, split-ring projector element.

surveillance in a reasonably sized, hydrodynamic package that could be towed more easily than existing projector arrays. This approach has two advantages. First, direct conversion of chemical energy to strain energy is more efficient than converting chemical energy into electricity and then into strain energy with magnetostrictive or piezoelectric materials. Second, the SRP, which is long and slender, provides a more hydrodynamic shape than other magnetostrictive or piezoelectric projectors.

Our FY 1992 study yielded the following results:

- At 20 Hz, the optimal radius for the SRP is 1 m; at this frequency, the corresponding thickness of the steel shell is 24.4 cm.
- The chemical-to-acoustic energy conversion efficiency is low, about 1.5% for a length of 20 m.
- Acoustic powers of ~363 kW or 226.4 dB (referenced to 1 µPa) at 1 m can be attained with an input of 310 MJ of chemical energy. The peak stress is within the elastic range for high-quality steel.
- The projector acoustic output has the temporal characteristic of $P_0e^{-\alpha t}\sin\omega t$, where P_0 is the peak pressure, α is the decay constant, t is time, and ω is the decay frequency. Our experimentally validated analytical model predicts $\alpha = 0.095$ s^{-1} for this shell radius and projector frequency.

From our engineering assessment, we determined that in an array of large SRPs, the 2σ individual project timing specification must be 0.005 s. It will take approximately 60 s to recycle a projector after it fires, including the time to purge the exhaust and reload the fuel and oxidizer for the next shot.

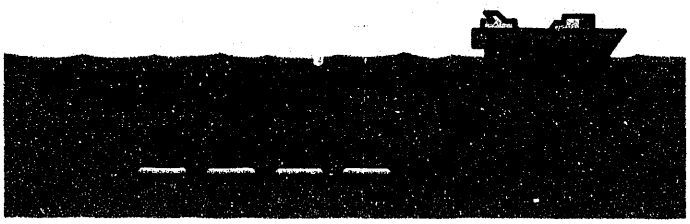

Figure 2. Configuration of the ship-towed Odin projector.

A five-element projector array with a per-element power of 226.4 dB will enable detection ranges in excess of 260 km. We believe the Odin projector is feasible, and we are discussing it with the U.S. Navy.

Underwater Structural Acoustics

Identifying and reducing the acoustic signature of submarines is important to designing "quiet" hulls. We identified the critical structural acoustic phenomena required to simulate submarine target strength and to develop algorithmic solutions.

We addressed two issues in this project: normal modeling discrepancies and their ramifications on the imposition of the kinematics boundary conditions for doubly curved fluid-loaded shells, and the study of frequency proliferation in fluid-loaded shells. To prepare LLNL's time-domain structures codes DYNA3D and NIKE3D for structural acoustics applications, we will develop an explicit fluid module, which is expressed in terms of the scalar fluid pressure rather than fluid displacement. We will validate the code in two dimensions with an analytical solution for an infinite cylinder with internal plate, as well as in three dimensions for spherical scattering. We also will study the acoustic radiation from submerged stiffened panels using an acoustic cell model that examines the multipath energy conversion for a single panel and support unit.

For FY 1992, we began linking the two-dimensional, explicit fluid module into existing NIKE3D code. First, we constructed the proper interface in NIKE3D. Then we validated the combine code PING on structural fluid acoustics problems. This process involved comparing the computed results of PING with well-known, simple analytical shapes, then with more difficult shapes such as structures with internal supporting beams and bulkheads. Although these problems have never been analytically solved before, we were able to derive analytical results for generalized supported plates and for cylinders with internal supports to compare with our code.

We also produced an important three-dimensional analytical solution for fluid-loaded prolate spheroids to validate the three-dimensional version of the code, which will be developed during FY 1993. The next step will be to compare PING code results with experimental data. ◆

Special-Purpose Munitions

B. R. Bowman, S. J. DeTeresa, S. E. Groves, S. W. Kang, H. E. Lorenzana, and A. K. McMahan

Special-purpose munitions are needed to meet the requirement of the special forces to be equipped with weapons that are light, portable by humans, and effective in covert operations. Each of the projects described here can contribute significantly to meeting that requirement.

Portable Composite Launch Tube

Our goal was to develop lightweight, fiber-composite munitions for special forces operations. An advantage of fiber-composite materials is that the strength of structures can be tailored in different directions via fiber orientation. By controlling this anisotropy, we achieved circumferential strength exceeding that of structural metals in a first-generation, cylindrical launch tube (Figure 1).

The composite component of the portable launcher weighs 3 kg and is designed to withstand an internal launch pressure of 550 MPa. This prototype will be used to launch composite projectiles and as part of a test for barrel integrity. The launch tube was manufactured with an open breech end and fitted with a wedge attachment to allow rear access to the propellant charge.

We fabricated several composite projectiles using a wet-filament winding process and materials and fiber architecture that yield structural compressive strengths of about 700 MPa. Firing tests from gas guns into foundry stone at 900 m/s were marginally successful. The projectiles survived the compressive loads but were damaged by offaxis impact. The angle of impact was skewed from 90 deg because of the projectile's asymmetric mass balance and problems with sabot attachments. We have designed new sabots and projectile profiles and will test them using the composite launcher in FY 1993.

Basic material studies show how matrix properties, especially yield strength, improve the composite compressive strength. We achieved compressive strengths greater than 2000 MPa with relatively low-cost materials. We will focus on translating these strength levels to structures in FY 1993.

Preliminary work with fiber combinations or hybrids indicates that a mixture of boron fibers and carbon fibers yields a composite with 1500 MPa compressive strength. We will investigate further optimization of both cost and performance in FY 1993

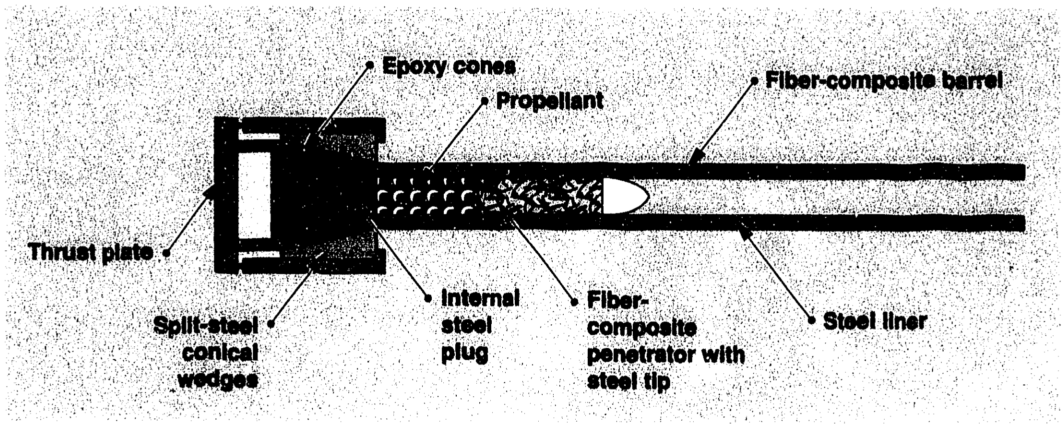

Figure 1. Fiber composites provide improved design capabilities for advanced penetrating warhead and gun launch systems.

using both inexpensive glass fiber with boron fiber for axial compressive strength and carbon fiber for circumferential tensile strength in cylindrical structures.

Miniature Recoilless Rifle

We designed a lightweight, projectile-launching system that can destroy a field bunker or equivalent target but can be carried by an individual. A typical field bunker has a 1-m-thick layer of sandbags in front of a 0.3-m-thick layer of reinforced concrete. This is a difficult target to destroy unless heavy armor is present for support. Our system uses LLNL-developed technology to provide a lightweight device, known as a miniature recoilless rifle, that is capable of destroying this target.

The recoilless rifle comprises a projectile, carbon-fiber-composite barrel, and high-carbon steel nozzle (Figure 2). The projectile uses a cermet nose cone and a fiber-composite body that contains a small, high-explosive charge and fusing system. A steel-nosed version of the projectile has been tested and survived impact velocities of 45 m/s into foundry stone, which has the consistency of limestone. A larger closed-breech version of the barrel (150 mm in diameter) has been tested to breech pressures exceeding 200 MPa, while launching a 45-kg projectile at 250 m/s.

We calculated the penetration capability of the projectile using a computer model based on Young's (1988) equations. Our computer model allows us to analyze penetration into as many as 20 layers of soil, concrete, ice and frozen soil, or rock over a full range of parameters (penetrator weight, diameter, nose configuration, impact velocity, and impact angle relative to the horizontal). Incorporating the field bunker target and a 1.1-kg projectile into this code, we determined that an impact velocity of 425 m/s is required to breech the concrete wall. We used this information to establish pressure requirements in the propellant section of the rifle barrel and to design the nozzle.

The propellant charge (M-6) and nozzle design will propel the projectile at 500 m/s (allowing a margin of error), which should easily penetrate and defeat the target. We are studying a nozzle design and propellant load that will propel the projectile at 670 m/s. The total weight of the system shown in Figure 2 is about 3.4 kg. The projectile carries an high-explosive payload weighing about 0.11 kg.

We are fabricating the barrel from carbon fibers supported in a phenolic resin. The wall thickness is about 8 mm, and the barrel can withstand 50,330 MPa of internal pressure. We selected carbon steel for the nozzle and will also incorporate it into the barrel winding.

We will test the system and analyze the results in FY 1993. Assuming a successful test, two questions then remain: Will the high explosive be initiated upon impact at these velocities? Can we design a fuse system that will survive both acceleration and impact?

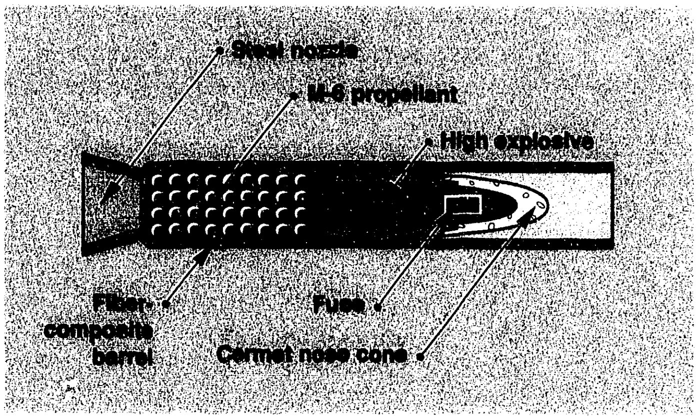

Figure 2. Design of the miniature recoilless rifle. This rifle is short and lightweight and can be carried by one person in a covert action.

Feasibility of a Shaped-Charge Projectile Launcher

We studied the feasibility of launching a 0.5-kg projectile at a velocity greater than 4 km/s using a shaped-charge jet. The launch system consists of a shaped-charge jet, a cermet, and a projectile. A cermet was selected because it is resistant to penetration by projectiles.

We proposed to direct a shaped-charge jet to the rear surface of a tube containing a cermet and projectile (Figure 3). The impinging jet imparts sufficient momentum to the cermet, causing dilatation in the cermet. The resulting axial expansion propels the projectile at high velocities. We included a tamper to accommodate the dilatation of the cermet when impacted by the jet.

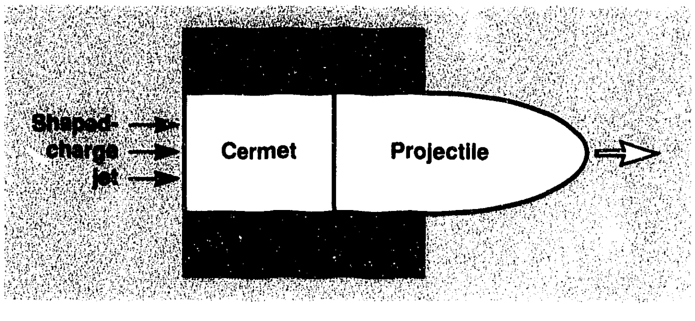

Figure 3. Conceptual design of the shaped-charge launcher.

We performed scoping calculations using the momentum and energy equations to determine the viability of such an approach. We first studied the system without the cermet, i.e., pointing a shaped-charge jet at the rear of the projectile and capturing the momentum to propel the projectile forward. We assumed that the jet would not penetrate the projectile and determined that the jet could accelerate a 0.5-kg projectile to a velocity of 4 km/s.

Our assumption that the jet would not penetrate the projectile is uncertain. We inserted a cermet between the jet and the projectile on the premise that the axial expansion of the cermet will capture the jet momentum and propel the projectile at high velocities. Unfortunately, the equation of state and strength models for ceramics and cermets are not well developed, so good computational models are unavailable. However, using models developed for cermet materials, we performed preliminary calculations using the CALE computer code to examine the physical behavior of the cermet when impacted by a jet.

Our numerical results show that, given the physical models of the launch system's materials (a steel tube, cermet, and steel projectile), it is theoretically possible to accelerate a 0.65-kg projectile to a velocity of 4 km/s by impinging on the cermet with a shaped-charge jet at 6 km/s. We note that these theoretical results depend on the material response of the cermet.

Having determined that a shaped-charge jet can in principle push a projectile to a high velocity, we analyzed the jet material and a configuration that will impart as much momentum and kinetic energy as possible to the projectile. The shaped-charge design forms a slowly stretching jet that has a short, thick cross section and contains most of the liner material moving forward. We selected copper for the liner material because it is well understood and readily available; however, a particulating material like a ceramic or cermet may be more appropriate. We will increase the jet's speed by varying the liner thickness and the contour of the high explosive. The charge will be single-point initiated from the rear and placed at a standoff from the receiver that corresponds to the distance where the jet has developed its full momentum and kinetic energy.

We will conduct a proof-of-concept experiment to verify the theoretical assertion of the feasibility of the proposed concept. Our tests will yield useful information on the physical behavior of the cermet under great stresses. Because there is uncertainty in the cermet model, this experiment, even if it fails, will provide valuable information that will help improve the concept. These tests will also provide information on manageable acceleration of the projectile during launch and on guidance and control of the projectile.

High-Energy-Density Materials

Theoretical calculations by Mailhiot et al. (1992) suggest that a phosphorus-like or polymeric form of nitrogen may exist metastably at atmospheric pressure as a hard insulating solid with an energy density per unit volume three to four times greater than HMX (octahydro-1,3,5,7-tetranitro-1,3,5,7-tetrazocine). Such a substance could be used as a high-energy-density material in portable infantry munitions, allowing a significant reduction in weight and size without losing its effectiveness.

Mailhiot et al. (1992) predicted that the polymeric phase of nitrogen would be stable at high pressures, so we could use a high-pressure diamond anvil cell (DAC) for proof-of-existence experiments. We synthesized the polymeric phase of nitrogen using technology available at LLNL. Experiments comparing signatures (e.g., optical, x-ray) to theoretical predictions will help us understand and identify observed high-pressure phases.

Comparing theory to experiment should improve our predictions as well as our understanding of the physical mechanisms that produce the polymeric phase of nitrogen. We believe that high pressure is the most important factor of this endeavor, so we are preparing to pressurize nitrogen samples to above 2 Mbar with the DAC. We expect the transition to be sluggish (for the same reasons that make this new compound stable at ambient conditions); therefore, pressure alone may not be adequate to induce the transformation fully. Consequently, we also plan to "jolt" our samples using in situ laser heating to more than 4000 K at megabar pressures.

We developed new facilities to supplement the existing experimental infrastructure and have purchased diamonds specially optimized for ultrahigh pressures. We are preparing to conduct room-temperature, multi-megabar experiments in FY 1993. We will also manufacture custom DAC bodies and an optical cryostat to provide helium-temperature capabilities because we expect that low temperatures will be instrumental in stabilizing metastable new phases. ◆

References

Mailhiot, C., L. H. Yang, and A. K. McMahan (1992), "Polymeric Nitrogen," *Phys. Rev. B* **46**, 14419.

Young, C. W. (1988), *Equations for Predicting Earth Penetration by Projectiles: An Update*, Sandia National Laboratories, Albuquerque, NM, SAND88-0013.

Advanced Strategic Strike System: Development of Warhead Concept

R. D. Streit, N. J. Colella, P. A. Hurst, T. Slavik, K. Peterman, and S. Chidester

The Advanced Strategic Strike System, AS^3, is a cost-effective, near-term approach for developing nonnuclear ballistic missiles. AS^3 will deliver the kinetic energy from a ballistic missile system, via projectiles dispersed from the reentry body, to a target with a minimum of undesired damage. Low excess damage is achieved by a well-defined dispersal pattern and essentially "pinpoint" accuracy. For FY 1992, we focused on designing the warhead concept and a hypersonic grenade and on developing a dispersal system for the kinetic-energy projectiles (KEPs) using high explosives (HEs). We chose this approach because it is consistent with a low-cost, near-term operable system and is compatible with existing system hardware. We designed a hypersonic grenade, and hydrodynamic testing of the dispersal mechanism was successful.

The warhead package forms the structural member of the reentry system. KEPs are dispersed from the reentry vehicle using a tailored HE charge. The KEP velocity is generated from the reentry vehicle, with a radial dispersal scheme required for the area distribution of projectiles. Design of the KEP package, explosive thickness, amount of tamping, and free expansion are blended to obtain the desired KEP mass and velocity profile. Because the large projectile size and low radial velocity are significantly different from those required in a typical warhead design, an existing database was not available. An analysis and supporting test program was essential to establishing the feasibility of our concept.

We completed three key tests during FY 1992. In the first test, we evaluated the ability to disperse KEPs at a prescribed velocity and with a minimum of mass loss. We confirmed the analytical predictions for KEP separation and velocity and demonstrated that mass loss from HE detonation jetting can be kept to less than 5%.

In the follow-up test, the scope was expanded to produce a predictable particle geometry and generate the particles over a range of velocities required for radial dispersal. The KEP package was designed using the computer code CALE to obtain details of the HE behavior, jetting, particle trajectory, and tamping required (Figure 1). We confirmed the predicted dispersal pattern and velocity profile from 100 to 400 m/s in the experiment and reconfirmed the low loss of mass demonstrated in the first hydrodynamic test.

The third test investigated the ability of the KEP to penetrate the reentry-vehicle structure at low velocities using LLNL's gas-gun facility. The test series verified that the velocity loss and reentry-vehicle penetration behavior were within the predicted response envelope.

Together, the three tests provide a strong technical foundation for subsequent development of the warhead concept. ◆

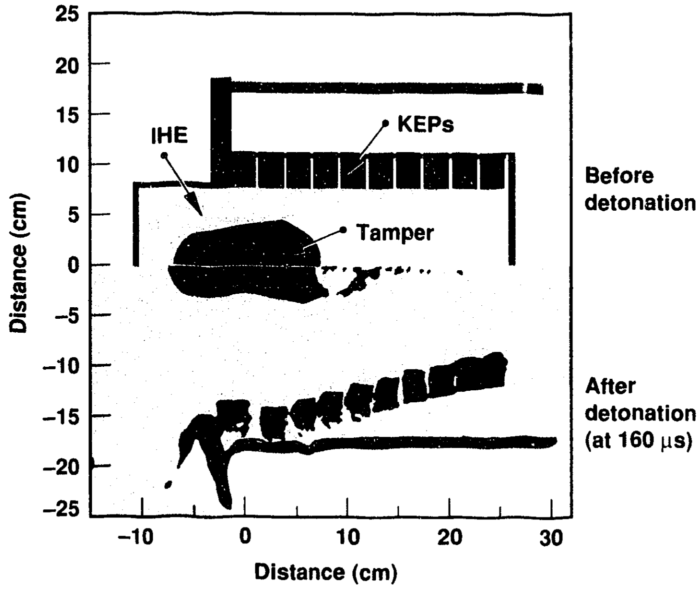

Figure 1. Before and after detonation, showing device configuration, high explosive, and tamping. After detonation, the KEPs develop a linear-velocity profile with the velocity being greatest at the tamped, thick, high-explosive end and decreasing toward the open end.

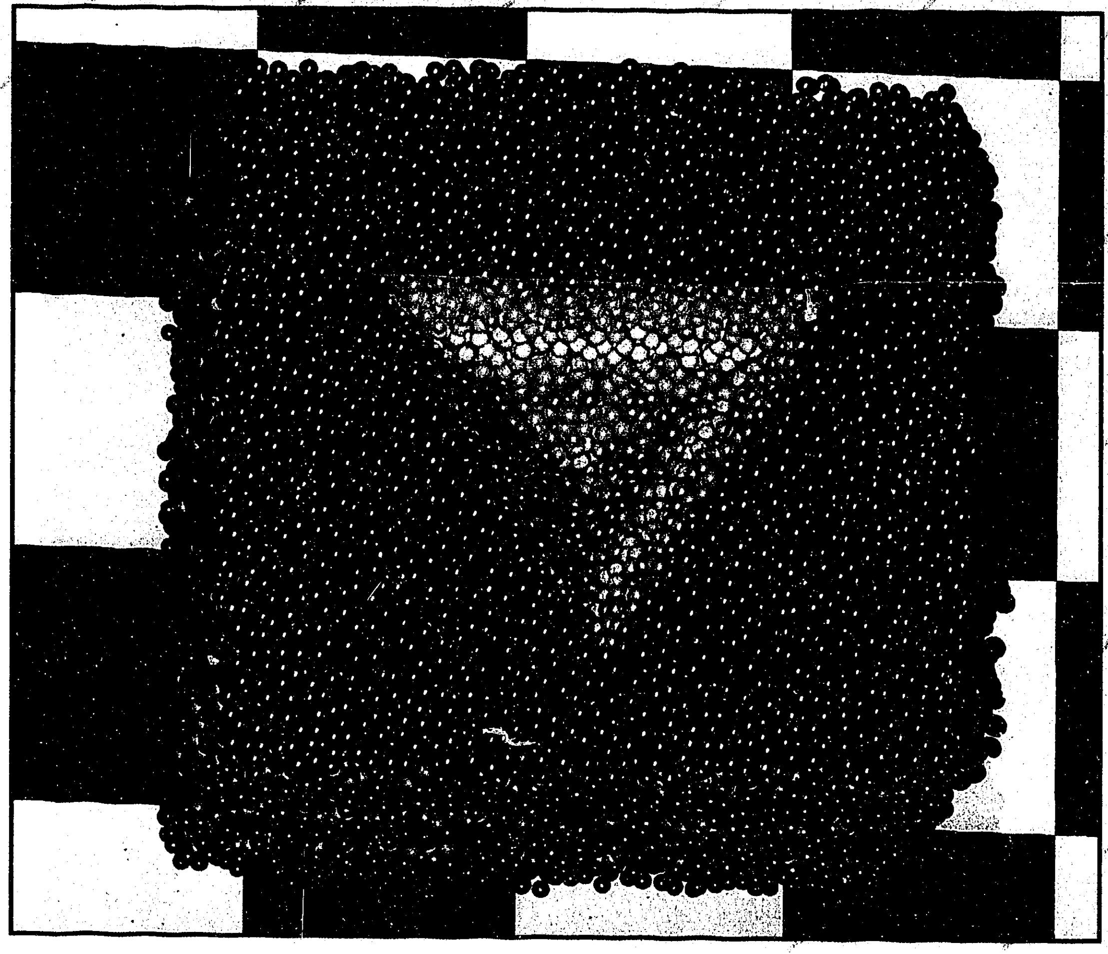

Advanced Materials and Manufacturing Technology

Laboratory Directed Research
and Development FY 1992

On the previous page. Numerical simulation of the indentation of 300,000 silicon atoms with a diamond indentor. Using a simulated, x-ray and electron diffraction technique that follows structural change, we observed the transformation of a crystalline form of silicon to the amorphous phase, under high-pressure indentation.

Molecular Aerogels

R. W. Pekala, M. S. Gebert, and C. T. Alviso

Aerogels are a special class of open-cell foams. These materials have an ultrafine cell and pore size (<50 nm), high surface area (400 to 1100 m^2/g), and a solid matrix composed of interconnected colloidal-like particles or fibrous chains with characteristic diameters of 10 nm.

The most common aerogels are inorganic, usually derived from the sol-gel polymerization of metal alkoxides, followed by supercritical drying. The first organic-based aerogels were synthesized from the aqueous polycondensation of resorcinol (1,3 dihydroxybenzene) with formaldehyde. These low-density materials have structure and properties similar to silica aerogels. A major disadvantage of resorcinol-formaldehyde (RF) aerogels, however, was their dark red color, which resulted from oxidation products formed during the sol-gel polymerization. This color is disadvantageous in applications where transparent insulation is necessary. In our project, we formed colorless, organic aerogels based on the polycondensation of melamine (2,4,6-triamino-s-triazine) with formaldehyde.

We developed two synthetic approaches to prepare melamine-formaldehyde (MF) aerogels: the monomer and oligomer approaches. In the monomer approach, we mix melamine and formaldehyde under alkaline conditions at 70°C to form a homogeneous solution. We then acidify the solution (pH = 1.7), pour it into glass vials, and cure it at 95°C. In the oligomer approach, we dissolve a low-molecular-weight MF polymer (Resimene 714; Monsanto Chemical Co.) in water and acidify it with hydrochloric acid (pH = 1.5 to 3). We then pour this solution into glass molds and cure it at 95°C. After gelation, we slowly replace the water in the pores of the cross-linked gels with acetone and supercritically dry the gels from carbon dioxide at 40°C and 10 MPa to obtain aerogels. In FY 1992, we showed that the MF polymerization can be performed in nonaqueous solvents such as dimethylacetamide and dimethylformamide. The resultant gels can be placed directly in the supercritical extractors, thus eliminating the solvent-exchange step.

The growth and aggregation of clusters formed during a sol-gel polymerization determine the underlying structure of an aerogel. To better understand the growth processes leading to gelation, we used a viscosity-sensitive probe to monitor the local viscosity during the polymerization. In a cross-linked gel, the local viscosity can be significantly less than the bulk viscosity if the probe is small enough to reside in the pores. In our experiments, we dissolved dicyanovinyl jujulodine (DCVJ) in the starting solution and excited

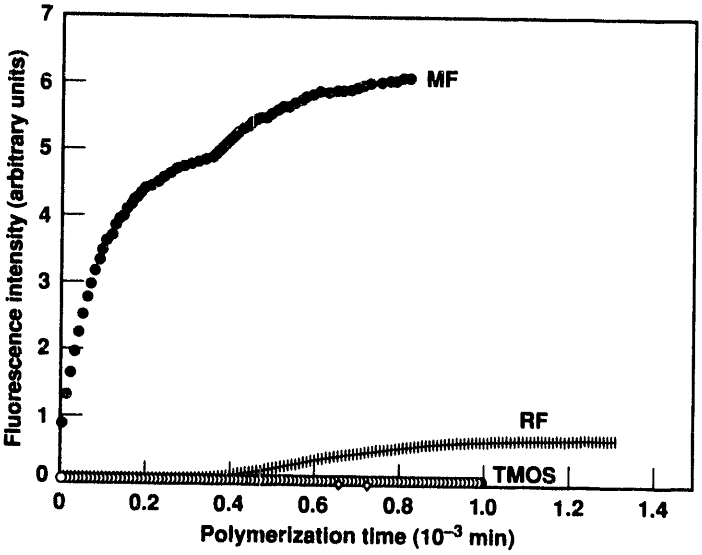

Figure 1. Fluorescence intensity as a function of polymerization time for melamine-formaldehyde (MF), resorcinol-formaldehyde (RF), and base-catalyzed tetramethoxysilane (TMOS) aerogels. Concentrations equal 15% MF, 10% RF, and 10% TMOS. We used dicyanovinyl jujulodine as the probe molecule.

it at a wavelength of 450 nm. DCVJ requires a rotational volume of approximately 0.1 nm^3 to dissipate its energy; otherwise, it returns to its ground state via fluorescence at 500 nm. Figure 1 shows the fluorescence intensity as a function of polymerization time for the MF polymerization and compares it with RF and silica (TMOS). The much higher fluorescence intensity indicates that more linear polymer forms in MF than in RF or TMOS. As such, the resultant MF aerogel would be expected to be more "polymeric" than its RF or silica counterparts. In fact, the polymeric nanostructure manifests itself in the form of higher surface area and better mechanical properties for MF aerogels than colloidal RF or silica aerogels.

We produced MF aerogels with densities from 0.1 to 0.8 g/cm^3 and surface areas of 880 to 1020 m^2/g. Gas adsorption analysis shows that two pore-size regimes can be differentiated in MF aerogels: micropores with diameters less than 2 nm, which reside within the individual MF fibers, and mesopores (2 to 50 nm), which span the distance between the interconnected fibers. The ultrafine cell and pore size of MF aerogels is responsible for their optical clarity and low thermal conductivity (~0.015 W/m · K). MF aerogels are better thermal insulators than silica aerogels, and their thermal conductivity is almost identical to RF aerogels, with the additional advantage of being colorless rather than dark red. Potential applications for this new type of organic material include inertial confinement fusion targets, transparent window insulation, acoustic impedance matching devices, and chemical sensors. ◆

Nanoscale, Magnetic, Ultrathin Films and Surfaces

J. G. Tobin, G. D. Waddill, D. P. Pappas,* P. A. Sterne, and S. Y. Tong†

The availability of circularly polarized light from synchrotron sources allows us to study ferromagnets using x-ray absorption and core-level photoemission. These studies rely on the helicity dependence of the interaction of the x rays with the magnetic material. The absorption experiments are the x-ray counterparts of the magnetooptic Kerr effect. The photoabsorption cross section at the L edges of ferromagnets depends on the relative orientation of the photon spin and sample magnetization, and the results can be interpreted in terms of the spin-split density of states above the Fermi level (E_F). We can describe dichroism observed in core-level photoemission studies by spin-selective dipole transitions in the presence of spin-orbit coupling. The surface sensitivity and elemental specificity of these studies make them particularly useful for investigating surface and thin-film magnetism.

In FY 1991, we demonstrated perpendicular magnetic dichroism in x-ray absorption measurements at the $L_{2,3}$ edge of iron films on a Cu(001) substrate. In FY 1992, we present results for Fe 2p and 3p core-level photoemission for the same Fe/Cu(001) system, in which the Fe p electrons are excited to free-electron states far above E_F. We compare our results with analogous studies of bulk iron, concentrating on differences in the two systems and how those differences can help us understand surface magnetism.

We used circularly polarized x rays with core-level photoemission to probe the magnetic structure of ultrathin films of Fe/Cu(001). Figures 1 and 2 show examples of photoemission magnetic circular dichroism. The Fe 2p states are split by a spin-orbit interaction into $2p^{3/2}$ and $2p^{1/2}$ peaks. An additional splitting, a type of exchange splitting, shifts the $2p^{3/2}$ and $2p^{1/2}$ positions. The shift is affected by the circular polarization (helicity) and magnetization directions. The spin-orbit splitting of the Fe 3p states is small, so we see an overall shift of the single peak caused by another exchange

---

*Naval Research Laboratory, Washington, DC.

†University of Wisconsin, Milwaukee.

splitting. Circularly polarized x rays allow us to probe the spin-dependent electronic and geometric structure in an elementally specific fashion, thus permitting us to probe nanoscale (10^{-9} nm) magnetic effects. We consistently observe smaller splittings than are observed in bulk iron.

Our results demonstrate magnetic x-ray dichroism in core-level photoemission from monolayer films. We observed the effect by exciting spin-dependent transitions with circularly polarized light, thus showing the underlying splitting of core levels through an exchange interaction of the d electrons. We observed systematic differences between monolayer iron films and bulk iron samples that can help us understand the mechanisms of surface and thin-film magnetism. ◆

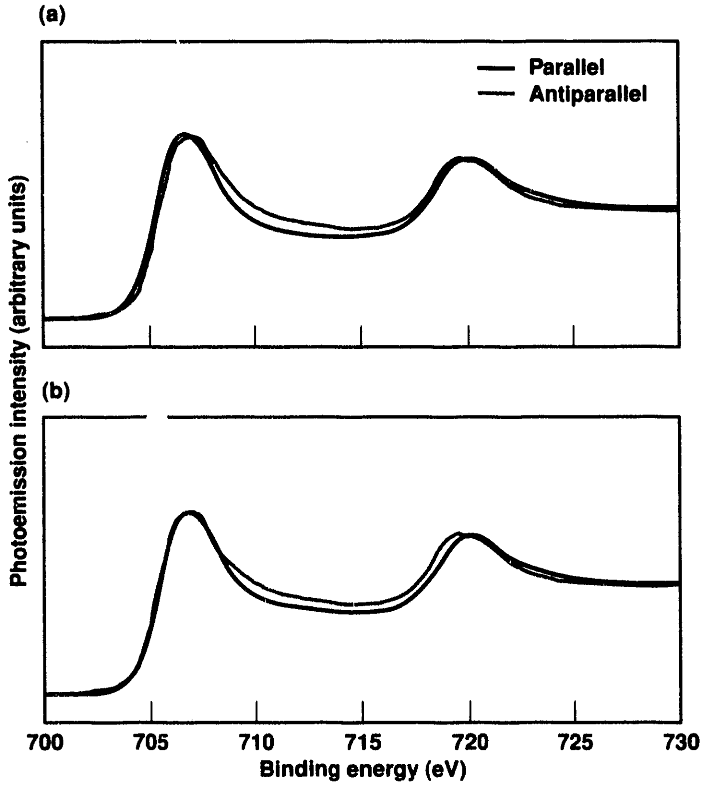

Figure 1. Fe 2p spectra for Fe on Cu(001) taken with $h\nu$ = 900 eV and positive photon helicity. Black lines show a parallel orientation of photon spin and sample magnetization; green lines show an antiparallel orientation. We achieved the two orientations by fixing the photon helicity and reversing the magnetization of the sample. (a) The spectra show the differences in binding energy for the $2p^{3/2}$ and $2p^{1/2}$ levels for the two helicity and magnetization orientations.
(b) The spectra have been shifted to align the leading edge of the $2p^{3/2}$ energy level to emphasize line-shape differences between the two orientation extremes.

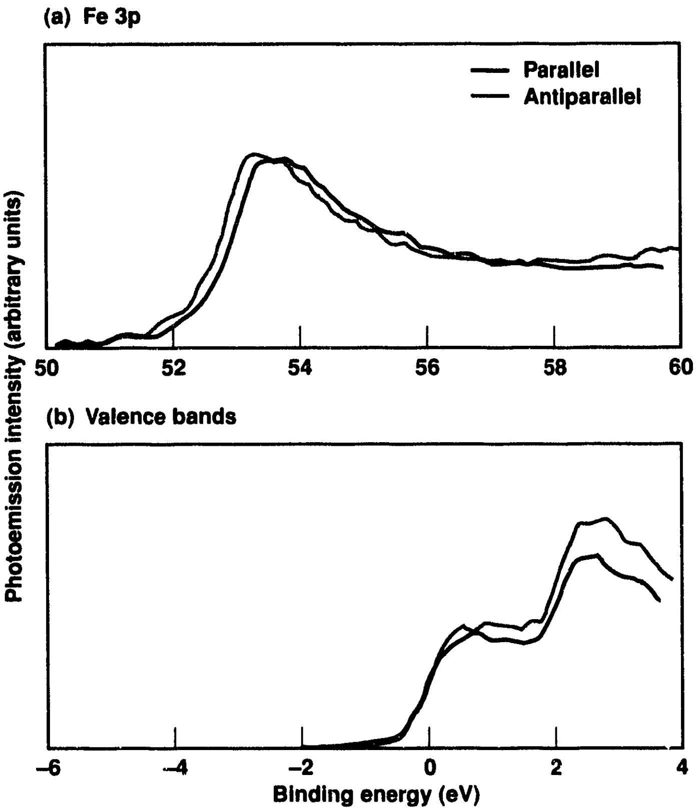

Figure 2. Fe 3p spectra for Fe on Cu(001) taken with $h\nu$ = 150 eV. Black lines show parallel orientation; green lines show antiparallel orientation. (a) Core spectra. (b) Valence bands and Fermi edge (binding energy of zero) used for energy-scale calibration.

Structural Transformation and Precursor Phenomena in Advanced Materials

P. E. A. Turchi, L. T. Reinhard, and S. C. Moss*

The study of the formation and stability of complex crystalline structures, especially those based on tetrahedrally close-packed lattices, is of crucial importance for both the technological and theoretical fields of condensed matter physics. To modify, optimize, and control the formation of these phases, we are using experimental and theoretical tools to probe their nucleation and growth processes at very early stages. In particular, we are studying, at the atomic level, precursor phenomena (namely, local chemical order and static atomic displacement fields) and transient structures that may act as seeds for structural transformation. These studies are both theoretical, with an emphasis on applications of modern electronic structure theory of phase stability, and experimental, in which scattering and surface techniques are applied to body-centered cubic (bcc) Fe–Cr alloys that undergo transformation to a complex sigma phase upon cooling.

Theoretical Studies

We have examined ordering tendencies in Fe-Cr and Fe-V bcc-based alloys using a recently developed ab initio methodology (Turchi and Sluiter, 1992; Turchi et al., 1992a, b). Around equicomposition, Fe–Cr showed a tendency toward phase separation, whereas Fe–V exhibited a tendency toward a CsCl type of order (Turchi et al., 1991). Further analysis showed that although Fe–Cr ultimately phase-separates, a metastable phase may exist at low temperature. This alloy is a prototypical case in which competition occurs between alloying effect (in favor of phase separation) and local chemical order (Turchi et al., in press).

We extended this work to a series of equiatomic bcc-based alloys, including Fe–Ti, Ti–Cr, Ti–V, Ti–Mn, and V–Cr. Our conclusions are that (1) the strength and the nature of the chemical order are controlled by the average number of valence electrons and the difference in the numbers of valence electrons of the alloy species, and (2) transformation to a complex phase may be associated with weak ordering tendencies (Turchi and Sluiter, 1992; Turchi et al., 1992b). This study clarifies, at an atomic level, the possible role of ternary additions in the stabilization of complex phases or ordered superstructures—a phenomenon that may not be observed in binary combinations.

Monte Carlo simulations based on a kinetic Ising model reproduce the general features of the structure function $S(\mathbf{k},t)$ for Fe–Cr, defined as the Fourier transform of the time-dependent pair correlation function (this quantity provides useful information on the time dependence of the local chemical environment in the alloy). But the simulations fail to explain the experimental effect on the kinetics of decomposition as a function of thermal history. This type of simulation, together with the energetic quantities obtained from first-principles electronic structure calculations, shows that, for a Ti–V alloy prepared in the high-temperature disordered configuration and quenched below the temperature of the spinodal decomposition, an ordered B32 phase, slightly unstable with respect to clustering, spontaneously forms before evolving toward phase separation. Experimental evidence would be highly desirable.

Experimental Studies

We selected Fe–Cr because it is a prototype of many commercially interesting alloys. Fe–Cr exhibits a bcc-solid solution above 1094 K near equicomposition, and

---

*University of Houston, TX.

it transforms into a sigma phase upon cooling. We obtained single crystals with a high-temperature crystalline structure (about 47 at.% chromium).

X-ray-scattering experiments on an $Fe_{0.53}Cr_{0.47}$ single crystal were performed with J. L. Robertson of Oak Ridge National Laboratory (Reinhard et al., 1992a, b). We investigated inelastic phonon scattering as well as diffuse elastic scattering close to the Bragg reflections (Huang scattering). The results of the phonon dispersion measurements have been fully analyzed (Robertson et al., in press). The observed softening at 2/3⟨111⟩, accompanied by a broadening of the phonon linewidths, is a generic signature of the typical omega phase transformation. No indication exists, a priori, that this alloy exhibits a transformation to a complex sigma phase.

We used the pair-interaction energy parameters deduced from the diffuse x-ray scattering experiments to compute the Fe–Cr phase diagram. The calculated miscibility gap is in excellent agreement with the assessed one. These results lead to interesting comparisons with first-principles electronic structure studies in this system.

In the area of surface physics, we performed a low-energy electron diffraction (LEED) investigation of the possible surface-induced, bcc-to-sigma transformation in oriented Fe–Cr single crystals along ⟨110⟩ and ⟨111⟩. This investigation was performed in collaboration with J. E. Houston of Sandia National Laboratories, New Mexico. Preliminary results show (1) no surface segregation, (2) a ⟨110⟩ reconstructed surface, and (3) kinetics of the sigma-phase formation that is significantly slowed on a clean single crystalline surface in ultrahigh vacuum. This study initiated a more quantitative investigation based on x-ray grazing incidence diffraction at the National Synchrotron Light Source at Brookhaven National Laboratory (with K. S. Liang of Exxon), and the results are still being reviewed.

We are also studying the role played by atomic orbital directionality in the stability of complex phases and the effect of ternary addition on the stability of complex phases. Codes are being developed to study, at an atomic level, structural transformations with a combination of electronic-structure calculations and molecular-dynamics simulations. We are addressing fundamental questions on (1) surface reconstruction and segregation in the bcc phase prior to the bcc-to-sigma transformation, (2) orientation relationships between bcc and sigma near the surface, and (3) the kinetics of transformation near the surface. This program will provide new insights into the formation and stability of complex phases by an effort combining atomistic characterization of the early stage of transformation with modeling by state-of-the-art approaches. ◆

References

Reinhard, L., J. L. Robertson, S. C. Moss, G. E. Ice, P. Zschack, and C. J. Sparks (1992a), "Anomalous X-Ray Scattering Study of Local Order in bcc $Fe_{0.53}Cr_{0.47}$," *Phys. Rev. B* **45**, 2662–2676.

Reinhard, L., J. L. Robertson, S. C. Moss, G. E. Ice, P. Zschack and C. J. Sparks (1992b), "Anomalous X-Ray Scattering Study of Local Order in bcc $Fe_{0.53}Cr_{0.47}$," *Proc. TMS Symp. on Kinetics of Ordering Transformations in Metals*, H. Chen and V. K. Vasudevan, Eds. (TMS Publications, Warrendale, PA), pp. 37–52.

Robertson, J. L., D. A. Neumann, S. C. Moss, and L. Reinhard (in press), "Inelastic Neutron Scattering Study of Phonon Dispersion in FeCr near the σ-Phase Transformation," *Acta Metall.*

Turchi, P. E. A., and M. Sluiter (1992), "Real-Space Multiple Scattering Description of Phase Stability in Alloys," *Mater. Res. Soc. Symp. Proc.* **253**, 227–242.

Turchi, P. E. A., L. Reinhard, M. Sluiter, and G. M. Stocks (in press), "First-Principles Study of Local Order in bcc-Based FeV and FeCr Alloys," *Phys. Rev. B.*

Turchi, P. E. A., M. Sluiter, F. J. Pinski, D. D. Johnson, D. M. Nicholson, G. M. Stocks, and J. B. Staunton (1992a), "First-Principles Study of Phase Stability in Cu–Zn Substitutional Alloys," *Phys. Rev. Lett.* **67**, 1779–1782 (1991); Erratum, *Phys. Rev. Lett.* **68**, 418.

Turchi, P. E. A., M. Sluiter, and G. M. Stocks (1992b), "First-Principles Prediction of Alloy Phase Stability," *J. Phase Equilibria* **13**, 391–399.

Turchi, P. E. A., M. Sluiter, and G. M. Stocks (1991), "A Comparative Study of Short Range Order in Fe–Cr and Fe–V Alloys around Equiatomic Composition," *Mater. Res. Soc. Symp. Proc.* **213**, 75–80.

The Absence of Circular Dichroism in High-Temperature Superconductors

T. W. Lawrence, A. Szöke, and R. B. Laughlin

Superconductivity, the loss of all electrical resistance in a material, is known to occur in certain metals at temperatures below 10 to 15 K. Two recipients of the 1987 Nobel Prize in Physics, J. G. Bednorz and K. A. Müller, discovered that superconductivity also occurs in certain ceramic materials at much higher temperatures and coined the term "high-temperature superconductivity." The mechanisms behind the high-temperature superconducting transition have yet to be convincingly explained.

The anyon theory, which describes the pairing of electrons by gauge forces analogous to those known to occur in the fractional quantum Hall effect, is a leading candidate for explaining high-temperature superconductivity (Laughlin, 1988). If the anyon theory is correct, high-temperature superconductors should microscopically violate parity and time-reversal symmetries, much as a ferromagnet does. Circular dichroism, which is the differential absorption of right-vs-left circularly polarized light, is one signature of parity and time-reversal violation. A group at AT&T Bell Laboratories observed a temperature-dependent circular dichroism in these materials; the magnitude of the effect was only about 10 times smaller than that observed with a saturated iron magnet. If the interpretation of their data was correct, the AT&T group's observation would strongly support the anyon theory (Lyons et al., 1990). However, as originally reported, their measurements included a spurious cross-term (which they claimed should be very small) that does not indicate time-reversal violation (Levi, 1991).

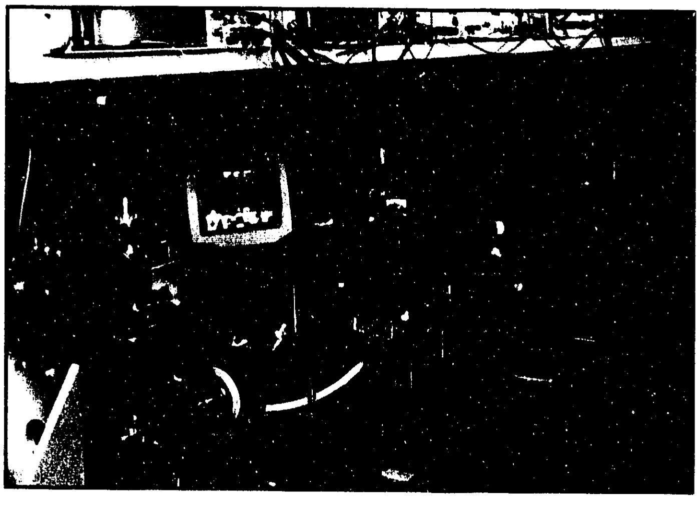

Figure 1. Experimental setup of the circular-dichroism experiment showing all major components. The main elements are described in the text.

Our goal was to improve upon the AT&T measurements, reproduce the circular-dichroism data, and investigate the spurious cross-term. We found a simple way of discriminating against the cross-term (after discovering the source of it in our apparatus) and then found no indication of a temperature-dependent circular dichroism in any sample we studied. Although our results certainly do not support an anyon hypothesis, they do not refute it either. The theoretical prediction is for *microscopic* symmetry violation, whereas our apparatus measures *macroscopic* quantities. However, any theory based on a microscopic anyon mechanism must predict that the symmetry violation is suppressed in a macroscopic system.

In our experiment, we reflected light from a high-temperature superconductor (in this case, $YBa_2Cu_3O_7$ [YBCO]) and observed changes in its polarization state, particularly circular dichroism. However, measuring circular dichroism with standard detection techniques is difficult. Ordinary stress birefringence overwhelms the detector, producing a signal 100 to 1000 times larger than the circular dichroism we hoped to measure. Thus, our apparatus had to be capable of discriminating between true signals and spurious ones, and we had to

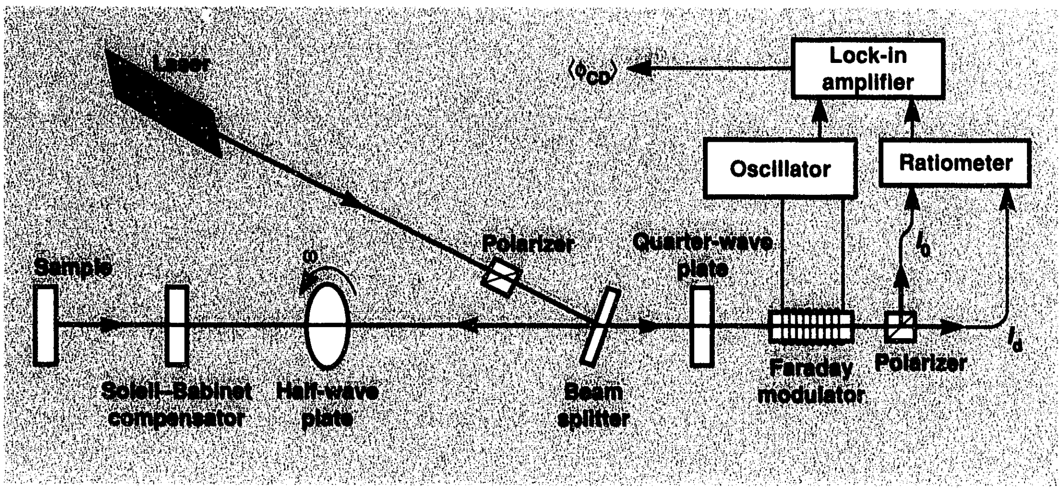

Figure 2. Layout of the circular-dichroism experiment.

measure the polarization amplitudes and phases absolutely to an accuracy of 10^{-5} (10 μrad). Also, we had to carefully determine the nature of, and then eliminate, the cross-term in the original AT&T data.

Our apparatus (Figures 1, 2) successfully accomplished these goals. The setup consisted of a single-mode, single-frequency, diode-pumped, doubled Nd:YAG laser (λ = 532 nm); a flowing liquid-helium cryostat with a high-quality, low-stress vacuum window; a rotating half-wave plate; a stationary quarter-wave plate (to make our apparatus sensitive to ellipticities); and a polarization amplitude detector that combines a Faraday modulator with crossed polarizers and two intensity detectors fed to a ratiometer and then a lock-in detector. In addition, we used a Soleil–Babinet compensator to minimize the overall linear birefringence of the beam train.

The half-wave plate rotates the plane of linearly polarized light delivered to the sample. In principle, the linear birefringence errors change sign when the half-wave plate is rotated 90 deg, whereas circular dichroism is independent of angle. Thus, the rotation averages out the residual linear birefringence errors coming from the sample, cryostat window, and optics. However, this averaging is not perfect, and an additional cross-term from ellipticity is induced when linear birefringence lies along a different axis than linear dichroism. By adding a second intensity detector to the system and performing an analog divide, we effectively averaged out this spurious cross-term as well. Figure 3 shows the experimental test results of this ratio technique and demonstrates our technique's insensitivity to this cross-term and the degree to which we can average out linear birefringence.

Figure 4 compares the results of our circular-dichroism measurements as a function of temperature with those of the AT&T group. These data were taken with a thin film of YBCO in the cryostat; we also saw similar results on three other films and a single crystal specimen. For comparison, we measured two samples that were also measured by the AT&T group and found no circular-dichroism signal. We saw a temperature-dependent signal only before we implemented the ratio technique, and we had a poor (inadvertent) vacuum in our cryostat. This observation led us to conclude that changes to the sample's surface (in this case, due to condensation) could cause a spurious signal (Lawrence et al., 1992).

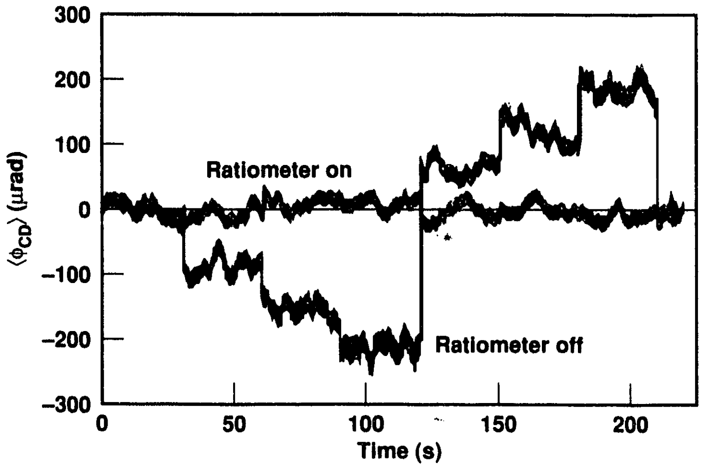

Figure 3. Data showing that our new ratio technique averages out the spurious cross-term. The curve labeled "Ratiometer off" shows the fake circular dichroism, $\langle\phi_{CD}\rangle$, produced by a known amount of linear dichroism crossed with respect to the Soleil–Babinet compensator, which is used to dial in the indicated amounts of linear birefringence, *g*. With the ratiometer on, this fake signal is averaged out. The residual noisiness of the data indicates the degree to which we can average out these spurious signals.

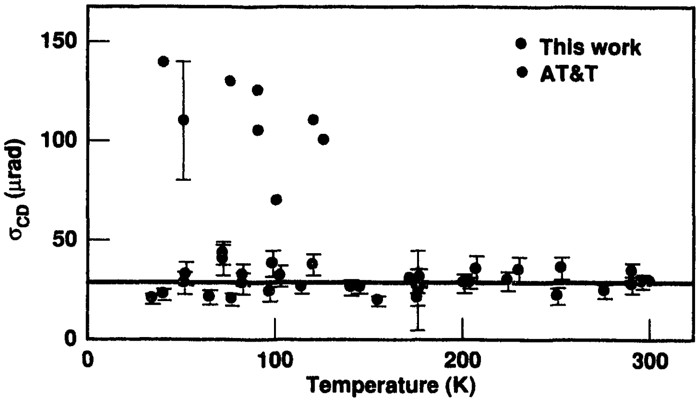

Figure 4. Our data on an 80-nm film of YBCO (superconducting transition temperature of 87 K) on a MgO substrate compared with AT&T data on 50-nm films of YBCO on MgO, where σ_{CD} = the standard deviation of the angle. This graph demonstrates our improvement in the experiment's overall sensitivity and the absence of a temperature-dependent signal in our data.

In this experiment, we provided one of the world's most precise measurements of circular dichroism, with an accuracy approaching 1 part per million. Although we did not find evidence for a temperature-dependent signature of parity and time-reversal violation, our results will become a key part of the fascinating story that will eventually lead to an explanation of high-temperature superconductivity. ◆

References

Laughlin, R. B. (1988), "The Relationship between High-Temperature Superconductivity and the Fractional Quantum Hall Effect," *Science* **242**, 525.

Lawrence, T. W., A. Szöke, and R. B. Laughlin (1992), "The Absence of Circular Dichroism in High-Temperature Superconductors," *Phys. Rev. Lett.* **69**, 1439.

Levi, B. G. (1991), "The Hunt for Anyons in Oxide Superconductors Is Inconclusive," *Phys. Today* **44**, 17.

Lyons, K. B., J. Kwo, J. F. Dillon, Jr., G. P. Espinosa, M. McGlashan-Powell, A. P. Ramirez, and L. F. Schneemeyer (1990), "The Search for Circular Dichroism in High-T_c Superconductors," *Phys. Rev. Lett.* **64**, 2949.

Computer Modeling of Plasma-Processing Reactors

T. D. Rognlien, V. Vahedi,* R. H. Cohen, C. K. Birdsall,* J. R. Hiskes,* and M. A. Lieberman*

Many industries now use plasma-processing reactors to deposit materials and to etch circuits and other patterns on substrates. These reactors use a plasma to produce a concentration of reactive radicals from different feed gases. Historically, the demand for ever-smaller devices has favored processes for producing three-dimensional structures that give precise pattern transfer and directional control. As a consequence, the microelectronics industry has shifted from "wet" processes, which use chemicals in solution, to "dry" processes, which use plasma discharges. Therefore, we must understand these plasma-processing devices so that we can optimize existing processes and invent new ones.

The plasma in these devices is important for two reasons associated with nonthermal electron and ion energy distributions. First, energetic, nonthermal electrons with energies greater than 3 eV (with bulk temperatures of ~1 eV) efficiently dissociate the feed gas into free radicals that can etch surfaces or be deposited on them. The proportion of different neutral molecules and atoms in the discharge depends on the details of the electron distribution function, which in turn, is determined by electron collisions and the method of energy input maintaining the discharge.

Second, the ions gain substantial energy prior to striking the substrate; they are accelerated by the plasma-sheath electric field formed normal to the surface at the plasma-material boundary. The energetic

---

*University of California at Berkeley.

ions and neutral particles that strike the surface catalytically enhance the etching rate of the thermal neutral radicals by an order of magnitude. Collisions with neutral gas particles deflect the ions and limit our ability to maintain a highly directional etch.

Our goal was to create a computer simulation code, based on fundamental physics and chemistry models, that describes the detailed properties of the plasma and the neutral particles in plasma devices. This computer-aided-design tool can replace the present practice of empirically developing and operating such devices because it can answer questions about optimum gas pressure, about how to power the discharge, and about the effects of different gases and of a magnetic field.

We modeled the plasma and the neutral gas as an ensemble of individual ion, electron, and neutral particles rather than as a fluid. Although the fluid model computes more quickly than the particle model, the fluid approach misses the crucial details of the nonthermal effects described earlier. We also modeled neutral species as particles, so that the neutral molecules, electrons, and ions interact via collisional processes such as ionization, excitation, dissociation, detachment, recombination, and charge exchange.

These codes are highly interactive; they run on different types of workstations and on Cray supercomputers. We began with an existing code, PDP1, which had three velocity space dimensions and one spatial dimension. The current version includes two spatial dimensions (PDP2), which is important because the two-dimensional code answers questions about the uniformity of etching over a finite-sized substrate. We also developed an extensive X-Windows graphics display system to monitor diagnostic quantities such as densities, distribution functions, power input, and fluxes to the substrate.

As we built the codes, we improved the numerical algorithms, added a general collision package, and made specific calculations for existing devices. We implemented two schemes that decreased the code execution time an order of magnitude for numerical algorithms. The first scheme is a direct-implicit method for advancing the electrostatic fields. This scheme relies on a numerical estimate of particle positions at an advanced time. The second uses different classes of particles based on speed, allowing the numerous slower particles to be advanced only occasionally.

We developed a general model for the many collisional interactions. These collisions are implemented as a Monte Carlo–type scattering of the simulation particles. We included a detailed kinematic model of each type of collision for how the momentum and energy are partitioned among the reactants, and we compiled an extensive set of cross sections for oxygen. These collisions result in nonthermal distributions for all species, which affect both the plasma discharge and the etching characteristics.

We made specific calculations in one dimension for a radiofrequency (rf) planar discharge operating at 13.56 MHz with ~500 V applied between two parallel plates separated by several centimeters. For two dimensions, the discharge is surrounded by a conducting box with part of one side driven by the voltage source. We modeled the injection of argon and oxygen gases. Our calculations compare well with experimental measurements of the nonthermal, electron distribution function in argon. We studied the negative-ion formation in oxygen discharges used for etching photoresist in the production of circuits. With the two-dimensional code, we reproduced the experimental observation that adding a magnetic field parallel to the etching surface results in a higher density plasma that can etch faster and with improved uniformity. Adding the magnetic field also allows us to operate at lower gas pressure and voltage for the same etching rate. We found that operating at higher frequencies is equivalent to introducing a magnetic field.

Figures 1 and 2 show results from a two-dimensional calculation. The plasma is formed in a 5- × 3-cm rectangular box. The sides are grounded, except for a 3-cm electrode in the middle of one 5-cm side that is driven with 500 V at 13.56 MHz in argon at 4.67 Pa. The angle at which the ions strike the electrode is important for a directional etch.

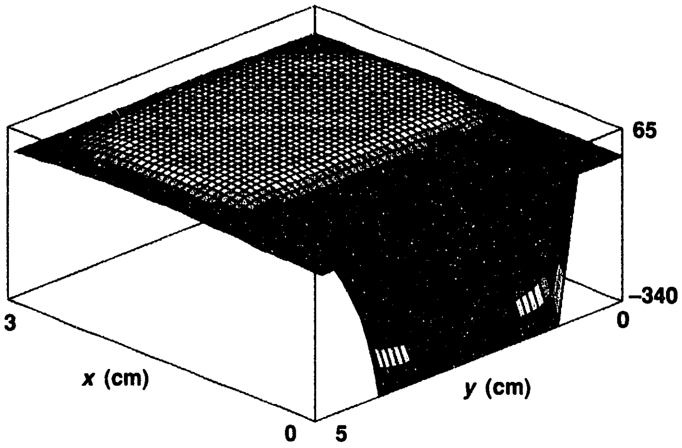

Figure 1. Time-averaged electrostatic potential in an rf discharge driven by 500 V along the central part of the $x = 0$ axis and showing the ion-accelerating potential.

The combined neutral and plasma model is challenging because of the wide range of timescales involved—from the electron plasma frequency ($\sim 10^9$ Hz) to the equilibration rate for the neutral gas ($\sim 10^4$ to 10^2 Hz). As a result, one simulation run to equilibrium takes about one day even on fast workstations like the Sparc-2. Because of the long run time and because we believe we must extend the calculation to three spatial dimensions to resolve uniformity, we are investigating massively parallel computing for these calculations.

In FY 1992, we made substantial progress toward our goal of developing a computer-aided-design tool to simulate plasma reactors. We verified experimentally measured properties of the plasma, and we correctly predicted the advantages of using higher rf frequency to produce the plasma. ◆

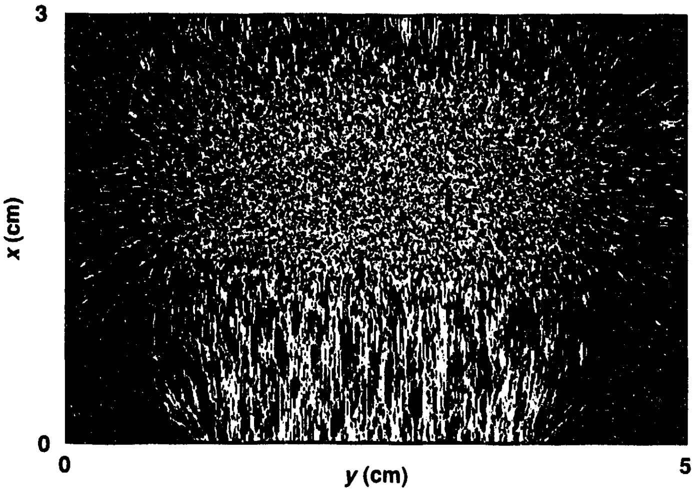

Figure 2. Trajectories of ions in the rf discharge of Figure 1 with ions accelerated into the substrate along the $x = 0$ axis. Ion-neutral collisions cause the irregular motion.

Holographic Atom Imaging of Interfaces

L. J. Terminello and J. J. Barton*

Atomic-resolution structural probes of single crystals, surfaces, and other unique interfaces provide new ways of learning about solid-state chemical bonding. Although many solid-state structural probes already exist, few can provide atomic-resolution images. Scanning tunneling microscopy can image a surface with stunning atomic resolution but cannot directly reveal what is below the surface. Other penetrating probes, such as x-ray crystallography, give detailed structural information but only indirectly. The recently pioneered technique of photoelectron holography can image not just the surface of a solid-state sample but the near-surface region as well (Szöke, 1986; Barton, 1988; Harp et al., 1990). Such imaging is possible because the structural information contained within the electron angular distribution that is obtained from a sample can be extracted by numerical inversion of the diffraction pattern, i.e., by holographic imaging.

Experiments with Prototype Imaging Systems

In FY 1992, we achieved several milestones in the development of photoelectron holography as a buried-atom imaging tool. These include imaging of bulk atoms within a single-crystal copper sample and surface imaging of chlorine on single-crystal copper, Cl/Cu(001). In the near-surface copper atom system, we used a multiple-wavenumber, phased-summing variant of the photoelectron holography technique. We intend to apply the information gained from these simple prototype systems to more complicated and technologically interesting systems.

---

*IBM Research, Yorktown Heights, NY.

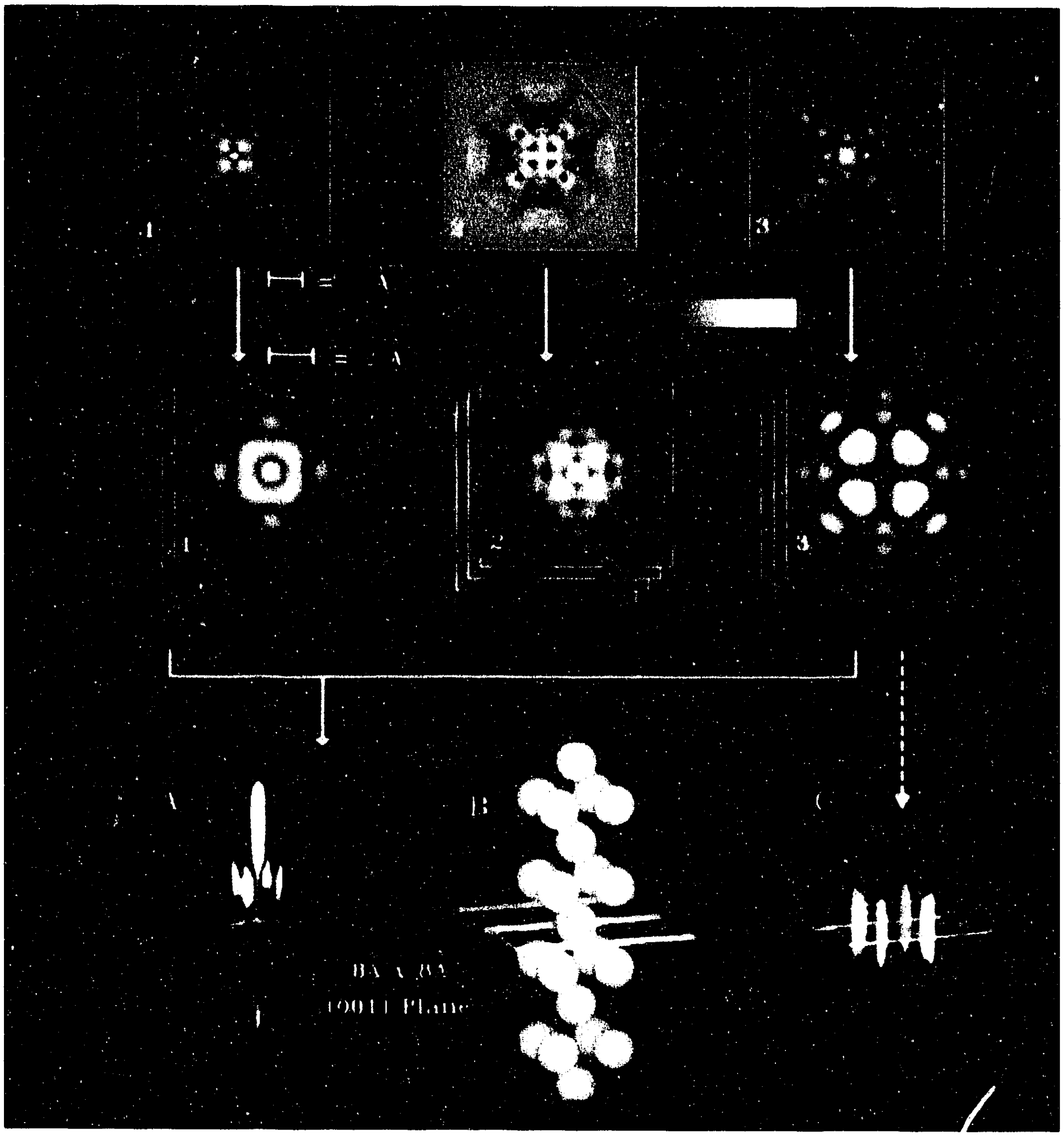

Figure 1. Series of copper 3p photoelectron holograms measured from a Cu(001) crystal face at several electron kinetic energies. The holograms have been numerically inverted to form real-space atom images. Panel A shows the image-enhancement capabilities of the multiple-wave-number, phased-summing procedure. Panel B shows a model of the system, and Panel C shows a single-energy atom image.

In the prototype bulk-atom imaging system, we measured copper 3p photoelectron holograms from a clean Cu(001) crystal face that was prepared according to well-established cleaning and annealing procedures. To obtain copper 3p photoelectron holograms at several kinetic energies, we had to perform these measurements with monochromatized synchrotron radiation as the excitation source. Our measurements were conducted on the IBM/U8 beamline at the National Synchrotron Light Source, which provided the photons needed for this experiment. The total collecting time for a single hologram was four hours; the time would have been nearly an order of magnitude greater if a typical hemispherical electron analyzer had been used. Figure 1 shows the results of this measurement.

Our results show that photoelectron holography has sufficient resolution and accuracy, as well as a high enough capability for improved atom images, to be used with more complex solid-state systems. ◆

References

Barton, J. J. (1988), "Photoelectron Holography," *Phys. Rev. Lett.* **61**, 1356.

Harp, G. R., D. K. Saldin, and B. P. Tonner (1990), "Atomic Resolution Electron Holography in Solids with Localized Sources," *Phys. Rev. Lett.* **65**, 1012.

Szöke, A. (1986), in *Short Wavelength Coherent Radiation: Generation and Applications*, D. T. Atwood and J. Boker, Eds. (American Institute of Physics, New York, NY, 1986), AIP Conference Proceedings No. 147.

Ductile-Phase Toughening of Refractory Metal Intermetallics

G. A. Henshall and M. J. Strum

The search for improved lightweight structural materials for high-temperature service (e.g., gas-turbine engines and aerospace applications) has led to many investigations of high-melting-point intermetallic compounds. Service temperatures of up to 1400°C may be possible for intermetallics based on the Group VB and VIB refractory metals. Such temperatures are well above the projected 1000°C useful limit of currently used Ni-based superalloys and well-studied aluminides, such as Ti_3Al. However, because of their complex crystal structures, refractory metal intermetallics lack the ambient-temperature toughness required for damage tolerance.

To solve this problem, we are exploring ductile-phase toughening. In this method, a ductile phase (which itself must have a high melting point) is dispersed in the intermetallic matrix. The ductile phase may increase toughness by "bridging" the crack faces, thereby inhibiting crack opening, or by blunting the crack tip.

First, we are exploring in situ methods of synthesizing V–V_3Si composites, in which we disperse the ductile phase—a solid solution of Si in the refractory metal vanadium, V(Si)—within the brittle V_3Si intermetallic matrix by phase separation during solidification. Next, we have begun to perform mechanical property testing and finite element method (FEM) analyses to identify the microstructures that improve the toughness of V_3Si at low temperatures while maintaining superior high-temperature creep properties. From these efforts, we expect to understand how these microstructures influence toughness and creep.

We used vacuum arc-casting methods to produce four in situ V–V_3Si composites having a range of ductile-phase fractions: 30, 50, 70, and 100 vol%. Indentation testing of these materials has shown that cracks are easily formed in the intermetallic. However, when these cracks reach the V(Si) phase, they abruptly end or jump from one V_3Si particle to the next while the interspersed areas of V(Si) remain uncracked. These observations supply evidence that the V(Si) phase provides effective toughening by crack-tip blunting and crack bridging.

Preliminary fracture-toughness test results support this conclusion. The V(Si) phase has a fracture toughness more than 10 times that of the intermetallic. The composites have intermediate toughnesses that decrease as the V_3Si content increases. For example, the 50% intermetallic composite has a fracture toughness of 10 $MPa \cdot m^{1/2}$, which is about half that commonly required for gas turbine hot-section materials and twice that of Al_2O_3, a common structural ceramic. We expect to further improve the toughness of the V–V_3Si composites by increasing the ductility of the V(Si) phase through a reduction in the oxygen and nitrogen impurity levels or through microstructural refinements achieved by hot working of the arc castings.

Efforts to understand the micromechanical basis of the toughness and creep resistance of ductile-phase–toughened composites are under way. We began FEM calculations to establish the stress-displacement relationship of the ductile phase under the constraint imposed by the intermetallic matrix when a far-field stress is applied. This is the major step in calculating the work of fracture for ductile-phase–toughened composites. Our results show that as the displacement increases, the stress rapidly increases because of the matrix constraint and subsequently decreases because of a loss of this constraint. Furthermore, by allowing for debonding of the interface between the two phases, we simulated a decrease in the maximum stress that is similar to that observed experimentally.

Our calculations are the first to demonstrate that FEM analysis can be used to quantitatively simulate the important effects of interface properties on the mechanical behavior of ductile-phase–toughened composites. We are also using FEM to study high-temperature creep deformation of the composites. Preliminary results indicate that the composite creep rate deviates from that predicted by a simple weighted average of the rates of the individual phases. The more complex behavior is caused by the presence of nonuniform stresses that redistribute during creep.

In FY 1993 and 1994, we aim to improve the toughness of the V–V_3Si in situ composites. First, we will produce conventionally cast and directionally solidified materials with reduced impurity contents. In addition, we will explore the effects of hot extrusion on microstructural refinement and the fracture toughness of these composites. Then we will experimentally evaluate the dependence of the creep behavior on microstructure in these materials. Finally, we will continue the FEM modeling to better understand the micromechanical mechanisms of ductile-phase toughening and composite creep. ◆

Fundamental Studies of Particle–Solid Interactions

T. Diaz de la Rubia, M. W. Guinan, and A. Caro*

The synthesis and processing of materials are at the forefront of current scientific issues that will define future economic competitiveness. Ion-beam interactions with solids have played a key role in the development of the electronics industry. In particular, ion-implantation technologies have led to improved semiconductor doping and processing methods and, hence, lower manufacturing costs.

Ion-beam–solid interactions may serve not only as a basis for semiconductor doping techniques but also for processing large classes of materials under highly nonequilibrium conditions. The usual thermodynamic barriers to material modification can be surmounted by the use of ion beams. The ion-beam method forms metastable phases and other nonequilibrium structures, such as intermixed layers of immiscible materials and buried quantum wires in semiconductors. These structures are produced by the controlled introduction of defects into the system.

Simulation of Ion-Beam–Solid Interactions

We use molecular-dynamics (MD) computer-simulation methods to study the cascades of atomic displacements generated by energetic particle–solid interactions. Our goal is to gain insight into the mechanisms by which defects and metastable phases, such as disordered structures, appear in irradiated materials. To perform the simulations, we have developed an MD code that uses the architecture of today's massively parallel computers. The simulations use computational models in which up to one million atoms interact in three dimensions through realistic, semiempirical, interatomic potentials from which forces are computed. The forces are then used to integrate Newton's equations of motion.

Our approach is singular in that it enables us to study, at an atomistic level, the fundamental processes that control material modification by ion beams. Our state-of-the-art computers and computational algorithms make us world leaders in this rapidly growing field.

Figure 1 shows the evolution of the chemical short-range order (SRO) and the degree of crystallinity in the region of a cascade that was begun by a 5000-eV recoil in an initially ordered Cu_3Au crystallite. The large energy deposition drives the system into a locally molten state with a volume of about 10,000 atoms. However, the rapid quenching rate (~10^{15} K/s) and large thermal gradients (~1000 K/nm) of the cascade region provide a kinetic barrier to the loss of the chemical SRO. Analysis of the system after equilibration shows that long-range order is lost in a region equivalent to the

---

*Paul Scherrer Institute, Villigen, Switzerland.

transient molten volume. Similar results were found for Ni_3Al intermetallics.

Our MD code for massively parallel architectures has enabled us to study more computationally intensive systems. At present, we are using MD methods to study ion-beam–induced atomic mixing in semiconductor heterostructures and transition-metal multilayered systems. We are also studying, both experimentally and with MD simulation, radiation effects in nanocrystalline materials, a new class of bulk solids. The high concentration of grain boundaries in these materials may improve resistance to radiation environments, including those expected in fusion reactors. ◆

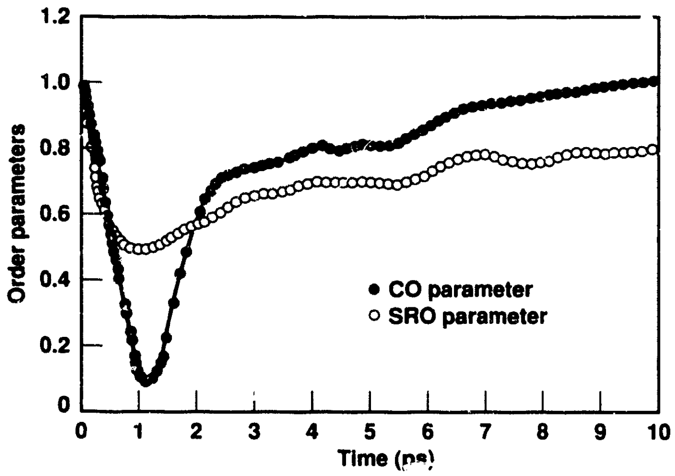

Figure 1. Development of the chemical SRO parameter and the crystallinity order (CO) parameter of the underlying lattice in the region of a 5000-eV displacement cascade in Cu_3Au. CO follows the evolution of the underlying fcc lattice. It is defined in terms of the occupancy of cubes of side length $a_0/4$ centered on perfect lattice position. It has a value of 1 for the perfect lattice and 0 in the liquid phase.

Electronic Structure Evolution of Metal Clusters

M. J. Fluss, R. H. Howell, V. V. Kresin, and W. D. Knight*

The electronic properties of free-metal clusters (unperturbed by strong interactions with a substrate) are of significant interdisciplinary interest and high application potential because they can be used for new materials, microelectronics, and catalysis. We are particularly interested in the growth of cluster spectra and are designing a novel positron-spectroscopy setup at LLNL's linear accelerator to study positron-cluster collisions and investigate the evolution of cluster electronic properties according to mass size. We are also studying cluster collisions at the UC Berkeley Cluster Laboratory so we can understand the evolution of surface properties and intermolecular interaction. We are completing theoretical work on cluster properties as well.

Size-Sensitive Experiments

By using data collected in these investigations, we hope to map the step-by-step evolution of the Fermi surface of a small particle. We will start by intersecting a high-intensity, monochromatic positron beam with a beam of alkali clusters. Then using coincidence spectroscopy, we will perform a size-sensitive experiment on the positronium formation in these metal clusters. The experiment will cover cluster size *N*, which equals about 2 to 100 atoms per cluster. By simultaneously detecting a cluster ion and a gamma ray, we can identify the precise origin of the annihilation event that gave rise to the gamma ray. We designed and manufactured the experiment's vacuum system in FY 1992. We plan to complete the cluster source and mass-spectrometer designs and the positron transfer-line installation in FY 1993.

**University of California at Berkeley.*

Collision Processes

We also completed a detailed study of collisions between alkali clusters and various gas targets. This study, which was the first investigation of cross sections for a range of alkali-cluster masses, directly measured the electron capture and associated processes with a separate probe. The measurements provided information on long-range interactions, electron-transfer processes, and primordial chemisorption of clusters (Figure 1). This study was similar to our positron-impact project because the same collision and electron-transfer channels were active in both. By combining these data, we hope to separate probe effects from cluster physics in FY 1993.

For our theoretical work, we are analyzing electronic excitations and scattering processes in metal and carbon clusters. We found that calculations based on models for collective motion in nuclei describe several cluster phenomena such as the cluster-absorption spectra. ◆

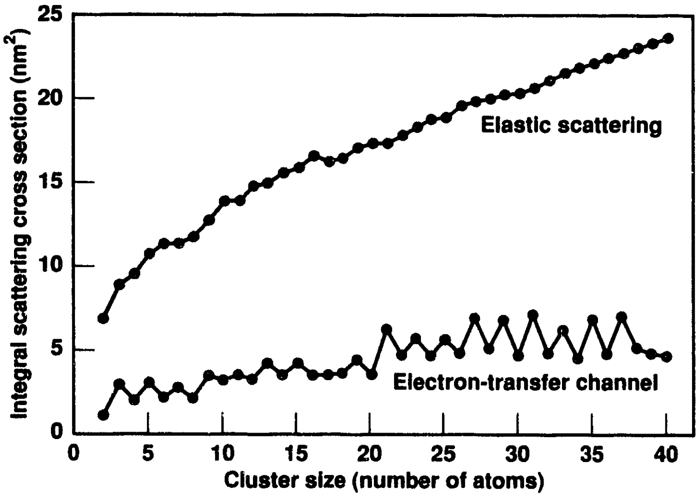

Figure 1. Large charge-transfer and elastic interactions in scattering of Na_2 clusters by Cl_2. This was the first investigation of cross sections for a range of alkali-cluster masses.

Nanoscale Lithography by Scanned Probe Microscopy

M. Balooch and W. J. Siekhaus

A means of fabricating nanometer-scale patterns on silicon surfaces would be of great importance to the electronics industry. Such a capability could be used to make narrow trenches and ultrathin oxide masks. The scanning tunneling microscope (STM) is an attractive instrument for nanoscale lithography because its characteristics (operation at low voltage, but with a high and localized electric field) can minimize damage to nearby structures and to the substrate. Moreover, it is compact and flexible and can operate under many conditions. The objectives of this project are twofold: (1) to investigate the chemical reactivity induced by phenomena occurring between the tip and substrate in an STM, and (2) physical modification of the substrate by the tip of an atomic force microscope (AFM). In the work reported here, we examined a variety of electronic substrates such as Si, SiO_2, and SiC.

To study the etching and deposition processes occurring between the tip and substrate, we built a reaction chamber for our STM and AFM. The chamber can handle a variety of gases and is used to study STM-induced oxidation of silicon substrates. We adopted an elaborate technique to remove the native oxide and hydrogen-terminate silicon surface atoms. This method prevents the oxidation of a silicon surface in air for at least one hour.

Pattern Generation on Silicon Substrates

We have grown patterns of thin oxide of nanoscale dimensions by increasing the voltage between the tip and the surface to 4 V from 1.5 V typically used for imaging. Figure 1 shows the sequence used to write the letters LLL as silicon oxide lines 1.5 nm high and 0.2 nm wide on a Si(100) surface. In FY 1992, we improved our technique to generate 10-nm-wide patterns.

We have studied the details of STM-induced reactivity by applying voltage pulses, varied in duration and frequency, between the tip and substrate. A depression is observed at short pulse durations, presumably due to removal of hydrogen from the surface. At longer pulse durations, however, growth of oxide is apparent. We also investigated the effects of field strength and polarity and oxygen partial pressure on oxide growth. The dependence of oxidation rate on pulse duration enabled us to measure, for the first time, the surface diffusion

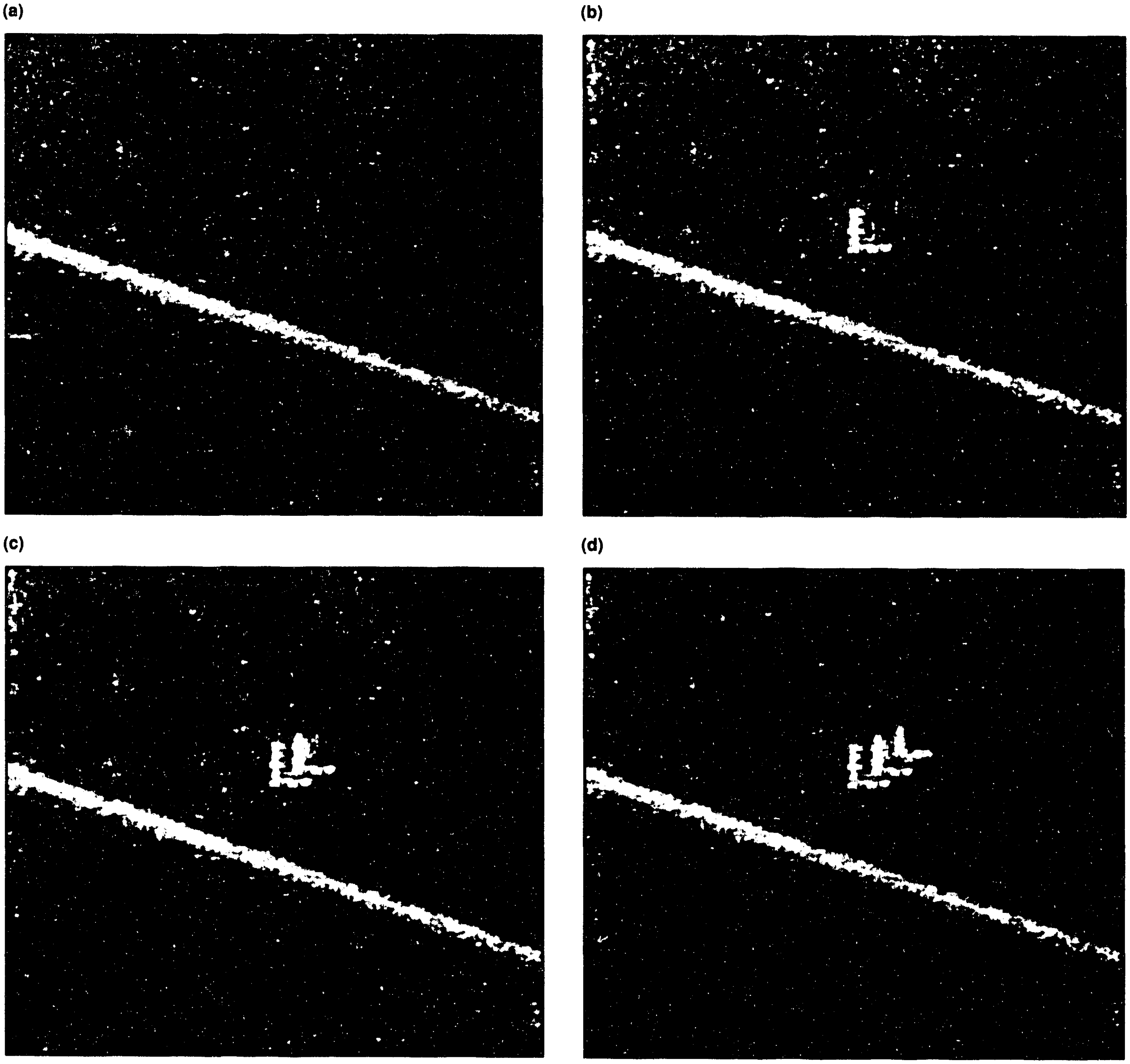

Figure 1. (a–d) Sequence used to write the letters LLL with silicon oxide lines 1.5 nm high and 0.2 nm wide. The oxide lines are formed on clean silicon by an STM-induced reaction. The white line across each figure represents oxide formation on a line defect that existed on the silicon surface. It is used for reference and to locate the patterns.

rate of reactants on silicon surfaces and the bulk diffusion rate of atomic (or ionic) oxygen through the film at room temperature.

We plan to modify the reaction chamber for Si etching by XeF_2 and for SiC etching by suitable gases. We will also study the detailed kinetics of STM-induced etching by applying voltage pulses to the tip. To find the optimum conditions for enhanced etching, we will investigate the effects of (1) polarity and intensity of the field between the tip and substrate, and (2) tunneling current density.

In summary, we have used an STM to produce nanometer-scale patterns of thin oxide on silicon surfaces and have identified the parameters responsible for enhanced oxidation. Making STM-based nanostructure fabrication technology a reality, however, requires the development of STM-based methods that are compatible with the existing microelectronics processing environment. The development of such methods will present new challenges. ◆

Fabricating Amorphous Diamond Coatings

S. Falabella, D. B. Boercker, and D. M. Sanders

Amorphous diamond (a:D) is a hard, electrically insulating, inert, and transparent form of carbon. It has the sp^3 bond character of crystalline diamond but lacks a long-range, ordered structure. Amorphous diamond can be used for cutting tools, surface protection, medical implants, tribological surfaces, and spacecraft. Indeed, a:D is preferred to chemical vapor deposition (CVD) diamond for many applications. Our goal was to produce and characterize a:D, to determine the conditions under which it forms, and to model a:D and its deposition using molecular-dynamics codes.

Diamond's physical properties make it ideal for many critical applications. However, natural diamond is rare and expensive. Thin diamond films can potentially provide the physical properties of diamond without the expense of the natural product. Four problems must be solved, however, before a thin-film diamond coating can be practical: temperature of deposition, adhesion to substrate, stress, and smoothness of coating. If processing temperatures are high, aluminum, tool steels, glasses, and polymers cannot be used as substrate materials. Thin films rely on the substrate for much of their mechanical integrity, depending on adhesion to the substrate for support. Intrinsic stress limits the permissible thickness of a coating when stress in the coating causes delamination or deforms the substrate. Smoothness is essential in tribological applications for low friction and long life. CVD-produced diamond films have difficulty in all four areas: deposition temperature is generally above 800°C, adhesion is poor, stress is often excessive, and the polycrystalline films produced have rough surfaces.

Amorphous diamond coatings are more successful in these areas. Amorphous diamond coatings are produced by condensing carbon ions on room-temperature substrates. The coatings replicate the substrate surface finish and can be very adherent. Because the process is ion-based, substrate biasing can form a diffuse, adherent interface. We used a high-voltage bias for the first few seconds of coating to produce coatings on tungsten-carbide tool bits with adhesion above 69 MPa (the limit of the tester). Stress in the film can be lowered by radio-frequency- (rf-) biasing the substrate during deposition to increase the incident ion energy, by increasing the substrate temperature, or by incorporating impurity elements in the film. We reduced the intrinsic stress in a:D films a factor of 5 by using bias and incorporating 7% nitrogen.

In FY 1992, we produced carbon films up to 8 μm thick using our filtered cathodic-arc ion source. We produced hard carbon coatings that are low in hydrogen content, which is critical because the hardness of carbon films is inversely related to the hydrogen content. For example, 10 to 20% hydrogen in a diamond-like carbon

(DLC) film reduces the hardness by a factor of 4. Using forward recoil scattering, we measured the hydrogen content of our coatings to be less than 0.1%. We measured the density of our films using film thickness and the areal density obtained from Rutherford backscattering. We measured the density of a:D to be 2.7 ± 0.3 g/cm^3, which is between graphite at 2.26 g/cm^3 and diamond at 3.5 g/cm^3.

We measured a coated tungsten-carbide tool bit with a standard Vickers indentation (500-g load) to have a hardness of 8000 to 12,000 H_v. We also assessed the hardness of the a:D coatings by abrading several hard materials against an a:D-coated plate. We were able to polish facets in all materials attempted, including natural and synthetic diamond, thus showing that the a:D coating is approximately as hard as diamond (H_v = 10,000). Quantitative hardness tests using an ultramicrohardness tester are in progress.

We characterized the fine structure of a:D with transmission electron microscopy (TEM) and with electron diffraction. TEM showed no evidence of an ordered structure down to 1 nm. Electron diffraction patterns showed only diffuse rings, thus confirming the lack of crystal structure. Unlike natural diamond or DLC, a:D has a flat transmission spectrum from 0.8 to more than 50 µm, which is due to its amorphous nature and lack of hydrogen. Also, we determined the index of refraction of our a:D to be between 2.47 and 2.57, which is close to the refractive index of natural diamond (2.42).

We used molecular-dynamics simulations to model the condensation of carbon atoms on a silicon substrate to see the effects of deposition energy on coating structure and stress. We used the code results to interpret the electron diffraction measurements and showed good agreement with the diffraction ring locations.

We showed that a:D films of practical thickness can be produced using a cathodic-arc source. When we used rf bias and added nitrogen, we significantly reduced the intrinsic stress in the films and thus made possible many new uses for these materials. ◆

Advanced Materials Design by Massively Parallel Computers

C. Mailhiot, A. K. McMahan, L. H. Yang, J. E. Klepeis, and M. F. Needels

Our goal is to provide LLNL with breakthrough capabilities in atomistic materials simulation through the use of innovative, massively parallel processing (MPP) algorithms, methods, and computers. The powerful materials-modeling methods that we develop will enable researchers to design novel materials with optimized properties solely from the identities of the constituent atoms and the laws of quantum mechanics, that is, by ab initio methods. To progress rapidly toward this goal, we are

- Developing widely applicable ab initio molecular-dynamics simulation methods.
- Implementing these methods on available MPP environments.
- Applying these methods to the study of important research projects: silicate microplasticity, interface adhesion and bonding, and the growth of multilayer x-ray optics components.

Major Accomplishments

In FY 1992, we developed ab initio total-energy, molecular-dynamics energy methods that simultaneously provide a self-consistent treatment of electron charge rearrangements and a description of ionic motions. These methods have led to the discovery of new energetic forms of polymeric nitrogen and have clarified the miscibility properties of planetary hydrogen/helium mixtures. We have implemented our set of molecular-dynamics algorithms on the BBN TC-2000 scalable MPP computer operated by LLNL's Massively Parallel Computing Initiative. Figure 1 compares the computer speed achieved on the BBN TC-2000 relative to that achieved by the conventional vector architecture of the Cray X/MP. This result is significant because it indicates the performance increases afforded by developmental MPP computers and suggests how large-scale atomistic simulations can be successfully performed using next-generation MPP production environments. In addition, we have made substantial progress in applying our advanced, atomistic materials modeling methods to several Laboratory research projects, including the study of tilt-grain boundaries in niobium, the study of silicide formation, and the machining of silicon.

In FY 1993, we plan to implement and optimize our ab initio total-energy, molecular-dynamics methods on other MPP environments, such as the Thinking Machine CM-5 and the Cray T-3D. ◆

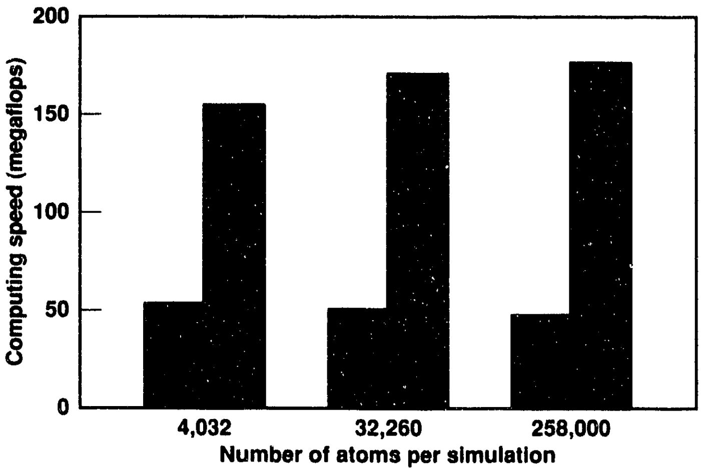

Figure 1. The computing speed of the BBN TC-2000 scalable MPP computer (gray) compared with that of the Cray X/MP vector machine (green) as a function of the number of atoms for a classical molecular-dynamics simulation.

Laser-Induced, Bond-Selective Reactions

J. L. Krause and A. E. Orel*

One central goal of molecular physics is to develop methods of using lasers for controlling and directing chemical reactions. For example, in the photodissociation of a triatomic molecule ABC at a photon energy capable of breaking either the A–B or the B–C bond, it is important to find the optimal way of selectively breaking one bond and not the other. The ability to selectively break bonds will affect many areas, including isotope separation, synthesis of high-energy-density materials, and efficient photodestruction of pollutant molecules.

The Phase-Control Approach to Chemical Reactions

In the past few years, two main approaches have emerged as serious candidates for controlling chemical reactions. The first involves the use of coherent phase control. The idea is to design a method with two independent paths to the same degenerate product state. Constructive and destructive interference between these routes provides the leverage for control of the product branching ratios.

In FY 1992, we demonstrated the principles of coherent phase control with calculations of the photoionization of krypton. We showed that by irradiating krypton with a superposition of a laser field and its second harmonic, and varying the relative phase between the two laser fields, the Kr^+ $^2P_{1/2}$ to $^2P_{3/2}$ branching ratio can be controlled by nearly a factor of 2 (see Figure 1). Our calculations are in quantitative agreement with experiments performed on this system at AT&T by Muller et al. (1990).

---

*University of California at Davis.

To extend these methods to molecular reactions, we proposed, in collaboration with an experimental group led by S. W. Allendorf and W. E. Conaway, an experiment to selectively dissociate either the OH or the OD bond in isotopically substituted water, HOD. The experiment involves pumping an overtone of the OH or OD stretching vibration, then bringing about dissociation with a combination of a visible laser and its third harmonic. The H to D product ratio will be controlled by varying the phase between the two laser fields.

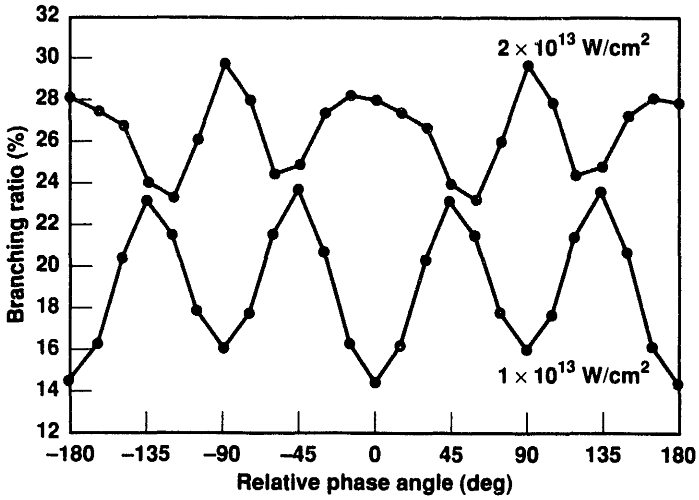

Figure 1. Kr$^+$ $^2P_{1/2}$ to $^2P_{3/2}$ branching ratio as a function of the relative phase difference between the fundamental (1064 nm) and its second harmonic (532 nm) at intensities of 1 and 2 × 10^{13} W/cm^2.

This experiment, which is under construction at LLNL, will be the first demonstration of the principles of coherent control in a system with chemically distinct products. Calculations on this system are under way to predict the experimental outcome and optimize the experimental parameters. Preliminary results indicate that control can be attained by properly selecting the laser wavelengths and intensities.

The Pulse-Shaping Approach

The second main approach for the laser control of chemical reactions involves the use of optical pulse shaping. In FY 1992, we initiated a collaboration with Kent Wilson at UC San Diego. Wilson's group is building a Ti:sapphire laser system as a source of intense, short-pulse continuum radiation. This light can be shaped by various methods. For example, the frequency and phase components of the pulse can be filtered with spatially varying masks. To predict the optimal field for a particular experiment, we are using a density-matrix formalism to study the effects of ensembles of initial states and realistic laser pulses in the modeling. The first system we are investigating is the photodissociation of I_2, for which extensive theoretical and experimental information is available in both the gas phase and solution. ◆

References

Muller, H. G., P. H. Bucksbaum, D. W. Schumacher, and A. Zavriyev (1990), "Above-Threshold Ionisation with a Two-Colour Laser Field," *J. Phys. B* **23**, 2761.

Modeling Superplastic Materials

D. Lesuer, C. Syn, P. Raboin, and C. S. Preuss

Superplasticity is the capability to deform crystalline solids in tension to unusually large plastic strains (often well in excess of 1000%). This phenomenon results from the capability of the material to resist localized deformation, much as hot glass does. The material also deforms with very low flow stress. Materials with superplastic properties thus provide the opportunity to form complex components into shapes very near final dimension. This capability greatly reduces machining and material costs and minimizes the amount of scrap produced.

Superplastic materials exhibit high elongations because a deformation mechanism known as grain-boundary sliding (GBS) is active. This deformation behavior occurs within a relatively narrow range of temperature and strain rate. If the strain rate is too high, a different mechanism, called diffusion-controlled dislocation creep (slip creep), is activated, and ductilities are substantially reduced. If, however, the strain rate is too low, a deformation mechanism known as diffusional flow prevails, and the ductility is also reduced relative to GBS. From a commercial standpoint, forming components at high strain rates is attractive because operations can be performed with less time and cost. This often means superplastically forming components at strain rates close to the slip-creep regime. Our work is therefore concentrated on the two higher strain-rate regimes: GBS and slip creep.

The active deformation mechanisms also strongly depend on the microstructure of the material (such as an ultrafine grain structure). Unfortunately, ultrafine grains can grow during deformation, resulting in loss of superplasticity. It is therefore important to gain a quantitative understanding of this process and its influence on material forming.

For these reasons, models of the constitutive behavior of materials during superplastic flow should account for the microstructure, its evolution, and changes in deformation mechanism throughout the deformation history. The objective of this project was to develop a model of these structural changes and their influence on stress-strain-strain rate behavior using mechanism-based constitutive laws.

Microstructural Evolution

Our experiments focused on two superplastic materials with significantly different microstructures: ultra-high-carbon steel (UHCS), which has a microduplex structure, and Coronze 638, which is quasi-single phase. The dominant microstructural change in both of these materials is grain growth. The UHCS has the composition Fe–1.8C–1.6Al–1.5Cr–0.5Mn. It had been thermomechanically processed to produce a matrix of ultrafine, equiaxed ferrite grains (mean linear intercept was about 0.74 μm) containing spheroidized carbides. Coronze 638 (Cu–2.8Al–1.8Si–0.4Co) is a commercial alloy that consists of essentially pure copper containing a submicrometer-sized dispersion of CoSi and $CoSi_2$ particles. The material was received as a repeatedly rolled and annealed sheet with a mean linear intercept grain size of 1.9 μm.

Figure 1 shows the influence of superplastic deformation at 750°C and a true strain rate of 0.001 s^{-1} on the microstructure of UHCS. Figure 1a was taken in the grip section of the sample, which was thus exposed to the testing temperature without plastic deformation. Figures 1b and 1c were taken in the gauge section of a sample deformed to true strains of 0.92 and 1.42. A comparison of the figures shows strain-enhanced grain growth in that the ferrite grains have grown. The carbide particles have also coarsened. The size of the ferrite grains appears to be determined by the intercarbide spacing. This observation suggests that the kinetics of grain growth are determined by the kinetics of carbide coarsening. The stress-strain curve in Figure 1d shows the importance of this grain growth on the deformation behavior of UHCS. Increasing the grain size from its initial value (0.74 mm) to the value at a strain of 1.42 (1.48 mm) has raised the flow stress from 28 MPa to more than 62 MPa. Grain growth has thus produced significant hardening, and grain size is an important parameter for characterizing the current mechanical state of the material.

We have examined the distribution of grain sizes in these materials and how they change with strain and strain rate during superplastic deformation. We have developed equations that describe the evolution of the mean value of these distributions as a function of strain, strain rate, and temperature. This alteration in the distribution of grain sizes can have a significant impact on the deformation mechanisms operating in the material and the resulting stress-strain-strain rate behavior.

Mechanical Response

We calculated the stress-strain-strain rate response using a distributed-parameters approach originally proposed by Ghosh and Raj (1981, 1985; Raj and Ghosh, 1981), in which stress is calculated from a distribution of grain sizes. In our case, this distribution evolves as a function of strain and strain rate. For our model, we assume that during deformation each grain in the material deforms with the same strain rate (which is equal to the strain rate imposed on the material). Additional details are provided in Lesuer et al. (1993).

Figure 2a shows the stress-strain behavior for Coronze at 550°C predicted by this model, and Figure 2b shows the stress-strain rate behavior at the same temperature. A single set of material constants was used for all of the calculations shown in Figure 2. The agreement between the calculations and experimental data is quite remarkable in that the entire stress-strain curve can be predicted (to the maximum in the stress-strain curve) for three strain rates over 2 orders of magnitude, and the stress-strain rate behavior can be reasonably predicted over the limits of experimental data (2 orders of magnitude).

The stress-strain behavior shown in Figure 2a is complicated by cavities that nucleate and grow during superplastic deformation of the Coronze alloy. Eventually, these cavities will interlink to cause fractures. We believe that the maximum in the stress-strain curve shown in Figure 2a and subsequent softening in this curve are probably caused by cavity interlinkage. In other materials that do not form extensive cavities, this maximum could be due to necking (flow localization) of the sample.

Figure 2b shows a model-predicted transition between GBS-dominated and slip-creep–dominated deformation taking place over about 1.5 orders of magnitude in strain rate. This observation is consistent with experimental stress-strain rate data in several superplastic materials. Figure 2c shows the volume fraction of slip creep predicted from the model during tensile testing at 550°C. Results are shown for the three strain rates reported in Figure 2a.

Substantial changes in the relative contributions to the strain from the deformation mechanisms can occur during testing for strain rates at or near the transition

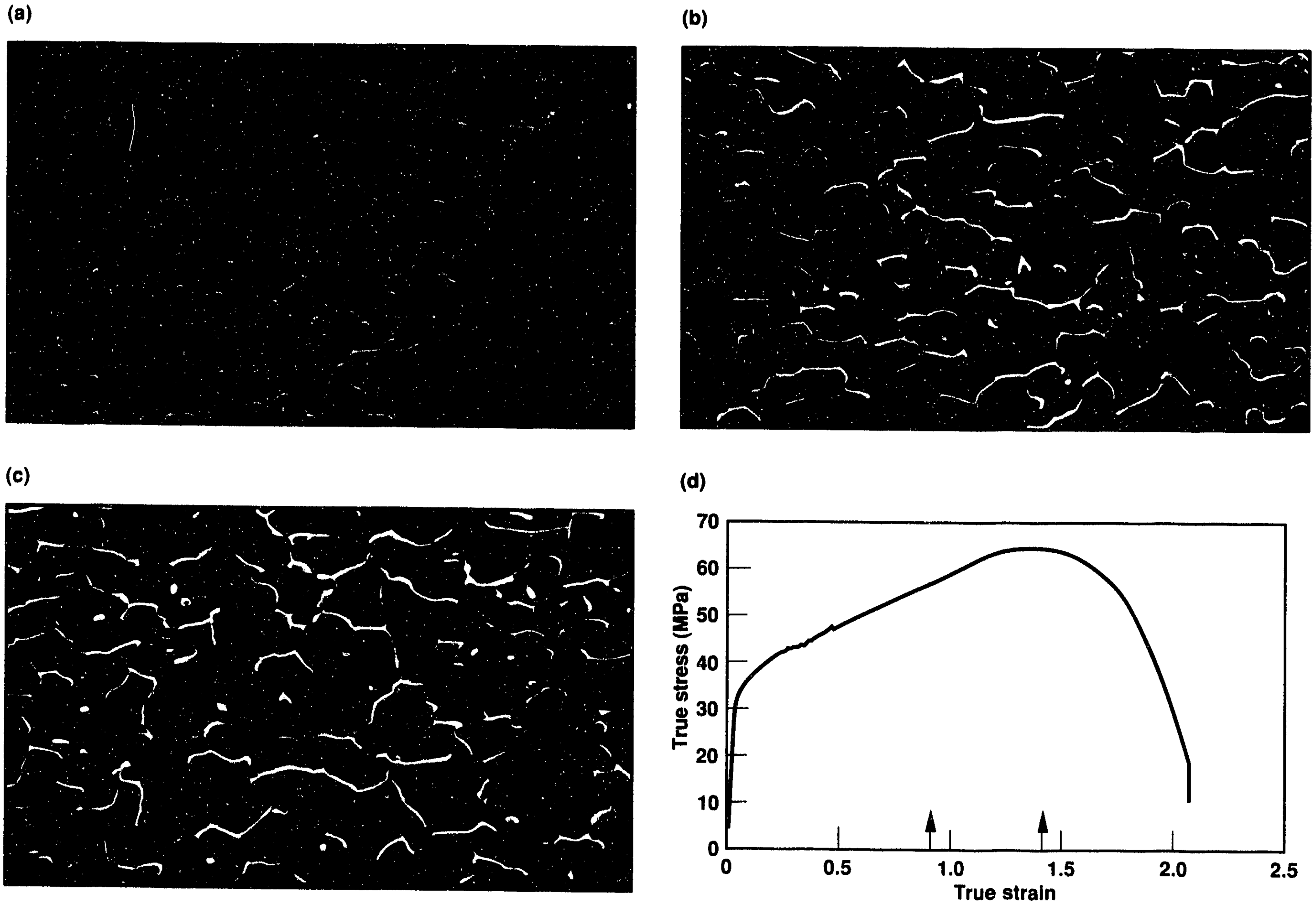

Figure 1. Microstructure of UHCS (a) before deformation, and (b and c) after superplastic deformation to true strains of 0.92 and 1.42, respectively. The microstructure consists of ferrite grains and iron carbide particles, both of which show growth because of superplastic deformation. (d) True stress–true strain behavior for UHCS.

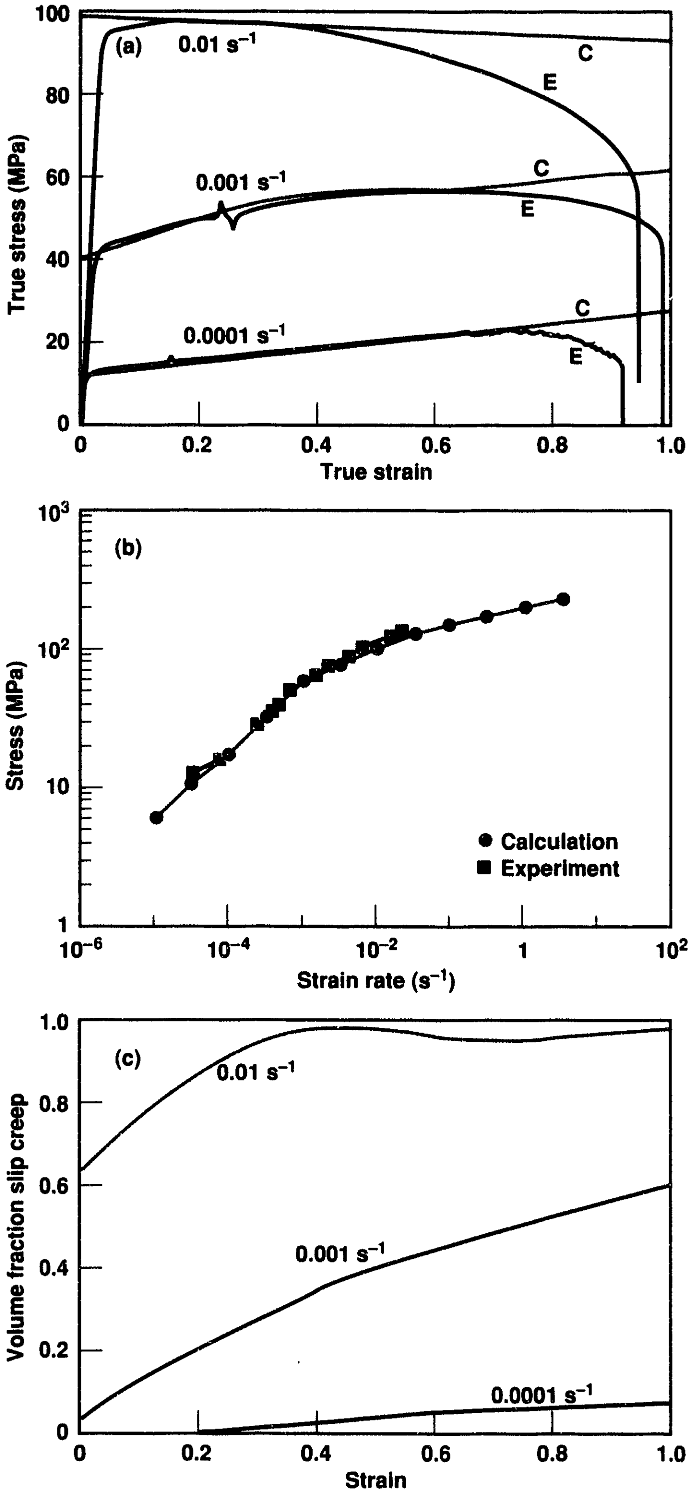

Figure 2. Comparison between calculated curves and experimental data for Coronze at 550°C. (a) Stress vs strain for three strain rates. C, model calculations; E, experimental data. (b) Stress vs strain rate. (c) Model-predicted volume fraction of deformation from slip creep during tensile testing.

between regions that are dominated by GBS or slip creep. In Figure 2, the curvature shown in the stress-strain curves is due to the increasing contribution of slip creep to the deformation as grain growth occurs. If the contribution of grain-boundary sliding to the deformation were constant throughout the deformation history, then the stress would increase in a linear manner with strain. Many true stress–true strain curves reported in the literature also show, for superplastic deformation under constant-strain-rate conditions, a linear dependence of stress on strain up to a stress maximum. ◆

References

Ghosh, A. K., and R. Raj (1981), "Grain Size Distribution Effects in Superplasticity," *Acta Metall.* **29**, 607–616.

Ghosh, A. K., and R. Raj (1985), "The Evolution of Grain Size Distribution during Superplastic Deformation," in *Proc. Int. Conf. on Superplasticity, Grenoble, France*, pp. 11.1–11.19.

Lesuer, D., C. Syn, K. L. Cadwell, and C. S. Preuss (1993), "Modeling Microstructural Evolution and the Mechanical Response of Superplastic Materials," in *Advances in Superplasticity and Superplastic Forming* (TMS Publications, Warrendale, PA).

Raj, R., and A. K. Ghosh (1981), "Micromechanical Modeling of Creep Using Distributed Parameters," *Acta Metall.* **29**, 283–292.

A New Class of Insensitive, High-Energy-Density Materials

P. F. Pagoria, C. L. Coon, and A. R. Mitchell

The standard for insensitive high explosives (IHEs) has been 1,3,5-triamino-2,4,6-trinitrobenzene (TATB). In the context of IHEs, "insensitive" refers to the relative ease of detonation by external stimuli, such as impact, friction, spark, or heat. The synthesis of new, insensitive, energetic materials with more energy than TATB would have a major effect on both nuclear and conventional weapon design. Indeed, high-energy-density materials have been designated as a critical defense technology by the Secretary of Defense.

We are designing and synthesizing a new class of insensitive, energetic, heterocyclic materials—compounds containing an atom other than carbon in the ring—predicted to be 10 to 30% more energetic than TATB. We attempted to integrate into these molecules many of the properties believed to give TATB its enhanced insensitivity, namely, a high degree of hydrogen bonding, good thermal stability, and graphitic structure. One method to do so is to use known, insensitive heterocyclic molecules with a high degree of hydrogen bonding as substituents on a parent energetic heterocycle. Figure 1 shows an example of such a substituent, 5-amino-3-nitro-1,2,4-triazole (ANTA).

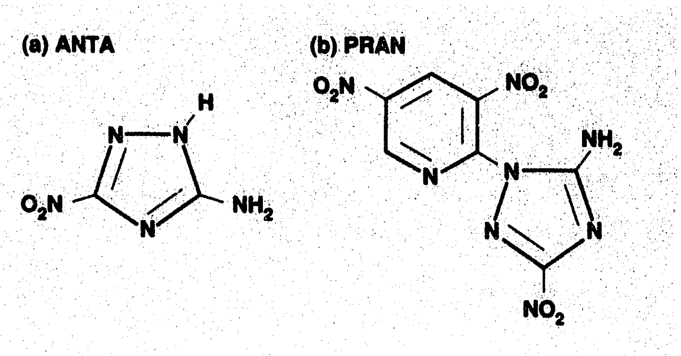

Figure 1. (a) ANTA, an insensitive heterocyclic molecule we have used as a substituent on a parent energetic heterocycle. (b) PRAN, an ANTA-derived target molecule we synthesized this year.

We chose heterocyclic parent compounds because of their advantages over carbocyclic analogs in higher molecular density and heat of formation, which are important contributors to the performance of an explosive. In addition, these molecules incorporate both amino and nitro substituents to help optimize the balance between energy and insensitivity. This approach produces multicyclic, insensitive, energetic materials with good thermal properties. In FY 1991, we synthesized the first target molecule in this new class of compounds and found it to have insensitivity and energy similar to that of TATB.

In FY 1992, we synthesized several ANTA-derived energetic materials by the condensation of halogenated, nitro-substituted heterocycles with the sodium salt of ANTA. The two most interesting are 2-(5-amino-3-nitro-1,2,4-triazolyl)-3,5-dinitropyridine (PRAN), shown in Figure 1, and 4-(5-amino-3-nitro-1,2,4-triazolyl)-6-(3-nitro-1,2,4-triazolyl)-5-nitropyrimidine (ANTNP). These materials have densities of 1.815 and 1.87 g/cm^3, respectively, and they are predicted to be 10 to 15% more energetic than TATB. We also began studying pyridazine and pyridazine-N-oxides as IHE candidates and synthesized an energetic ANTA-substituted pyridazine.

We plan to complete the synthesis of a series of energetic pyridazines and pyridazine-N-oxides and to explore ways to make known high-energy explosives more insensitive by adding amino groups. This work will involve the nucleophilic substitution of hydrogen atoms on electrophilic aromatic rings with ammonia in the presence of an oxidizing agent. An example is the amination of 2,4,6-trinitropyridine in the presence of $KMnO_4$ to yield 3-amino-2,4,6-trinitropyridine.

We believe we can generate a new class of insensitive energetic materials that will have a significant effect on the weapons community. In addition, our work should provide insights into the molecular properties that govern insensitivity and help guide the synthesis of future candidate IHEs. ◆

References

Pagoria, P. F., C. L. Coon, A. R. Mitchell, and R. L. Simpson (in press), "The Synthesis, Scale-Up, and Characterization of 3-amino-5-nitro-1,2,4-triazole (ANTA)," *J. Propel. Expl. Pyrotech.*

Laser Technology and Materials Processing

R. S. Hargrove. B. E. Warner, and D. D. Kautz

We demonstrate the materials-processing capabilities of high-power, high-optical-quality, high-pulse-rate lasers using the unique dye and copper vapor laser systems developed for laser isotope separation (LIS) applications at LLNL. Lasers and laser technologies developed at LLNL, such as solid-state slab lasers, copper vapor lasers, dye lasers, and harmonic wavelength conversion, have many existing materials-processing applications and their unique properties provide the potential for new ones. LLNL laser systems have stimulated interest in several materials processes: precision cutting, precision hole drilling, high-speed cutting and drilling, processing of difficult materials, and surface treatments.

In FY 1992, we concentrated in three areas: advanced laser sources, optical delivery, and laser-materials interactions. In our advanced laser source work, we perfected the optical engineering of the copper laser so that we have a near-diffraction-limited (perfect) beam. Working with high magnification resonators and new injection seeding techniques, we routinely produce beams with less than 2 times the diffraction-limited divergence from 20- to 30-W oscillators. We extended the power range of this high-quality light to hundreds of watts by redesigning the oscillator-amplifier relay optics.

We made significant progress in the optical delivery of the copper laser and dye laser light to the laser materials processing (LMP) facility. We found, through precision cutting and drilling tests, that the nearly perfect, optical

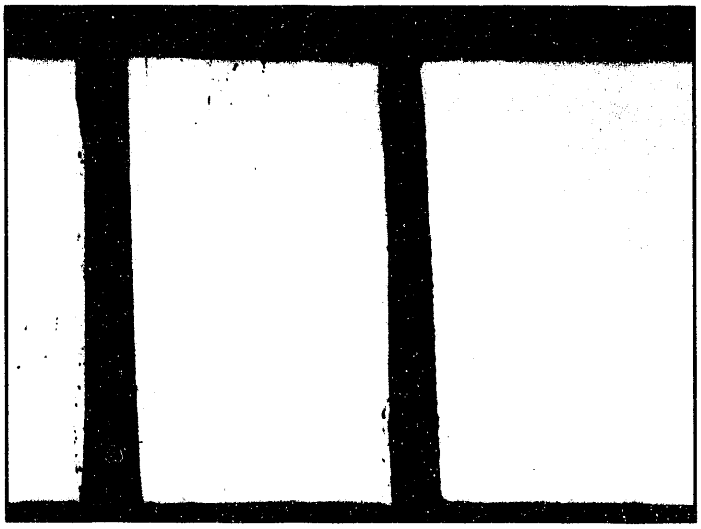

Figure 1. Cross section of a 0.038-cm stainless-steel sheet drilled by a copper laser. The holes are ~35 μm in diameter and have a 12:1 aspect ratio.

quality dye light was delivered with a vibration-induced pointing error that limited control of the cutting process. To correct this error, we introduced a high-bandwidth pointing and centering diagnostic and control mirror. Initial results indicate that this control system will allow diffraction-limited performance on the processing table. We also activated the copper laser delivery system, which delivers up to 700 W to the LMP facility. The system can potentially deliver 2 times this power.

We can now demonstrate advanced materials processes, primarily precision cutting and drilling processes, and we have started to assemble analytical tools and in situ diagnostics to extend our understanding of high-brightness, short-pulse laser-material interactions. Figure 1 shows a cross section of a 0.038-cm-thick stainless-steel sheet. A low-power, copper laser drilled the holes, which are ~35 μm in diameter and have an aspect ratio of 12:1. The hole diameter is only 2 times the diffraction limited spot size for green light through our optical system. The holes are clean and straight and have an almost undetectable heat-affected zone. ◆

Potential Applications of Reactive Multilayers

J. B. Holt, D. M. Makowiecki, M. O. Riley, and R. J. Foreman

The investigation of self-sustaining multilayer reactions is advancing the development of new applications in materials technology. The objective of our work was to examine the experimental parameters that control the rapid chemical reaction of reactive multilayers (RMLs) and to assess their potential applications. Specifically, we investigated the sputtering of titanium–boron (Ti–B) multilayers, measured the velocity of their spontaneous chemical reaction, and characterized the reaction products. The reaction velocities of Ti–B multilayers have important theoretical implications for solid-state reactions because of the ideal geometry. Since most of the reactions that we studied occurred in powdered mixtures of variable particle size, the geometry of the reaction interfaces was poorly defined.

We selected the Ti–B chemical system for study because of its strong exothermic reaction ($\Delta H_f = 323$ kJ/mol). The calculated adiabatic temperature for the reaction $Ti + 2B = TiB_2$ is 2900°C.

Multilayer Deposition

We deposited the titanium by direct-current magnetron sputtering and the boron by radiofrequency magnetron sputtering. The interlayer-pair thickness varied from 5 to 40 nm in the ratio of 5.35 nm Ti/4.65 nm B, as calculated from the equation $Ti + 2B = TiB_2$. For example, in a 20-nm-thick interlayer pair, the titanium layer was 10.7 nm, and the boron layer was 9.3 nm. We deposited reactive multilayers up to 2 μm thick on water-cooled substrates of glass, copper, single-crystal silicon, and Al_2O_3. The cooled substrate was essential to retard any reaction during the deposition process. Localized ignition of a multilayer by a mechanical or electric probe caused a flame front to spontaneously propagate parallel to the interfaces and entirely consume the multilayer in about 2 ms. If the correct ratio (as described above) is maintained during deposition, the reaction product is single-phase TiB_2.

The development of dense boron sputtering targets has recently made it possible to deposit optical-quality boron and Ti–B multilayer films. It took great effort to refine the deposition process to consistently produce interlayers of the correct ratio. If the boron layers are too thick, the excess boron acts as a diluent, decreasing the temperature and amount of heat per unit volume. Excess titanium, on the other hand, produces a two-phase product of TiB_2 and TiB. In either case, the overall reaction is less energetic.

Effect of Interlayer Thickness on Flame-Front Velocity

According to a theoretical model derived by Armstrong (1990), the velocity of the flame front is related to several experimental parameters: the Arrhenius constant, activation energy, gas constant, flame temperature, thermal diffusivity, interlayer-pair thickness, and initial temperature. The model shows that the velocity of the flame front is inversely proportional to the interlayer-pair thickness; as the thickness increases, a point is reached where ignition can no longer occur.

We measured the velocities of Ti–B multilayers on glass slides with interlayer-pair thicknesses of 5, 10, and 20 nm. The total thickness of the multilayer film was 2 μm in all cases. We first measured the velocities with a Hycam camera at speeds of up to 11,000 frames/s, which allowed the flame-front configuration to be observed. Later, we designed and built a device that measured the velocities with a series of photodiodes. The velocity of many samples was 14 ± 2 m/s at all three interlayer-pair thicknesses.

This value for velocity disagrees with the theoretical expectations stated above. One possible reason for the discrepancy is the effect of interdiffusion at the Ti–B interfaces that occurs in the sputter deposition process. Small amounts of a reaction product will act as an inert diluent. The relative amount of interdiffusion would be inversely proportional to the interlayer-pair thickness, and it could account for the reduced flame velocities. Interdiffusion may thus explain the dependence of constant velocity on interlayer-pair thickness. Late in the year, we made films with greater interlayer-pair thicknesses to test this theory but did not have time to measure their velocities.

Formation of TiB_2 Foils

During the reaction on the glass slide, the temperature was high enough to melt the glass and crater its surface. Because the reaction product is denser than the reactants, thin pieces of TiB_2 were expelled from the surface of the slide as shrinkage occurred during the reaction. The thin TiB_2 foils were composed of equiaxed nanocrystals with a size of about 20 nm. We should be able to control the size of the crystals by controlling the thickness of the interlayer pair, with thicker pairs producing larger crystals. Thin nanocrystalline ceramic films may have some ductility.

We made the following observations regarding the reactivity of the multilayers. (1) The reactions confirm that exothermic systems react in a self-propagating mode. (2) Ti–B multilayers ignite and react at much lower temperatures than the corresponding powder

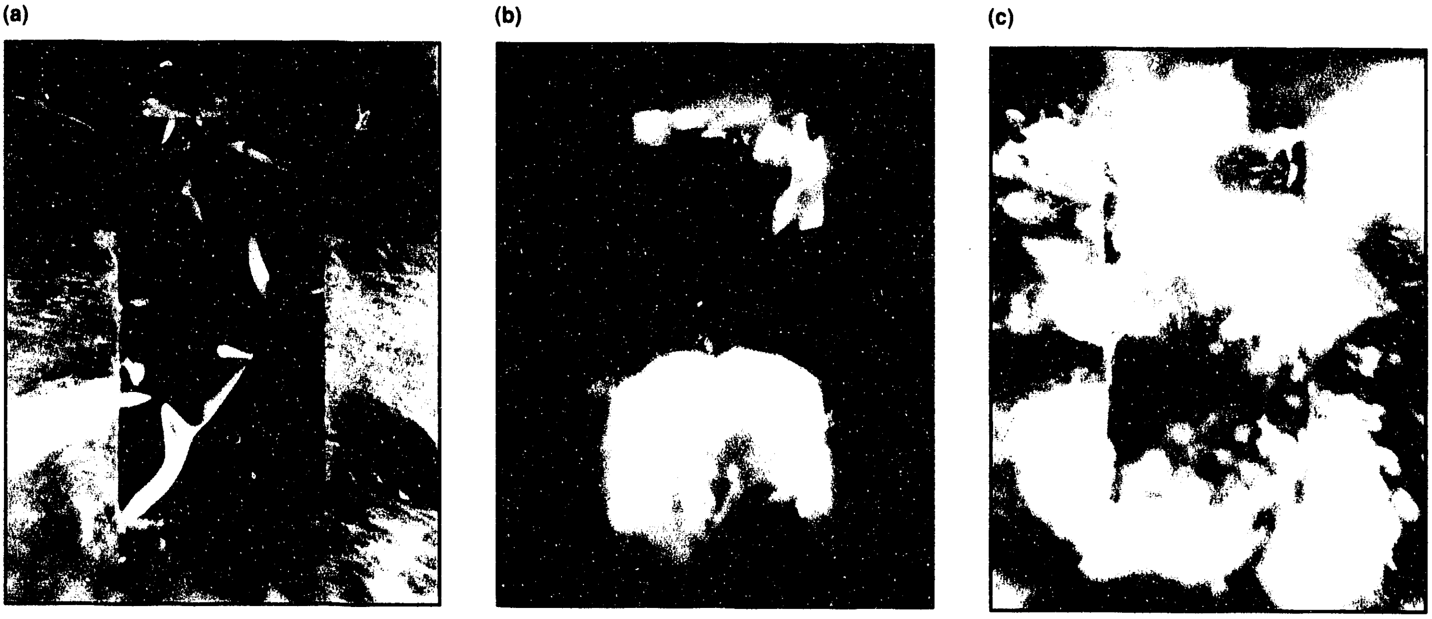

Figure 1. Photographic sequence of an exploding multilayer foil recorded at 6000 frames/s. (a) The 1-μm-thick foil consists of 10-nm layer pairs of titanium and boron. The 1-cm × 2-cm free-standing foil is supported by a thin aluminum frame. (b) The foil is ignited by a spark from the copper wire in the bottom part of this photograph. (c) The combustion continues at a velocity of about 15 m/s.

reactants. (3) The TiB_2 products are dense and have a unique nanocrystalline microstructure. (4) Flame-front velocities are fast—nearly 3 orders of magnitude faster than those of corresponding Ti–B powder reactions.

Possible Applications of RMLs

As a result of our work, we believe that RMLs can be used in many applications. The possibilities include the following.

- Explosive films. A 2-µm Ti–B reactive multilayer produces enough heat during a reaction to melt 5-µm-thick aluminum and gold films.
- Joining of ceramic–ceramic or metal–ceramic components. Diamond films may be joined to metal or ceramic substrates by using Ti–B reactive multilayers as a heat source to fuse a low-melting metal, e.g., aluminum.
- Superhard coatings. TiB_2 is a hard ceramic material and, with modification of the RML process, may produce coatings.
- Tamper-proof seals. RMLs are sensitive to mechanical, thermal, electrical, and chemical intrusion.
- Miniature fuses. Ignition occurs at the electrical current threshold.
- One-cycle switches. RMLs are conductive reactants to insulating products.
- Smart materials. RMLs respond to different physical stimuli. ◆

References

Armstrong, R. (1990), "Models for Gasless Combustion in Layered Materials and Random Media," *Combust. Sci. Technol.* **71**, 155–174.

Three-Dimensional Computer Simulation and Visualization of Deformation Processes

W. Hoover,* F. Wooten,* A. De Groot,* C. Hoover, J. Kallman,* M. Allison, and S. Lee

We used the SPRINT-2 computer (designed and built by Anthony De Groot) to simulate, visualize, and analyze three-dimensional processes, on a nano- and microscale. Specifically, we simulated isothermal indentation and plastic flow of crystalline and amorphous models of silicon. These models contained as many as 1 million atoms. (For more information about our three-dimensional simulations, see Hoover, 1991; Hoover et al., 1990, 1992; Kallman et al., 1992.) We studied silicon because its electrical, mechanical, and thermal properties are unique and of great commercial importance.

Many studies at the Laboratory involve high-strain-rate deformation, but no reliable theoretical model has been developed for these studies. For example, the Precision Engineering Department's single-point diamond-turning machine makes flat silicon or glass surfaces, which can be spoiled in the polishing process. In our project, we aim to provide a model in which strain rates can be reliably predicted, thus providing scientists an economical and efficient way to make ultrasmooth optical surfaces.

Simulations produced on the SPRINT-2 computer cost significantly less than those produced on the alternative a Cray supercomputer. For instance, our simulations, performed on a $30,000 desktop computer, would have taken more than 5000 hours on a single-processor Cray Y-MP supercomputer, costing millions of dollars. Using a simulated, x-ray and electron diffraction technique that follows structural change, we observed the transformation of a crystalline form of silicon to the amorphous phase, under high-pressure indentation. Our observations agree well with recent experimental findings.

---

*University of California at Davis.

To understand the fundamental mechanisms of these changes, we used visualization tools developed from the three-dimensional computer program, VRENDER. Figure 1 shows an indentation simulation. Despite the complex nature of the plastic flow, we characterized the surface and bulk energies separately, with 1% accuracy. This characterization allowed us to measure the plastic yield strength for this nominally brittle material. In the future, we hope to receive funding to combine these atomistic simulations with partially and fully continuum models using the DYNA3D program. ◆

References

Hoover, W. G. (1991), *Computational Statistical Mechanics* (Elsevier, North Holland, Amsterdam).

Hoover, W. G., A. J. De Groot, C. G. Hoover, I. F. Stowers, T. Kawai, B. L. Holian, T. Boku, S. Ihara, and J. Belak (1990), "Large-Scale Elastic-Plastic Indentation Simulations via Nonequilibrium Molecular Dynamics," *Phys. Rev. A* **42**, 5844–5853.

Hoover, W. G., A. J. De Groot, and C. G. Hoover (1992), "Massively Parallel Computer Simulation of Plane-Strain Elastic-Plastic Flow via Nonequilibrium Molecular Dynamics and Lagrangian Continuum Mechanics," *Comput. Phys.* **6**, 155.

Kallman, J. S., W. G. Hoover, C. G. Hoover, A. G. De Groot, S. M. Lee, and F. Wooten (1992), *Molecular Dynamics of Silicon Indentation*, Lawrence Livermore National Laboratory, Livermore, CA, UCRL-JC-111115.

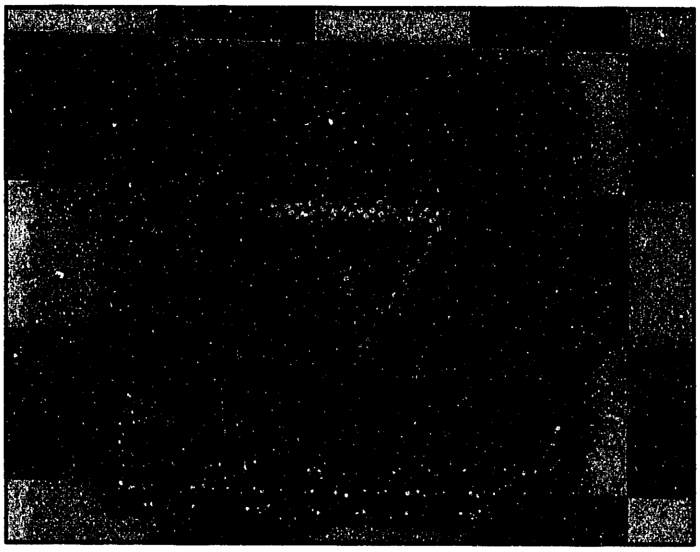

Figure 1. Indentation of 300,000 silicon atoms with a diamond indentor (Kallman et al., 1992).

Quest for Metallic Hydrogen

S. T. Weir, A. C. Mitchell, and W. J. Nellis

Hydrogen is the simplest of all atoms. By extension, hydrogen metal should be the simplest of all metals. However, scientists have not been able to measure the electrical conductivity of dense hydrogen and thus directly observe the approach of hydrogen to the metallic state. Researchers predicted, in 1991, that liquid hydrogen would metallize between 1.5 and 3 Mbar (150 to 300 GPa). In FY 1992, using 1 Mbar of pressure that we created with a reverberating shock wave, we compressed liquid hydrogen to a pressure of 1 Mbar and measured its electrical conductivity. By measuring the volume dependence of the hydrogen electronic bandgap at pressures derived from the electrical conductivity experiments, we can more accurately predict the pressure that will cause hydrogen to metallize. We can also establish a database to calculate the magnetic fields of Jupiter and Saturn, which are composed mostly of dense, high-pressure hydrogen.

To generate 1 Mbar of pressure, we accelerated an impactor to 7 km/s using a two-stage light-gas gun. The impact target was a thin layer of liquid hydrogen enclosed between sapphire disks (Figure 1). In this geometry, the shock wave reverberates between the sapphire disks, thus subjecting the hydrogen to a rapid series of shock waves. We "tuned" the pressure by changing the velocity of the aluminum impactor. Specimen density and pressure were calculated by computer simulation with LLNL's hydrogen database.

We used fast digitizing oscilloscopes to measure electrical conductivity and analyzed the data so we could determine the electronic bandgap vs density that leads to the metallizing pressure. Because conductivity results from the thermal excitation of electrons from the valence to the conduction bands, our experiments yielded information on the bandgap width. The reverberating shock method that we used to compress the hydrogen is quasi-isentropic; therefore, it is ideal for measuring electrical conductivity. Because the temperature is less than the bandgap, the dense hydrogen remains in the condensed-matter phase.

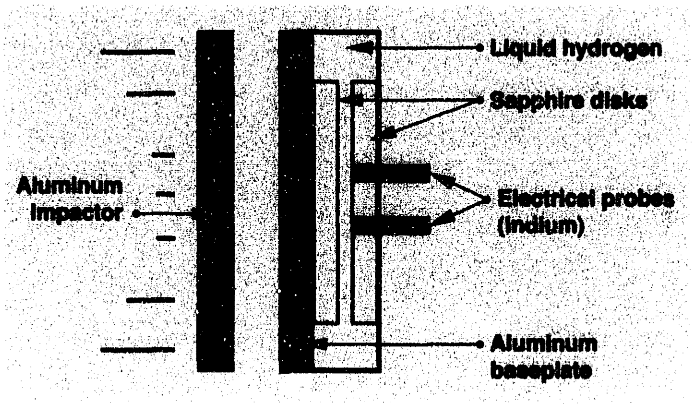

Figure 1. Schematic of electrical conductivity setup for measuring shock-compressed liquid hydrogen. This is the first measurement of the electrical conductivity of dense hydrogen at megabar pressures.

Electrical conductivity data for deuterium shocked to 1 Mbar were on order of 10 $(\Omega \cdot \text{cm})^{-1}$ and agreed with our predictions. The calculated temperature was 2440 K. The calculated density was 1.18 g/cm^3, a factor of 7 greater than the initial density. By comparison, the density of metallized hydrogen is estimated at about 2 g/cm^3. Our conductivity data reflect the step-like increases in the temperature and density as the specimen reverberates between the sapphire disks. The experiment took about 100 ns. Our preliminary results indicate that the electronic bandgap is 7 eV at 1 Mbar, a considerable decrease from 15 eV at zero pressure. This data point is an increase in pressure by a factor of 5 over data we derived measuring a single, nonreverberating shock.

We have determined that hydrogen's conductivity is more than 200 times greater than sapphire's for our 1-Mbar data point. Although sapphire is readily available and good for developing experimental techniques, it conducts electrically at about 1.5 Mbar, thus limiting the pressure we can use. In FY 1993, we are planning to fabricate specimen-containing disks from diamond, which remains insulating up to pressures of about 2 Mbar. ◆

Section 8

Biology and Biotechnology

Laboratory Directed Research
and Development FY 1992

On the previous page. Computer-processed images of chromosomes that have been reacted to identify specific genes.

Isotope-Labeled Immunoassay for Chlorinated Hydrocarbons and Small Haptens

J. S. Vogel, K. W. Turteltaub, and C. E. Frantz

Immunoassays are a common tool for detecting natural or introduced compounds in biological or ecological systems. Such assays exploit the natural binding a class of proteins called antibodies to specific chemicals. Virtually any compound can be detected by immunoassay if an animal host can be induced to make antibodies through an immunological reaction to the compound. Small molecules, such as drugs or chemicals that do not themselves induce an immunological response (haptens), must be attached to larger proteins to bring about antibody production in an animal. Alternatively, a cultured cell line can be established that produces the desired antibodies in purer form.

Immunoassays can be performed in many ways. The essential elements are a labeled antibody or anylate, an equilibrium reaction of the antibodies and anylates, and then separation of bound antibodies and anylates from remaining unbound components. The amount of label separated with the bound fraction or left behind in the free fraction is quantified to determine the fraction of total bound anylate.

The radioimmunoassay (RIA) remains the conceptually most simple immunoassay. A radioactive label with a high specific activity, such as a short-lived isotope of iodine, is easily detected through its decay products. However, high-specific activity in a labeled compound or protein implies that the amount of label changes with time and thus requires corrections for radioactive decay. The stock of the labeled compound must also be renewed as the label decays.

To avoid such difficulties, to reduce radioactive waste, and to simplify equipment, researchers have developed several other labeling schemes. Examples are the enzyme immunoassay (EIA) and fluorometric or chemiluminescent assays. These schemes often involve attaching larger molecular labels, although some depend, like RIA, on the inclusion of a single, rare ion. Some assays also include chemical amplification of the labeling effect to increase sensitivity.

Direct and Competitive Immunoassays

Researchers can use any assay label to design direct or competitive immunoassays. Direct assays demonstrate simple binding kinetics and can be used in developing assay protocols for new compounds. In one direct assay, the labeled target compound is equilibrated with known amounts of antibody to quantify the degree of binding after suitable separation. In another direct approach, an excess of labeled antibody is used with the anylate immobilized in or on a vessel. After binding, the free antibody is removed by washes, and the remaining label is a direct measure of the amount of immobilized ligand.

Neither the antibody itself nor the compound to be assayed is labeled in a competitive assay. This type of assay is more appropriate for most environmental or medical applications because few prelabeled chemicals are used as drugs or result in toxic contaminants. A labeled version of the target anylate is added to a solution containing the sample to be assayed along with a limited amount of antibody that binds both the labeled chemical and the compound to be quantified with similar affinity. Separating and quantifying the bound labels provide a measure of the unlabeled molecules also bound to the separated antibodies. Calibration curves provide the final concentration of the unknown sample.

The Isotope-Labeled Immunoassay

In the past two years, we developed direct and competitive forms of an isotope-labeled immunoassay (ILIA) that maintains the simplicity of a single radioisotopic label. The assay greatly increases sensitivity by directly quantifying the isotopic label through accelerator mass spectrometry (AMS) instead of detecting radioactive decay. Because we efficiently use long-lived isotopes, such as ^{14}C or even ^{129}I (half-life ≈ 16 million years), stable and chemically exact labeled analogs can be used in direct assays to investigate protein-binding kinetics and in competitive assays to quantify compounds in natural solutions.

In short, mass spectrometry with a tandem electrostatic accelerator extracts isotopic ions from a sample and identifies and counts them with an efficiency of 1 to 10%. Whereas 83 years is required to count 1% of a ^{14}C sample using decay counting, our measurements are made in only a few minutes from samples as small as 0.2 to 2.0 mg. Figure 1 shows the sensitivity and the precision with which our AMS system can quantify small amounts of labeled compounds in solutions. We are most precise in quantifying 10 amol (1 amol = 10^{-18} mol) to 10 fmol (1 fmol = 10^{-15} mol) of ^{14}C in 1-mg samples, but the range is easily extended through dilution.

New Protocols and Experiments

Our goal is to mate the sensitivity of AMS to the specificity of competitive immunoassays. We first expanded on the results of a hybridoma research group at LLNL. This group had developed monoclonal antibodies to hydrophobic chlorinated hydrocarbons: heptachlor (an insecticide) and dioxin (or TCDD, the polychlorinated biphenyl that is toxic to rodents and can become concentrated in fatty deposits of exposed humans).

During our first year, we explored the kinetics of and protocols for binding and separating heptachlor. This work prepared us to develop an assay sensitive enough to detect chlorinated hydrocarbons in small fat biopsies. We also developed the methods for converting hundreds of carbonaceous samples per week into graphite for measurement by AMS. This high sample throughput is necessary for other biomedical applications of AMS, but it is particularly important in processing the many samples required to establish the response curves of assay protocols.

Our mating of technologies has been successful in the difficult quantification of small amounts (typically picograms) of hydrophobic compounds whose binding to hydrophobic sites on vessels and separation media could easily dominate the antibody binding. We used affinity chromatography materials to separate antibodies and their bound anylates from the assay solutions. Although protein-coated, macroporous glass beads worked well, the best types are no longer manufactured. We developed our own bead coatings and began investigating a new product whose protein coatings on a single,

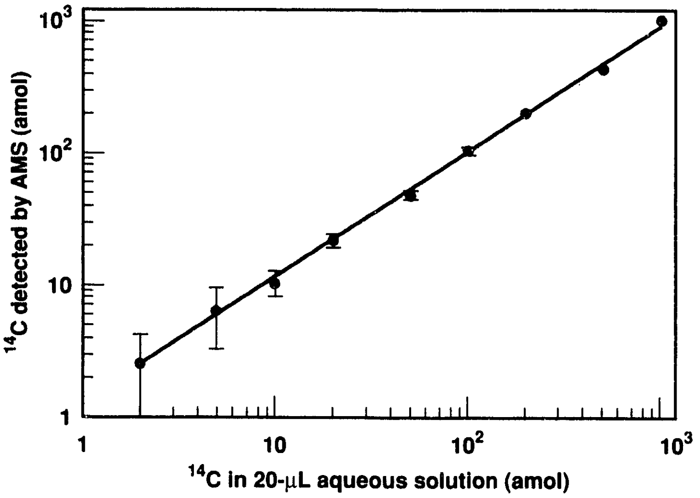

Figure 1. Average of three measurements by AMS of known amounts of a radiocarbon-labeled compound in a diluent (100 μL of 10-μg/μL tributyrin in methanol). These results demonstrate the sensitivity of AMS for attomole (10^{-18} mol) quantifications.

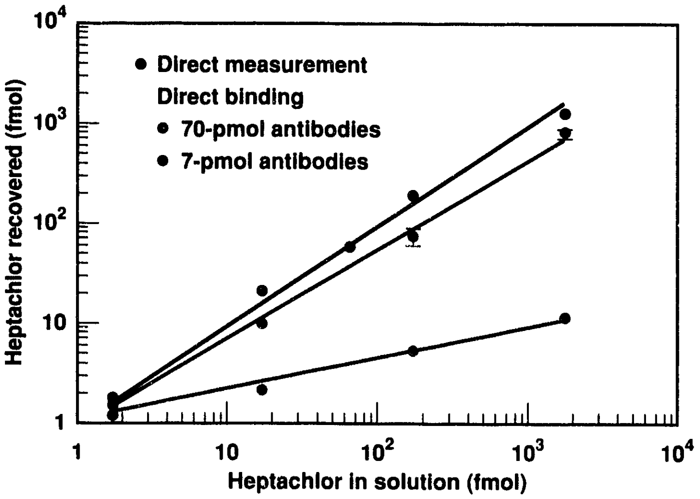

Figure 2. Direct-measure and direct-binding assays of heptachlor in solution. These results show the effectiveness of our separation and dilution protocols. The antibody binds too weakly to heptachlor for a low-concentration immunoassay to work.

large bead may provide even simpler separations. Because all samples must be dried for combustion to CO_2 and subsequent conversion to graphite, we maintained the integrity of the separated fraction by dilution in methanol containing tributyrin. As the methanol evaporates, the tributyrin retains the volatile heptachlor in micelles. Although we could quantify heptachlor through direct assays (Figure 2), the affinity constant (K) of the particular antibody was insufficient for sensitive, low-concentration assays ($1/K \approx 750nM$). We showed that this association constant was invariant over 6 orders of magnitude.

We obtained antibodies to the ubiquitous herbicide, atrazine, from researchers at UC Davis. The affinity of this antibody system is several orders of magnitude higher than that of the previous system, and it is suitable for assays in femtomole quantities. However, the antibody recognized less than 1% of the chemical fraction containing the ^{14}C label. One advantage of using ^{14}C as an isotopic label, rather than the more easily incorporated ^{3}H or $^{125,131}I$, is the stability of the label within an essential ring or invariant molecular structure. The label was intact within the atrazine ring, but a portion required for antibody recognition was not.

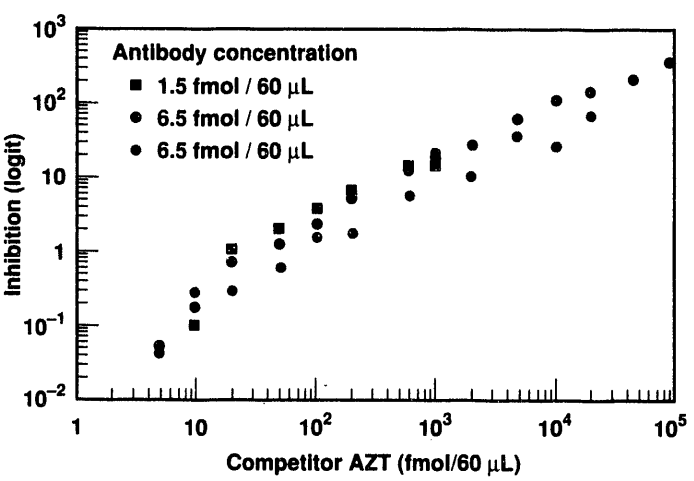

Figure 3. Measured response of our competitive ILIA vs added, unlabeled competitor AZT. Response is plotted as logit of inhibition, where logit $x = \ln[x/(1-x)]$. These data show that ILIA with AMS yields precise measurements over a wide range of concentrations.

We also demonstrated competition assays for azidothymidine (AZT), a drug that is effective in slowing HIV replication. Figure 3 shows the measured response (inhibition) as a function of unlabeled AZT added to a total volume of 60 μL containing 20 fmol of 92.3%-labeled ^{14}C-AZT and only 1 and 5% the amount of antibody recommended for RIA with this antibody. This competition assay can quantify the unlabeled AZT over 4 orders of magnitude using only a single concentration of labeled compound. ILIA extends the range of quantifiable concentrations because AMS measures the isotope label precisely, even at low concentrations. In other assays, especially RIAs, the signal from the label weakens as the unlabeled compound competes for antibody binding sites. Data from our direct-binding assays with this antibody show that the simple kinetics of a single mass-action binding describe the interaction well over 4 orders of magnitude with the association constant at low concentrations ($K \approx 1/714pM$), the same as measured in RIAs at higher concentrations.

We conclude that our ILIA can be a thousand times more sensitive than other assays using the same antibody. In collaboration with other researchers, we are ready to apply this new assay directly to studies of AZT interactions with DNA. We will also develop an ILIA for dioxin, for which new polyclonal antibodies may be developed with our collaborators. ◆

References

Vogel, J. S. (in press), "Rapid Production of Graphite without Contamination for Biomedical AMS," *Radiocarbon* **34**.

X-Ray–Laser–Based Biological Microimaging

R. London, M. Rosen, S. Maxon, D. Eder, and R. Ratowsky

Our project aims to improve x-ray lasers and x-ray imaging techniques so that new advances in structural biology research are possible. This project is particularly timely given that progress in genome mapping is helping scientists better understand the relation of structure and function in cellular biology. In FY 1992, we mainly focused our efforts in two areas: studying x-ray imaging modes, and theoretically advancing the design of x-ray lasers to pursue microimaging. These efforts included improving the output of lasers that work near 4.4 nm, the long wavelength end of the "water window" (the preferred wavelength band for biological x-ray microscopy); improving the spatial coherence of x-ray lasers; designing more efficient, water-window x-ray lasers that can be pumped by a kilojoule-class, table-top glass laser; and exploring new x-ray–laser schemes to work with 1-J-class, ultrashort-pulse lasers. In addition, we explored the role of x-ray–induced sample damage and exposure duration in microimaging. We worked with experimental scientists on x-ray–laser and microscopy experiments mainly at the Nova two-beam facility.

Imaging Modes

After analyzing the capabilities of various x-ray microscopy and holography schemes, we chose direct imaging using a multilayer mirror condenser and a zone-plate objective for initial studies. Then with a 4.5-nm tantalum laser, we made high-resolution (50-nm) images, first of test patterns and then of rat sperm-cell nuclei (Da Silva et al., 1992). Figure 1 shows an image of this nucleus. We studied damage caused by x-ray–induced chemistry and hydrodynamics and determined that images of 30 nm or less will likely require exposures of less than 1 μs to avoid chemical diffusion. Exposures of about 30 ps may be required to avoid hydrodynamic blurring. Such short exposures can only be made with an x-ray laser, not with a synchrotron-based source.

X-Ray–Laser Designs

We explored designs for nickel-like lasers (e.g., tantalum at 4.5 nm) that achieve higher gain by using higher-density and higher-temperature plasmas than the current lasers. We also designed nickel-like x-ray lasers using light-element (e.g., lithium) ion cooling. For x-ray lasers with very short wavelengths (1.0 to 1.5 nm), we pursued designs to create a very hot x-ray source by illuminating a solid target with ultrashort-pulse, high-intensity beams. The x rays create a population inversion in an adjacent lasant material by rapid inner-shell photoionization. Finally, we pursued the creation of x-ray lasers with table-top, joule-class, ultrashort-pulse lasers by experimenting on lithium-like oxygen at 17.3 nm.

In the area of x-ray–laser coherence, we extended a modal theory to include realistic, smooth gain and density profiles. We developed ray-optics–based scaling laws for coherence that agree well with more detailed wave optics models. We also developed computer codes for detailed x-ray propagation calculations to predict the beam pattern and the coherence function. These

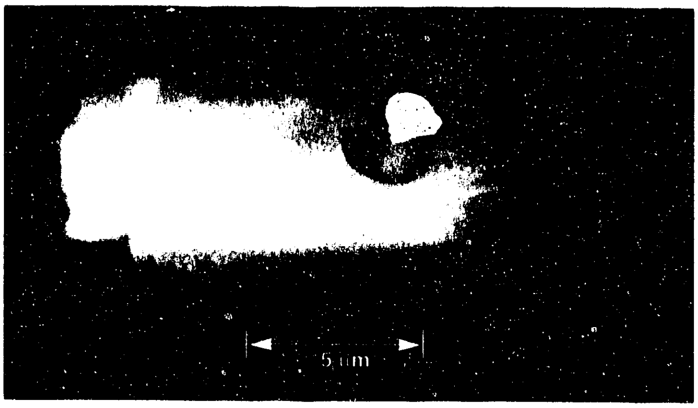

Figure 1. X-ray–laser microscope image of a rat sperm cell nucleus. We created this image with a 4.5-nm tantalum laser.

codes are being used to model measurements and to design lasers with better coherence. Last, we started work on the effect of plasma-density inhomogeneities on coherence.

To improve both efficiency and coherence, we are considering using x-ray multilayer mirrors to create multipass amplifiers. We developed a modeling code for x-ray multilayer mirror performance, including the effects of x-ray heating from the laser plasma. With this code, we have successfully modeled reflectivity measurements of x-ray–heated mirrors. We are now using this code to test alternative mirror materials. ◆

References

Da Silva, L. B., J. E. Trebes, R. Balhorn, S. Mrowka, E. Anderson, D. T. Attwood, T. W. Barbee, Jr., J. Brase, M. Corzett, J. Gray, J. A. Koch, C. Lee, D. Kern, R. A. London, B. J. MacGowan, D. L. Matthews, and G. Stone (1992), "X-Ray Laser Microscopy of Rat Sperm Nuclei," *Science* **258**, 269.

Development of Transgenic Mouse Technology

L. H. Thompson, C. A. Weber, J. S. Capehart, and R. L. Balhorn

A transgenic mouse is one that is genetically altered by experimental manipulation. Two kinds of transgenics are proving to be scientifically invaluable in biomedical research. In the first approach, a foreign gene is introduced into the single-cell mouse embryo (the pronuclear stage) by a method called pronuclear injection. The "trans" gene is inserted into a chromosome of the embryo and becomes a permanent part of its genetic makeup as the embryo develops into a mouse. The second approach, which is more complex and requires greater scientific expertise, seeks to alter the expression of a specified mouse gene. The goal may be simply to destroy the function of a gene, an alteration called a gene knockout. However, more subtle changes allow researchers to modify the properties of a gene without destroying the protein it encodes—a procedure generally known as gene targeting. Our goal is to acquire the technical capability and knowledge to perform both of these experimental procedures at LLNL.

In FY 1992, we achieved the goal of producing transgenic animals by pronuclear injection. We used a gene that codes for protamine, a protein that is essential for the development of the mature sperm. Protamine molecules facilitate the extremely tight packing of DNA in the dense sperm head. Normal mice have two types of protamine genes, protamine-1 and -2. To study how protamine accomplishes the amazing packaging of DNA, we constructed a mutated version of the mouse protamine-2 gene. The mutant gene should make protamine-2 in which two of its amino acids are altered from lysine to arginine.

Among 50 offspring arising from fertilized eggs that were injected with the mutant gene, we identified two mice carrying the mutant gene by analysis of DNA from a portion of the tail. We will breed these two mice to propagate the transgene and create a larger supply of animals whose sperm can be analyzed biochemically. We hope to find that the mutant gene produces a protein. If so, these new animals should allow us to study how a minor, specific change in the structure of protamine-2 influences sperm architecture as well as fertility. We will apply this knowledge to study men in which abnormally shaped sperm may relate to infertility.

We have also made progress toward the goal of gene targeting, a gene-replacement process. This manipulation is done by using cells, derived from a mouse embryo, that grow in culture but maintain their ability to participate in embryological development when introduced into another embryo. Hence, these cells are called embryonic stem (ES) cells. We can introduce foreign DNA into ES cells and enrich for rare cells in which a gene segment has been replaced with one containing a desired alteration. The resulting mutant cells are then cloned, i.e., grown into large, genetically pure populations. DNA samples from many clones must be analyzed to test whether the desired mutation is present. Once identified, mutant cells are injected into embryos at the blastocyst stage. As these embryos develop into mice, some are chimeras, i.e., genetic mosaics, recognizable by predictable coat color patterns. Our goal is to obtain chimeras in which the germ tissue (ovaries or testes) contains the mutation. Germline chimeras can be bred to "fix" the mutation into all cells of the mice in the next generation.

ES cells are notoriously fastidious in terms of culture conditions, and they become chromosomally abnormal if grown too long. We have succeeded in establishing ES cultures beginning with 3.5-day-old mouse embryos. Chromosome analysis suggests that several of these cell lines may be suitable for making chimeras, a process that will require several months to evaluate.

Once we have high-quality ES cells, we plan to produce a gene knockout for a DNA-repair gene that is required for rejoining breaks in the DNA molecule. A repair-gene targeting vector is now available for this work. Transgenic mice that are defective in repairing damage to their DNA are of great interest for several reasons. First, they should be unusually susceptible to mutation by radiation or chemical mutagens, thereby providing a more sensitive test system to study the origin of mutations. Second, repair-deficient mice will provide animal models for the rare human genetic disorders in which DNA repair is defective and associated with elevated cancer risk.

In FY 1993, we must make additional transgenics for the protamine-2 gene. We expect variability in the level of expression of the mutant protein, and some transgenes may not express well. The sperm of mutant mice expressing the mutant protamine will be studied in detail elsewhere. To perform gene targeting, we aim to first produce chimeric mice from our own ES cells to validate the transgenic procedures. We will then attempt to derive ES cells that are mutated in a DNA-repair gene and to obtain a mouse that is defective in repair. ◆

Low-Level Detection of DNA and Protein Damage

J. S. Felton and K. W. Turteltaub

The United States is spending billions of dollars to manage environmental problems and to protect human health from harmful chemicals, primarily carcinogens. The expenditure of funds is prioritized by a rationale that assumes rodents are the same as humans and that high-dose exposures are proportional to low-dose exposures. These assumptions were impossible to test until recently.

Measuring Molecular Damage

We have taken advantage of the highly sensitive measurement of DNA–chemical and protein–chemical interaction using accelerator mass spectrometry (AMS). We coupled this approach with traditional methods of ^{32}P-postlabeling and two-dimensional gel electrophoresis to examine the dosimetry problem. DNA–chemical and protein–chemical interactions are indicators of how the body handles chemical exposure and what effects may result.

Our methods, particularly AMS, allow us to measure molecular damage that leads to mutation and cancer in the DNA of specific tissues at doses equivalent to dietary and environmental exposures. For many cases, the exposures are 10^6- to 10^7-fold lower than the doses used in animal cancer studies on which today's risk estimates are based. Comparing how molecular markers behave at high vs low doses is critical to understanding how animal cancer tests relate to human cancer risk from chemical exposure. Preliminary results suggest linearity during acute exposures over 5 magnitudes of dose; however, chronic exposure may be more complicated.

Dietary Carcinogenesis

In one series of studies, we followed the DNA–chemical interactions that occur with a carcinogen present in the typical American diet. This carcinogen, called MeIQx, is found in cooked grain and meat products. We added MeIQx to a rodent diet so the animals would consume an amount of MeIQx equivalent to what a human would receive eating 200 g of cooked ground beef per day (approximately two hamburgers). Then we monitored interactions of the chemical and DNA to determine the levels of interaction and the time for the damage to stabilize.

We found the DNA–MeIQx interaction took almost 40 days to stabilize, whereas the chemicals stabilize in the tissues after only 2 to 10 days (Figure 1). The levels of MeIQx–DNA interaction at this dose 7 days after beginning the study were proportional to those for the rodents fed 10^6-fold greater doses for the same length of time.

Comparison with other endpoints for toxicological and mutational damage and across species will ultimately allow regulatory risk-assessment scientists to judge whether we have set our environmental cleanup priorities properly. ◆

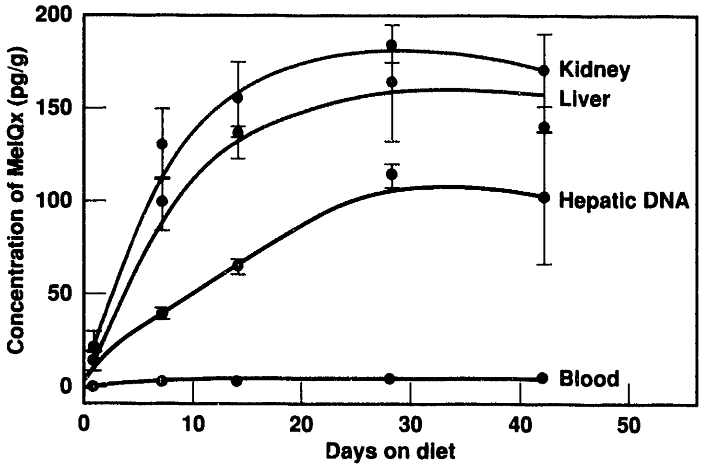

Figure 1. Concentrations of radioactively labeled MeIQx in tissues and hepatic DNA of rats fed daily doses of this carcinogen equivalent to that in the typical American diet.

Developing Tritium and ^{41}Ca as Tracers for Biomedical Applications of Accelerator Mass Spectrometry

M. L. Roberts, J. R. Southon, I. D. Proctor, and J. S. Vogel

We are using accelerator mass spectrometry (AMS) to develop tritium and ^{41}Ca as isotopic tracers for biomedical research and clinical use. Although tritium, with its short half-life, is routinely measured using scintillation counting techniques, the factor of 100 gain in sensitivity theoretically obtainable with AMS makes development of biomedical tritium AMS worthwhile.

In FY 1992, we explored accelerator-related backgrounds and tritium sample preparation techniques. We obtained calibration standards from water samples that had a known tritium content determined from scintillation counting techniques. These water samples were diluted, chemically reduced, and the resulting gas absorbed into titanium metal in a sealed-tube sample preparation process. We demonstrated sensitivity to tritium to hydrogen ratios between 10^{-9} and 10^{-14} using 5-μL water samples. We also obtained a tritium to hydrogen background ratio of 10^{-14} in these trials. Figure 1 compares measured and expected tritium to

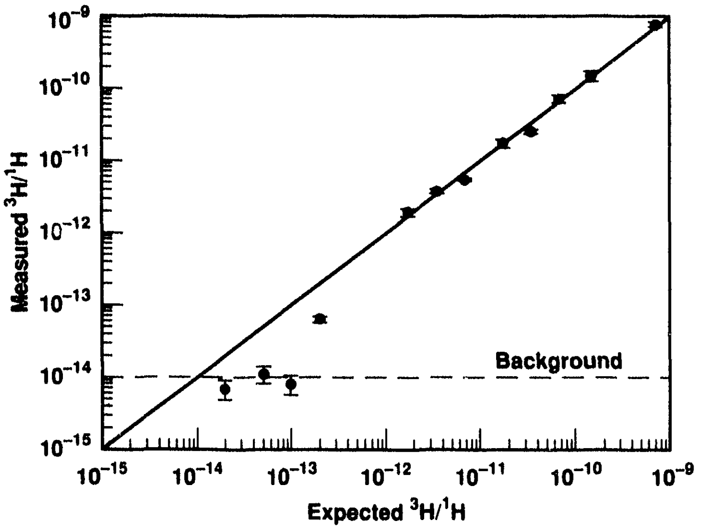

Figure 1. ^{3}H/^{1}H ratios as measured on the present spectrometer compared to expected ^{3}H/^{1}H ratios. Both measured and expected ratios are based on a diluted standard and demonstrate sufficient sensitivity for pilot biomedical studies.

hydrogen ratios based on dilution of a standard. The sensitivity and linearity obtained are adequate for pilot biomedical experiments. In future work, we will extract tritiated materials from organic samples.

Initial runs with ^{41}CaF$_2$ samples, which produce a ^{41}CaF$_3^-$ beam, demonstrated a sensitivity and efficiency acceptable for clinical experiments. We obtained a ^{41}Ca:^{40}Ca sensitivity of 3 x 10^{-13}. We are developing sample preparation chemistries for CaH$_2$, a compound that produces negative beams more efficiently so that more rapid and precise measurements can be made.

In FY 1993, we will collaborate with researchers at UC Davis. We will conduct experiments using ^{41}Ca as a tracer to study cell damage caused by massive uptake of calcium when the blood supply to heart tissue is interrupted. ◆

Algorithms for DNA Sequence Analysis

E. W. Branscomb, Shin-yee Lu, M. E. Colvin,* and R. S. Judson*

A major current objective of the LLNL Human Genome Center is to complete a physical map for chromosome 19. In coming years, we will place more emphasis on completely sequencing large stretches of chromosome 19 DNA and analyzing these sequences. Our project aims to develop the algorithms and computational tools required by this shift of emphasis.

In DNA, genetic information is encoded in the sequence of four, paired nucleotide bases: adenine, thymine, cytosine, and guanine. The process of DNA sequencing, or mapping these bases, has typically been done by a so-called "shotgun" approach. The method involves sequencing randomly overlapping, small fragments of DNA—200 to 500 base pairs (bp)—taken from a much larger piece, such as 40,000 bp. However, the total number of base pairs that must be sequenced is actually 5 to 10 times the size of the original piece, representing a five- to tenfold redundancy. The original, large sequence can be recovered, in principle, by pasting together fragments that share common subsequences.

The sequence-assembly step is computationally difficult for two reasons. First, we require many fragments (1000 or more), and directly comparing every pair to determine which pairs contain common subsequences is slow. Second, errors arise from data collection,

---

**Sandia National Laboratories, Albuquerque, NM.*

imperfections in the fragmentation processes, and the statistical nature of fragment selection. Existing assembly methods use sequence-alignment programs to determine overlap between fragments and optimization methods to paste overlapping fragments together. Such methods generally do not perform well for assembling large sequences.

We have developed a new approach that uses a key-search method. First, we encode every 15-base segment of every fragment into an integer, called a key. Keys are sorted and stored in a table together with pointers to the fragments in which they were found and the locations along those fragments. Starting from any key, we can determine the adjacent key (to the right or left) in the original sequence by examining all fragments that contain the current key (say, bases 1 through 15), thus generating a consensus for the next base (base 16). "Consensus" in this context refers to our statistical confidence that the next base is actually adjacent, as it is in the original DNA. We generate the next key from bases 2 through 16 and repeat the process, key by key, until we detect an end condition.

The computational complexity of this approach is nearly linear, with respect to the size of the DNA sequence, rather than proportional to the square of the size, as in current methods. Error correction is automatically built into the method through the consensus calculation at each base.

To evaluate our approach, we tested a known DNA sequence (~33,000 bp), which we fragmented synthetically using a program that simulates shotgun sequencing. A representative simulated fragmentation would assume tenfold coverage, 200- to 400-bp fragment length, and random cutting sites. We then corrupted the sequence with errors at a realistic rate determined from published data. Errors increased exponentially along the length of the fragment, from 1% for lengths <200 bp to 7% at 500 bp. In contrast, our assembly program reconstructs the complete sequence except for a residual error rate of about 2%.

The reconstruction uses <40 min on a Sun Sparc Station II. We also tested the program with fragment data sets corresponding to lower coverage (eight-, nine-, and tenfold coverage). However, as the coverage decreases, the reconstruction can only generate islands because some regions of the original sequence are not covered in the fragment database. (From Monte Carlo simulation, tenfold coverage is the minimum required to cover the entire sequence reliably.)

Our current push is to reconstruct a large sequence from an actual fragment data set from chromosome 19 produced by collaborators at the National Institutes of Health (NIH). Because the NIH data set has a relatively low coverage of five- to sixfold, we expect to find gaps in the original sequence. However, early results show the reconstruction code to function well, generating several islands in the 6,000- to 10,000-bp range for a total sequence of approximately 40,000 bp. Other real fragment data sets are being generated at the LLNL Human Genome Center. We will test our assembly program on these and other data.

The major advantages of our approach are computational efficiency and the potential for generating more reliable reconstructions. Our method can generate a complete consensus sequence, the exact location at which each fragment resides along the consensus sequence, and locations where errors occur. This information provides data necessary to statistically estimate confidence in the reassembled sequence. Biologists consider such estimation critical for their applications and often fault current assembly methods for lacking the ability to estimate confidence. ◆

Cancer-Risk Assessment for Chemicals

K. T. Bogen, J. N. Lucas, and T. Straume

Correlations between mutagenic and carcinogenic potency, even if fairly weak, offer the possibility of assessing the potential cancer risks arising from complex mixtures or unidentified compounds, such as those in mixed-waste samples from hazardous waste sites. However, cytotoxicity (cell killing) is a confounding factor in any such application of dose-response relations observed in animal bioassays of chemical carcinogenicity. For nongenotoxic compounds, for example, the cytotoxicity that may be observed at high doses is not expected at very low doses. Therefore, carcinogenic potencies measured in animal bioassays may grossly overestimate true cancer risks presented by low-level exposures to compounds such as chlorinated solvents associated with DOE hazardous waste sites.

Database Construction

We are exploring the interplay between induced genotoxicity (damage to the genetic material, DNA) and cell killing and the potential role of this interaction in cancer-risk assessment. First, we constructed a database of mutation- and cancer-potency information for ~100 carcinogenic and mutagenic chemicals. We extracted information from seven published volumes of Ames-test data (on bacterial mutagenicity) and three published volumes of rodent-bioassay cancer-potency (TD_{50}) data. To assist in the data analysis, we (Bogen, 1992a) completed a Mathematica-based program called RiskQ. We are focusing on the extent to which observed correlations between mutagenic and carcinogenic potency may improve when the analysis is restricted to direct-acting, potent mutagens. We will supplement our analysis using newly published carcinogenicity data.

Mathematical Modeling

In a second effort, we attempted to more reliably establish empirical relations between chemical genotoxicity and cytotoxicity. We (Bogen, 1992b) developed a mathematical model to predict the level of cytogenetic damage in human peripheral-blood lymphocytes (PBLs) after exposure to x rays, taking into account radiation-induced cytotoxicity. As shown in Figure 1, this model, when combined with models for radiation-induced cytogenetic damage and cell killing based entirely on in vitro dose-response data, adequately predicts previously published data on the loss of abnormal DNA structures in PBLs sampled from human patients treated with x rays (Buckton, 1983). We are now pursuing more general dosimetric applications of our model.

Fluorescence In Situ Hybridization

We are also contributing to the first experimental application of fluorescence in situ hybridization technology developed at LLNL. In this work, we are assessing cytogenetic damage induced by a genotoxic chemical in human PBLs. After unexpectedly finding that needed liver-activation enzymes are toxic to PBLs, we are modifying our original protocol. ◆

References

Bogen, K. T. (1992a), *RiskQ: An Interactive Approach to Probability, Uncertainty, and Statistics for Use with Mathematica (Reference Manual)*, Lawrence Livermore National Laboratory, Livermore, CA, UCRL-MA-110232.

Bogen, K. T. (1992b), *Reassessment of Human Peripheral T-Lymphocyte Lifespan Deduced from Cytogenetic and Cytotoxic Effects of Radiation*, Lawrence Livermore National Laboratory, Livermore, CA, UCRL-JC-111762.

Buckton, K. E. (1983), "Chromosome Aberrations in Patients Treated with X-Irradiation for Ankylosing Spondylitis," in *Radiation-Induced Chromosome Damage in Man* (A. R. Liss, New York, NY), pp. 491–511.

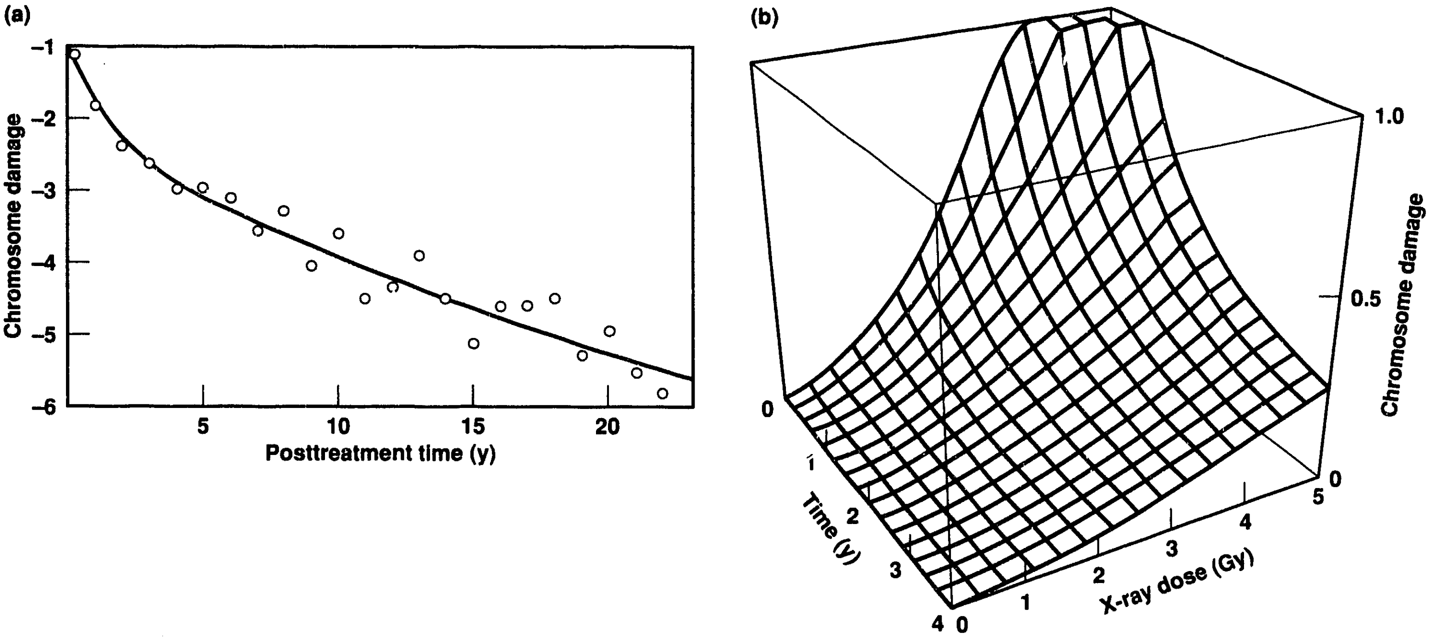

Figure 1. (a) New model (curve) of cytogenetic damage to human peripheral-blood T-lymphocytes. This model predicts previously published data (Buckton, 1983) on the loss of unstable, abnormal DNA structures (dicentrics plus centric rings per cell on a logarithmic scale). The cells were sampled from 190 ankylosing spondylitis patients up to 22 years after 10 treatments with 250-kV x-ray doses delivered over 2 weeks. (b) The same model of unstable chromosome damage as a function of both time and single, acute 250-kV x-ray dose.

Vibrometry: A Potential Screening Tool for Carpal Tunnel Syndrome

S. Burastero, P. Tittiranonda, K. Noonan, J. Spickard, D. Rempel,* and Y. So*

Repetitive motion injuries (RMIs) have been termed the "industrial epidemic of the nineties." Nationally, RMIs account for about 60% of the occupational illnesses reported in 1992 (U.S. Department of Labor, 1992). Carpal tunnel syndrome (CTS) is the most debilitating RMI and is common to jobs that involve sustained, repetitive movements or awkward postures of the hands and fingers, such as microelectronics assembly, data entry, and word processing (Silverstein et al., 1987).

Vibrometry measures the vibrotactile sensory threshold level of the fingertip at seven frequencies (between 8 and 500 Hz) and can detect CTS in its early stages, before irreversible nerve damage and disability occur. For years, measurement of nerve conduction velocity (NCV) was the standard CTS diagnostic tool. This method, however, is expensive (up to $500 per test), uncomfortable, difficult to administer, and prone to false negative results in early stages of CTS. As a result,

---

**University of California at San Francisco.*

suspected CTS cases are often treated empirically, without proper objective diagnostic documentation. In contrast, vibrometry is inexpensive (about $20 per test), noninvasive, simple to administer, and easy to interpret. Lundborg et al. (1986) used vibrometry in a referral hospital setting on 76 patients with severe CTS and showed a diagnostic sensitivity of 84%.

We began a workplace trial of vibrometry involving a sample of early onset CTS cases with standardized NCV testing. At least 100 LLNL employees with symptoms of CTS will be tested using vibrometry. We conducted preliminary tests of 39 LLNL employees (60 hands) with occupationally induced CTS. Preliminary vibrometry tests of 60 hands with CTS suggest 88% sensitivity compared with standardized NCV results. Typically, in the early stages of CTS, the peak threshold between 125 and 250 Hz is decreased. In advanced CTS, the vibration threshold is severely impaired at all frequencies, with the greatest decrements seen in the highest frequency ranges (Figure 1). Follow-up vibrometry scores correlated well with clinical assessments.

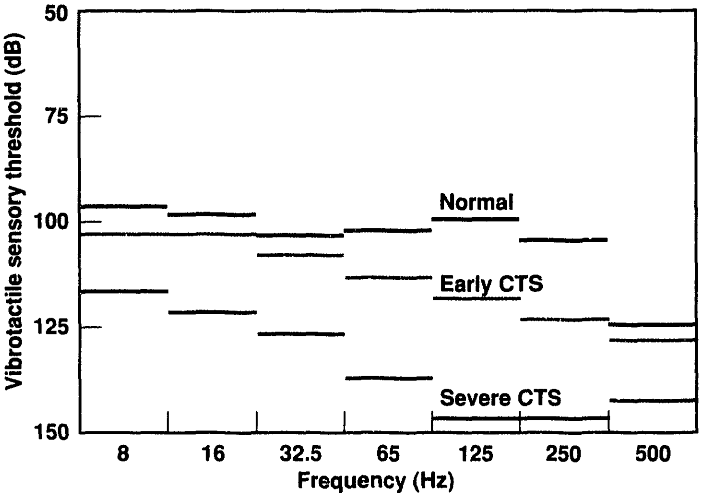

Figure 1. Typical vibrometry scores in CTS patients compared to normal scores.

In FY 1993, we will conduct a pilot test using vibrometry as a surveillance tool for relatively healthy employees who are at high risk for cumulative trauma injuries and will compare these readings with baseline population scores. We will then use a receiver operator curve to determine the optimal cutoff point for a positive test. We will follow these patients clinically to observe any development of CTS symptoms.

If ongoing research validates vibrometry on a large scale, it could be adopted as an "ergonomic biomarker" in surveillance programs for workers at risk of CTS, similar to audiometry in hearing conservation programs. Patients could then be treated early before their CTS becomes debilitating. Vibrometry might also be used as a screening tool for workers suspected of having nerve damage from exposure to solvents, pesticides, or other neurotoxic agents and may prove useful in field-testing new ergonomic equipment designs. ◆

References

Lundborg, G., A. Lie-Stenström, C. Sollerman, T. Strömberg, and I. Pyykkö (1986), "Digital Vibrogram: A New Diagnostic Tool for Sensory Testing of Compression Neuropathy," *J. Hand Surg.* **IIA**(S), 693–699.

Silverstein, B. A., L. Fine, and T. J. Armstrong (1987), "Occupational Factors and Carpal Tunnel Syndrome," *Am. J. Indus. Med.* **11**, 343–358.

U.S. Department of Labor (1992), *BLS Reports on Survey of Occupational Injuries and Illnesses in 1992, Bureau of Labor Statistics*, Washington, DC, USDL-92-548.

Identifying Biochemical and Micromechanical Processes through Acoustic Signals

W. J. Siekhaus, R. L. Balhorn, and M. Balooch

Medical professionals monitor the function of internal organs of a biological organism (e.g., the heart and lungs) by placing a listening device (stethoscope) onto the surface of the organism. In materials science and engineering, we assess the performance and failure of structural elements under load by acoustically monitoring their fracture. The recent development of scanning-probe microscopes has made it possible to locate with atomic resolution (1) biological molecules performing sophisticated functions, (2) sites on the surface of atoms where corrosion, gasification, or catalytic reactions occur, and (3) atomic sites where fracture occurs. This development is referred to as atomic force microscopy.

In our project, we use the scanning-probe microscope to position a microdetector in a stationary manner onto an identified site or object. We then electronically process the signals emitted by the site or object. Our goal is to identify microprocesses by characteristic signals emitted during specific reactions. The results of our work can be applied to biomechanical, biochemical, and inorganic reactions and to mechanical processes. Specifically, we aim to detect characteristic pulsations, configurational changes, or phonon emissions associated with the processing of DNA by polymerase. If successful, we will be able to establish an alternative procedure for sequencing DNA.

In FY 1992, we modified electronics, computer programs, instrumentation, and the environment so that we could place the microscope's cantilever tip in a stationary manner onto a submicrometer-sized object. We also modified the signal-processing electronics of the detector so that we could record the cantilever's vibrations. To demonstrate our ability of measuring acoustic vibrations in such small objects, we monitored a shrimp "egg" in its natural saline environment. We kept the egg in this environment because monitoring the biological function of enzymes requires that they be placed in liquid. We monitored the egg from its dry stage until the nauplius emerged from the egg. We then monitored the beat frequency of the nauplius at about 10 Hz (Figure 1). In summary, we developed a sensitive "microstethoscope" capable of working in liquid.

We reduced the electronic noise in our experiments by acquiring improved electronics, and we reduced the environmental noise by shielding the system from floor vibrations, air currents, and drift induced by thermal variation. In this manner, we reduced the total amount of noise by a factor of about 20, to 0.07 nm in the dry cell, while operating in the stationary mode. In the liquid cell, the noise was higher by about a factor of 2 because of the particular laser and detector that we used. By imaging objects of known size (dendrimers) in a range from 1 to 40 nm, we bonded and found enzyme-like objects on a suitable substrate.

In FY 1993, we plan to monitor vibrations of objects at the nanometer scale. Using techniques developed in

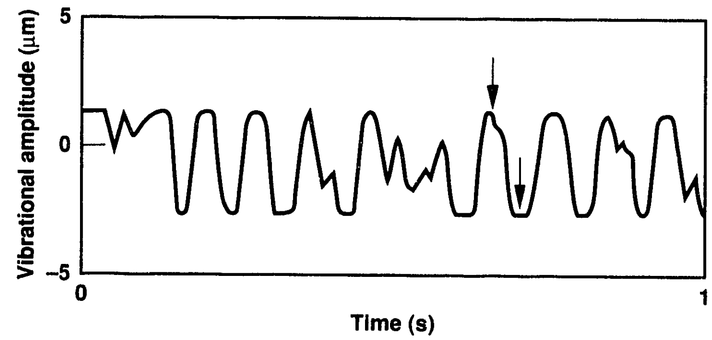

Figure 1. Vibrations of shrimp nauplius observed with atomic force microscopy. The vibrational frequency is about 10 Hz, and the amplitude (shown as the distance between arrows) is 2.77 μm.

the Biomedical Department, we will begin by holding *Escherichia coli* bacteria stationary on a substrate. We will locate the motor (100 nm) driving the cilium using imaging and monitor the vibrations associated with the motor (up to 300 Hz).

Ultimately, we will monitor vibrations of the Klenow fragment (the active part) of polymerase. First, we will place this fragment, with primer and substrate adsorbed, onto a substrate. Then after adding the water-soluble form of the bases that make up DNA to this liquid, using different concentrations for each base, we will identify the individual base being processed by the vibrations emitted, or we will identify the DNA base sequence by the time elapsed between vibrations. ◆

Digitally Enhanced Mammography

C. Logan, J. M. Hernandez, L. Mascio, R. Boroff,* G. Krauter, K. Noonan, and L. Fajardo†

Breast cancer is an important national health problem. In the United States, it kills 45,000 women each year, and the incidence of new cases increases annually, even when corrected for our aging population. To help mammographers screen the large number of mammograms, we developed a computer algorithm to locate microcalcifications in digitized mammograms. This improvement and others may help doctors detect breast cancer at an early stage, when treatment is more successful, and thus would increase the survival rate.

Breast x-ray imaging, or mammography, in combination with physical examinations is the most effective means for detecting breast cancer at an early stage, when it can be treated successfully. Mammography is the only method to detect microcalcifications, which often accompany breast cancer before it is palpable—that is, when a cancer is too small to feel in a physical breast exam. Because microcalcifications absorb x rays more strongly than soft tissue, they are visible in a transmission x-ray image.

However, to detect these microcalcifications, mammographers must systematically search the traditional x-ray film, using a magnifying glass. This task is tedious, time consuming, and subject to errors caused by fatigue or distraction. "Missed" malignancies are relatively common. For example, Bird et al. (1992) found that in 320 cases of breast cancer, 77 cancers (24%) were missed by screening mammography.

We use digitizing equipment and software developed for Defense Programs to convert standard film mammograms to digital format. We are the first to apply high spatial resolution (70 μm) and 12-bit (4096) contrast resolution to entire mammograms.

In FY 1992, we developed a computer algorithm to locate microcalcifications in digitized mammograms. Our algorithm combines numerical methods that accentuate high-frequency information in the images. We extract high-frequency information with respect to intensity (preserving structures of the image that change quickly in brightness) and with respect to size, or spatial frequency (preserving structures of the image that are small). We apply an adaptive-thresholding algorithm to the high-frequency result to yield a binary image, where suspicious spots are shown in white and everything else is black. The structure of soft tissue is absent from this image, so the mammographer can clearly observe patterns formed by the microcalcifications.

The final step is to categorize and encircle suspicious spots on the original digital image. We use color-coded

---

*Valley Care Imaging, Pleasanton, CA.
†University of Arizona, Tucson.

circles to highlight areas of particular interest. Figure 1 shows part of a digitized mammogram, the binary image, and the final highlighted image.

Our computational approach can best be thought of as a "mammographer's associate," which objectively and reproducibly detects microcalcifications and flags them for the mammographer. This work may enable mammographers to perform better by freeing them from the routine searching task, thus allowing them to concentrate on diagnosis. ◆

References

Bird, R. E., T. W. Wallace, and B. C. Yankaskas (1992), "Analysis of Cancers Missed at Screening Mammography," *Radiology* **184**, 613–617.

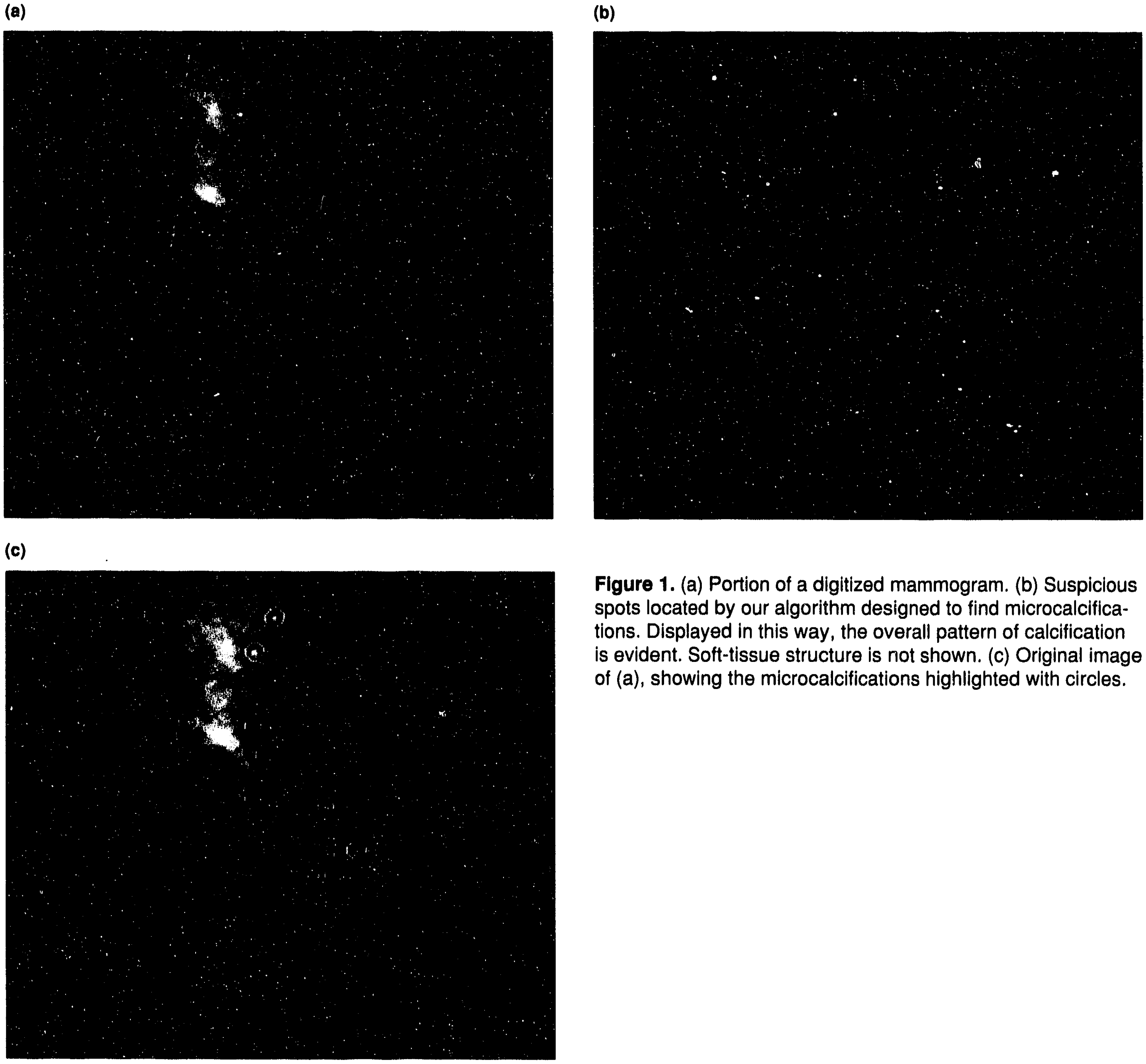

Figure 1. (a) Portion of a digitized mammogram. (b) Suspicious spots located by our algorithm designed to find microcalcifications. Displayed in this way, the overall pattern of calcification is evident. Soft-tissue structure is not shown. (c) Original image of (a), showing the microcalcifications highlighted with circles.

Flow Cytometric Assay of HLA-Locus Mutations in Human Lymphocytes

W. L. Bigbee

Our preliminary experiments are demonstrating the utility of flow cytometric and flow sorting methods to extend a new mutation assay we have developed for live (in vivo) human white blood cells (lymphocytes). In essence, we use a laser beam to detect distinct fluorescent signals and thus automatically identify circulating (peripheral) blood T-lymphocytes that express somatic mutations. T-lymphocytes are of interest because they can be easily obtained from peripheral blood samples, and cell-culture techniques are established that allow mutant cells to be cloned (copied) and characterized at the DNA level.

Labeling T-Lymphocytes

We have developed and applied a two-color scheme for immunolabeling lymphocytes with combinations of the dye fluorescein, which fluoresces green, and another dye, phycoerythrin, which fluoresces orange. Both of these dyes can be attached to—or conjugated with—monoclonal antibodies (proteins) that specifically recognize different forms of the T-lymphocyte protein, called HLA-A, residing on the cell surface.

This surface protein varies slightly among individual humans. Researchers have been able to identify these differences and to produce mouse monoclonal antibodies that can specifically recognize the different forms. The different forms of the HLA-A protein are coded for by different forms of the HLA-A gene, called alleles. Individuals who have inherited two different forms of the HLA-A gene are referred to as HLA-A heterozygotes.

Our assay measures mutations in heterozygous individuals who inherited a specific allele called HLA-A2. Our objective was to use a monoclonal antibody specific for the HLA-A2 protein and two-color flow cytometry to count the rare HLA-A2 allele-loss variants in blood samples from such heterozygous individuals. These variant T-lymphocytes result when somatic mutations occur at the HLA-A2 gene in the DNA so that the HLA-A2 protein is not expressed. Such mutant cells would fail to bind the HLA-A2-specific antibody that we add during our assay.

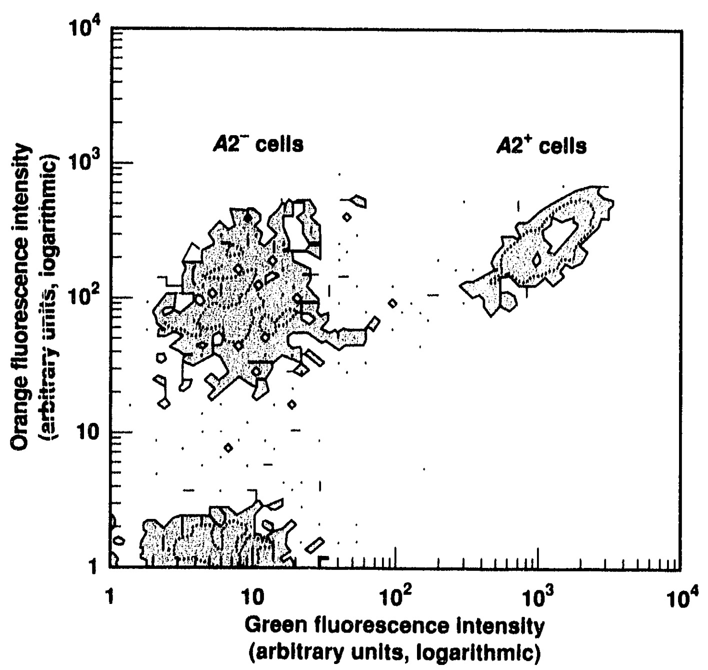

Figure 1. Two-color contour plot of cellular fluorescence intensities measured on a mixture of HLA-A2 positive and negative human lymphocytes. We isolated lymphocytes from two people, mixed them in a one-to-one ratio, and labeled them with a fluoresceinated HLA-A2-specific monoclonal antibody (green fluorescence) and a phycoerythrin-conjugated monoclonal antibody (orange fluorescence) that recognizes all allelic forms of the HLA antigens. As expected, both cell types in the mixture are labeled at similar orange fluorescence intensities; however, A2 positive cells fluoresce at about a hundredfold greater green intensity than A2 negative cells. Signals at the lower left are from dead cells and fluorescent debris.

Experimental Results

To test the specificity of various antibody and labeling combinations, we prepared and immunolabeled one-to-one mixtures of lymphocytes isolated from HLA-A2 positive and negative donors. Figure 1 shows a flow contour plot from our analysis of such a mixture labeled with a pair of fluoresceinated and phycoerythrin-conjugated monoclonal antibodies. The results are typical of many labeling combinations that we investigated and demonstrate that A2-positive cells are labeled at about a hundredfold greater fluorescence intensity than are A2-negative cells.

We conclude that our methodology can be used to detect rare A2 allele-loss variants. We will use these positive preliminary results to support long-term funding proposals to the National Institutes of Health and the DOE to validate and apply our new mutation assay system. ◆

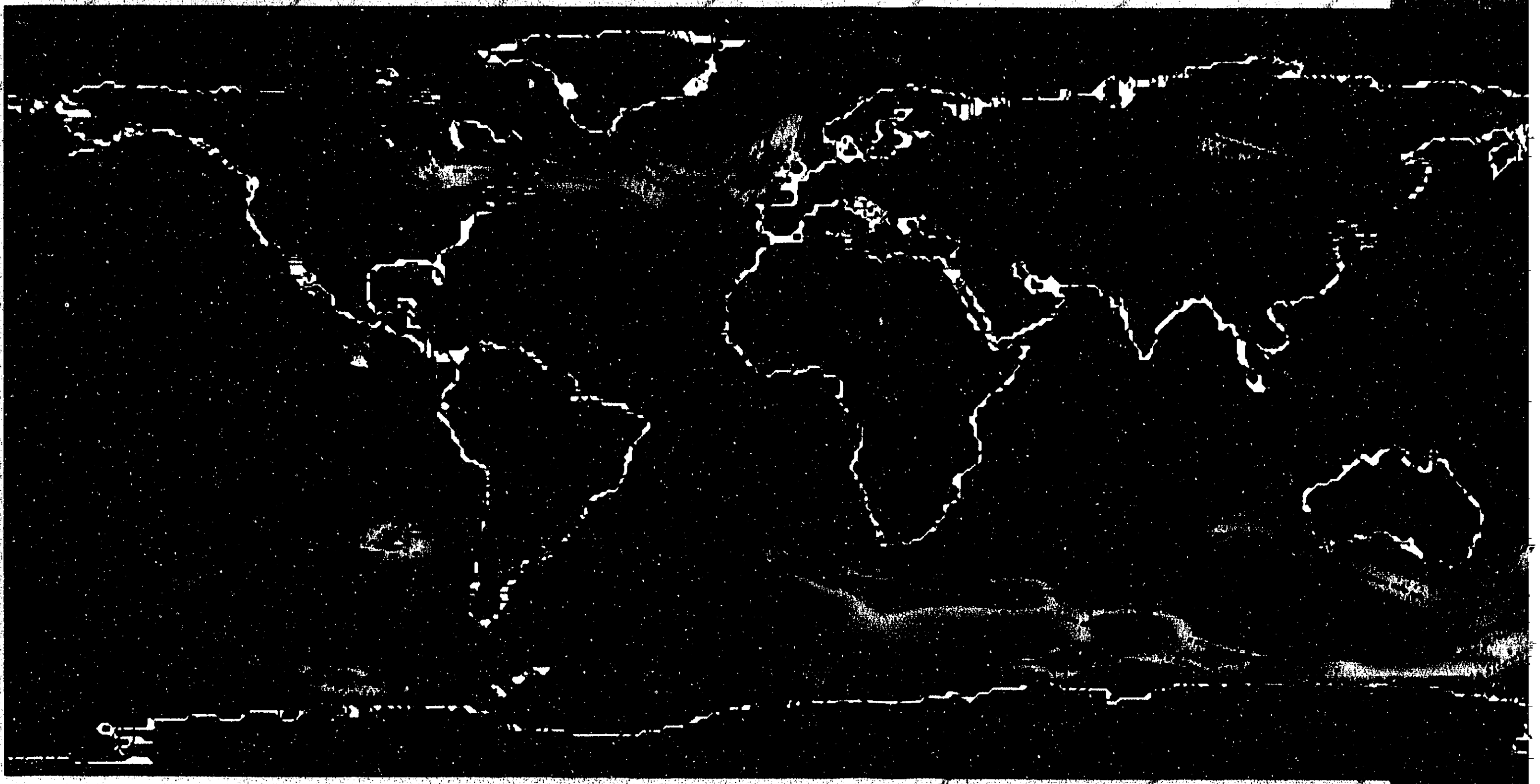

Atmospheric and Geologic Sciences

Laboratory Directed Research
and Development FY 1992

On the previous page. A computer-generated snapshot of atmospheric motion near an altitude of about 10 km, from a simulation with a parallellized general atmospheric circulation model. Streaklines are color-coded through the spectrum from red, which depicts the highest windspeed, to blue, which depicts the lowest windspeed.

Rhenium–Osmium Isotopic Geochemistry

S. Niemeyer and B. K. Esser

We have used rhenium–osmium isotopic analysis to yield time and provenance information to study the early evolution of metals in the solar system. We also initiated work on terrestrial problems; e.g., the evolution of the earth's crust and mantle, sediment geochronology, and noble-metal marine chemistry.

In FY 1992, we conducted a series of experiments to further elucidate conditions under which erroneous results arise during the acid dissolution of iron meteorite samples. We found that minor changes in the procedure could cause incomplete equilibration between spike osmium and sample osmium. We emphasize that our data give absolute rhenium–osmium ages because our osmium spike was calibrated against the primary standard used in the half-life measurement of ^{187}Re by Lindner et al. (1989).

The data for six of the nine meteorites we analyzed lie on an isochron; the remaining three are interpreted as disturbed, probably by a shock event subsequent to their formation. The isochron corresponds to an age of 4.56 ± 0.15 billion years; the initial ^{187}Os/^{188}Os ratio is identical with that reported for iron meteorites by Horan et al. (1992). The concordance between the isochron age and the accepted age of the solar system supports the ^{187}Re half-life by Lindner et al. (1989) and demonstrates that iron meteorite studies during the 1980s by other groups, which cast doubt on the half-life experiment, were themselves in error. The recent work by Horan et al. (1992) is in excellent agreement with our results, an encouraging sign of progress for use of this chronometer, but our work also indicates that the techniques are still vulnerable to slight changes in the dissolution and distillation procedures.

We are using our refined techniques to study the marine geochemistry of noble metals recorded in ferromanganese crusts. Ferromanganese crusts from the Pacific Basin often contain high concentrations of platinum, a strategic metal. The mechanism for this enrichment is not understood: One interpretation is that this reflects enhanced scavenging of platinum-group metals from seawater; another alternative is that the excesses are due to hydrothermal or extraterrestrial inputs.

In collaboration with McMurty and VonderHaar from the University of Hawaii, we have determined an osmium concentration and isotopic composition profile in a crust from an Hawaiian Archipelago seamount. A platinum and osmium peak in concentrations is observed in a 2-cm interval. Above and below this peak, the ^{187}Os/^{188}Os ratios range between 0.60 and 0.84, values typical of marine ferromanganese deposits. These ratios are lower than seawater because they contain an extraterrestrial component. Over the interval of the platinum and osmium peak, the osmium isotopic ratios are constant at 0.40. A value this much lower rules out the theory that the enhanced concentrations are due to enhanced seawater scavenging.

The present database does not yet allow us to distinguish between hydrothermal and extraterrestrial sources, but expansion of this initial result to a broader spatial distribution and inclusion of other platinum-group metals should clarify which of these two sources is responsible for enrichments of platinum-group metals in ferromanganese crusts. ◆

References

Horan, M. F., J. W. Morgan, R. J. Walker, and J. N. Grossman (1992), "Rhenium-Osmium Isotope Constraints on the Age of Iron Meteorites," *Science* **255**, 1118–1121.

Lindner, M., D. A. Leich, G. P. Russ, J. M. Bazan, and R. J. Borg (1989), "Direct Determination of the Half-Life of ^{187}Re," *Geochim. Comsochim. Acta* **53**, 1597–1606.

Shock Temperature Measurements of Iron: A New Technique with Geophysical Implications

C.-S. Yoo and N. C. Holmes

We have measured the shock temperatures of iron, the major constituent of the earth's core, to obtain its melting temperatures T_m at 1 to 3 Mbar of pressure. We have found a knee on the iron Hugoniot between 2.5 and 3.0 Mbar, which is an indication of melting. This result, $T_m = 1938 + 29.23P - 0.0433P^2$, provides an upper limit of 6870 ± 500 K for the earth's inner-outer core temperature, a critical constraint for modeling the chemical composition and energy balance of the earth's core and, thus, for understanding the earth's dynamics.

Studies of melting and of the phase diagrams of elements at extremes of pressure and temperature are crucial for developing condensed matter theory. These studies also have geophysical implications for understanding the earth's interior. The phase diagram of iron is particularly important for modeling the chemical composition and energy balance of the earth's core. The earth's core is mostly iron distributed in two layers: the solid inner layer of nearly pure iron and the liquid outer layer of iron alloys combined with lighter elements like sulfur, oxygen, hydrogen, silicon, and magnesium. Thus, the iron melting temperature at the pressure (330 GPa) of the earth's inner-core and outer-core boundary (IOB) will provide an upper limit for the temperature. The recrystallization of iron occurring at the boundary releases the latent heat and gravitational energy that are primary sources of the earth's internal energy, which determines the dynamics of the earth's interior (Anderson, 1990).

Current earth-core models rely on extrapolations of the melting data of iron below 100 GPa. However, these extrapolations not only give a large uncertainty in the IOB temperature ranging from 4000 to 9000 K (Anderson, 1990), but they also yield phase diagrams that are qualitatively different at the IOB conditions (Williams, 1987; Boehler et al., 1990).

An alternative way to obtain melting temperatures of a few thousand kelvins at well above 100 GPa is to measure shock temperatures. Optical pyrometry is typically used to measure shock temperatures exceeding 2000 K. However, because iron is nontransparent and because the rarefaction wave releases the iron pressure to ambient conditions at the free surface, we place an optical window against the surface of the metal film to retain the shock state. Thermal radiation is measured from the metal-window interface.

However, before we can obtain reliable shock temperatures from this method, we must address some important issues: characterization of the iron film and iron film-window interface, optical property changes of window materials at high pressures and temperatures, and thermal conduction occurring across the interface (Nellis and Yoo, 1990).

High-quality, well-characterized iron films (~2 μm thick) are prepared by sputtering onto diamond substrates held at 200°C (Yoo et al., 1992a). The iron film–diamond sample is sandwiched between a diamond-turned iron baseplate and a sapphire disk. We generate the shock wave by striking a tantalum disk on the iron baseplate with a two-stage gas gun. Shock pressures are determined by impedance matching using accurately known equation of states of various materials. We measure thermal emission from the iron–diamond interface with two detectors: a streak camera system and a photomultiplier tube system.

Typical time-resolved emission spectra of the shocked iron show an intensity rise at 455 ns owing to the shock-wave arrival at the iron-diamond interface. The broad spectra suggest that the emission is thermal.

The emission intensity remains nearly constant during the shock-wave transit through the diamond window, indicating that thermal equilibrium is achieved in the interface region and that the optical properties of the shocked diamond remain unchanged.

This study suggests that diamond is transparent in the entire pressure range to 300 GPa. The experiment is completed when the shock wave enters the sapphire disk and the emission intensity rapidly decreases, probably owing to the partial opacity of the shocked sapphire (Yoo et al., 1992b). We have also observed a transient emission after the shock wave enters the sapphire, but we have not yet clearly characterized this increase.

We fit the measured emission intensity to a gray-body equation to determine T_i and then convert T_i to the release shock temperature of iron T_r. Finally, we correlate T_r to the shock temperature on the principal Hugoniot of iron T_h with a Mie-Grüneisen thermal relationship.

Figure 1 presents the measured shock temperatures of iron between 100 and 400 GPa and the iron phase diagram (Yoo et al., 1992a). The measured temperatures systematically increase with increasing pressure and clearly show a knee at the pressure region between 250 and 300 GPa. We believe the knee indicates melting. The pressure (250 GPa) at which the solid iron Hugoniot intersects the melting line is then consistent with the shock anomaly pressure of 243 GPa previously observed in sound-velocity measurements (Brown and McQueen, 1980).

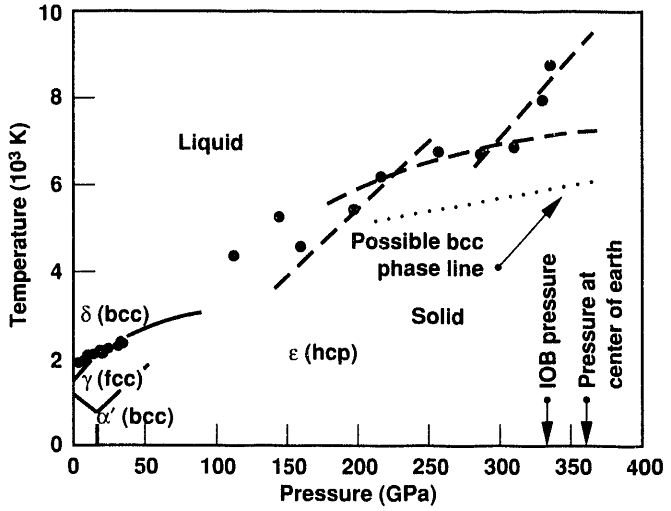

Figure 1. Iron shock temperatures (black circles) between 100 and 400 GPa and the phase diagram of iron. In the phase diagram, our data (green circles) confirm the melting line determined in earlier, static high-pressure studies. The proposed α′ (bcc) phase of iron appears near the iron melting curve (Ross et al., 1990).

The iron phase diagram (Figure 1) is well known at pressures below 20 GPa. We reproduced the melting line and the ε/γ-phase boundary at higher pressures from the Boehler et al. (1990) data. Our experimental work confirms Boehler's melting line to 40 GPa. The iron melting temperatures, as determined by shock temperatures, are substantially higher than the extrapolation of the low-pressure melting line. This result may mean that the melting line above 200 GPa is consistent with the α′ body-centered cubic (bcc) phase suggested near the melting line (Ross et al., 1990). The iron melting temperature T_m in the pressure range between 200 and 400 GPa is $1938 + 29.23P - 0.0433P^2$. This melting curve yields the Grüneisen parameter $\gamma = 1.06 \pm 0.10$ in the pressure range of 250 to 300 GPa. A Grüneisen parameter of 1.06 is well below the critical value 1.60, where many solid elements exhibit a systematic structural change of a close-packed phase to bcc to liquid with elevating temperatures; it is consistent with the new bcc phase (Ross et al., 1990).

Our work provides an experimentally determined melting line and a new phase diagram whose qualitative aspects are consistent with most existing data. The melting temperature of iron is 6870 ± 500 K at 330 GPa, which is an upper limit for the earth's IOB temperature. The 1-ns, time-resolved spectroscopy developed in this study is the state-of-the-art technology for shock-wave studies at megabar pressures. ◆

References

Anderson, O. L. (1990), "The High-Pressure Triple Points of Iron and Their Effects on the Heat Flow from the Earth's Core," *J. Geophys. Res.* **95**, 21697.

Boehler, R., N. von Bargen, and A. Chopelas (1990), "Melting, Thermal Expansion, and Phase Transitions of Iron at High Pressures," *J. Geophys. Res.* **95**, 21731.

Brown, J. M., and R. G. McQueen (1986), "Phase-Transition Grüneisen Parameters and Elasticity for Shocked Iron between 77 and 400 GPa," *J. Geophys. Res.* **91**, 7485.

Nellis, W. J., and C. S. Yoo (1990), "Issues Concerning Shock Temperature Measurements of Iron and Other Metals," *J. Geophys. Res.* **95**, 21749.

Ross, M., D. A. Young, and R. Grover (1990), "Theory of the Iron Phase Diagram at Earth Core Conditions," *J. Geophys. Res.* **95**, 21713.

Williams, Q., R. Jeanloz, J. Bass, B. Svendsen, and T. J. Ahrens (1987), "The Melting Curve of Iron to 250 Gigapascals: A Constraint on the Temperature of the Earth's Core," *Science* **236**, 181.

Yoo, C. S., N. C. Holmes, M. Ross, D. Webb, and C. Pike (1992a), *Shock Temperatures, Melting, and Phase Diagrams of Iron at Earth Core Conditions*, Lawrence Livermore National Laboratory, Livermore, CA, UCRL-JC-112242.

Yoo, C. S., N. C. Holmes, and E. See (1992b), "Shock-Induced Optical Changes in Al_2O_3 at 200 GPa," in *Shock Waves in Condensed Matter–1991*, S. C. Schmidt, R. D. Dick, J. W. Forbes, and D. G. Tasker, Eds. (North-Holland, Amsterdam), p. 733.

Physics and Chemistry of Earth Materials: Melt Segregation and Diffusion

F. J. Ryerson, W. Minarik,* E. B. Watson,* D. Farber,† and Q. Williams†

The separation of partial melt from its source rock, melt segregation, is the most important planetary chemical fractionation process. In our project, we use high-pressure and high-temperature experimental techniques to obtain information on phase equilibria and transport kinetics for the earth's mantle. We aim to experimentally determine effective diffusion coefficients in polycrystalline materials containing fluid phases, which may be important in geochemical fractionation processes. These fluid phases include silicate magmas, aqueous and carbonate fluids, and molten-metallic alloys.

The spatial distribution of the fluid phase within the aggregate—its connectivity—is critically important in determining the effects of grain-boundary fluids in polycrystalline materials. A fluid phase that is not interconnected will not affect mass transport nor will it segregate from its host rock by gravity-driven percolation. It can only segregate when the host has undergone appreciable melting. We measure effective bulk diffusion coefficients in rocks containing fluids of various compositions to investigate fluid interconnectivity. These measurements have direct bearing on melt segregation processes in planetary bodies, as diffusion enhancement can be the result of interconnectivity.

Before measuring transport rates at high pressure, we must sustain operating conditions at high pressure (up to 25 GPa) and temperature (up to 2500°C). We use a multi-anvil press for this purpose. To reduce the expense of these experiments, we are implementing a variety of cost-saving procedures. Our most important improvement has been to replace machined ceramic parts with those made using castable ceramics and molds. By using castable pressure media, we cut costs and increased pressure-generating efficiency and reproducibility among operators. We are also evaluating different types of castable ceramics to optimize mechanical and thermal properties.

Carbonate-rich melts (carbonatites) may play an important role in fractionation of the primordial earth's mantle. To investigate how readily such a melt could segregate from the mantle and at what melt fractions, we measured the enhancement of bulk Fe–Mg diffusion in an olivine–carbonate melt aggregate at 2.5 GPa and 1300°C. The melt is nominally Na_2CO_3. At melt fractions near 0.1 wt%, the Fe–Mg diffusion coefficient is about 100 times greater than that in melt-free samples, which indicates that the fluid-filled grain edges are fully connected. Further enhancement of the diffusivity at higher melt fractions is due to an increase in the radius of these channels. Below 0.1 wt%, the diffusivity drops with the melt fraction until it reaches that of the melt-free aggregate at ~0.005 wt%. This decrease is caused by the pinching off of fluid-filled channels. The interconnectivity determined in these experiments indicates that carbonatite melts can segregate from their mantle source region at melt fractions as low as 0.1 wt%. Such melts would be expected to be highly enriched in incompatible trace elements and have a strong influence on mantle trace element geochemistry.

We have also begun experiments on the distribution of metallic melts in mantle lithologies at 1500°C and 12 GPa to investigate core-formation processes. At low pressures, metallic melts (Fe–Ni–S system) form isolated pockets in silicate polycrystals because of the large difference in surface energies for these materials. As such, an interconnected network of metallic melt cannot form, and melt segregation by percolation is impossible.

---

*Rensselaer Polytechnic Institute, Troy, NY.
†University of California at Santa Cruz.

Segregation of metal from silicate, therefore, requires melting of the silicate. This implies that the earth's core must have formed from a largely molten planet. However, increased pressure could alter the composition of the molten metal such that an interconnected network forms, thus enabling segregation by percolation. If this postulation is valid, the earth's core may not have necessarily formed from a largely molten planet. Our preliminary textural results indicate that the Fe–Ni–S melt is still not interconnected at 1500°C and 12 GPa (the run was five hours long), precluding segregation by melt percolation at these conditions. We are extending these experiments to different pressure–temperature conditions. ◆

Geodesy Initiative

J. B. Rundle

The objective of the Geodesy Initiative is to observe, process, and analyze various geodetic data to study earth system processes. In FY 1992, we developed and used various software packages to model and interpret crustal deformation processes. The initiative could be important to various LLNL defense activities such as test-ban verification and navigation in terrestrial and marine environments. Geodesy could also help us assess the natural hazard potential from earthquakes, volcanoes, and landslides; evaluate subsidence from mining, fluid withdrawal, or other human activities; and monitor global changes in ice sheets, glaciers, and sea level.

We have developed global positioning systems (GPS) for observation, data reduction, and modeling and have installed various crustal deformation software codes that include:

- Codes to compute vertical and horizontal deformation caused by arbitrarily oriented faults in elastic and inelastic earth models.
- Codes to calculate the three-dimensional stress field from arbitrarily complex fault geometries in a homogeneous medium.
- Inversion codes using observations of GPS data and surface gravity data to calculate seismic slip on faults.
- Statistical analysis (covariance) codes to determine the optimal design of geodetic networks.

We used some of these codes to calculate deformation caused by the June 1992 Landers earthquake sequence in southern California (Figure 1). We also joined University Navstar Consortium (UNAVCO), a university consortium for GPS research, and are purchasing an ASHTECH GPS receiver to gain access to UNAVCO's GPS observations.

In our second project, we used surface gravity changes and level lines to observe crustal deformation in the Long Valley Caldera in eastern California. During the past 12 years, the Long Valley Caldera, which is a very young (only 700,000 years old), active caldera, has risen about 0.7 m and continues to display a large, ongoing horizontal strain rate that is 20 to 30 times greater than the strain rate of the San Andreas Fault system. The deformations were caused by the injection of more than 200 million m^3 of magma at a shallow depth. Using Lacoste–Romberg Model G gravity meters, we conducted a series of surface-gravity observations over a network of about 40 benchmarks that have been periodically observed since 1982 by investigators from various institutions. Once these observations are processed, we will use our codes to model and interpret the data. Additionally, the U.S. Geological Survey conducted first-order leveling observations over a benchmark network that was established along major roads in this area in 1900. We will model and interpret their data. Preliminary leveling results show that the central part of the caldera has risen about 12 cm since 1988.

Finally, we are planning to fly an airborne laser altimeter over the Nevada Test Site in FY 1993 in an experiment to develop new techniques for conducting rapid and highly precise onsite monitoring and verification of suspected clandestine nuclear tests. We will use a NASA airborne geophysical observatory that monitored ice sheets in Greenland. ◆

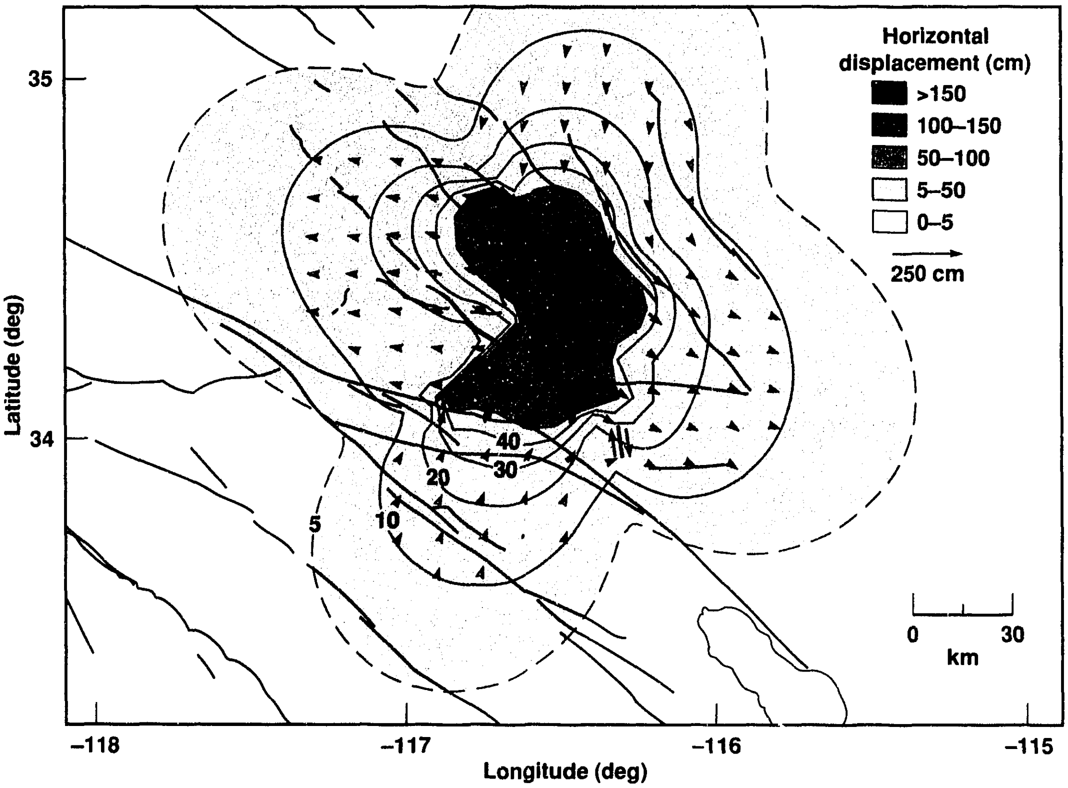

Figure 1. Horizontal displacement field, Landers earthquake sequence, 1992. We used GPS technology to show deformation around the Landers event.

Applying Neural Networks to Earth Science Problems

J. G. Berryman, B. P. Bonner, F. U. Dowla, L. A. Glenn, L. L. Rogers, and H. F. Shaw

Geoscience researchers study complex interactions among multiple physical and chemical processes. Conventional modeling techniques cannot be applied to these problems when the relationships among the variables are highly nonlinear and the underlying equations governing a system are unknown. Our goal was to determine if artificial neural networks, a powerful new computational tool, could be applied to such problems. Neural networks "learn" to solve new problems by generalizing from known solutions to similar problems. We investigated three neural-network applications in the geosciences: optimization, estimation, and discrimination.

Optimizing Groundwater Remediation

During groundwater remediation programs, pumping wells must be installed to contain plumes of contaminated water, maximize contaminant removal, and reduce cleanup time and cost. It is often difficult to site wells so that these goals are met simultaneously. Standard remediation-optimization methods require separate and sequential computer calculations for each pumping scenario. These calculations can take days of computer time and limit the number of scenarios that can be modeled for each problem.

In contrast, we used conventional flow and transport codes to generate solutions to numerous pumping strategies. Then we used these solutions to create a training set for a neural network. The trained network duplicated the function of the conventional code except that it calculated an "answer" instantaneously. We used genetic algorithms in conjunction with the trained neural network to find optimal pumping strategies. We verified these strategies by checking the results against the predictions of conventional codes. Figure 1 shows the results for a remediation scheme at LLNL involving 23 extraction wells and 5 injection wells. The mass of volatile organic compounds that the trained neural network predicted would be removed agrees well with the predictions of the conventional code, and the neural network approach proved fast and cost effective.

Estimating Explosion Yields and Paleoclimates

We also applied neural networks to problems in estimating hydrodynamic yields and extracting paleoclimate information from tree-ring records. Our scaling results for hydrodynamic yield were better than those from expert systems. However, the backpropagation

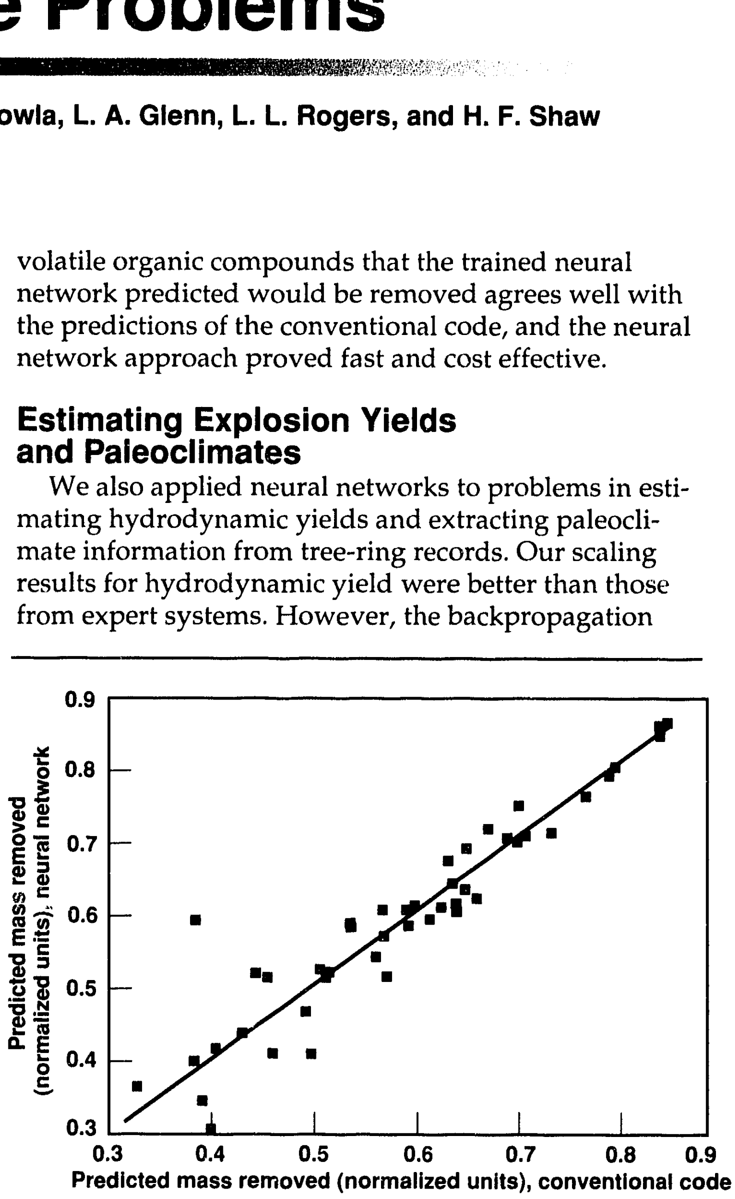

Figure 1. Predictions of mass removed from 50 pumping scenarios for a 28-well remediation problem. The *y* axis represents the predicted mass removal. The *x* axis represents the predictions of a conventional code. The straight line represents perfect agreement between the two procedures. The squares represent the neural-network prediction. The agreement between the methods is good.

network we used to solve the paleoclimate problem proved no better than conventional linear regression methods. In FY 1993, we will explore other network architectures to solve this problem.

Discrimination of Acoustic Signals

In a final study, we used backpropagation neural networks to solve an acoustic-signal discrimination problem. Characteristic acoustic emissions can be used to infer the mechanisms by which a solid (such as a rock) deforms or fails when it is subjected to thermal or mechanical stresses. The neural network easily classified mechanical-excitation sources by using the power-spectral values of the acoustic-response signal.

In FY 1993, we will conduct heat-treatment experiments to separate acoustic signals caused by irreversible thermal damage in the material from interfering noise caused by reversible sliding along grain boundaries. We will also develop a user-friendly computational "toolbox" for neural analysis. ◆

Applying Lattice-Gas Methods to Fluid-Flow Problems

C. R. Carrigan, H. W. Stockman,* T. Ladd, and A. Tompson

A lattice gas is an imaginary system of particles constrained to move about like beads on an interconnected framework or lattice in a more or less random fashion. All the particles have the same mass and travel about the same speed (one lattice link per time step). Inevitably, collisions will occur in this simple system, and these are constrained to conserve both mass and momentum. This microcosm of colliding particles averaged over many time steps can behave as a fluid. Numerical models of fluids treated as collections of particles readily permit the simulation of both multifluid and multiphase flows.

Fluid-Dynamic Simulation

Many problems, such as the eruption of a volcano, the flow of oil and water mixtures in a pipeline, and the coextrusion of molten polymer blends can involve fluid-dynamic regimes that are not easily simulated using standard numerical methods. In particular, when moving interfaces between two distinct fluids must be tracked or when it is necessary to simulate the flow of a nonuniform mixture of two fluid components, lattice-gas techniques offer significant advantages over the standard finite-difference and finite-element methods.

In FY 1992, we completed a general, lattice-gas, fluid-flow simulation program. The program can simulate the two-dimensional, isothermal flow of two fluids with different physical and chemical properties or the nonisothermal flow of one fluid with temperature-dependent physical properties such as viscosity. The program is computationally efficient, having an execution rate on a dedicated 486 PC that is comparable to the typical turnaround times for programs on time-shared supercomputers running finite-element or finite-difference flow simulations. We are applying this program to several problems of interest to earth scientists and engineers.

Two-Component Magma Flows

One problem we are exploring is how very viscous magmas can erupt onto the earth's surface by flowing through narrow fractures that penetrate much cooler host rock. In volcanic intrusions and lava flows, very viscous magmas are often seen in association with magmas of lower viscosity. Our theory suggests that the lower viscosity magmas lubricate the rise of the more viscous components, which substantially improves the probability that they will successfully reach the surface

---

*Sandia National Laboratories, Albuquerque, NM.

and explains the association between higher and lower viscosity components observed at the surface (Carrigan and Eichelberger, 1990).

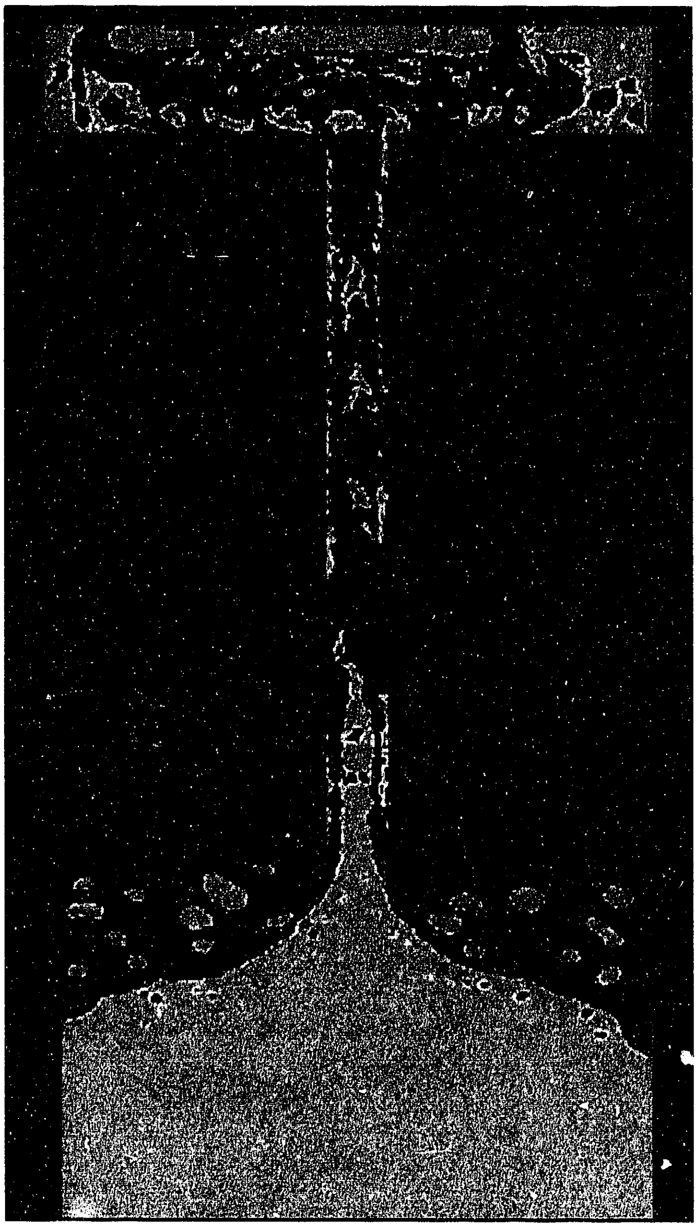

Figure 1. Two-component flow in a volcanic system consisting of a stratified reservoir with heterogeneities and a conduit. This type of model illustrates how the lubrication-redistribution process occurs when two components rise in the conduit.

Our numerical simulations seem to bear out our theory for volcanism and are useful for studying the evolution of two-component magma flows. In particular, our simulations support the notion that the components with their different viscosities are arranged by fluid-dynamic processes so that viscous dissipation in the flow is minimized. In other words, the two-component magma becomes self-lubricating. Furthermore, our modes suggest that the nature of a lava flow at the surface strongly depends on the geometry of the volcanic plumbing and the manner in which magma is stored at depth. Thus, we are attempting to model the entire subsurface volcanic system with the aid of the lattice-gas program (Figure 1). Simulation involving a multicomponent magma has not been attempted before, and we anticipate that such modeling will significantly contribute to our understanding of how very viscous molten rock can rise to the surface in a volcanic eruption.

The flow processes that we have mentioned are often three dimensional, and in FY 1993, we hope to simulate them. We also anticipate extending our simulations to potential industrial applications such as the coextrusion of multicomponent, molten polymers through capillary dies to produce composite plastic fibers. The resulting predictions of flow behavior could provide valuable preproduction, diagnostic information. ◆

References

Carrigan, C. R., and J. C. Eichelberger (1990), "Zoning of Magmas by Viscosity in Volcanic Conduits," *Nature* **343**, 248.

The Computational Earthquake Initiative

G. L. Goudreau, P. Kasameyer, F. Heuze, D. McCallen, and D. Schauer

We use site-specific data from small earthquakes to predict rock motion at those same sites during large earthquakes. We combine this capability with nonlinear soil dynamics and structural-dynamics, finite-element computer codes to predict the response of the Dumbarton Bridge and other structures in northern California to large earthquakes on the Hayward and San Andreas faults.

The Computational Earthquake Initiative combines earth-science and engineering efforts. The initiative consists of four teams that work closely on four subjects: propagation of the ground motion from the fault to the rock base of a site, nonlinear response of soil deposits from the rock base to the bottom of overlying structures, dynamic analysis of structures with nonlinear response, and detailed damage analysis in reinforced-concrete structural members.

Seismologists synthesize large-motion histories at a site where small motions have been measured and traced to a fault source. Seismologists do not predict the

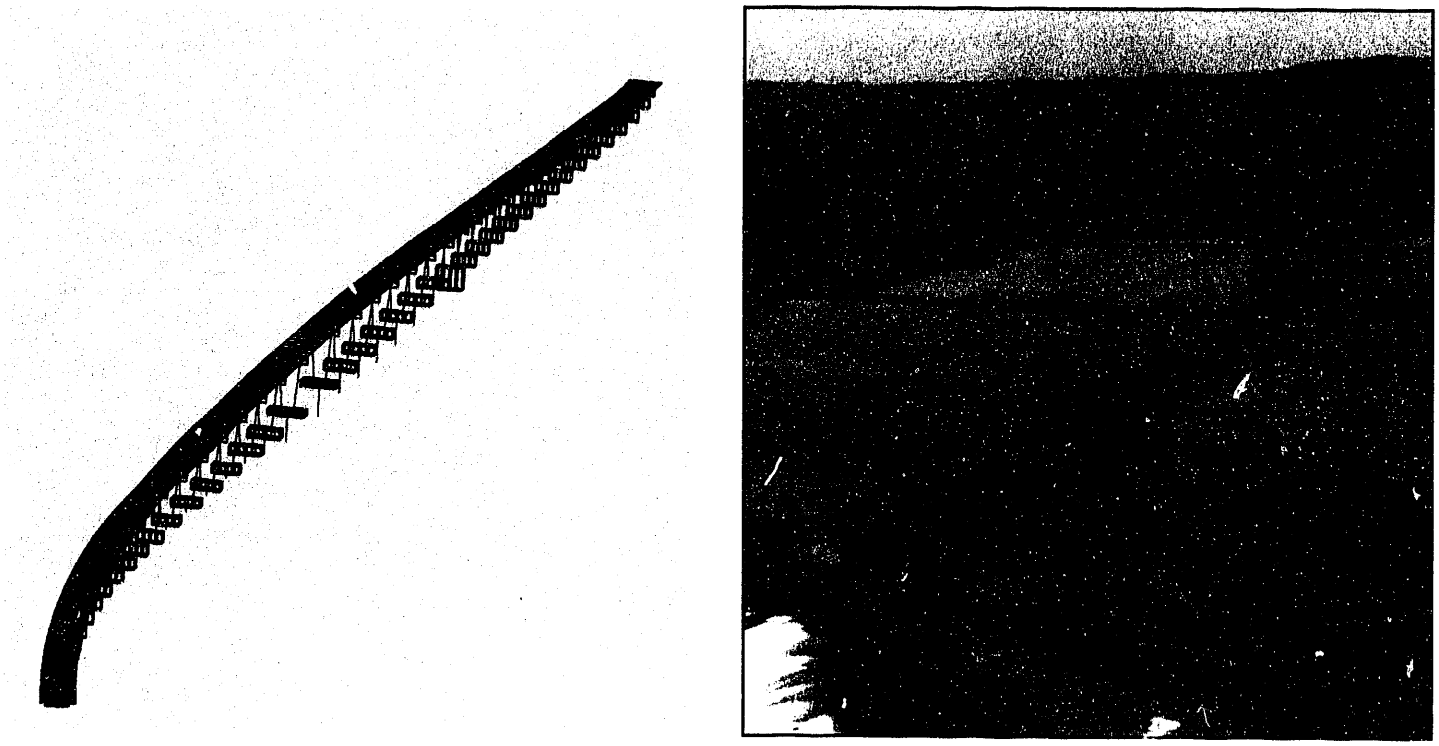

Figure 1. A complete structural model of the entire Dumbarton Bridge allows us to analyze the effects of a major earthquake on the structural members of the bridge.

occurrence or magnitude of earthquakes, but they can predict the time-history propagation of a postulated event through the otherwise unknown geology from fault to site and estimate the resulting rock motion. We have calibrated our method for 25 sites in the San Francisco Bay Area with data from the Loma Prieta earthquake. We are making preliminary predictions of rock motion at the Dumbarton Bridge, but we await data from new boreholes so that we can measure small, earthquake-created motions at rock depth.

The soil dynamics project uses powerful, nonlinear, finite-element models to predict large soil motions. These models simulate the interaction of soil and fluid and can estimate the liquefaction potential of soils (loss of strength) at large motions. We will apply these models to studies of soil motions at Treasure Island and at the Dumbarton Bridge.

Our seismic engineering analysts are the first to apply the nonlinear, finite-element structures code NIKE3D to earthquakes (McCallen et al., 1991). A full, computer-aided design (CAD) model of the Dumbarton Bridge has provided the initial geometry for a sequence of structural models (see Figure 1). We expect to calculate, for the California Department of Transportation (Caltrans), forces on the bridge's structural members that would result from a major earthquake on the Hayward or San Andreas fault.

In a related study, a computer simulation of the Painter Street overcrossing in Rio Dell, California, is helping us understand the response of that structure during the Petulia earthquake sequence in April 1992. Caltrans has drilled a series of moderate to deep holes at Painter Street. We have set up our instruments and are assessing micromeasurements from the site. Comparable drilling at the Dumbarton Bridge will commence in FY 1993.

In the final phase of the project, we will analyze the failure of reinforced-concrete critical members. Modeling of rebar-concrete interaction is too detailed to be incorporated in the global dynamics model. A joint study with a Caltrans-sponsored research team at UC Berkeley, however, is leading to a better understanding of this complex phenomenon and to the design of simpler, nonlinear models for global dynamics analysis.

The method we are developing and validating will be applied to the seismic response analysis of critical federal, state, and Laboratory facilities. ◆

References

McCallen, D. B., K. M. Romstad, and G. Goudreau (1991), "Dynamic Response of a Reinforced-Concrete, Box-Girder Bridge," in *Thrust Area Report FY91: Engineering Research and Development*, Lawrence Livermore National Laboratory, Livermore, CA, UCRL-53868-91.

Earth-Systems Modeling

M. C. MacCracken, W. P. Dannevik, J. E. Penner, C. C. Covey, and J. R. Kercher

To be able to understand and project the environmental impacts of energy-related activities, we must be able to simulate the coupled interactions of the global climate system. In the Earth-Systems Modeling project, we are connecting an increasingly comprehensive set of models that represent the interactive physical, chemical, and biological behavior of the atmosphere, oceans, and land surface. Our objectives are to develop a prototype Earth-Systems Model (see Figure 1) that can dynamically interconnect component submodels spanning a wide range of time and space scales and to test the components and couplings by examining sensitivities and comparing results to observational constraints.

We are taking advantage of computational advances in highly parallel computing to adapt, develop, and connect component models that can efficiently simulate climatic, biogeochemical, and ecosystem dynamics. In FY 1992, we started to incorporate a restructured atmospheric model from UC Los Angeles and an oceanic model from the Geophysical Fluid Dynamics Laboratory at Princeton University into a flexible computational framework. This framework will couple these components and permit easier interfacing with other major system submodels and with alternative representations of physical, chemical, and biological processes within the models. We base our design on an information database, constructed for each model run, that can be accessed by the component packages. Information in this database is stored and retrieved symbolically in generic form with accompanying attributes that describe the data. We are now designing and testing related interface tools.

We are also testing for consistency among the interacting components, including:

- The time-dependent behavior of the couplings of the models by examining interannual climatic fluctuations, which are controlled by ocean–atmosphere interactions.
- The species-dependent behavior of the couplings by examining the cycling of selected chemical species between domains, which in turn alters the radiation balance by changing atmospheric composition.
- The spatial-dependent aspects of the couplings by examining the interactions of climate and terrestrial vegetation, which change land-surface characteristics.

We are using our capability to simulate radionuclide transport in the ocean to analyze model simulations of the oceanic distributions of ^{14}C generated by atmospheric nuclear testing. We are comparing these results to observations in two different types of calculations to test alternative formulations for representing vertical transport in the oceans.

To test species-dependent couplings, we have started to examine the roles of different carbon reservoirs in determining the future abundances of CO_2. Our component models include spatially disaggregated reservoirs of carbon in terrestrial ecosystems, ocean biogeochemistry, and the atmosphere. As a second aspect of our biogeochemical studies, we are developing a model component that treats soil hydrology, temperature, and vegetation cover to simulate the emissions of important trace species from various ecosystems. Initially, we are testing process interactions by generating an emissions inventory for NO_x. We will use this inventory to examine

Figure 1. Conceptual design of our Earth-Systems Model. We initially are coupling two sets of components: (1) atmosphere and ocean dynamics with the land surface, and (2) atmosphere and ocean chemistry with terrestrial vegetation. We also have started to cross couple these sets.

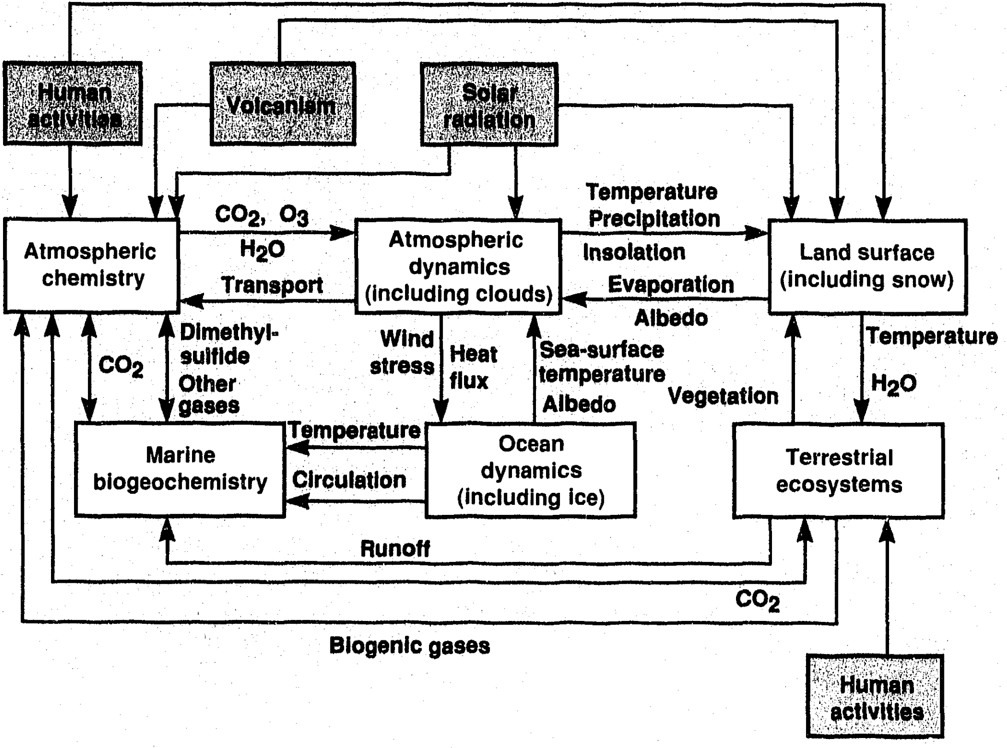

the biogeochemical functioning of ecosystems, including controls on carbon and nitrogen storage and partitioning and the seasonal and spatial variability of trace-gas fluxes.

During FY 1993, we will couple our atmospheric model to a global version of our terrestrial ecosystem model. We plan to simulate the cycle of CO_2 in the atmosphere, the sensitivity of atmospheric CO_2 concentration to ocean CO_2, and the sensitivity of atmospheric CO_2 to uncertain parameters in the ecosystem model as a means of analyzing system behavior. We expect to include an ocean productivity model to further explore system couplings. ◆

Seismic Imaging of Regional Earth Structure

G. Zandt, H. M. Benz,* and C. J. Ammon†

Recent seismic studies provide new tomographic images of the upper mantle of the earth under California. These images are maps of seismic P-wave velocity variations to a depth of 230 km with an average spatial resolution of about 50 km. Variations in the arrival times of teleseismic P waves recorded on a network of seismic stations are caused by lateral velocity variations beneath the network to depths comparable to the network aperture. We obtained the tomography results by linearized inversion of the P-wave arrival times recorded on the U.S. Geological Survey's California seismic network. Interpretations of these images place important constraints on mechanisms of regional tectonic processes and small-scale, convective flow patterns in the earth's upper mantle.

Some of the new results in Figure 1 show two prominent high-velocity anomalies (black areas have velocities >3% higher than the average background velocity) found in a cross section from the Klamath Mountains through the Sierra Foothills to the southern Sierra Nevada (cross-section A–A′ in Figure 1). Upper-mantle velocity variations are most sensitive to temperature variations, with higher velocities corresponding to lower temperatures and visa versa. A deep, high-velocity (>3%) anomaly (labeled GOR) under the Klamath Mountains and northern Great Valley delineates the "cold" oceanic Gorda plate subducting beneath the "warmer" upper mantle under the North American plate. The subduction process is currently active in North America only north of Cape Mendocino.

The deep, high-velocity anomaly (labeled SGV) under the southern Great Valley is a prominent, but enigmatic, anomaly that reaches a depth of 230 km. The SGV anomaly delineates either a remnant of a subducted slab that ceased sinking about 30 million years ago or a more-recent, convective, mantle downflow. These results are among the first detailed, regional-scale images of the upper mantle that directly reveal structures related to possible small-scale convection in the upper mantle. Previously, small-scale convection was postulated in numerical simulations and inferred from possible tectonic influence on the overlying lithosphere.

The feature's geologic age, magnitude of the anomaly, and potential flow velocity associated with the SGV anomaly are all consistent with development of an unstable thermal-boundary layer and subsequent initiation of small-scale mantle convection. The convection analysis places constraints on the viscosity, temperature fluctuations, and flow rates in the upper mantle under California. These parameters may also be representative of the upper mantle in other high-heat-flow, tectonically active, continental regions. ◆

**U.S. Geological Survey, Denver, CO.*
†University of California at Santa Cruz.

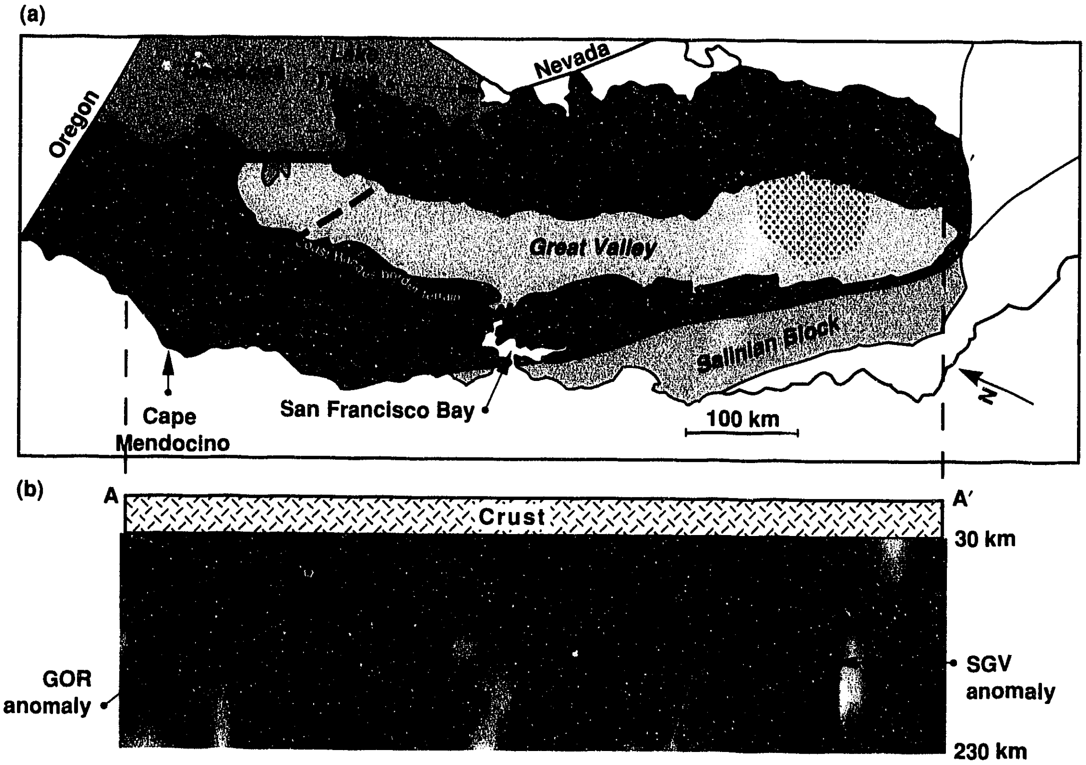

Figure 1. Upper-mantle, seismic P-wave velocity anomalies beneath California. (a) In map view, solid lines outline major geologic provinces. The stippled area in the southern Great Valley represents the location and size of the SGV anomaly over the depth of 150 to 190 km. The dashed line extending from Cape Mendocino to Lake Tahoe on the California–Nevada border marks the southernmost extent of the subducting Gorda plate. (b) Cross-section A–A′ shows the depth extent of high-velocity anomalies GOR and SGV. In the cross section, the gray scale represents velocity variations from −3% (low; shown in white) to +3% (high; shown in black). Thus, black areas have velocities >3% higher than background velocity.

Tectonic Escape Caused by the Indo-Asian Collision

F. J. Ryerson, T. M. Harrison,* H. Leloup,* and P. Tapponnier†

The northward convergence of India into Asia during the past 50 million years has led to the development of the Himalaya Mountains and the Tibetan Plateau. The relative youth and magnitude of these features allow an excellent opportunity to study the mechanics of mountain building. Details of the timing and mechanisms responsible for the present distribution of topography have long been debated and remain controversial. For example, a major controversy concerns the relative importance of thickening caused by (1) movement along east-west–oriented thrust faults and (2) lateral extrusion of crustal blocks along strike-slip faults. However, because both views of continental deformation describe tectonic response to large-scale forces, this question remains open to lively debate.

We believe that the Ailao Shan–Diancang Shan metamorphic belt in southern Yunnan, People's Republic of China, is a Tertiary, intracontinental, ductile strike-slip shear zone along which Indo-China was extruded eastward as a result of the collision (Schaerer et al., 1990; Tapponnier et al., 1990). The sense of shear in the deformed Miocene-age rocks exposed in the core of the Ailao Shan and Diancang Shan is left-lateral, consistent with this hypothesis. Deformed granites in the Ailao Shan yield Miocene uranium–lead mineral ages (23.0 ± 0.2 million years [Ma] [Schaerer et al., 1990]) and thus provide an upper limit for the cessation of ductile behavior within this portion of the shear zone. Tapponnier et al. (1990) suggest that the total amount of left-lateral offset during the Tertiary may have been as much as 500 km. These observations of the timing and sense of movement suggest that the Ailao Shan–Diancang Shan shear zone is the contemporaneous strike-slip counterpart of the Himalayan Main Central Thrust, which is probably responsible for most of the uplift of the Himalayas. The proportion of convergence absorbed by continental escape along this shear zone is estimated to be 14 to 20% of the total shortening of Asia since collision began (approximately 2300 km of total convergence).

To gain a better understanding of the pressure–temperature history (P–T path) of the shear zone, we analyzed compositional zoning patterns from garnets in the metamorphic rocks of the Diancang Shan. In rocks with appropriate mineral assemblages, pressure and temperature control the composition of a growing garnet. Since diffusion in garnet is slow, the initial growth profile is preserved and can be used to calculate the P–T path during growth. Then we used this P–T path to infer the tectonic history of the sample.

The garnets from the Diancang Shan preserve a P–T path characterized by isothermal decompression (Figure 1). Thermochronological results from adjacent samples indicate that the isothermal decompression

---

**University of California at Los Angeles.*
†*University of Paris, France.*

observed in this sample immediately preceded rapid cooling, which terminated at ~20 Ma. These results also suggest that ductile slip ceased while the presently exposed rocks were at peak pressure–temperature conditions and that the gneisses were partially unroofed immediately following the left-lateral activity.

Because of our findings, we support the view that extrusion of Indochina occurred along the left-lateral Diancang Shan shear zone between about 32 and 16–19 Ma and that lateral extrusion was important in accommodating the Indo-Asian collision during this period. ◆

References

Schaerer, U., P. Tapponnier, R. Lacassin, P. H. Leloup, D. Zhong, and S. Ji (1990), "Intraplate Tectonics in Asia: A Precise Age for Tertiary Large-Scale Movement along the Ailao Shan–Red River Shear Belt, China," *Earth Planet. Sci. Lett.* 97, 65–77.

Tapponnier, P., R. Lacassin, P. H. Leloup, U. Schaerer, D. Zhong, S. Ji, H. Wu, J. Zhong, L. Zhang, and X. Liu (1990), "The Ailao Shan/Red River Metamorphic Belt: Tertiary Left-Lateral Shear between Indochina and South China," *Nature* 343, 431–437.

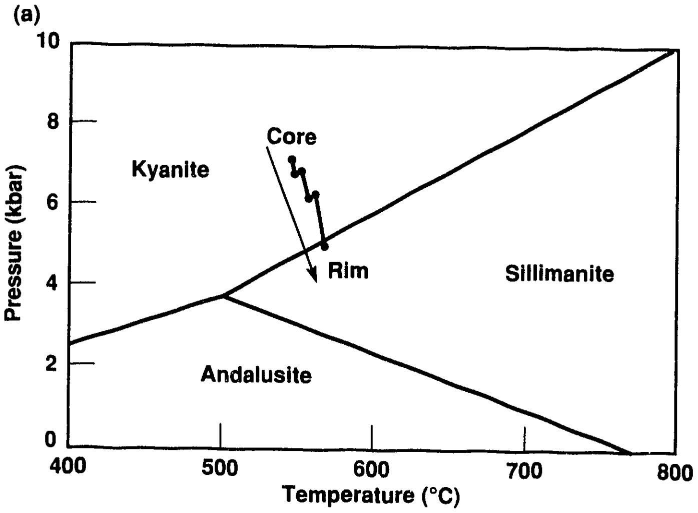

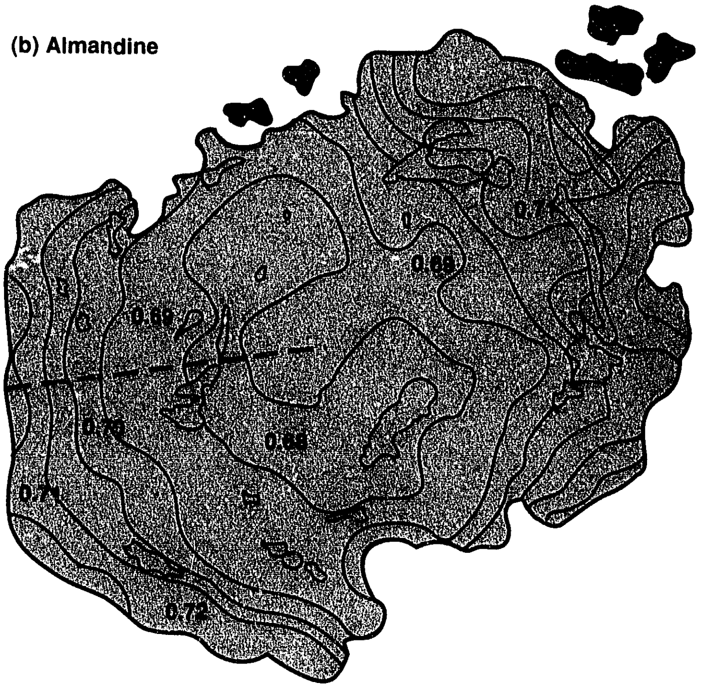

Figure 1. (a) Pressure–temperature (P–T) path determined by analyzing zoning profiles in garnets collected from metamorphic rocks in the Diancang Shan shear zone. The P–T path indicates that the garnet grew along an isothermal decompression path, which represents rapid uplift. (b) Zoning patterns in almandine, an iron–garnet component, showing the analyzed values of Mg/Mg + Fe.

Equations of State and Electrical Conductivities of Planetary Liquids

W. J. Nellis, S. T. Weir, and A. C. Mitchell

The outer envelopes of the giant planets Jupiter, Saturn, Uranus, and Neptune are composed primarily of hydrogen. Researchers believe that the external magnetic fields of Jupiter and Saturn are generated by the convective flow of electrically conducting hydrogen at high pressures and temperatures. Shock-compression experiments with liquid hydrogen and deuterium are known to produce pressures and temperatures comparable to those in the giant planets.

Although liquid hydrogen is thought to be the most abundant planetary component, Uranus and Neptune also contain considerable "planetary ice," which we represent in the laboratory with a liquid mixture called "synthetic Uranus," a representative mixture of water, ammonia, and alcohol. In FY 1992, we measured electrical conductivities and the equation of state of hydrogen at pressures and temperatures that represent giant planet interiors to obtain data for planetary models.

We achieved single-shock compression by accelerating planar tantalum projectiles to 5 to 7 km/s with a two-stage gun that propelled them against an aluminum specimen holder. We cooled the cryogenic specimen holders to 20 K with liquid hydrogen and condensed specimens from the gas phase. We used deuterium specimens because their temperatures and resulting conductivities are much higher and easier to measure than those of hydrogen. The properties of hydrogen or deuterium can be calculated from data for either one as long as the isotope is considered. We measured electrical conductivities using a two-probe method. We calibrated cell resistance experimentally and used a three-dimensional electrode representation.

The points measured for liquid deuterium are plotted in Figure 1 as log(σ) vs T^{-1}. The straight-line fit shows that these data fit:

$$\sigma = \sigma_0 \exp\left(-E_g/2k_BT\right), \qquad (1)$$

between 7.2 and 7.8 cm^3/mol, 13 to 20 GPa, and calculated temperatures of 2900 to 4600 K, where log(σ) is the logarithm of measured conductivity, σ_0 is a constant, E_g

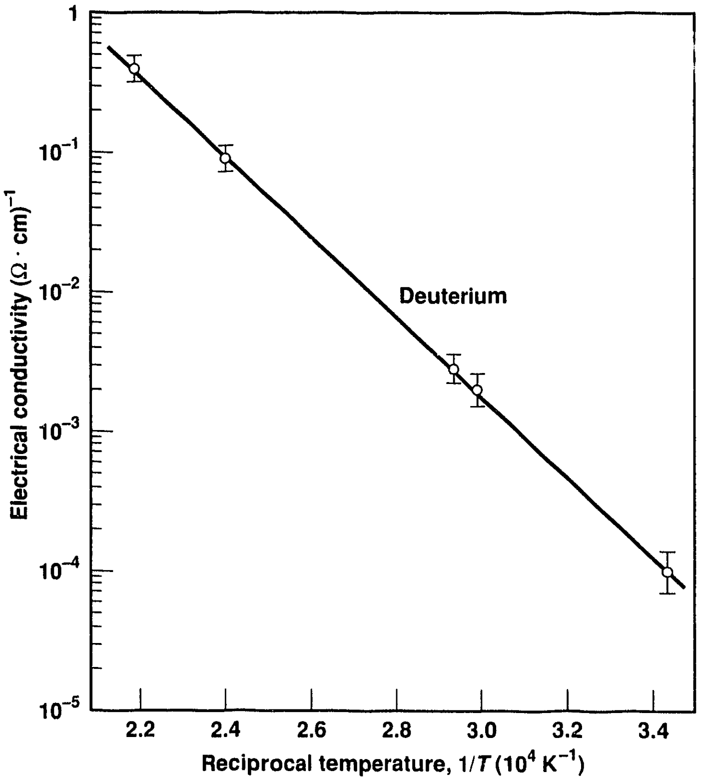

Figure 1. Logarithm of electrical conductivity of shock-compressed liquid deuterium vs reciprocal temperature in the pressure range 13 to 20 GPa. This direct measurement is the first of the hydrogen gap at high pressures.

is the electronic energy gap, k_B is Boltzmann's constant, and T is temperature (Nellis et al., 1992). Initial volume is 24 cm^3/mol, so the compressed volume is nearly constant. The fit in Figure 1 corresponds to $E_g = 11.7$ eV and $\sigma_0 = 1.1 \times 10^6$ $(\Omega \cdot \mathrm{cm})^{-1}$. E_g is 70% larger and σ_0 is 10^3 larger than previously proposed (Kirk and Stevenson, 1987). The semiconducting hydrogen energy gap of 12 eV at 8 cm^3/mol derived from the conductivities agrees with recent theoretical quasiparticle calculations by researchers at UC Berkeley. This direct measurement is the first of the hydrogen energy gap at high pressures.

When we measured the electrical conductivity of liquid deuterium at peak-impact velocity, we found that it was 4 orders of magnitude greater than hydrogen at the same velocity because the calculated temperature is 4600 K for deuterium and 2900 K for hydrogen. Our measurements are the only data for an outer planetary material at an interior planetary pressure range. ◆

References

Kirk, R. L., and D. J. Stevenson (1987), "Hydromagnetic Constraints on Deep Zonal Flow in the Giant Planets," *Astrophys. J.* **316**, 836.

Nellis, W. J., A. C. Mitchell, P. C. McCandless, D. J. Erskine, and S. T. Weir (1992), "Electronic Energy Gap of Molecular Hydrogen from Electrical Conductivity Measurements at High Shock Pressures," *Phys. Rev. Lett.* **68**, 2937.

New Tracers for Geochemical Applications of Accelerator Mass Spectrometry

I. D. Proctor, J. R. Southon, M. A. Caffee, R. S. Finkel, M. L. Roberts, and L. J. Harris

Accelerator mass spectrometry (AMS) measures extremely low concentrations of selected radioisotopes at sensitivities 3 to 6 orders of magnitude greater than those achieved by decay-counting techniques. With AMS, we can measure some naturally occurring cosmogenic isotopes at abundance sensitivities of $1{:}10^{-15}$ for the radioisotope to stable-isotope ratio. We have developed separative chemistries for naturally occurring materials to remove the chemical element for analysis and to reduce elements that interfere in the isotopic measurement process. Our sample preparation facilities at LLNL are in unclassified laboratories and are readily available to outside collaborators. In FY 1992, we developed accelerator operating procedures for AMS measurement of the isotopes ^{7}Be, ^{10}Be, ^{26}Al, ^{36}Cl, and ^{129}I. Table 1 summarizes sensitivities, accuracies, and operating characteristics for these isotopes.

We performed about 20 runs for ^{7}Be and ^{10}Be, measuring 750 unknowns primarily for atmospheric transport studies and paleoclimate records from ice cores. We measured ^{7}Be and ^{10}Be in aerosol filters collected at Alert, Canada, and on polar snow samples. The concentrations of these nuclides, which depend on their production rates and on the atmospheric residence time of the aerosol to which they become attached, are higher in the stratosphere than in the troposphere. Our measurements provide information about stratosphere–troposphere exchange in polar regions. We also measured several cosmogenic radionuclide concentrations in the GISP2 Summit, Greenland, ice core to investigate cosmogenic isotope production and atmospheric transport during the end of the last glacial period, the glacial transition, and the current warm period.

We performed 13 runs for ^{36}Cl, measuring 700 unknowns, and 7 runs for ^{26}Al, measuring 300 unknowns. We used natural and bomb-produced ^{36}Cl as a tracer to study groundwater movement and recharge rates. In addition, we measured the buildup of ^{36}Cl, ^{26}Al, and ^{10}Be in recently exposed rocks to study erosion and deglaciation histories. Study areas include Baffin Island, Canada (deglaciation history), Hawaii (river-valley formation mechanisms), Cima Volcanic Field (flow dating and soil formation rates), sand samples from several sites (sand formation history and mechanism), and several glaciated sites in the Sierra Nevada.

We performed three ^{129}I runs in which we checked calibration standards and established backgrounds. These data will become baseline and historical dosimetry for releases from reprocessing facilities and accidental releases such as those that occurred at Three Mile Island and Chernobyl. The incidence of thyroid cancer in children living near the Chernobyl reactor has risen dramatically. If we measure ^{129}I in soil samples from the suspected plume area, we can infer the thyroid dose received from short-lived iodine isotopes. This information should aid medical personnel in the former Soviet Union in treating residents of this area.

We can process beryllium, aluminum, and chlorine samples at rates equivalent to or better than those achieved at other AMS facilities. In addition, we can process more isotopes (including our existing ^{14}C capability) for geochemical research than any other facility. In FY 1992, we processed samples for LLNL research projects and for 65 collaborators from universities and government agencies. ◆

Table 1. Geochemical isotope performance in FY 1992.[a]

Isotope	Sample	Sensitivity ($\times 10^{-15}$)	Accuracy (%)
^{7,10}Be	1 mg BeO	5	2–3
^{26}Al	2 mg Al_2O_3	2	2–3
^{36}Cl	5 mg AgCl	3	2–3
^{129}I	5 mg AgI	0.03	3–5

[a] The sample is the chemical form of the material as it is placed in the ion source for analysis. Accuracy is given in percentage of abundance for a radioisotope abundance of $1{:}10^{-12}$. Samples near the sensitivity limit have a typical accuracy of about 10%.

High-Performance, Global Climate Modeling

A. A. Mirin, D. E. Shumaker, and M. G. McCoy

We are rewriting an existing, atmospheric, general-circulation model for massively parallel processors. We are converting to massively parallel processing because conventional vector supercomputers cannot perform affordable, long-time calculations at adequate spatial resolution. This project is a major step toward creating a high-performance, comprehensive earth-systems model that can project climatic changes with the detail and quantitative confidence necessary to plan energy, economic, and environmental studies.

The Atmospheric Model

We have acquired the atmospheric, general circulation model (AGCM) developed by Arakawa and coworkers at the University of California at Los Angeles (Arakawa and Lamb, 1977) and have recast it in portable, parallel form. This computer code uses a rectangular latitude/longitude discretization and a normalized pressure coordinate to represent altitude. The model consists of two major components: hydrodynamics and column physics. The hydrodynamics component uses a conservative, explicit, finite-difference procedure on a staggered mesh. The hydrostatic approximation effectively reduces the three-dimensional problem to a collection of two-dimensional problems. Because of meridianal convergence of the grid near the poles, we use a longitudinal filtering procedure to eliminate unwanted modes.

The second major component of the model, column physics, refers to physical-process representations that proceed independently in each vertical column and are coupled only through the hydrodynamics component. Examples include long- and short-wave radiation transfer and cumulus convection of heat and moisture.

Parallelization Strategy

To rewrite AGCM for parallel computing, we have implemented a strategy that uses two-dimensional latitude/longitude domain decomposition with message-passing. Subdomains consist of contiguous, vertical columns of rectangular cross section in both latitude and longitude that extend from the earth's surface to the upper atmosphere (see Figure 1). We chose to decompose in only two dimensions because the column processes strongly couple the elements within the column and hence do not adapt naturally to parallel strategies along it. In addition, the number of mesh points in the vertical direction is usually small. We chose a two-dimensional decomposition instead of a one-dimensional decomposition because a one-dimensional decomposition does not provide the necessary concurrence for mesh sizes of interest and has an asymptotically larger communications cost.

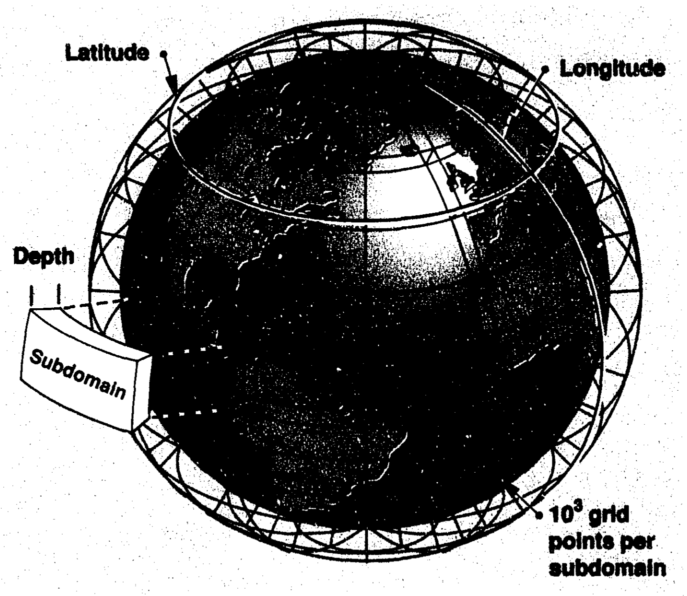

Figure 1. Two-dimensional domain decomposition used to recast the atmospheric model for parallel computing.

Subdomains are assigned to processors in a deterministic manner, and data are transmitted between subdomains in the form of messages. Adjacent subdomains overlap to minimize the amount of message traffic. Thus, information is passed only once, and it is stored in the region of use.

Portability

The rapid evolution of computing technology has resulted in the production of many different machines from many different vendors. Because we want to carry out scientific studies in a reliable production environment and, at the same time, develop advanced computational versions for high-performance systems, a portable source code is of paramount importance.

We are addressing two issues that affect portability: dynamic memory management and interprocess communication. Allocating memory at run time, rather than at compile time, allows memory to be used more efficiently and makes it easier to resize subdomains dynamically (for example, when balancing the load between processors). Because the language constructs for dynamic memory management are not standard, we are using the M4 preprocessor to implement macro constructs that are processed prior to compilation. This practice confines

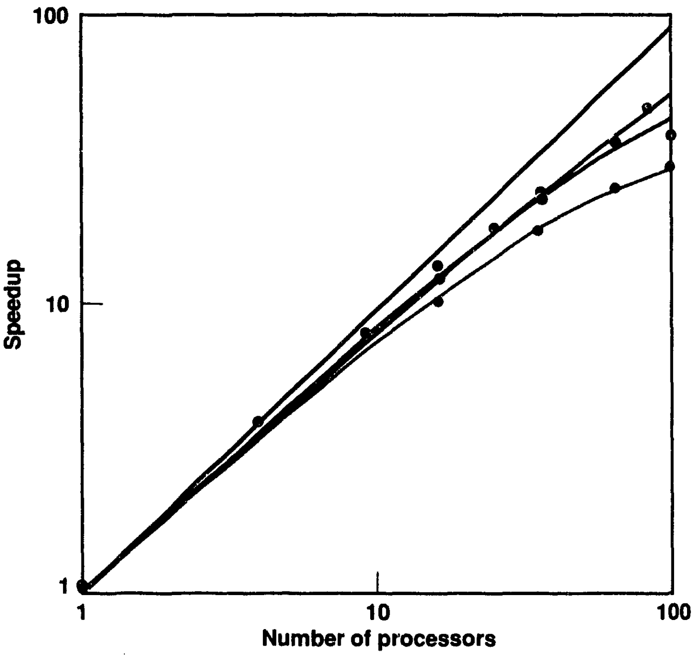

Figure 2. Observed (data points) and predicted (curves) increase in computing speed obtained from parallelization of the atmospheric model on the BBN TC-2000. Dark green curve shows hydrodynamics without filters; light green curve shows hydrodynamics with filters; and gray curve shows hydrodynamics with filters and column physics. Black curve shows 100% efficiency.

nonportable constructs to the bodies of the macros and allows them to be easily modified to accommodate new computer architectures.

Message-passing constructs vary from machine to machine. We are also constructing macro commands for sending and receiving messages. These constructs, along with directives using the CPP preprocessor, will allow movement between many machines with only a few parameter changes.

Parallel Performance

The parallel performance of any code depends on different factors. First, the computational load must be balanced so that some processors do not idle unnecessarily while others are working. It is also important to minimize interprocessor communication costs.

The increase in computer speed obtained from parallelization can be defined as the time for a serial calculation divided by the time for the same calculation in parallel. A perfectly efficient calculation will, in a parallel environment, exhibit an increase in speed equal to the number of processors applied to the problem. If we assume the arithmetic time is inversely proportional to the number of active processors, the increase in speed becomes a function of the communication time relative to the time needed to carry out the arithmetic computations.

For the two-dimensional, domain-decomposition strategy used in the atmospheric model, the increase in computing speed is asymptotically proportional to the square root of the number of processors applied to the problem (Dannevik et al., 1992). This relationship assumes a load-balanced computation for a fixed-size problem having subdomains of nontrivial size. Figure 2 shows the performance of the code on the BBN TC-2000 machine. As the processor count increases, the increase in computing speed agrees with theoretical predictions. When longitudinal filtering is added, the efficiency is reduced because of associated communication costs. The addition of (simulated) column physics increases the efficiency, however, because column physics does not involve communication.

Future Directions

We will proceed in several directions. We will port the AGCM to next-generation platforms such as the Thinking Machines CM-5 and the Intel Paragon, where we can test the scalability of the algorithms. We will investigate improvements to the algorithms, particularly in the filtering procedure, and we will initiate a detailed study of load balancing. We will couple the atmospheric code to an ocean model in a portable, multimodule, computational framework. Our work suggests that an advanced, coupled, climate-simulation model with teraflop performance is indeed possible. ◆

References

Arakawa, A., and V. Lamb (1977), "Computational Design of the Basic Dynamical Processes of the UCLA General Circulation Model," in *Methods of Computational Physics* (Academic Press, New York, NY), vol. 17, p. 173.

Dannevik, W. P., P. G. Eltgroth, M. G. McCoy, A. A. Mirin, and M. F. Wehner (1992), "Development of a Portable Parallel Atmospheric General Circulation Model," in *The 1992 MPCI Yearly Report*, E. D. Brooks III, Ed., Lawrence Livermore National Laboratory, Livermore, CA, UCRL-ID-107022-92.

A Global, Three-Dimensional Tropospheric Ozone Model

C. S. Atherton, J. E. Penner, and J. J. Walton

The troposphere contains hundreds of reactive gases. Predicting the concentrations of those that are harmful pollutants and greenhouse gases requires photochemical modeling on a global, three-dimensional scale. Such modeling is computationally expensive because gas concentrations vary over many orders of magnitude, both spatially and temporally.

Predicting Ozone and Methane Concentrations

Two important gases are ozone (O_3) and the hydroxyl radical (OH). Ozone is both a greenhouse gas and a regulated pollutant. It forms when carbon monoxide (CO), methane (CH_4), and nonmethane hydrocarbons (NMHCs) react in the presence of nitric oxides (NO_x) and sunlight. The hydroxyl radical is ubiquitous, and reaction with it is the primary sink for virtually all gases in the atmosphere. Formation of OH is initiated by the photodissociation of O_3. Evidence is growing that tropospheric ozone levels have dramatically increased during the last 150 years. Despite ozone's importance, few groups in the world can model three-dimensional atmospheric chemistry on a global scale.

We have developed a three-dimensional, global atmospheric-oxidant model that predicts tropospheric concentrations of O_3 and OH, among other species. We used the framework of GRANTOUR, a three-dimensional chemistry-transport-deposition model. However, earlier versions of GRANTOUR contained highly simplified chemistry. During FY 1992, we completed installing $CO/CH_4/NO_x/OH/O_3$ chemistry into GRANTOUR. Both CO and CH_4 are long-lived and ubiquitous, and the resulting chemistry represents the "background" chemistry of the troposphere.

Reducing Computation Time

Atmospheric-chemistry modeling is computationally expensive because of the number of species involved and the mathematical stiffness of the system. During FY 1992, we implemented a streamlined set of chemical reactions, which saved 30% in central processing unit time. Next, we altered the logic within the chemistry subroutines to save an additional 30%. The predictor–corrector proved to be the most time-efficient integration technique of several that were investigated because it completely vectorizes. We also fully converted the code to run under the Unix operating system. We can now debug and test the code on a Sun workstation and still conduct production runs on the Cray.

We used the Unix version of GRANTOUR to analyze the global CH_4 budget. A total sink for CH_4 + OH was calculated by using the GRANTOUR-predicted OH fields and specifying CH_4-based observations. Reaction with OH is the only appreciable sink for CH_4. We presented our estimate of a CH_4 sink, 510 Tg/y, at the North Atlantic Treaty Organization's Advanced Research Workshop on Methane (Atherton et al., 1991), and it compared well with total global source estimates presented there.

In addition, we used natural and anthropogenic sources of NO_x to calculate current O_3 and OH fields for present-day conditions (Figure 1). These "background" values are in reasonable agreement with measurements made at remote locations. ◆

References

Atherton, C. S., J. E. Penner, and J. J. Walton (1991), "The Atmospheric Methane Cycle: Three-Dimensional Model Simulation of the Global Budget," in *NATO Advanced Research Workshop on the Atmospheric Methane Cycle, Timberline Lodge, OR, October 1991.*

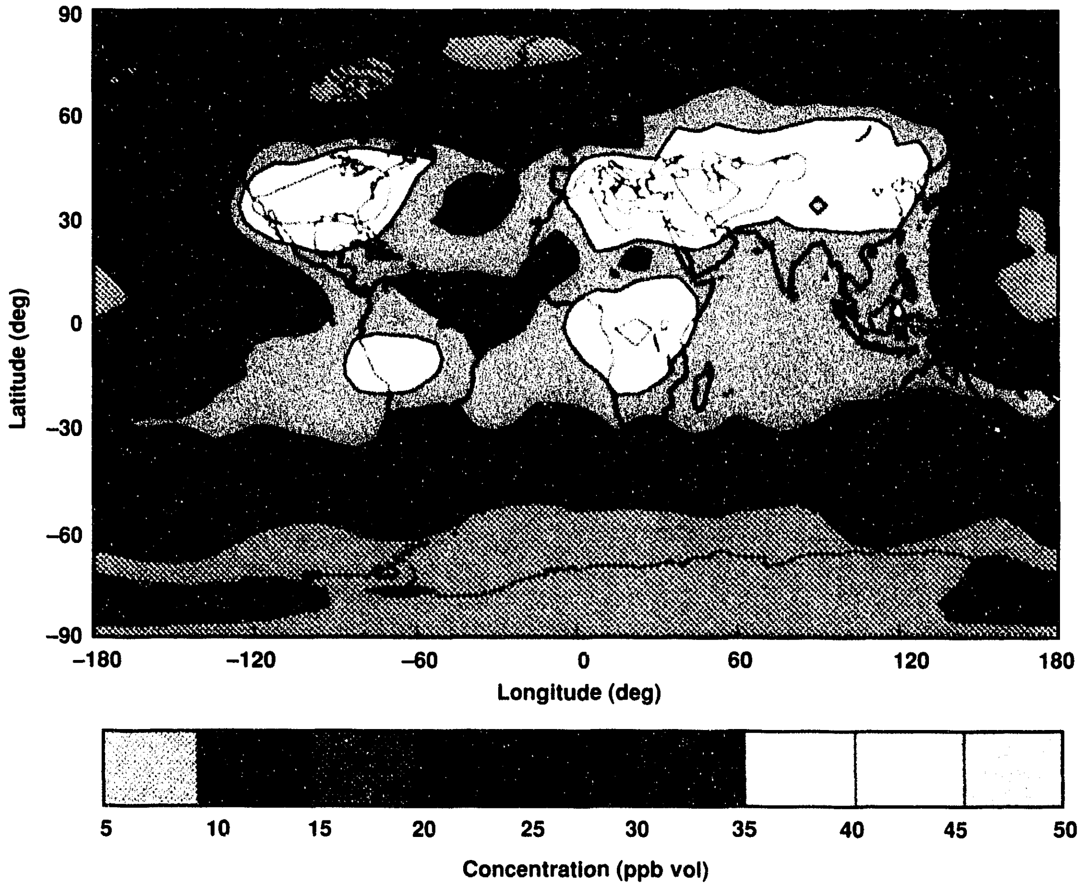

Figure 1. Predicted ozone concentrations (ppb vol) at 926 mb for July 1992. Elevated O_3 concentrations are due to anthropogenic NO_x sources from fossil-fuel combustion (Northern Hemisphere) and biomass burning (Southern Hemisphere).

Using Neural Networks to Forecast Earthquakes

F. U. Dowla, J. B. Rundle, J. J. Hopfield,* T. F. Hauk, and G. Zandt

Many seismologists believe that the seismicity patterns preceding an earthquake can be used to forecast the actual shock. They use trial-and-error methods that rely on recognizing regional patterns to predict local earthquakes, but the predictions are often inaccurate. Our goal was to determine if backpropagation neural networks could more accurately decipher precursory earthquake information.

Backpropagation Neural Networks

Backpropagation networks use parallel processing units to solve difficult pattern-recognition problems. These networks "learn" from previous examples, then apply their knowledge to determine the algorithm needed to solve a new problem. We created an extensive training database for our network with information gathered from the U.S. Geological Survey and many U.S. universities.

---

*California Institute of Technology, Pasadena.

Seismologists have systematically recorded earthquakes for only about 60 years. But to accurately predict these events, they must study recordings of thousands of years seismicity patterns. Because no computer model exists that will generate such long sequences of seismicity data, we developed one. We based our model on the Burridge–Knopoff cellular automation model in which a sliding plate moves against the surface of interconnected blocks linked by nearest-neighbor springs.

We designed a neural-network architecture with a small number of interconnections based on one hidden layer and seven hidden units. We used many more seismicity examples than interconnections so that the network would behave less as a memory system and more as a generalizing, or predicting, system.

Earthquake Forecasting Strategy

Figure 1 shows our earthquake forecasting strategy. The network analyzed seismicity data (location and time) from the Southern and Northern Hayward faults to predict the next earthquake on the Southern Hayward Fault. We measured the performance of our forecasting system by calculating the correlation coefficient between the predicted and actual earthquake. The correlation coefficient is a statistical measurement that can take any value between –1 and +1. The best case is +1, and the worst case is -1.

We trained the network with 100 events from the Southern and Northern Hayward faults, then tested it with the next 76 events. The correlation coefficient between the predicted and actual earthquakes was 0.37. For computer models trained with a database containing 4989 computer-generated test events, the correlation coefficient was 0.23. These numbers are not high enough to indicate that neural networks would be useful as sole forecasting tools but do suggest that they would be useful as one component in a complex forecasting system.

Our method generalized earthquake phenomena using past data but did not explain the physical mechanisms of the earthquake phenomena such as how various faults are related and how they affect the duration and force of the earthquake. In FY 1993, we will determine if trained networks can clarify some of these unknown physical mechanisms and if we can improve our forecasting by including them in our database. ◆

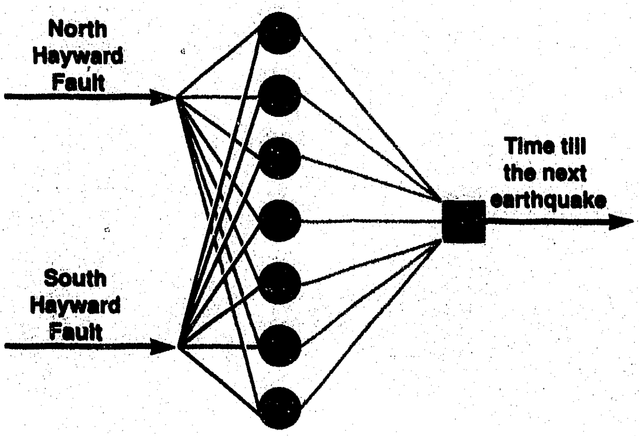

Figure 1. Backpropagation neural network. Information on past and present seismicity on the Hayward Fault transferred through seven hidden units (green circles) and one hidden layer (black square). The correlation coefficient was not high enough to indicate that neural networks would be useful as sole forecasting tools but does suggest that they would be useful as one component in a complex forecasting system.

Aerosol and Cloud Interactions in a Global Climate Model

J. E. Penner, C. R. Molenkamp, and C. C. Chuang

Although clouds have a major influence on global climate, the effects of aerosols on clouds and clouds on aerosols are not accounted for in climate models. Aerosols are injected into the atmosphere and formed in situ from photochemical reactions. When clouds form, water is condensed onto aerosol particles (called cloud condensation nuclei). If aerosols increase, cloud droplet concentrations will increase, creating clouds with smaller drops that take longer to coalesce into raindrops, thereby affecting the lifetime of the clouds and perhaps precipitation frequency. Because rain is one way of removing aerosol from the atmosphere, a longer cloud lifetime could mean longer aerosol lifetimes. To assess the possible magnitude of aerosol-induced cloud effects on climate and the effects of clouds on aerosols, we are revising our climate model to include a treatment of the interactions between clouds and aerosols.

Climate and Aerosols

We plan to link our aerosol model to a version of the Hamburg climate model ECHAM, which includes a prognostic treatment of cloud water and will allow us to determine if increased anthropogenic aerosol concentrations can change average cloud cover and climate by changing cloud lifetime.

In FY 1992, we began improving our parameterization of the effects of sulfur aerosol on initial droplet-number concentration and size distributions (Figure 1). We surveyed the literature to determine realistic aerosol-sulfur size distributions over continental areas (where anthropogenic sulfur emissions are the largest source) and over marine areas (where the emission of dimethylsulfide by marine phytoplankton is the major source). We used these size distributions in a detailed microphysical model to determine the number of droplets formed as a function of updraft velocity. The results have been fitted by an analytical function to make them easier to work with in the climate model. We are further developing this parameterization to examine regions with mixed marine and continental aerosol size distributions. To test the adequacy of the predicted size distributions, we are introducing the parameterization into the CCM1 climate model

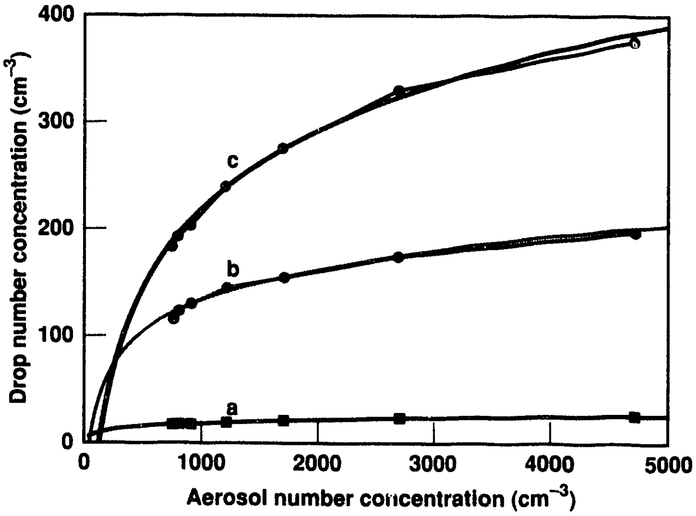

Figure 1. Predicted concentration of drops as a function of aerosol number concentration at cloud base for vertical velocities of (a) 0.01 m/s, (b) 0.1 m/s, and (c) 0.2 m/s. Droplet concentrations increase rapidly with aerosol number concentration at low aerosol concentrations and when updraft velocities are higher than 0.1 m/s, but sensitivity decreases at high aerosol concentration and for low velocities.

(developed at the National Center for Atmospheric Research). The predicted change in cloud reflection was large (–2 W/m^2) and as a result, we are refining our treatment of the effects of aerosols on droplets.

In FY 1993, we will link our aerosol model to the ECHAM model and begin adding the parameterization to that model. We plan to calculate the reflection of solar radiation by anthropogenic sulfate aerosols and the effects of aerosols on clouds. ◆

References

Chuang, C. C., and J. E. Penner (1992), "Effects of Anthropogenic Sulfur Aerosols on Climate," in *Nucleation and Atmospheric Aerosols*, N. Fukuta and P. E. Wagner, Eds. (Deepak Publishing, Hampton, VA), pp. 501–504.

Impact and Phase Transitions in Geologic Materials

W. J. Nellis and A. J. Gratz

Comets and asteroids colliding with planetary bodies generate high pressures and temperatures. A key issue for planetary scientists is determining deformation effects caused by these impact-induced pressures and temperatures, including phase transitions, microstructure changes, and chemical reactions. In FY 1992, we performed shock-recovery experiments on planetary materials and on rocks ejected from explosive volcanism so we can better understand high-velocity impacts.

High Shock Pressures

In FY 1992, we investigated shock-induced phase and microstructural transitions in geologic materials and compared them with those in nature. We propelled projectiles against target specimens to generate pressures of 1 to 50 GPa (10 to 500 kbar), accelerating the projectiles to velocities as high as 4 km/s with a 6.5-m-long, two-stage light-gas gun. Next, we applied high shock pressures to the target geologic specimens. The very high quench rates induced by the high shock pressures retained the specimens' phase and microstructural features. Then we studied the quench rates of the rapidly decreasing shock pressures and temperatures. These dynamic experiments were controlled by accurately measuring the velocity of the projectiles and by using relatively thin target specimens with a shock wave that required several reverberating waves to reach the final pressure.

Our new containment capsules simulate natural specimen loading because we can create temperatures much closer to those of a natural impact. If we heat the specimens to create higher initial temperatures, that is, temperatures closer to planetary conditions, we need less shock pressure to reach a given high-pressure phase. For example, we can recover shocked SiO_2 quartz in an amorphous state above about 40 GPa. In addition, a different and rare initial form of SiO_2, called cristobalite, underwent a transition to the high-pressure amorphous phase at much lower pressures and a narrower pressure range than quartz. This result raised questions about the magnitudes of shock pressures assigned in nature and about the nature of geologic materials prior to impact events.

Formation of the Cretaceous–Tertiary Boundary

The Cretaceous–Tertiary (K–T) boundary is a layer of the earth that contains high concentrations of quartz and feldspars with microstructures similar to our shocked mineral samples. Most scientists accept that an asteroid colliding with Earth caused this layer, the signature of the mass extinction of species. Others, however, speculate that explosive volcanism caused the K–T boundary. To test this second hypothesis, we simulated volcanic explosions by heating rock targets and striking them with projectiles to observe damage in the ejecta. Figure 1 proves that volcanic explosion is too weak to produce the shock effects found at the K–T boundary and that meteorite impacts rather than volcanism caused the mass extinction of species (Gratz et al., 1992). We also showed that meteorite impacts produce weakly damaged, high-velocity ejecta, explaining why relatively undamaged lunar and Martian rocks reach Earth after ejection from those bodies. ◆

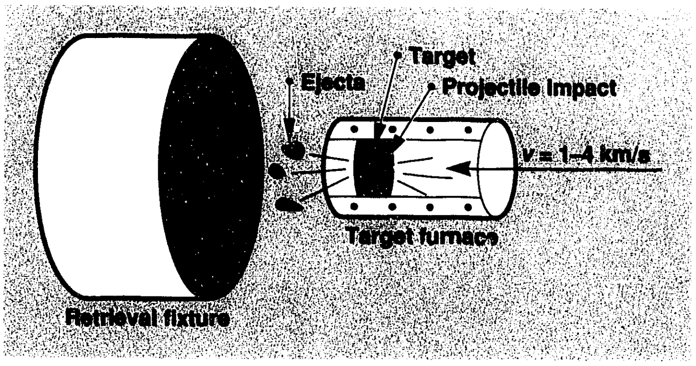

Figure 1. Simulating a volcanic explosion. We heated the rock target to about 600°C before striking it with a projectile at 1 to 4 km/s. The experiment shows that impact-induced pressures are too weak to produce the shock effects found at the Cretaceous–Tertiary boundary.

References

Gratz, A. J., W. J. Nellis, and N. A. Hinsey (1992), "Laboratory Simulation of Explosive Volcanic Loading and Implications for the Cause of the K/T Boundary," *Geophys. Res. Lett.* **19**, 1391.

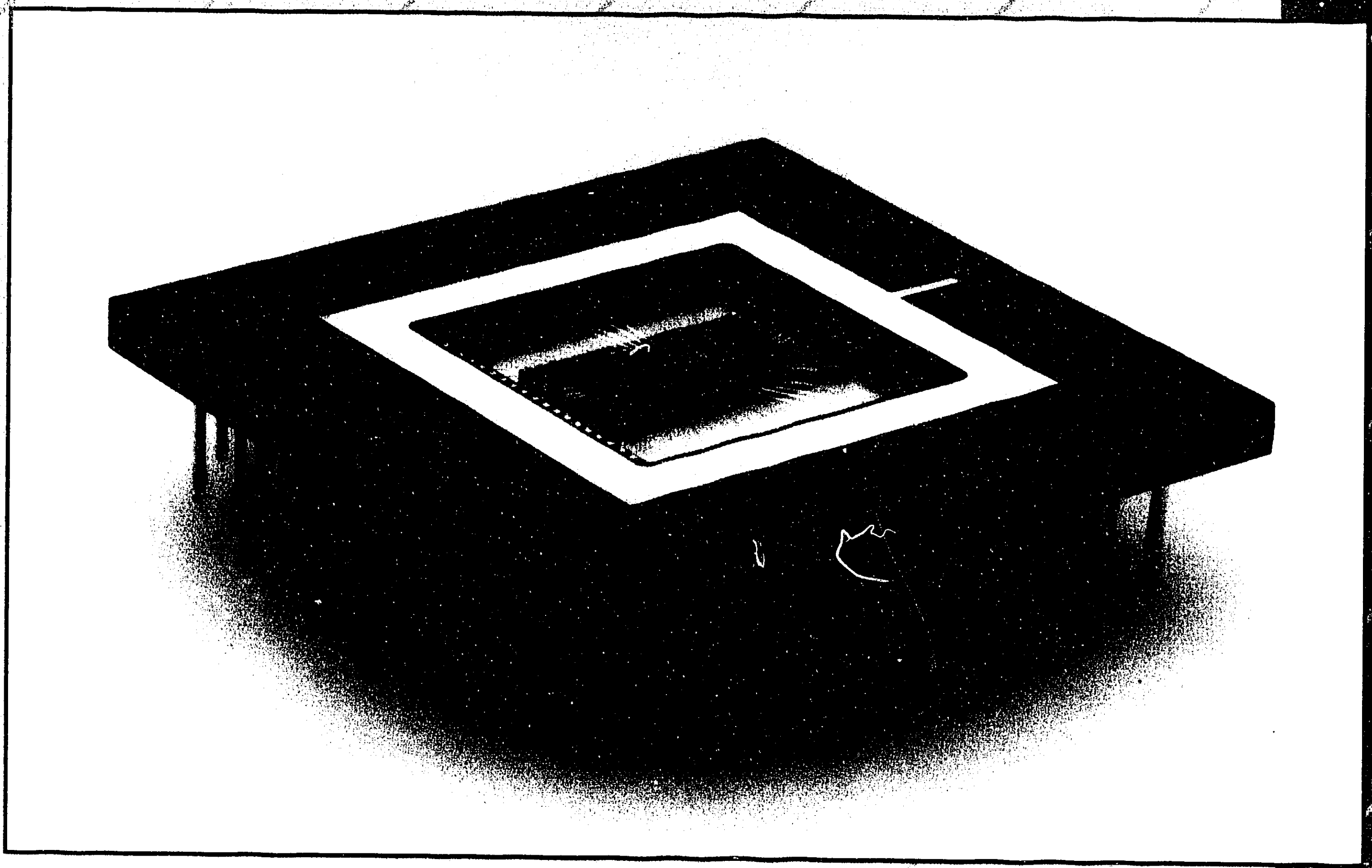

Advanced Sensors and Instrumentation

Laboratory Directed Research
and Development FY 1992

On the previous page. Synaptic-array chip used to test a neural-network board. The chip consists of 34,000 2-MΩ resistors and has a packing density of 0.2 million resistors/cm^2.

Enabling Technologies for Microinstruments on a Chip

J. A. Folta, N. F. Raley, D. J. Nikkel, and R. I. Pratt

Highly miniaturized flow systems and components, namely pumps and valves, have received wide attention in recent years. Successful development of such systems will affect various fields, including chemical and biochemical analysis, industrial process control, clinical diagnosis, and environmental monitoring.

In FY 1991, we designed a thermopneumatically actuated peristaltic diaphragm pump (Figure 1). The pump consists of three silicon wafers bonded together: a flow-channel wafer, a diaphragm wafer, and a heater wafer.

To operate the pump, we energize the leftmost heater to heat and expand the fluid within the thermopneumatic chamber. The expanding fluid causes the left diaphragm to bulge downward into the flow channel. The flow channel geometry closely matches that of the bulging diaphragm so that the fully bulged diaphragm displaces liquid in the channel and seals off the channel to prevent backflow. We then energize the center heater to bulge the center diaphragm downward to induce flow along the channel. We energize the right heater while turning off the left one, to expel fluid from the pump and simultaneously draw more fluid in. Repetitive cycling of the three actuators results in a peristaltic pumping action. A valve operates similarly but consists of only a single actuator that seals against the bottom of the channel.

An advantage of the pump design is that its pulsed mechanism may provide precise and repeatable volumes of liquids with each cycle, thus mitigating the need for flow meters in a future integrated system. In addition, the pump's simple three-wafer design minimizes the complexities of multiple-wafer bonding, which are common with four-wafer designs.

We performed transient thermal analysis of the heating and cooling cycles of the thermopneumatic actuator to provide insight into how the heater location affects the maximum frequency of operation. We determined that the heater should be suspended within the thermopneumatic chamber to allow all of the heat to transfer to the thermopneumatic fluid. If we mount the heater on the chamber wall, 98% of the heat is lost directly into the silicon because the single crystal silicon is extremely conductive. The thermal analysis also indicated that we can operate the pump at about 20 Hz, which will provide flow of 7 μL/min at 100 kPa.

We fabricated diaphragms with areas of 1 and 4 mm^2 from silicon nitride, lightly doped silicon

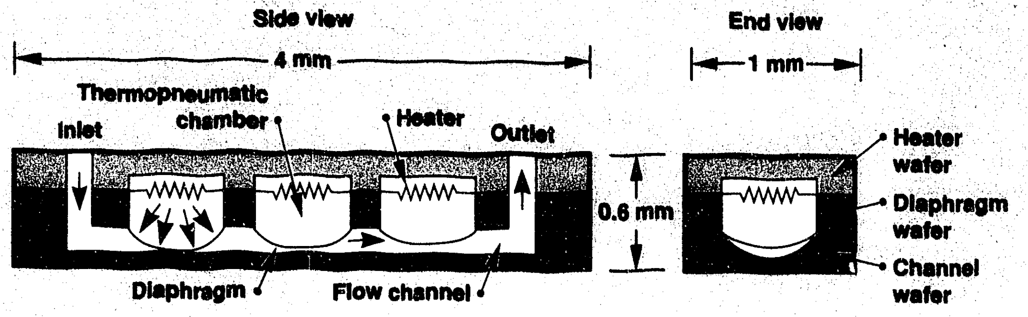

Figure 1. Cross-sectional diagram of the micropump. Heating the thermopneumatic chamber fluid causes the diaphragms to bulge into the channel. Bulging the diaphragms in series results in a peristaltic pumping action.

(electrochemical etch stop), and heavily doped silicon (boron etch stop). We tested them for their deflection response to applied pressure and ultimate burst strength. Next, we measured deflection of the bulging diaphragms with a noncontact optical profilometer. Burst pressures ranged from 40 to 400 kPa, and all three diaphragm materials gave usable deflections of 10 to 20 µm. We selected heavily boron-doped silicon diaphragms for the micropump because of their high burst strength, ruggedness, ease of fabrication, and compatibility with silicon fusion bonding techniques. We pressure cycled such diaphragms more than 1 million times and witnessed no cycling fatigue or other degradation.

The pump must be designed to properly mate the flow channel geometry to the bulging diaphragms; the channel must be shallow (10 to 17 µm deep at center), 1000 µm wide, and gently curved across the width. Such a channel was difficult to fabricate because the radius of curvature of the channel bottom was much larger than existing micromachining techniques could provide.

Figure 2 shows the finished flow channel and diaphragm wafers. Each wafer pair contains three pumps of slightly different sizes. The three center diaphragms on each pump are used for actuation. The outer holes are used as inlet or outlet ports or as alignment holes for the external plumbing fixture. The present pump designs are about 1 cm long to provide adequate space to allow external pneumatic actuation. Initial calculations indicate that a pump as small as 2 mm by 0.2 mm is possible.

Figure 3 shows how the flow of nitrogen through the pump could be reduced by applying pressure to one of the diaphragms. For a nitrogen inlet pressure of 35 kPa, 140 kPa of pressure applied to a diaphragm reduced the flow to 20% of its original rate. We did not apply higher pressures because of limitations of the external fixture. We then primed the pump with water by applying vacuum to the outlet and allowing water to fill the channel without trapping air bubbles. Figure 3 also shows how water flow forced through the pump with 35 kPa of pressure could be reduced by applying pressure to one of the diaphragms. By applying 140 kPa of pressure to a diaphragm, we reduced the water flow to 8% of its original rate. The two additional data points collected at 100 kPa showed that the other two diaphragms were also effective in modulating the water flow.

To demonstrate pumping of water, we vented the pump inlet and outlet ports to ambient pressure while we pulsed the three diaphragms sequentially in a typical peristaltic pattern at 1 Hz. However, we detected no

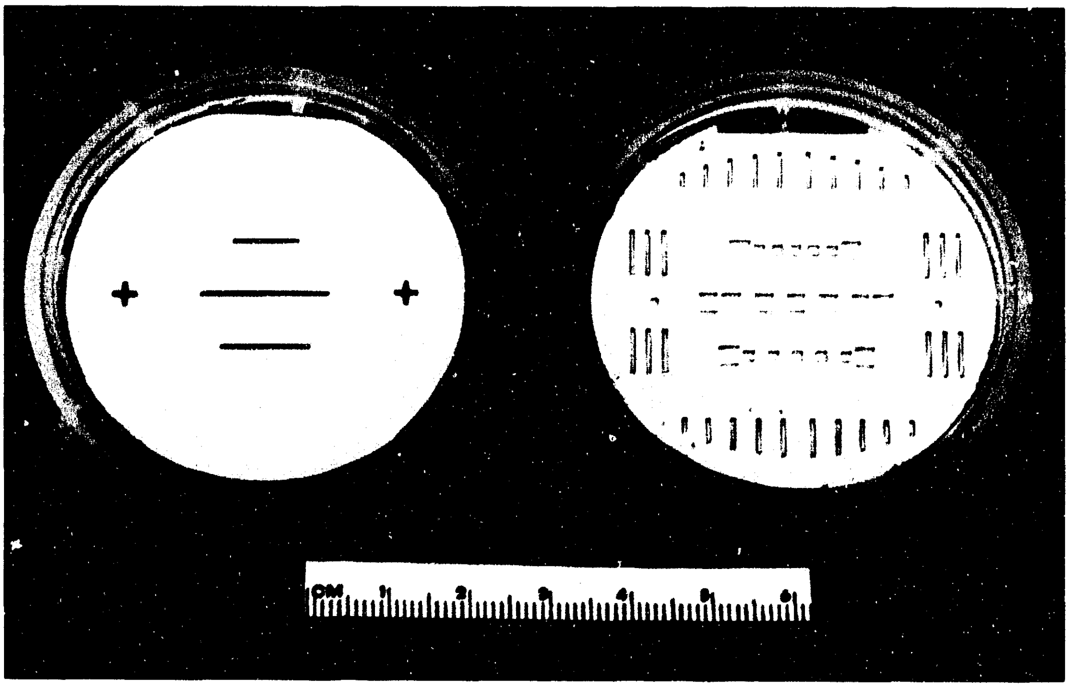

Figure 2. The completed channel and diaphragm wafers prior to bonding and fixturing. Direct silicon fusion bonding requires no adhesives and allows highly accurate alignment of the diaphragms to the flow channel.

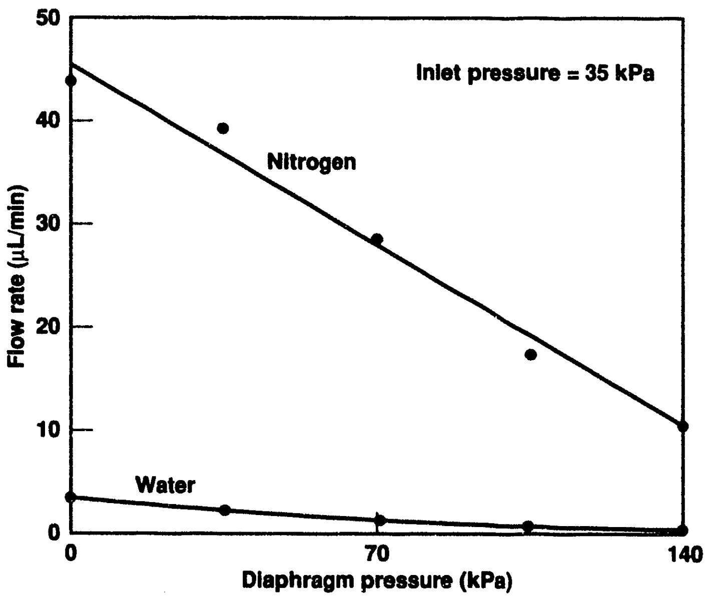

Figure 3. Flow rate of nitrogen and water as a function of diaphragm pressure. To demonstrate valving action, the diaphragms were pneumatically deflected into the channel to modulate fluid flow through the channel.

flow in the outlet capillary. The diaphragms may not be rigid enough to provide a restoring force to the original flat positions, which resulted in a lack of pumping action. However, the thermopneumatic actuators do provide a restoring force for the fully integrated actuators.

Experiments are under way to verify this interpretation. Vacuum can be applied to the diaphragms during the relaxation phase to simulate the effect of a cooling thermopneumatic liquid or condensing vapor bubble. We are changing the external pneumatic test apparatus to prevent a drop in pressure on one diaphragm as another is pressurized. We are also applying acoustic microscopy to measure the diaphragm positions during the experiments. ◆

Infrared-Sensitive Photocathode

R. Mariella, Jr., G. A. Cooper, R. Chow, C. Mailhiot, and Z. Liliental-Weber*

Optical detectors sensitive to light wavelengths between 1 and 12 µm (the infrared [IR] wavelengths) are of particular interest for imaging. The peak wavelength of electromagnetic radiation from a blackbody depends on its temperature. The peak emission of a room-temperature blackbody occurs at a light wavelength of about 10 µm; the peak emission from a blackbody at 100°C occurs near 8 µm. Thus, IR imagers can help us analyze rocket plumes; detect subsurface mines, warm vehicles, and troops; and "see" temperature differences through camouflage. In the future, IR imagers may also be used to analyze and map integrated circuits and printed circuit boards. Medical applications will be possible if the costs of IR images can be lowered and performance improved.

Detectors for wavelengths longer than 1.4 µm are solid-state devices. However, solid-state devices are limited by high noise levels and low gain; they are susceptible to "blinding" by ionizing radiation and are unsuitable for photon counting. Vacuum tube detectors using photocathodes can be used in photon counting and suffer less from these effects, but they are not available for light

---

**Lawrence Berkeley Laboratory, Berkeley, CA.*

wavelengths greater than 1.4 µm. We wanted to make an IR-sensitive photocathode that responds to light with wavelengths greater than 1.4 µm.

Our work builds on two previously demonstrated concepts. The first is the transferred-electron photocathode demonstrated by Varian (now Intevac) in which photons are absorbed in a low bandgap (E_g) material and the photogenerated electrons are moved to the emitting surface by an applied electric field (Bell, 1973; Bell et al., 1974). Figure 1 shows a schematic of this concept.

In the second concept, strained-layer superlattices of $InAs/Ga_xAl_{1-x}Sb$ absorb light for wavelengths from 4 to 12 µm (Kim et al., 1990). Our ultimate goal is to use the $InAs/Ga_xAl_{1-x}Sb$ superlattice as the IR absorber. However, we can achieve two intermediate milestones if, in the interim, we use GaSb as the IR absorber for wavelengths less than 1.7 µm and InAs as the IR absorber for wavelengths less than 4 µm. All three IR absorbers are lattice matched to GaSb and $Ga_{1-y}Al_ySb$.

In FY 1992, we focused on developing:

- Materials compatible with our growth technique, molecular beam epitaxy (MBE), on available substrates that absorb and convert infrared photons into mobile electrons and holes.
- Surfaces capable of emitting electrons in a vacuum.
- Transition structures that allow the efficient transport of electrons from the IR absorber to the electron emitter.

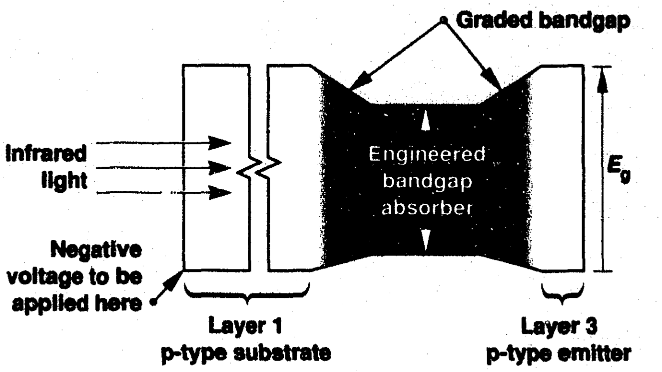

Figure 1. Schematic of energy bands vs position in an infrared-sensitive photocathode. The upper line represents the conduction band minimum, and the lower line represents the valence band maximum. E_g is the minimum energy gap between the valence band and the conduction band. The engineered bandgap absorber has a smaller E_g; it can absorb light with longer wavelengths than the substrate can. Thus, an IR photon can pass through the substrate and be absorbed, which promotes an electron from the valence band up to the conduction band. If a negative electrical bias is applied to the left side of the device, the electron can be transported to the p-type emitter and then be emitted into the vacuum.

Materials

We grew GaSb epilayers and strained-layer superlattices of InAs and $Ga_xAl_{1-x}Sb$ as IR absorbers. Figure 2 shows a cross-sectional transmission electron micrograph (TEM) of an InAs/GaSb superlattice grown on a GaSb substrate. The layers of InAs and GaSb are approximately 1 nm thick. Initial measurements of these superlattices as IR detectors showed unacceptably high noise due to electrical leakage ("dark current"). We believe we can correct the leakage and improve the quality of the layers by reducing the doping levels and the density of crystal defects.

Electron Emitters

We designed and built a system for activating and optically testing our MBE-grown photocathode materials. Our system allows us to heat and cool a sample of photocathode material under ultrahigh vacuum conditions, to apply a bias voltage across the sample, to deposit cesium and cesium oxide on its electron-emitting surface, to illuminate the sample with IR radiation from the front or the rear, and to collect and measure the emitted electrons.

We built a spectrometer-based, tunable, monochromatic light source with microwatt power for illuminating our photocathodes from visible to 5-µm wavelengths.

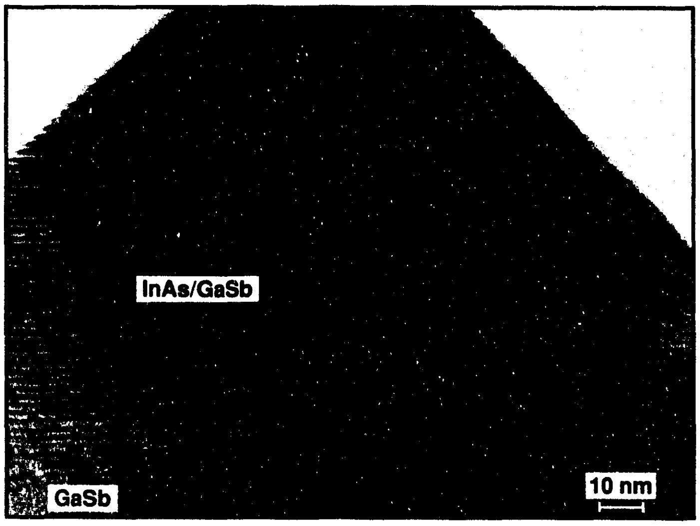

Figure 2. Transmission electron micrograph of an InAs/GaSb superlattice grown on our MBE system. Each layer is 1 nm thick. The darker layers are InAs.

Our 1-mW lasers provide 0.633- or 1.3-µm light. We developed a surface activation process that heats the sample to 400°C for several hours, cools the sample to room temperature, and deposits cesium on its emitting surface (with a controlled trace of oxygen). Thus, we can produce GaAs photocathodes with responsivities equivalent to those produced at the Stanford Linear Accelerator Center (SLAC).

The most efficient photoemitter is p-type GaAs. We initially used MBE to grow single-crystal GaSb and InAs/Ga$_x$Al$_{1-x}$Sb superlattices on GaAs substrates, including a strained-layer superlattice of GaAs/GaSb as a buffer. Although the atomic spacing of the GaAs crystal does not match that of the GaSb system, we had hoped that the strained-layer superlattice buffer would deter, as it does in the GaAs/In$_x$Ga$_{1-x}$As system (Mariella et al., 1990), crystal defects from entering the IR absorber. In the GaAs/GaSb case, however, large numbers of crystal defects appear where the lattice constant changes, and these defects propagate throughout the epilayers. Thus, we could not grow high-quality GaAs as the final electron emitter for our IR photocathode.

Instead, we invented a new photoemitter that will lattice match to the GaSb and to the InAs/Ga$_x$Al$_{1-x}$Sb superlattice and perform well as an electron emitter. Because Ga$_{1-y}$Al$_y$Sb with $y = 0.7$ has an E_g similar to that of GaAs (1.4 eV) and because Ga$_{1-y}$Al$_y$Sb has the requisite lattice content, we investigated Ga$_{1-y}$Al$_y$Sb as a photocathode material. We grew Ga$_{0.3}$Al$_{0.7}$Sb in our MBE system, and found that Ga$_{1-y}$Al$_y$Sb performed in our photocathode test chamber almost as well as GaAs. We have invented the first new photocathode in 20 years.

Bandgap Transition Structures

We used 0.633-µm light to demonstrate photoemission from several p-type Ga$_{1-y}$Al$_y$Sb surfaces with responsivities comparable to our p-type GaAs photocathodes. Ga$_{1-y}$Al$_y$Sb is an important emitter because it lattice matches to GaSb and because its composition can be graded during growth to provide a transition between the E_g of GaSb (0.7 eV) and the E_g suitable for emission (1.4 eV) (Figure 1). If we want to generate the internal electric field required to assist the transport of photogenerated electrons to the surface, we must apply a voltage across the photocathode. Therefore, we designed a metal grid structure and incorporated it in the emitting surface of several photocathode test structures. We demonstrated photoemission using these emitters with grids, proving that postgrowth processing of the emitting surface does not destroy photoemission. ◆

References

Bell, R. (1973), *Negative Electron Affinity Devices* (Clarendon Press, Oxford).

Bell, R., et al. (1974), "Far-Infrared Absorption Spectra Measured in InAs/Al$_{0.36}$Ga$_{0.64}$Sb Quantum Wells," *Appl. Phys. Lett.* **25**, 645.

Kim, J. H., et al. (1990), "Transferred Electron Photoemission from InP," *Appl. Phys. Lett.* **56**, 1901.

Mariella, R., Jr., J. Morse, and Z. Liliental-Weber (1990), "InGaAs-Graded Superlattices in Photodetectors for Wavelengths beyond 1 µm," *Proc. Mat. Res. Soc. Symp.* **198**, 297.

An X-Ray Streak Camera that Can Resolve 100-fs Events

M. W. Bowers and R. L. Shepherd

Researchers have opened a new realm of physics by producing ultrashort (tens of femtoseconds) high-power lasers that can create plasma densities comparable to solids. To study the properties of these plasmas before they expand to liquid or gas, we are designing a streak camera that can resolve 100-fs events.

Single-shot autocorrelation techniques can collect information on one plasma property in a short timeframe, but for most experiments, we need information on many properties. If researchers want to learn about spectrum, temperature, density gradients with respect to space and time, and recombination rates from a single shot, they must use a more complicated detector such as a streak camera. However, the best streak camera can only resolve 1.5-ps events (Murnane et al., 1990). Faster resolution is needed for solid-density and plasma-opacity experiments.

Electron Spectral Filter

In FY 1992, we designed and modeled a streak camera with the temporal resolution required for solid-density-plasma physics (Figure 1). Current streak cameras employ electron optics that allow substantial temporal spreading of photoelectrons with initial energies of less than 1 eV. Our streak camera, however, only uses the electrons with energies from 1 to 1.5 eV that are emitted from a cesium-iodide photocathode and filters out the rest. This selectivity results in better time responses (Figure 2). This 1- to 1.5-eV region is the most sensitive of a very sensitive photocathode.

Other x-ray streak cameras have potassium-iodide or potassium-bromide photocathodes, both of which are at least a factor of 2 less sensitive than cesium iodide. By filtering 1- to 1.5-eV electrons, we compensate for temporal and spatial aberrations that plague other streak cameras, such as focusing time-of-flight distributions and acceleration-energy-spread distributions. We also incorporated a time-compensation lens for the time deviation introduced at the energy-dispersing photocathode region of the streak camera.

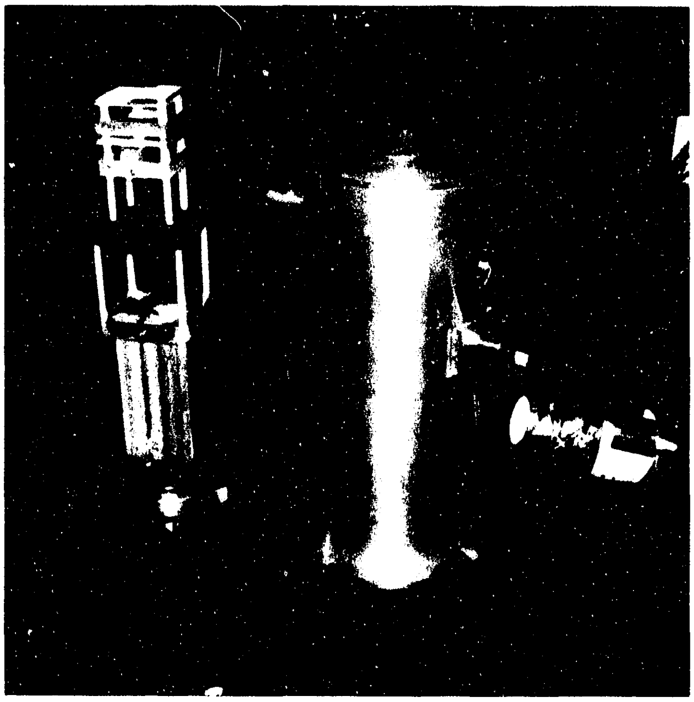

Figure 1. Streak camera with electron spectrometer. This streak camera can resolve 100-fs events.

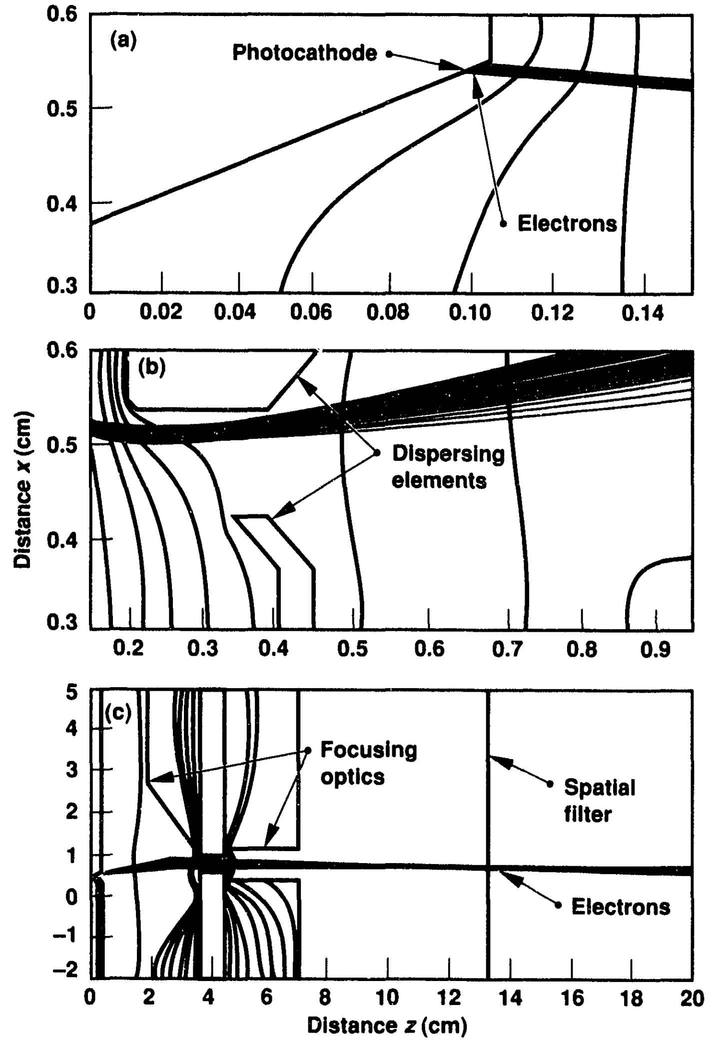

Figure 2. Electron trajectory plots from a computer model tracking electrons through an electron spectral filter. Distance *z* is measured in the propagation direction. Distance *x* is measured in the direction of the deflection. Note the different scales on each plot. (a) Electrons leave the photocathode and (b) pass through the spectral dispersing element of the filter. (c) Then the electrons are focused down to a spatial filter that blocks all electrons possessing less than 1 eV of energy in the propagation direction *z*. The lines in a, b, and c are all equipotential.

In FY 1992, we designed two deflectors for the streak camera. The first is a conventional parallel-plate deflector in which we include an ultrafast high-voltage drive designed at LLNL. This drive is the only one in the world that can drive our plates with the required risetime, voltage, and jitter. The second deflector has an impedance-matched termination on the deflection structure that provides a faster risetime on the plates. In addition to these deflectors, we worked with EG&G, Santa Barbara, to design a traveling-wave deflector. The traveling-wave deflector deflects electrons faster than standard streak-camera deflector plates. It uses an order of magnitude less voltage and still imposes few aberrations on the electron beam.

We first tested our electron spectrometer with a known energy source. However, the aberrations, from the fringing fields, induced near the photocathode made the test inadequate. Next, we tested the spectrometer using a direct current x-ray source and a cesium-iodide photocathode. We reproduced the known electron-energy spectrum of the cesium iodide on a phosphor-coated fiber-optic faceplate that we digitized using a charge-coupled-device camera. Our results reproduced the electron-energy distribution graph of cesium iodide and agreed well with our theoretical calculations.

The Camera System

In FY 1992, we tested the camera system on a 20-ps, laser-induced plasma source to evaluate its focusing characteristics under pulsed conditions. All focusing aspects worked according to plan. Next, we tested the deflection structures and their performances on a 100-fs laser source, but the ultrafast sweep speeds (approximately the speed of light) required for this design caused many aberrations in the fringing fields and limited the camera to a time resolution of 1 ps. In FY 1993, we will develop technology to modify the sweep structures so we can produce ultrafast deflection without aberrations and test the limits of our camera. ◆

References

Murane, M., H. Kapteyn, and R. Falcone (1990), "X-Ray Streak Camera with 2-Picosecond Response," *Appl. Phys. Lett.* **56**, 1948.

The MACHO Project

C. R. Alcock, T. S. Axelrod, R. A. Allsman, D. P. Bennett, K. H. Cook, R. Hills, H.-S. Park, S. Marshall,[*] C. Stubbs,[*] S. A. Perlmutter,[†] W. Sutherland,[†] K. Griest,[‡] K. C. Freeman,[**] B. A. Peterson,[**] P. J. Quinn,[**] and A. W. Rodgers[**]

Evidence is overwhelming that a "halo" of invisible matter surrounds the bright, observable disks of the Milky Way and other spiral galaxies. The most compelling evidence comes from analyzing our own galaxy, the Milky Way. Astronomers estimate its mass by studying the nearly circular motion of the stars and gas around the galaxy's center and by applying Newton's laws, in much the same way that they determine the mass of the Sun by analyzing the planetary orbits around it.

However, the estimate obtained is more than 10 times greater than the estimated total mass of visible stars and gas, which is calculated from the total light emitted by the galaxy. This calculation suggests that most of the matter in our galaxy is in the form of invisible components we call dark matter.

The nature of this dark matter is unclear. If it were made up of normal stars or gas clouds, it could readily be detected. Therefore, astrophysicists speculate that it could consist of hypothetical elementary particles such as axions, massive neutrinos, or weakly interactive massive particles (WIMPs). Alternatively, it could be made

---

[*] *University of California at Santa Barbara.*
[†] *University of California at Berkeley.*
[‡] *University of California at San Diego.*
[**] *Australian National University, Canberra.*

up of brown dwarfs, or planets like Jupiter, neutron stars, or black-hole remnants of primordial stars, which are called MACHOs (massive compact halo objects).

We have designed and constructed a telescope, cameras, and software to use in determining if the dark matter in our galaxy's halo consists of these massive objects. In our definitive search, we will use the gravitational microlensing signature proposed by Bohdan Paczynski (1986), which should yield millions of convincing events. If we see no events, we can eliminate MACHOs as candidates for the dark matter. This conclusion would be profound because it would imply that exotic elementary particles must make up the dark matter.

The Signature—Gravitational Microlensing

Gravitational microlensing occurs when a MACHO moves close to the line of sight between Earth and a background star outside our galaxy. The gravitational field of the MACHO acts as an amplifying lens. As the MACHO moves across the field, the star appears to brighten and then return to its original intensity. Because all objects in our galaxy are in motion, a highly characteristic pulse occurs in the brightness of the star and provides the MACHO signature.

Figure 1 shows a schematic of gravitational microlensing. The typical angular separation of the images that we expect to see is ≤0.001 arcsec so they cannot be distinguished from each other. Paczynski showed that the "optical depth" for microlensing by the dark halo of our galaxy is about 5×10^{-7}; therefore, at any given time, about one star in two million will be microlensed, amplifying the brightness by a factor of 1.34 or more. We expect to see a wide range of peak amplifications and some events with amplification factors greater than 5.

The stars of the Large and Small Magellanic Clouds, two nearby galaxies, are optimum background sources, and we have chosen them to amplify MACHO events. Figure 2 shows the relative locations of the Milky Way and the Magellanic Clouds. These extragalactic clouds are far enough away to be outside most of the halo, but their line of sight traverses much of the halo. They are close enough that individual stars may be seen using ground-based telescopes, and they provide a sufficient number of stars ($>3 \times 10^6$ brighter than $m = 19.5$, where m is the apparent magnitude of the star) to carry out a reasonable search.

The duration of a microlensing event depends primarily on the mass of the MACHO. It would be approximately two days if the mass equaled that of Jupiter and scaled as the square root of the mass. This the duration is somewhat affected by other important parameters such as the velocity of the MACHO. Measuring an event duration will give us a MACHO mass estimate that we could not obtain by any other technique.

Astronomical Background

One of our most significant challenges will be the "astronomical background"—known classes of stars that spontaneously vary in brightness. Separating microlensing events from these background variations will require considerable care. We can distinguish the microlensing light curves from the background of variable stars because they are achromatic, time-symmetric, and nonrepeating. In addition, the microlensing light curve is described by just three parameters: the maximum amplification, the time of the maximum amplification, and the event duration.

We will carry out the most comprehensive photometric survey of any kind in the history of astrophysics as part of a second research project. Exploring the astronomical background will reveal a scientific gold mine. Our data will become the prime sources of information on variability of all celestial objects, including regular variable stars, explosive outbursts in stars, and quasars. Analyzing and interpreting these data will take years.

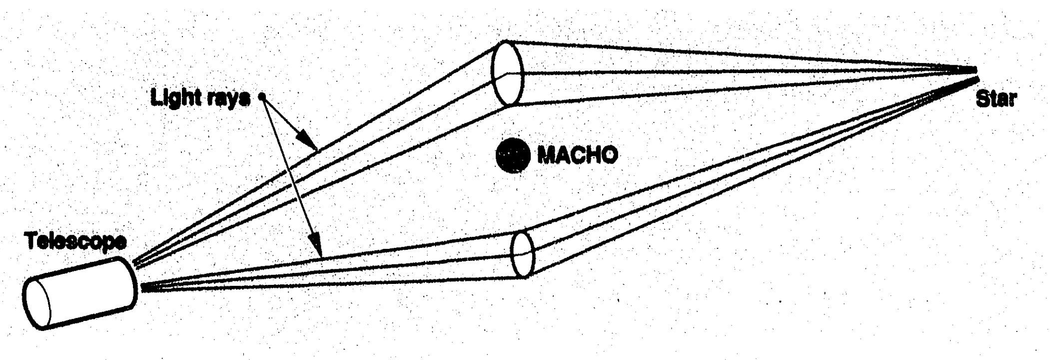

Figure 1. Gravitational lensing, showing the paths of light rays bent by the MACHO. The gravitational field acts as an amplifying lens. A highly characteristic pulse occurs in the brightness of the star and provides the MACHO signature.

The Telescope

To search for MACHO events, we must make regular photometric measurements on millions of stars to counteract the very low optical depth. Because we do not know which event duration is most probable, we must use a variety of sampling rates. These rates will range from only once every several nights to 6 times/hour and give us sensitivity to event durations ranging from 30 min to months or even years.

Existing instruments could not do this work. In FY 1992, we modified a telescope with designs we engineered the previous year. We used the 1.27-m reflecting telescope (the Great Melbourne Telescope) of the Mount Stromlo and Siding Spring Observatories (MSSSO) located on Mount Stromlo, near Canberra, Australia. We chose Australia because the Magellanic Clouds are only visible from the southern hemisphere. Our modifications included new drives and encoders, a new top ring and focus carriage, and new trusses to support the top ring and the mirror cell, which was moved back along the optical axis about 40 cm. In FY 1992, we began operating the telescope, which performs well in its new configuration.

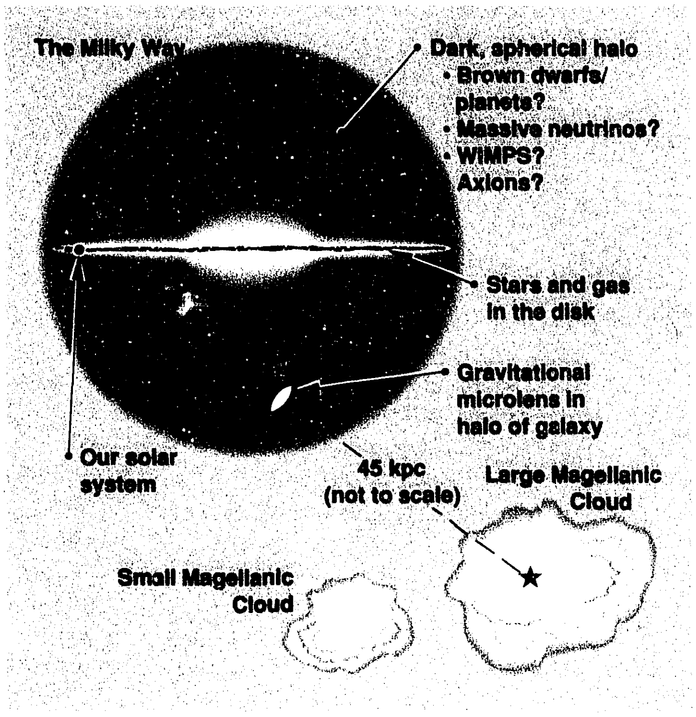

Figure 2. The Milky Way and the Magellanic Clouds, showing the relative positions of the solar system, the potential gravitational microlens, and a target star.

The Optics

To make the unprecedented number of photometric measurements this survey requires, we need an exceptionally wide field of view. The Australian telescope mirror is a classic, parabolic reflector. Because a parabolic mirror does not have good offaxis performance, we designed a system of corrector lenses to reduce the offaxis coma and astigmatism to acceptable levels. Specifically, the image of a point source always falls within a 15-μm-diam circle throughout the field of view, which has a diameter of 1 deg. In addition, we use a dichroic filter to split the beam into two channels—410 to 620 nm and 620 to 840 nm—to give simultaneous imaging in two filter bands.

In FY 1992, we successfully installed a new corrector cell, fabricated by ACO Applied Optics. The image quality throughout the image plane is exceptionally good. This system provides the widest field of view of any astronomical telescope equipped with digital detectors.

The Cameras

Working with our UC collaborators, we built the two largest charge-coupled-device (CCD) cameras in the astronomy world. Each contains a 2 × 2 mosaic of four 2048- × 2048-pixel CCD imagers (Figure 3), which were fabricated by Loral Aerospace (formerly Ford Aerospace). In FY 1992, we constructed the electronics for the control and data handling in these cameras. The electronics can handle the exceptionally large data volume these cameras produce. In FY 1992, we mounted the cameras on the telescope, and they are now in routine use.

Figure 3. Top view of CCD-array camera, with faceplate removed to show the CCD imagers. The array is 6 × 6 cm.

Analysis Techniques

The cameras produce image data at a prodigious rate. Approximately every 6 min, 32 million pixels are read out. Each image consists of 64 Mbytes of data, and the system routinely generates 10 images/hour. The addition of important camera diagnostic information doubles this data volume. We must process each night's data within 24 hours so we can keep up. Our ultimate goal is real-time processing that reduces each image to photometry during the exposure of the next image.

The primary data processing is performed by a four-processor Solbourne computer. This computer also controls the entire telescope system. It issues commands to the telescope, controls the camera system, and manages the data flow from the camera system through data analysis and archiving. In FY 1991, we designed the software, which now effectively manages the ongoing operations.

The MACHO project has successfully brought to operation the most powerful photometric survey system in the history of astronomy. When we complete our survey, we will have analyzed nearly 10 billion photometric measures. ◆

References

Paczynski, J. B. (1986), "Gravitational Microlensing in the Galactic Halo," *Astrophys. J.* **304**, 1.

Large-Format Charge-Coupled-Device Mosaics for Maximum Focal-Plane Use

K. H. Cook, S. E. Deustua, M. Lesser,[*] and C. R. Alcock

The charge-coupled-device (CCD) detector has eliminated photographic media in many astrophysical applications. However, because of low yields in manufacturing large-area CCDs, this technology has not been applied to high-resolution imaging of large fields. In FY 1992, using recent improvements in producing CCDs with 4 megapixels at reasonable yields, we constructed the two largest focal-plane arrays in the world—each containing 16 megapixels. We are using these arrays to search for "dark matter" in the universe (Figure 1).

Normally, CCDs have control and signal circuitry spaced uniformly around the periphery. Our arrays have four 2048- x 2048-pixel CCDs in a square and no circuitry on the interior edges. This mosaic has about 50 times less dead space than other CCDs and, therefore, more imaging space. John Geary of the Smithsonian Astrophysical Observatory designed the CCDs, and Loral Aerospace constructed them. Each CCD has two readout amplifiers to speed readout time.

To be used as detectors in the x-ray, ultraviolet, near-ultraviolet, and blue regions, CCDs must be modified so that the incident photons are absorbed near the metal-oxide-silicon capacitor where the photoelectrons are stored. The quantum efficiency of an unmodified CCD is essentially zero below 400 nm. For astrophysical applications, a CCD is often modified by thinning and illuminating it from the backside. A thinned CCD is less than 20 μm thick and quite fragile. Commercially available CCDs suffer from variable thinning and wrinkling.

We solved this thinning problem by building a jig that laps a 10-cm wafer, which contains four CCDs, down to a thickness of 250 μm and a flatness of 1 to 2 μm. Consequently, we lap each CCD to a flatness of better than 0.5 μm, well within the tolerance needed for the acid-etch thinning that completes the process. We improved our

---

[*] *University of Arizona, Tucson.*

Figure 1. Two 16-megapixel arrays. Array on right has CCDs bonded to focal-plane assembly; array on left has CCDs wire-bonded to interface circuit boards.

thinning process so that we could etch to the epitaxial layer in all areas of the CCD wafer within 20 min. This speed and our thinning process create a center-to-edge uniformity of well under 1 μm.

We acquired a 10-cm wafer-scale, flip-chip bonding machine so that we could bond our CCDs to a stabilizing substrate before thinning them. This machine bonds CCDs from about 0.25 × 2.5 cm to 10 × 10 cm. We used indium bumps on the CCDs and substrates to provide good electrical and mechanical connections. We experimented with pressure, temperature, and holding times to ensure positive bonds and found that bump thickness is critical to successful bonding.

Using techniques from our thinning and bonding experiments, we designed modular focal-plane arrays with replaceable CCDs that conform to tight focal-surface tolerances. In our first arrays, we bonded thick CCDs into a mosaic before cold testing them. We have since modified the mosaic design and are constructing new mosaic packages. In the new packages, we bump-bond the CCDs (in groups of four as on the wafer) to a silicon substrate and then place nonconductive epoxy between the substrate and CCDs for mechanical strength. Using acid, we thin the four CCDs as one silicon piece and then cut them into four CCD substrates. Next, we epoxy each CCD substrate onto a flat, custom-made package that can be tested and aligned independently in the mosaic. In FY 1993, we will construct a 16-megapixel mosaic of thin CCDs that are blue-region sensitive. We will follow this mosaic with a monolithic array. This array will have more than 50 times the sensitivity of photographic emulsions. ◆

Smart Retina Architecture

F. Eeckman, N. G. Smiriga, and T. Axelrod

The detection and tracking of small objects in images in adverse signal-to-noise conditions require novel and sophisticated techniques. Current technology has neither the speed nor the robustness to perform real-time target tracking. Yet, systems with the desired capabilities do exist in biological organisms, and promising hardware based on biological nervous systems has been developed (Mead and Ismail, 1989).

Inspired by these successes, we attempted a "biological solution" to our target-detection problems in LLNL's wide field of view (WFOV) telescope. The WFOV telescope views 6 million pixels at 30 frames/s. We developed a retinal algorithm for detecting small moving objects against cluttered backgrounds. We modeled the algorithm after the afoveate retinas of lower vertebrates, which consist of five layers of processing elements. We used a standardized test series to quantitatively measure the performance of this algorithm and discovered that it was competitive with more conventional methods for target detection. In a test series of 50 images with Gaussian blob targets embedded in Gaussian noise backgrounds, the retinal motion detector (RMD) was as sensitive as a thresholding method with a probability of false alarm (i.e., detecting an object where none exists) at 0.04. However, the false alarm rate of the RMD was 0.0004. Only sophisticated statistical techniques using sequential hypothesis testing performed better than the RMD.

The RMD has other advantages over the classic approaches, the most important one being that the RMD is an inherently parallel algorithm. Although we have not implemented the RMD in analog very-large-scale integration (VLSI), there is a very direct mapping of this algorithm into silicon. Researchers (led by Carver Mead) at the California Institute of Technology have implemented similar retinal models into analog VLSI. However, the conventional statistical methods are hard to parallelize at micro levels, and their performance on a given task is only marginally better than RMD for the same computational complexity (i.e., the same number of floating-point operations performed per pixel).

Thresholding algorithms have been implemented, but they offer no solution to contrast reversals and other common problems faced by real-time, in-the-field, target-detection systems. (One implementation, the ACE chip, was developed at LLNL in collaboration with the University of Idaho at Moscow.)

In FY 1992, we extended our smart retina technology to applications in target tracking against moving backgrounds, as if the detectors were located on an airborne platform. We used a reduced form of the RMD, consisting of only two layers, to condition the images for a neural network that matches the background motion. Without the retinal conditioning, the neural network weights never converge because of noisiness of the input images. To test the algorithm in a realistic setting, we used images from space shuttle missions and added artificially imbedded targets.

We also extended our technology to process images for pattern recognition. The application we chose was face recognition. On the basis of an elastic matching algorithm developed at the University of Southern California (by Christof von der Malsburg and Joachim Buhmann, and perfected by J. Buhmann while he was a postdoctoral researcher at LLNL), we compared our combination of retinal preprocessing and elastic matching to elastic matching alone. The results showed that retinal preprocessing increased the accuracy of recognition rates from 50 to 80% under certain lighting conditions.

The smart retina technology developed at LLNL has applications in target detection, target tracking, and pattern recognition. In FY 1993, we hope to expand our research implementing the RMD in VLSI. ◆

References

Mead, C., and M. Ismail (1989), *Analog VLSI Implementation of Neural Systems* (Kluwer, Norwell, MA).

Superconducting Tunnel-Junction X-Ray Detectors

S. E. Labov, C. Mears, G. A. Morris, M. Le Gros, and E. H. Silver

We are developing a new class of high-efficiency x-ray detectors that will improve spectral resolution by an order of magnitude over existing semiconductor ionization detectors. Superconducting tunnel-junction (STJ) detectors potentially can provide high spectral resolution, position sensitivity, broad bandwidth, and high efficiency. These detectors will have a major effect on plasma physics, particle physics, chemical analysis by fluorescence spectroscopy, nondestructive testing, astrophysics, and atomic physics.

When an x-ray photon is absorbed in the STJ, some of the paired electrons that carry the superconducting current (Cooper pairs) are broken apart. This breaking results in an excess population of unpaired electrons, or quasiparticles. When a voltage bias is applied across the STJ's thin insulating barrier, or junction, the quasiparticles will tunnel through the barrier into a second superconducting layer. The charge pulse observed in the STJ is proportional to the number of quasiparticles and, thus, is proportional to the x-ray photon energy. Because the binding energy of a Cooper pair is typically about 1 meV, a 1-keV x ray will produce about two million quasiparticles. The resolution of such a system could, in principle, be only a few electron volts for a 6-keV x-ray photon.

We have assembled an STJ fabrication facility and produced several types of STJs using aluminum and tantalum. The current–voltage characteristics of these detectors are excellent, and we have observed x-ray pulses. To measure x-ray spectra with this detector, we must improve the quality of the films it produces and establish a geometry that will make x-ray spectral measurements possible.

In addition to constructing detectors at LLNL, we are working with a firm that fabricates superconducting electronics, Conductus, Inc., in Sunnyvale, California. This firm has used our designs to construct detectors from niobium and aluminum. These detectors were cooled to 100 mK and irradiated with x rays at 5.89 and 6.49 keV. Figure 1 shows the pulse-height spectrum. The narrow line near channel 496 is the response to an electronic pulse. The x-ray pulses with low pulse height (below channel 190) are caused by x rays that were absorbed in the silicon substrate under the STJ detector. The width of the 5.89-keV line is about 120 eV full width at half maximum, and the electronic noise width is about 50 eV.

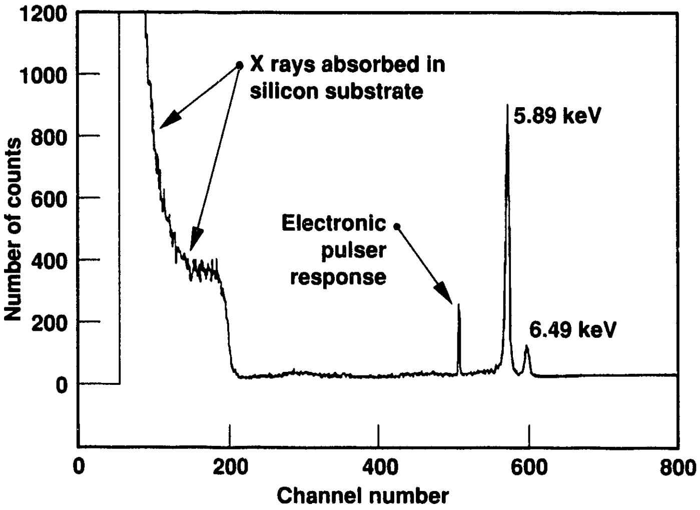

Figure 1. Pulse-height spectrum measured using the STJ x-ray detector. The width of the 5.89 keV line is about 120 eV full width at half maximum.

The x-ray spectrum in Figure 1 is still a preliminary result, and we have designed many improvements to the system that we hope to implement with outside funding. Our results are, nevertheless, encouraging. The spectral resolution of this STJ detector is better than that of semiconductor ionization detectors and is within a factor of 2 of the best resolution obtained with STJ detectors (Kraus et al., 1989; Zehnder et al., 1990; Labov et al., 1992). We should be able to improve this resolution by an additional order of magnitude. ◆

References

Kraus, H., F. von Feilitzsch, J. Jochum, R. L. Mossbauer, Th. Peterreins, and F. Probst (1989), "Quasiparticle Trapping in a Superconductive Detector System Exhibiting High Energy and Position Resolution," *Phys. Lett. B* **231**, 195.

Labov, S., C. Mears, G. Morris, C. Cunningham, M. Le Gros, E. Silver, A. Barfknecht, N. Madden, D. Landis, F. Goulding, R. Bland, and K. Laws (1992), "Superconducting Tunnel Junction X-Ray Detectors with Niobium Absorbers and Aluminum Quasiparticles Traps," *Proc. SPIE* **1743**, 328.

Zehnder, A., C. W. Hagen, and W. Rothmund (1990), "Superconducting Tunneling Junction Detectors," *Proc. SPIE* **1344**, 286.

Monte Carlo Simulations of Solid-State Photoswitches

P. W. Rambo and J. Denavit

Large increases in conductivity induced in gallium arsenide (GaAs) and other semiconductors by photoionization allow fast switching by laser light with applications to pulse-power technology and microwave generation. Experiments have shown that under high field conditions (10 to 30 kV/cm), conductivity can occur in the linear regime where it is proportional to the absorbed light, in the "lock-on" regime where it persists after termination of the laser pulse, or in the avalanche regime where multiple carriers are generated. We intend to apply self-consistent, Monte Carlo particle simulations to study these phenomena, including the effects of high-energy electrons that are far from equilibrium (i.e., hot electrons), which are important at high field strengths.

Our objectives are to understand the phenomena of lock-on and avalanche regimes present in laser-triggered, solid-state switches at high fields; these switches have promising applications to fast pulse-power technology. Additionally, we hope to bring the expertise acquired in advanced plasma simulation to bear on the modeling of semiconductor devices, which has broad applications, such as transistors.

Our code includes the necessary elements for time-dependent, one-dimensional, ensemble Monte Carlo simulation of charge transport in semiconductors. A multiple-valley, nonparabolic approximation to the band structure is used, and the standard scattering mechanisms are included for polar materials (such as GaAs) and nonpolar materials (such as silicon). In FY 1992, the extension was made to evaluate the Poisson equation for self-consistent, one-dimensional simulation. We used published results as benchmarks for the current-voltage characteristics of a GaAs diode and observed the formation of Gunn domains.

An important numerical constraint on these self-consistent simulations is the stability limit on the timestep imposed by plasma oscillations. We have analyzed the numerical stability of the most commonly used scheme for Monte Carlo device simulation. In the absence of collisions, we found that instability occurs for all values of the timestep. In practice, collisions allow stable simulation, provided the timestep is sufficiently small. These results have been verified with simulations, as shown in Figure 1. This work provides a guide for the choice of timestep size

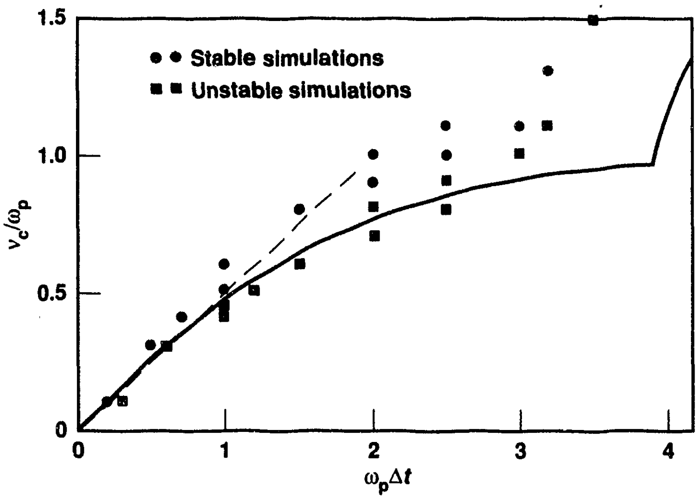

Figure 1. Our analysis predicts numerical instability for combinations of timestep, $\omega_p \Delta t$, and collisionality, v_c/ω_p, below the solid line; ω_p is the plasma frequency.

in Monte Carlo simulation, where efficient numerical methods are a significant concern.

We examined the physics of deep-level impurities (traps), which is thought to be essential for understanding the behavior of these photoswitches. Relevant trap-to-band, impact-ionization cross sections have been treated by the quantum defect method. We are also applying a two-step, collisional-radiative process to derive electron-impact ionization from known photoionization cross sections. Nonradiative emission and capture are represented using the multiphonon cross sections and activation energies for impurities (or defects) that have been characterized experimentally. These processes will be added to our code to allow simulation of photoswitches in FY 1993. ◆

Stereo Computer Vision

S.-Y. Lu, R. K. Johnson, and J. E. Hernandez

The DOE wants to automate the processing of hazardous waste generated from environmental restoration and waste management activities. Because of increased economic concerns and environmental and personnel regulations, DOE facilities need systems with better efficiency and worker safety. Automated robotic systems address this need.

In the future, hazardous waste storage containers will be opened, and their unknown contents removed and sorted by the type of material inside (e.g., metallic, combustible, or vitrifiable). Several related tasks can benefit from robotics, such as picking up overlapping objects from the storage containers or delicately placing objects to avoid damage and unnecessary contamination of the work area. Robust autonomous operation requires visual input. The goal of our research is to develop a three-dimensional (3D) computer-vision capability that allows robots to accurately grasp objects in unstructured environments.

Our approach is to use stereo computer vision to reconstruct the 3D object surface, which the computer then analyzes to plan for the robot grasp pose. Two cameras mounted above the robot work cell generate the required stereo images. Figure 1 shows an image from the left camera overlooking a simulated hazardous waste processing system. The four objects represent packages of hazardous waste. We developed a method to automatically calibrate the stereo camera system by using the robot to obtain the data necessary to effectively locate points in space given their position in the left and right images. We also developed a novel stereo-registration algorithm that is less complex than existing methods, produces accurate surface data, and can be implemented on a parallel computer. Then we use the dense range data—the uniform samples of the surface of the object—obtained from the algorithm to generate a complete 3D surface reconstruction of the objects. Figure 2 shows this reconstruction.

Currently, we analyze the shape of a two-dimensional projection from the top view of the object to locate a grasp pose that is valid for the available robot grippers. For simplicity, we keep the robot grippers perpendicular to the table supporting the object. We use the range data from our algorithm to determine the proper grasp height. However, our current approach is only effective for flat and smooth objects, and more robust grasp planning will require a complete 3D analysis of the reconstructed object.

Figure 1. Top view of hazardous waste objects in a simulated processing system. This image was taken from the left camera above the robot.

In FY 1993, we plan to develop new algorithms to perform a full 3D surface analysis and unconstrained robot grasp planning for both single and multiple overlapping objects. We will implement and demonstrate our results here at LLNL. We expect that our research will be applicable to a variety of problems requiring 3D surface analysis such as weapons assembly and disassembly, assembly and inspection of manufactured parts, autonomous space- and land-based exploration, and undersea salvage and rescue. ◆

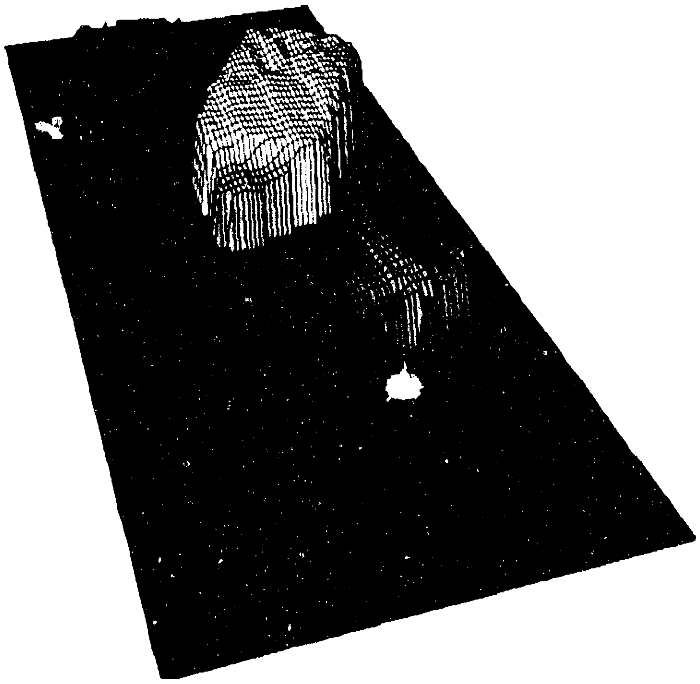

Figure 2. Three-dimensional reconstruction of hazardous waste objects. Using our new stereo registration algorithm, we can generate a 3D reconstruction of flat objects.

Developing a Personal Chemical Exposure Monitor

J. S. Johnson, P. M. Swearengen, J. C. Clark, and F. R. Weber

LLNL's Hazards Control Department has identified personal chemical exposure monitoring as a general industrial hygiene area that needs improvement. New Occupational Safety and Health Administration (OSHA) regulations and DOE orders also require expanded monitoring to determine employee exposure to toxic chemicals and physical agents. Active air-sampling systems are currently used, but they are large and bulky and present a significant inconvenience to many workers, especially for full-shift or multiple-day sampling. We have carefully examined current air-sampling pump designs and determined that the vane configuration represents the best design for miniaturization.

In FY 1991, we designed, fabricated, and tested a prototype miniature vane pump that meets the airflow needs for adsorbent-tube sampling. The miniature personal chemical exposure monitor (PCEM) collects a representative air sample on the adsorber tubes. We then analyze these tubes to determine the exposure level of toxic material in the employee's workplace. The miniature sampling pump, electronics, airflow-control system, and adsorber tubes have been integrated into a small package that can be conveniently worn behind the LLNL employee badge. Figure 1 shows this miniature PCEM.

The first prototype PCEM has a sampling volume of 5 to 200 mL/min and an operating time of 8 to 10 hours.

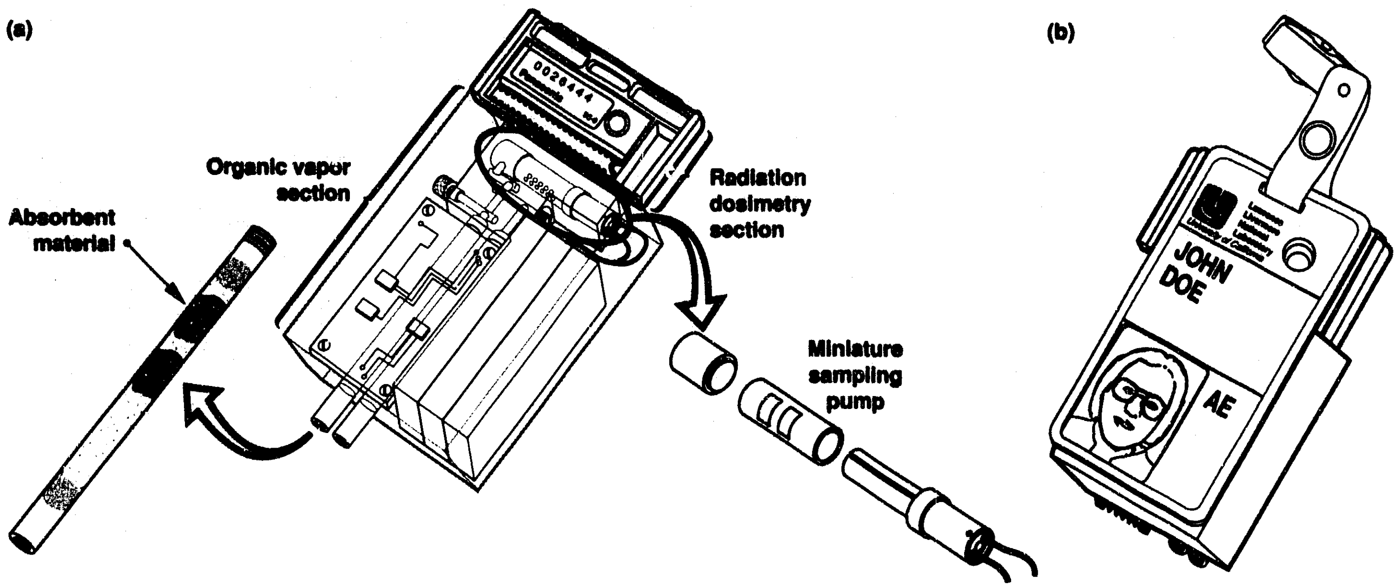

Figure 1. Our miniature PCEM. (a) The PCEM uses a miniature vane pump and adsorbers to test exposure to chemicals. (b) It fits conveniently behind the LLNL badge.

Space is also available for two adsorber tubes to allow for duplicate sample collection or the use of two different adsorber tubes. We will initially carry out field tests using this PCEM at LLNL to determine the utility of the current designs. Then, we will modify the designs as necessary to improve the PCEM performance before fabricating additional units. More extensive field performance evaluations of the final PCEM units will be performed at another DOE facility and at a private sector industrial site.

The miniature active PCEM will provide the industrial hygienist with a new tool to better characterize the variety of workplaces requiring evaluation. By incorporating the radiation dosimeter, security badge, and organic vapor monitor into one unit, we will make employee exposure monitoring less intrusive and more acceptable. Results from the expanded employee monitoring will be used to identify workplace hazards that require corrective action and confirm workplaces that are in compliance with DOE and OSHA regulations. ◆

High-Resolution Radar Imaging

M. R. Portnoff

High-resolution radar imaging is an active technique for remote sensing that transmits, receives, and coherently processes broadband electromagnetic signals to form an image of a target scene. This technique is especially valuable for remote sensing and reconnaissance applications because it produces high-resolution images in all weather, day or night. It can penetrate foliage and is sensitive to electrical properties of objects in the scene. In addition to the rendered image, processing of collected signals can provide information on object motion and terrain elevation.

Figure 1 shows an example of the collection geometry for an airborne side-looking radar. With a conventional radar system, the resolution in the range direction is inversely proportional to the bandwidth of the radar signal and is adequate for most applications. The resolution in the cross-range or azimuth direction, which is the azimuthal dimension of the antenna footprint, is directly proportional to the distance from the sensor to the scene and inversely proportional to the size of the antenna aperture.

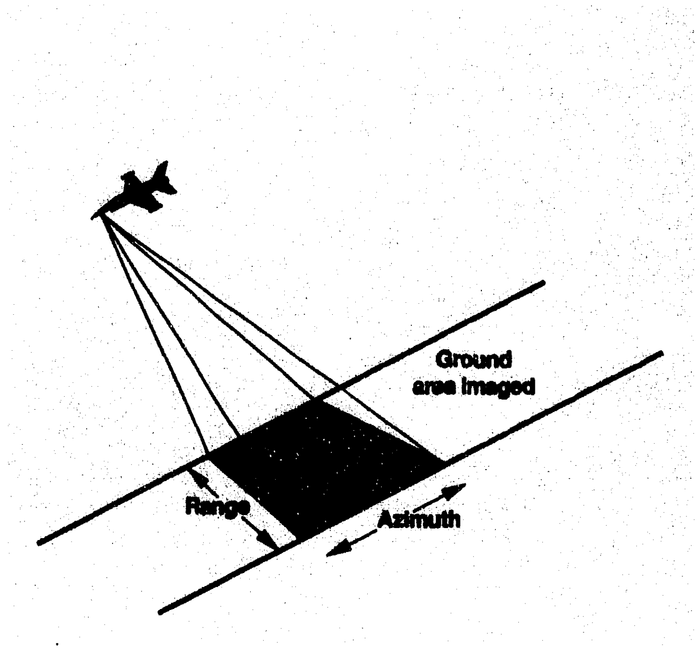

Figure 1. Example of collection geometry for airborne side-looking radar. By synthesizing an aperture that corresponds to the distance that the sensor travels while illuminating a fixed point on the ground, a SAR imaging system achieves a resolution much finer than the azimuthal dimension of the antenna footprint.

For airborne or spaceborne radar, the distance between the sensor and the target scene is usually so great that a physical antenna sufficient to provide useful resolution would be prohibitively large. Instead, a large antenna aperture is effectively synthesized by jointly processing all of the radar returns collected as the sensor flies over the scene. The result of such processing is a synthetic-aperture radar (SAR), which can produce an image whose resolution is independent of the distance from the sensor to the scene (Fitch, 1988). The price of such performance is the enormous computational task of forming the image from the radar measurements.

The goal of this project is to develop new techniques based on modern digital-signal processing and to apply them to high-resolution radar data. We have three main objectives. First, we are developing more efficient algorithms so that the massive computations can be performed on the inexpensive computer workstations typically found in a research and development environment. These algorithms can also improve the throughput of the supercomputers and parallel processors used in production processing of SAR data. Second, we want to improve image-formation algorithms so that better-quality imagery can be produced. Third, we will develop new techniques for exploiting SAR data for specific applications of national concern.

During FY 1992, we developed two algorithms, each of which addresses an important computational problem in SAR image formation. One of these algorithms is particularly significant because it eliminates a major computational bottleneck in SAR processing (Portnoff, 1993). It also has wide application in two-dimensional signal processing of very large data sets. We have obtained actual SAR data sets and plan to use our algorithms to process them as soon as possible. ◆

References

Fitch, J. P. (1988), *Synthetic Aperture Radar* (Springer-Verlag, New York, NY).

Portnoff, M. R. (1993), "An Efficient Method for Transposing Large Matrices and Its Application to Separable Processing of Two-Dimensional Signals," *IEEE Trans. Image Processing* 2(1).

High-Resolution, High-Sensitivity, X-Ray Imaging Using Hybrid Focal-Plane Arrays

C. Hailey, G. Sprehn, G. Jernigan,* and E. Arens*

The principal imaging spectrometer used in x-ray astronomy is the charge-coupled device (CCD). This detector has the desirable features of very high spatial and energy resolution, enabling it to obtain images and spectra of cosmic x-ray sources with unprecedented resolution. However, it has several disadvantages for space-based, x-ray astronomy, including susceptibility to radiation damage, reduced efficiency for detecting x rays at energies above a few kilo-electron-volts, and poor time resolution. CCD vulnerability to radiation damage is particularly problematic given future x-ray astronomy missions that will last 10 years or more. Reduced detection efficiency at high energies prevents these devices from observing the harder, nonthermal, x-ray emission from cosmic sources. Poor temporal resolution limits study of x-ray variability in objects whose fundamental processes vary on very short timescales, such as black holes. These disadvantages are caused by the CCD's internal architecture. The continued use of CCDs in x-ray astronomy is due to the lack of alternative detectors as well as their good performance.

**University of California at Berkeley.*

We began investigating an alternative to the x-ray CCD by studying an x-ray pin diode in the form of a hybrid focal-plane array (Figure 1). These devices have a deep depletion region, the active area from which x rays converted to electron-hole pairs can be efficiently collected, which leads to more stopping power for high-energy x rays. The charge is swept out of the diode and collected on individual amplifiers that define the imaging pixels. This contrasts with CCDs in which the charge is slowly transferred parallel to the detector surface through many pixels to a single amplifier. Collecting the signal without many charge transfers and over a short path to the individual amplifiers leads to great radiation hardness and very fast time resolution. The deep depletion region allows these detectors to operate at very high x-ray energies with excellent detection efficiency.

For x-ray pin diodes to replace CCDs, we must improve their energy resolution, which currently is not competitive with CCDs. We used standard focal-plane arrays, which are commonly used for infrared applications, as our x-ray pin diodes. These devices are not optimized for low-noise (high-energy resolution) performance because noise considerations are not as stringent in infrared applications.

We modified the array to reduce noise by an order of magnitude, which is consistent with CCDs. This involved

- Redesigning preamplifiers to reduce their noise contribution by a factor of 10.
- Writing specialized software to analyze system-throughput noise for optimizing the analog electronics chain.
- Refining system grounding schemes to reduce noise susceptibility.
- Optimizing the device's timing sequence (the series of electronic signals that controls the signal collection and processing).
- Writing software to collect the data, filter the noise, and display the resultant images.

Preliminary results on noise performance are encouraging. We are optimistic that we will reach our goal of obtaining noise performance on the order of 10 electrons—comparable to that obtained with currently operating x-ray CCDs. ◆

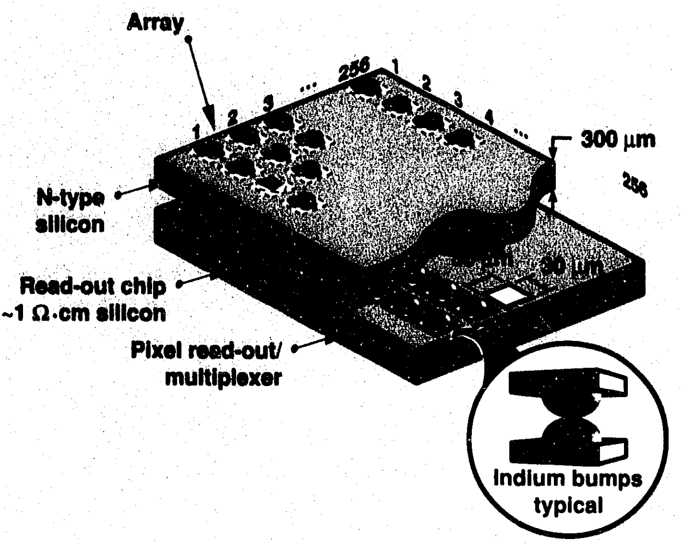

Figure 1. A pixel detector hybrid.

A Monolithic Pulse Source for Ultrawideband Radar

T. E. McEwan and G. A. Cooper

Many radar and communication systems of the future will be based on the radiation of brief impulses that lack a carrier frequency. These ultrawideband (UWB) systems, also known as impulse radar and impulse radio, promise increased use of existing spectrum space, simplified hardware, digital channel selection without tuners, and for UWB radar, extremely high-range resolution. Unfortunately, development of UWB systems is hindered by the lack of appropriate hardware. In this project, we developed a monolithic pulse compressor capable of generating 20-ps risetime pulses.

Our pulse compressor, or nonlinear transmission line (NLTL), is based on an LC ladder network with fixed inductances, L, and nonlinear voltage-dependent capacitors, C(V). The reverse-bias C(V) characteristics of semiconductor diodes are such that a negative dispersion can be introduced to pulses propagating down the network. NLTLs using monolithic geometries and high quality GaAs diodes have produced the fastest all-electronic pulses—approximately 1-ps risetime and several volts amplitude.

With existing NLTLs, the voltage amplitude is insufficient for UWB transmitters; an increase of at least an order of magnitude is needed even for radars operating at very close range. By using junction diodes instead of the more commonly used Schottky diodes, we were able to increase NLTL voltages to greater than 100 V at less than 20-ps risetime. Diode stacking techniques should improve performance to 1 kV at less than 10-ps risetime.

Our NLTL consists of a highly conductive GaAs substrate that supports lightly doped junction diodes interconnected with metal traces. The highly conductive substrate functions as a ground plane for the NLTL. We initially grew high-voltage diodes on the substrate using molecular beam epitaxy (MBE), but numerous physical defects accumulated in the relatively thick diode bulk region and limited the breakdown voltage to about 80 V. We were able to grow 200-V diodes by using a metal-organic chemical vapor deposition process. We applied ohmic contacts using a thin, highly doped GaAs layer and produced individual, mesa-etched diodes by etching back the surrounding material to isolate columns. The breakdown voltage for the complete mesa structure was limited to 160 V by, we believe, parasitic conduction down the walls of the mesa. Various wall treatments verified this theory, but we have not yet identified a stable solution.

Because the substrate is conductive, we insulated the interconnect metal with a 10-µm-thick polyimide layer that provided high breakdown strength with low parasitic capacitance. Figure 1 shows a 14-section prototype shock line with a compression ratio of 20:1.

We have discovered several patentable techniques: a means to generate a clean impulse from a shock line that contains ringing components, a structure that suppresses ringing or soliton formation, and a sinusoid-to-impulse converter that exhibits 20% efficiency in converting a 4-ns sinusoid to a 50-ps impulse. The waveform convertor will allow us to develop high data-rate digitizers.

The high-voltage NLTL will help advance the data rate of our LLNL-developed transient digitizer from 33 to 200 gigasamples/s. In FY 1993, we will apply the NLTL to other uses, including automotive collision-detection radar and radar-imaging systems. ◆

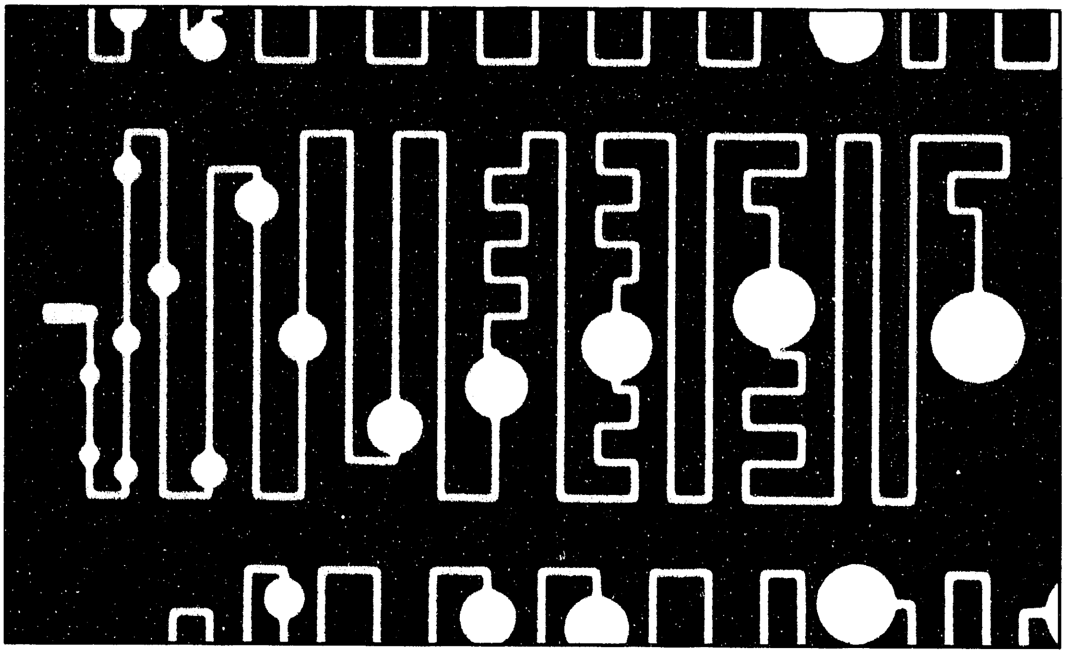

Figure 1. A prototype monolithic shock line. The long metal traces are inductors, and the circular regions are nonlinear variable capacitance diodes. Some traces have been folded for compactness.

Neural-Network Hardware and Applications

C. Y. Fu and G. F. Chapline, Jr.

The objective of this project is to develop a high-speed, neural-network, very-large-scale integration chip that can perform at a rate of 12 billion interconnects/s. This rate is 240 times faster than that of neural-network simulations conducted on the Cray X-MP. We have successfully demonstrated all of the components—input buffers, synaptic arrays, and neuron amplifiers—to accomplish our goal. We need to scale down the neuron size and its power consumption and improve the synaptic array for a 96-neuron, neural-network chip. In addition to a smart-fuze application, which was the goal of this project, our research on neural-network modeling has resulted in four potential applications:

1. Optical spectrometer data fusion and analysis for plasma and corona discharge monitoring and control.
2. Data compression for the projected $40 billion market in multimedia, computer-graphics stations, and high-definition television by the year 2000.
3. Noise filtering and signal processing in advanced medical diagnostics.
4. Real-time environmental monitoring and toxic-pollution analysis.

Hardware Improvements

In FY 1992, we increased the resistance of the resistors by tenfold to 2 MΩ and substantially improved the linearity (0.5% over ±5 V) of the synaptic characteristics (Figure 1). We assisted the Naval Air Warfare Center (NAWC) in designing, fabricating, and testing neurons and input buffers. We also developed a new laser process without using toxic reactants or producing toxic by-products. No metal traces or debris are seen with either an optical or a scanning electron microscope. Together with NAWC, we also designed a cascadable neural-network architecture that includes an input buffer amplifier for each input line, a fully connected synaptic array, and output neurons, representing a single-layer neural network. It has 96 neurons and 12,288 synapses (~100,000 resistors) in one chip. This single customizable chip can be used to build different architectures. The chip is expected to operate at a throughput of 12 billion interconnects/s and dissipate 0.7 W. Very large systems could be built by cascading these chips together.

In FY 1993, we plan to deliver an integrated neural-network chip, and we will work on the third-generation synaptic array. This new array will quadruple the packing density of the resistors, resulting in 0.8 million resistors/cm^2.

Research on Learning Algorithms

We investigated a new idea for a self-learning network, the Multi-Quadratic Continuous Hopfield neural network. Unfortunately, the results were disappointing. Recently, with hardware in mind, we have begun to investigate an approach to learning based on varying individual weights in discrete steps. The weights to be varied are chosen at random, and learning a training set requires several passes over the network. Perhaps this approach to learning could be implemented optoelectronically.

Potential Applications

We will continue our research on using an artificial neural network and fuzzy logic combination for plasma monitoring and control. We will also apply our current understanding of plasma-signature recognition to the areas of chemical warfare and remote sensing of toxic waste. Research will continue on using wavelet signal processing for still-image and video compression and decompression because we have demonstrated a factor-of-2 improvement in compression ratio and substantially better picture quality compared with the currently accepted Joint Photographic Experts Group algorithm. On the basis of our developed chip technologies, research will continue on an extremely fast coding and decoding chip for discrete cosine or wavelet transforms in real-time, high-resolution image compression and decompression. ◆

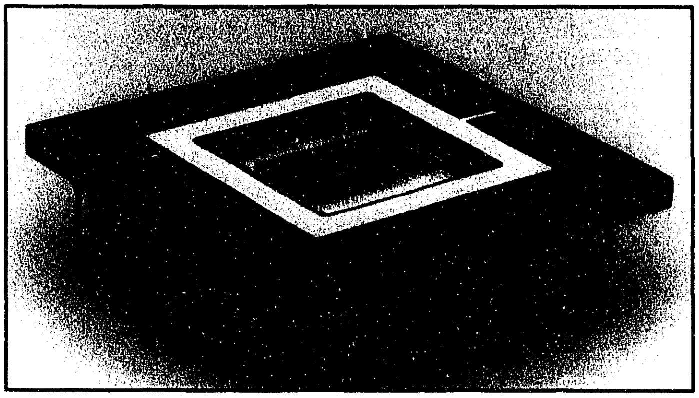

Figure 1. Synaptic-array chip used to test our neural-network board. The chip consists of 34,000 2-MΩ resistors and has a packing density of 0.2 million resistors/cm^2.

Advanced Environmental Sensing

M. Y. Ishikawa

The goal of the advanced environmental sensing (AES) project is to develop systems that automatically measure, categorize, and report signals emanating from strong sources, such as energy-generating equipment, over great distances. These "smart" sensor systems are required to be small, remotely located, highly sensitive, and capable of monitoring low- to midfrequency signals at distances of 10 to 100 km. Commercial environmental-measurement techniques are worker-intensive, of limited effectiveness, and only viable over much shorter distances.

In previous research, the AES project developed an improved theoretical model for signal propagation over a wide frequency spectrum. The project also conducted field tests, which culminated in a major experiment at the Eastern Test Range that tested both the theory and project concept under nonideal conditions. In FY 1992, our goal was to repackage the AES system in an evolved, compact form with the ultimate aim of deployment.

On the basis of the field experiment, we designed a new, smaller, optimized field-recording system for data collection. We then built and successfully field-tested a prototype unit. This new system is much more compact than the previous one, synchronizes data to less than 100 μm, and is easily carried in one hand and operated by an individual in six-hour blocks.

The data acquired by the AES system are complex because they are collected in multiple channels, at different locations, and with different sensors. This complexity required the development of an algorithm that passively tracks a moving target using an array of sensors. We developed the required algorithm and built a computer program incorporating this feature. We also produced an initial design for the advanced packaging of an AES hardware package for deployment over a wide range of conditions, such as arctic, desert, and canopy. Reduced-signature packaging was explored. These developments hold promise for further improvements in remote, highly sensitive, environmental sensor systems. ◆

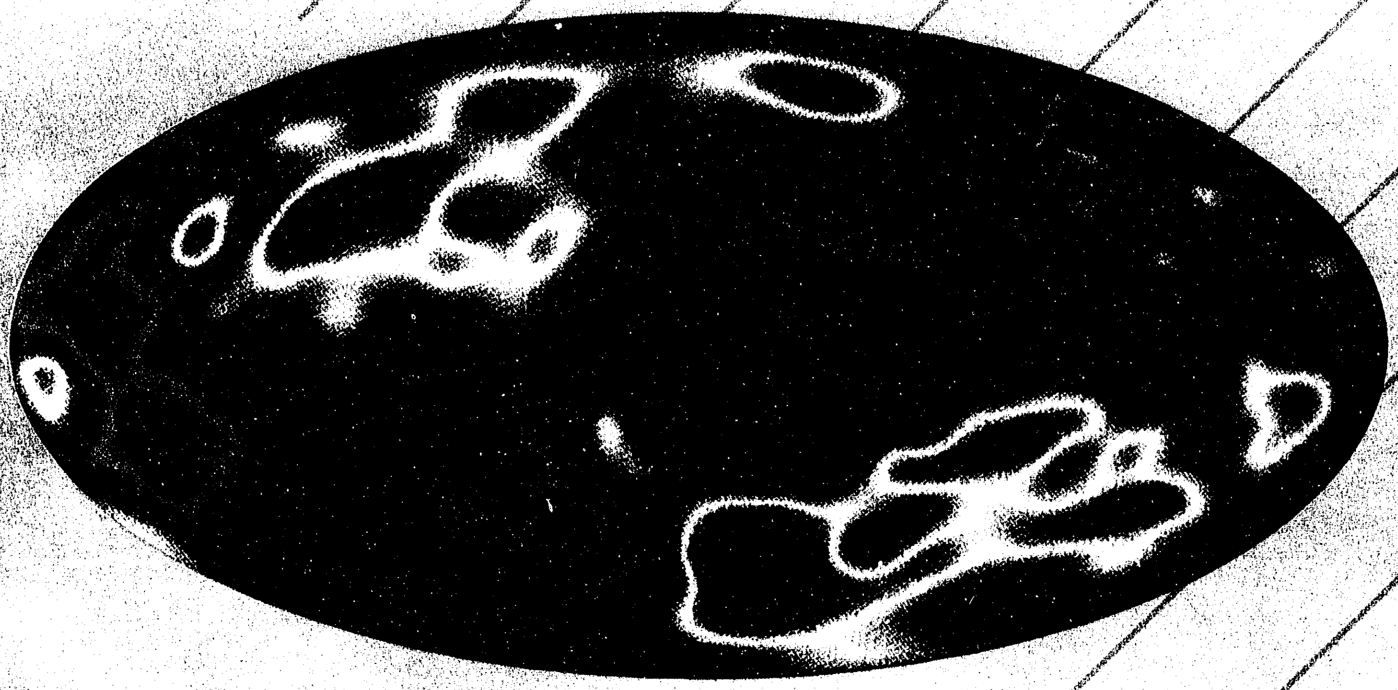

Space Science and Technology

Laboratory Directed Research and Development FY 1992

On the previous page. Simulation of fluctuations observed in the microwave background radiation by the Cosmic Background Explorer satellite.

Stellar Evolution and Supernovae

C. R. Alcock, G. W. Hawkins, C. J. Skinner, and J. R. Wilson

In the final stages of stellar evolution, stars exhaust their nuclear fuel and eject their outer layers, or envelopes, which contain 50% of their mass and 90% of their radius. After this ejection, one of three possible remnants is left behind. If the evolution ends with a gentle ejection of the envelope, a white dwarf star may remain. If the star explodes in a supernova, it may collapse into a neutron star or a black hole. In some cases, the envelope ejection leaves no remnant.

We are studying the gentle envelope-ejection mechanism and the influence of envelope ejection on nuclear burning in the final phase of stellar evolution. We are also investigating the mechanism of supernova explosions and plan to determine if either neutron stars or black holes result from supernovae. Finally, we are examining the impact of exotic phases of matter on stellar evolution.

Gentle Envelope-Ejecting Stars

We have obtained images of gentle envelope-ejecting stars in the mid-infrared region using the UC Berkeley–LLNL mid-infrared camera at the United Kingdom Infrared Telescope (the largest infrared telescope in the world). We have obtained images in the far-infrared region using the National Aeronautics and Space Administration's (NASA's) Kuiper Airborne Observatory during flights out of Christchurch, New Zealand. In many cases, the images show that the mass outflow is asymmetric, especially in carbon-rich stars with clear bipolar outflows. This observation is significant because theory suggests that generally, ejections should be circular. The images confirmed our one-time observation that envelope ejection proceeds in a series of discrete ejection events, spaced by a few hundred years (Figure 1).

Explosive Envelope-Ejecting Stars

We have included the momentum of the ejection material and the contribution of neutrinos to chaos and randomness in our supernovae models. These mechanisms are the most promising explanation of what causes explosive-envelope ejection. We modify nucleosynthesis in the model by the degree of randomness we assign to the ejecta. Preliminary calculations show that many intermediate-mass isotopes are created in this manner.

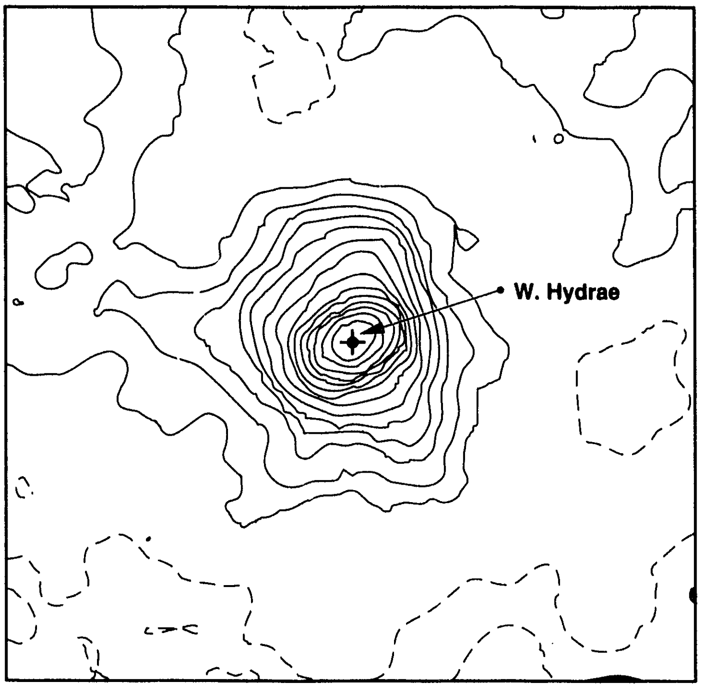

Figure 1. Far-infrared map of the mass-ejecting star W. Hydrae, showing the asymmetry in the ejected matter.

In FY 1993, we will observe both gentle and explosive envelope-ejecting stars, concentrating on the much hotter planetary nebulae to discover how the distribution of their materials relates to gentle ejection. The materials in the planetary nebulae form an intermediate stage between the gentle envelope-ejecting stars we have already observed and the white dwarfs that may remain. Our observations will help clarify how much material is ejected.

In addition, we will use spectroscopy to determine if most of the heavy elements in the planetary nebulae are in the gas phase or in grains. This determination is important to the study of interstellar matter because most heavy elements in interstellar matter are in solid grains, and the likely origin of these grains is the cool stellar outflow from gentle envelope-ejecting stars. If these grains are evaporated in the hot planetary-nebula phase, then some other mechanism is probably forming the grains.

In FY 1993, we will also study neutrino-mediated ejections in supernovae. We plan to confirm that this mechanism causes supernovae explosions and to clarify its effect on nucleosynthesis. ◆

Constraints on the Origin of Oxygen Isotopic Anomalies in Meteorites

F. J. Ryerson and K. D. McKeegan*

Nucleosynthetic variations in oxygen isotopic compositions are present among all meteorite groups and provide a means of classifying planetary materials. Such variations also characterize whole rock samples of refractory calcium-aluminum-rich inclusions (CAIs) from the Allende meteorite and other carbonaceous meteorites. If we plotted the concentration of $^{17}O/^{16}O$ against $^{18}O/^{16}O$ for minerals from these inclusions, it would be a single line with a slope close to unity. This "Allende array" can be described as a mixing line between a component of solar composition and another presolar component that is preferentially enriched in ^{16}O.

Clayton et al. (1977) attempted to identify the carriers of this anomalous component and revealed that the different minerals comprising CAIs contained varying and systematic concentrations of the oxygen component. The largest excesses of the ^{16}O-enriched component were found in spinels (about –4% excess), with clinopyroxene having a somewhat lower concentration. Melilite and anorthite, other meteoritic materials, have compositions that are more similar to the terrestrial composition. The patterns of isotopic anomalies observed in these materials represent the convolution of (1) the initial isotopic composition imposed by some mixture of nucleosynthetic components emanating from a variety of astrophysical settings and (2) mixing caused by nebular and planetary processes. If the efficiency of the various processes that caused the isotopes to mix can be described as a function of external conditions, then we may be able to constrain the history and conditions of these nebular events and reconstruct the isotopic composition of the interstellar material before it was processed within the solar nebula.

The systematic variation in ^{16}O excesses in different minerals suggests that chemical properties of the minerals involved control whatever process is responsible for the Allende array. Diffusive exchange of oxygen between the various minerals in CAIs and a gas reservoir could produce a consistent, systematic, and mineralogically controlled distribution of anomalous oxygen (Clayton and Mayeda, 1977). In this exchange, the initially uniform ^{16}O-enriched oxygen of the CAI would undergo

---

*University of California at Los Angeles.

partial isotopic exchange with more "normal" oxygen in the surrounding nebular gas. For the thermal history of any proposed solid–gas interaction, the time-integrated diffusivity of melilite and anorthite must exceed that of clinopyroxene, which in turn exceeds that of the more refractory oxides such as spinel.

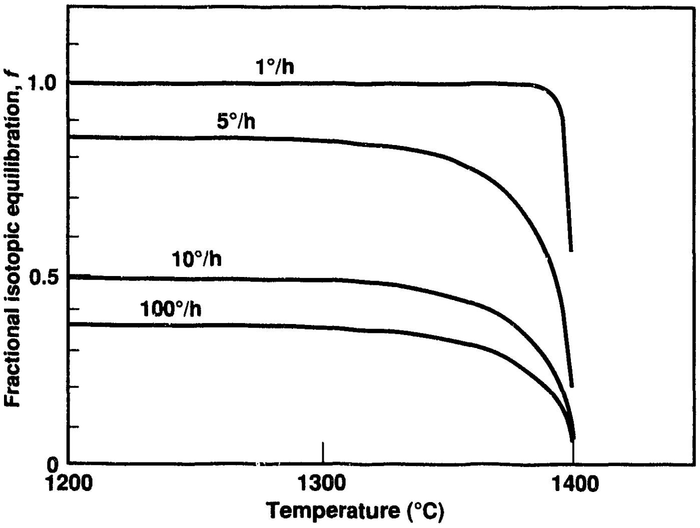

Figure 1. Fractional isotopic equilibration *f* in a partially molten sphere 1 cm in diameter, as a function of temperature for different cooling rates. We determined that the melt will be totally equilibrated for cooling rates of ~1 °C/h.

We determined oxygen-diffusion coefficients of the relevant minerals at appropriate conditions and found that it is extremely difficult to produce the necessary fractionation from an initially homogeneous inclusion. Therefore, we suggested that the pattern of anomalies resulted from partial reequilibration of the inclusion while it was molten. For this theory to be valid, the composition of the melt during the final stage of crystallization would have to fully equilibrate with a reservoir of terrestrial composition.

Using available diffusion data, we calculated the fractional equilibration *f* of a 1-cm molten sphere for various cooling rates over the crystallization interval (Figure 1). Our results indicate that the melt will be totally equilibrated ($f = 1$) for cooling rates of ~1°C/h. These rates are comparable to those inferred from textual studies and indicate relatively slow cooling rates for these objects. We are performing partial equilibration experiments on these materials to monitor the composition of the mineral phases during equilibration. ◆

References

Clayton, R., and T. K. Mayeda (1977), "Correlated Oxygen and Magnesium Anomalies in Allende Inclusions I: Oxygen," *Geophys. Res. Lett.* **4**, 295–298.

Clayton, R., L. Onuma, L. Grossman, and T. K. Mayeda (1977), "Distribution of the Pre-Solar Component in Allende and Other Carbonaceous Chondrites," *Earth Planet. Sci. Lett.* **34**, 209–224.

Advanced X-Ray Sources and Calibration Techniques for Space Applications

C. Hailey, L. Madison, C. Mauche, P. Springer, R. Thoe, and J. Wittmayer

Various enabling technologies must be developed for the United States to carry out scientific missions in space in the next century. Great effort has been put into improving x-ray detectors and optics for future missions. Unfortunately, these development efforts have, in many cases, outstripped the more mundane technologies that are essential to use these advances, such as x-ray calibrations. The importance of space optics calibrations was demonstrated by the problems of the Hubble Space Telescope.

Proper characterization of next-generation, high-angular-resolution, x-ray telescopes requires very-high-intensity x-ray sources placed greater than 500 m from the telescope to properly simulate the parallel beam of radiation that would emanate from a point-like cosmic x-ray source. The laboratory x-ray sources must operate reliably for long periods of time, provide x rays of many different monochromatic energies, and provide an x-ray beam of good, stable spatial uniformity.

For many years, LLNL has pioneered development of high-brightness, high-reliability, x-ray sources as part of its need to calibrate x-ray instruments for underground nuclear testing. Similarly, LLNL has been involved in several x-ray astronomy missions during the last five years. Consequently, we were well qualified to evaluate several concepts for providing high-performance x-ray sources for characterizing next-generation x-ray telescopes.

One concept involved a modified version of the LLNL-developed low-energy x-ray source (LEXS), the highest brightness x-ray source in existence above 1 keV. This electron impact, x-ray source is cooled with turbulent water for high-power operation. It is equipped with special electron-optics geometry to minimize x-ray polarization of the emitted x rays (essential for precision calibrations of x-ray optics that give different reflectivity for different x-ray polarizations).

We measured the emission distribution of x rays from this source to help modify the electron optics that would allow even smaller x-ray spots to be used. With smaller spot sizes, we could more accurately simulate cosmic x-ray sources using this laboratory x-ray source. We also evaluated a rapidly pulsing, table-top, laser-plasma, x-ray source coupled with an x-ray monochromator for calibrations below 1 keV. Such systems are being developed at LLNL for calibrating diagnostic instruments used on the Nova laser. With their great intrinsic brightness and ability to generate copious narrow-line emission, these laser-plasma sources are superior to the alternative x-ray sources below 1 keV that are currently available. Our comparative work demonstrated that both classes of x-ray sources substantially improve our ability to characterize the next generation of x-ray optics in the 0.05- to 10-keV range.

Absolute calibration of x-ray optics that is substantially better than current methods is also important for future x-ray space missions. Good calibrations are needed to determine precisely the strength of cosmic x-ray sources. We investigated how accurately the x-ray reflectivity of extremely smooth, x-ray, optical test flats could be determined. This involved acquisition of x-ray reflectivity data on the test flat using a specialized LLNL x-ray source with a crystal monochromator.

To accurately model the test flat, we determined its scattering properties in a separate x-ray scattering facility to properly correct for reduced reflectivity due to surface imperfections in the piece rather than the bulk reflective properties of its gold coating. We acquired x-ray data at a number of energies and fitted them to a model that takes into account the surface roughness of the test flat, dust and chemical contamination, and basic reflecting properties of the gold surface. Many systematic effects had to be accounted for in the experimental setup as well.

These measurements provided an unprecedented level of accuracy in the characterization of x-ray test optics. This established the feasibility of measuring reflectivities for x-ray astronomy with a few percent relative accuracy, the goal for next-generation space missions. We also uncovered certain anomalies in the reflectivity of such optics for x rays impinging at high angles of incidence that are not currently understood and are being investigated. ◆

Interaction of Radio Galaxies with Their Environments

W. J. M. van Breugel, S. E. Deustua, R. D. Rogers, and S. Charlot

We are studying the effects of active galaxies on their environments and the implications for modeling the formation and evolution of galaxies and cosmology. We have developed a model in which relativistic effects near the central black holes in the galaxy centers in the early universe can account for observed cosmic x-ray and gamma-ray backgrounds (Rogers, 1991).

The centers of powerful, extragalactic radio sources exhibit collimated outflows (jets) and ionizing radiation. We discovered that the effects of these radio jets and ionizing beams are visible as patches of blue continuum and line emission along the radio-source axes. The origin of this optical emission may be enhanced star formation induced by the radio source, scattered light from the galaxy nucleus, or optical synchrotron emissions associated with the radio components.

Detailed studies of this optical emission can be used to investigate various properties of radio galaxies and their environments. For example, in one of our studies, we used stellar-population-synthesis models to determine the age of a starburst that was apparently induced by a radio source. From this, we derived a speed for the radio-source bowshock of only a few thousand kilometers per second. If studies of other objects show similarly low bowshock speeds, we may have to reconsider some of the usual assumptions about particle-reacceleration processes and synchrotron losses in the hot spots of radio galaxies.

Radio sources can also be used to accurately pinpoint very-high-redshift, radio-galaxy candidates. One method is to select sources with steep radio spectra and relatively small angular sizes, both of which are correlated with redshift. We are using this method to conduct a large survey and have discovered numerous radio galaxies at high redshift (z > 2). Searches for high-redshift galaxies followed by detailed multicolor and spectroscopic observations provide important information on the formation and evolution of galaxies and cosmology.

We used Hubble Space Telescope (HST) images of the most distant galaxy known so far, 4C 41.17, at redshift z = 3.8 (Miley et al., in press). The HST observations show that the galaxy consists of several components closely related to the radio source (Figure 1). The physical origin of these optical and radio associations is still unclear but probably resembles those found in nearby radio galaxies. Further HST observations of this galaxy and similar high-redshift objects are needed to discriminate between the various possibilities. We must determine the origin of the optical and radio correlations to use distant radio galaxies for studies of galaxy formation and evolution. ◆

References

Miley, G. K., K. C. Chambers, W. J. M. van Breugel, and D. Macchetto (in press), "HST Imaging of Distant Galaxies: 4C 41.17 at z = 3.8," *Astrophys. J.*

Rogers, R. D. (1991), "Relativistic Enhancement of the Compton-Reflected Component in Active Galactic Nuclei," *Astrophys. J.* 383, 550.

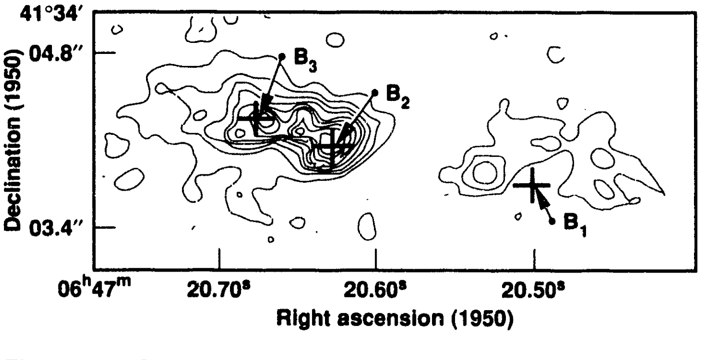

Figure 1. HST image of galaxy 4C 41.17. This galaxy consists of several optical components, some of which have associated nonthermal, radio emissions (B1, B2, and B3).

IRAS Survey

G. W. Hawkins, D. Proctor, and C. J. Skinner

The Infrared Astronomy Satellite (IRAS) surveyed 98% of the sky at 12, 25, 60, and 100 μm. Our original aim was to reanalyze data taken near the galactic plane to increase the number of recognized sources and to develop a more complete catalog of very young and very old stars frequently visible only in the infrared. In FY 1992, we modified this aim to include detailed study of the ejected envelopes of old stars, supplementing the IRAS data with data taken at ground-based observatories.

Progress

We made substantial progress in developing algorithms for extracting and identifying point sources in crowded fields observed with IRAS. The National Aeronautics and Space Administration (NASA) compiled the IRAS Point Source Catalog by running a one-dimensional square-wave filter across the detector data stream. This approach has many systematic problems in crowded and confused regions of the sky, especially when we resolve sources in the cross-scan direction. These crowded regions usually occur within a few degrees of the galactic plane (where new stars are forming) and are among our most interesting scientific targets.

We ran our detection algorithms on two-dimensional images and fitted a two-dimensional point-spread function to each suspected source. This approach properly takes into account contamination of the flux of a point source by its neighbors and allows us to use a lower threshold. For this approach, we adapted a code, DOPHOT, that was developed to reduce charge-coupled-device (CCD) images in the visible wavelength bands.

Our tests indicated that if we used DOPHOT, we could extract up to six times as many point sources in the vicinity of the galactic plane as were found for the Point Source Catalog using NASA's analysis of the IRAS data set. Thus, we could release a more complete catalog of point sources. Unfortunately, our access to the raw data was restricted by the NASA subcontractor, and we were unable to complete the catalog. When NASA releases these data, we will prepare the catalog.

Accordingly, we modified our program and concentrated on detailed studies of nearby mass-ejecting red giant stars. The principal aim of this work was to directly image the material recently ejected by the stars. We began an observational program of wide-field-of-view, direct CCD imaging of red giant stars with the 100-cm Nickel telescope at the Lick Observatory. We wanted to observe red giant stars with the extended dust shells seen by IRAS and to detect the shells in scattered light at one or more optical wavelengths. We used coronagraphs of different sizes to block light from the bright central stars and found several red giants with extended optical emission and probable circumstellar material.

We analyzed 21-cm observations of the red giant W. Hydrae taken with the Very Large Array (VLA) radio telescope in Socorro, New Mexico, to search for atomic hydrogen from the star's mass-loss envelope. W. Hydrae is a good candidate to search for neutral hydrogen because it has a large dust shell that has been seen with IRAS, it is one of the nearest asymptotic giant branch stars, and it has a high galactic latitude and high radial velocity. VLA observations revealed no neutral hydrogen emission at the position and velocity of the star. VLA observations did show a curious, long, neutral-hydrogen feature about 10 to 15 arcmin from the star with the feature's axis pointed along the line of sight to the star. If the neutral-hydrogen feature is at the same distance as W. Hydrae, its neutral hydrogen mass would be 0.0003 solar masses, a reasonable mass loss for a red giant.

We observed a similar star, AFGL 2343, with the UC Berkeley and LLNL mid-infrared camera. For the first time, we resolved the dust shell around this object (Figure 1) and showed a significant clumpiness in the outflow. ◆

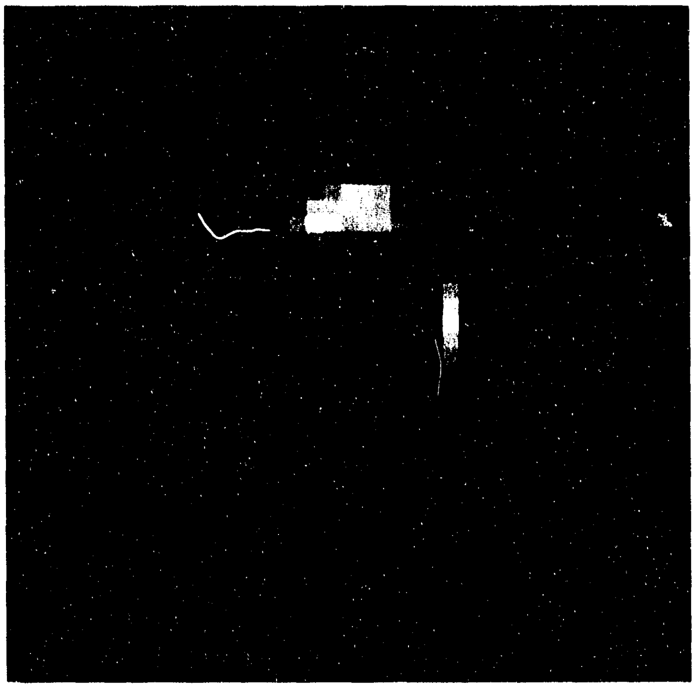

Figure 1. The dust shell around AFGL 2343 at 10 µm, resolved for the first time.

Microwave-Generated Plasma Thruster for Space Propulsion

E. B. Hooper and B. W. Stallard

Manned and large-cargo space travel are demanding on rocket propulsion systems. Energy and propellant mass must be used with efficiency because they are carried with the vehicle. Electric rockets ("thrusters"), in which the propellant is accelerated by electrical or magnetic forces to exhaust velocities greater than 10 km/s, are one option for an efficient propulsion system. Our goal is to create high efficiencies with the ruggedness and reliability required for a 10,000-hour roundtrip to Mars using microwaves to generate and heat propellant plasma. We also hope to send scientific missions to the solar system's outer planets.

Microwave Heating

When propellant plasma is heated by microwaves, the plasma electrons resonate and absorb energy when their magnetic-cyclotron frequency equals the frequency of the microwaves. The resulting hot electrons expand in the magnetic nozzle and transfer their energy to the plasma ions through electric potentials generated in the plasma by the charged particles. Previous attempts by researchers to use microwave techniques were limited because the plasma density must be low for the applied waves to propagate and because energy flowing along the magnetic field was lost to thruster walls. Using techniques and codes developed in LLNL's Magnetic Fusion

Energy Program, we are modeling a device that eliminates the low-density requirement by using whistler plasma waves, which can propagate at high densities. Also, the lack of electrodes, a large magnetic-mirror ratio, and the heating geometry of this device reduce energy losses to the walls.

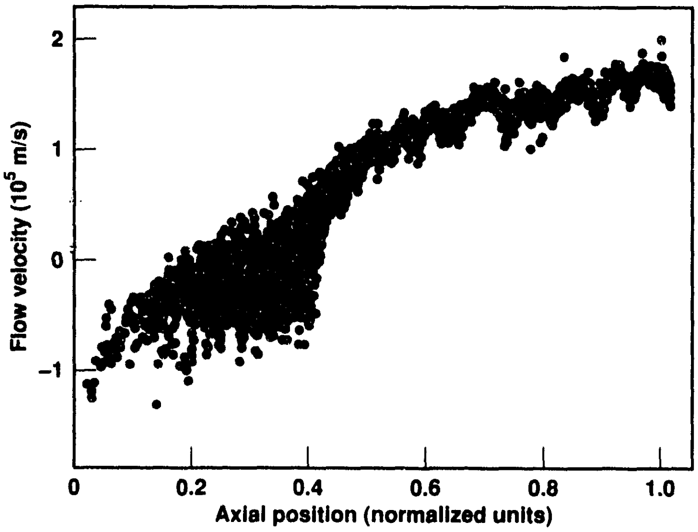

Figure 1. Ion-flow velocity in the magnetic nozzle. Propellant gas is injected between 0.3 and 0.4, and the heating is at 0.2. Flow velocities assume hydrogen propellant. Exit is to the right. This geometry accelerates the plasma to produce thrust and operates at high efficiency by minimizing energy and particle losses.

Wave Coupling

In FY 1992, we modeled details of two critical thruster aspects: (1) the coupling of the microwaves to the whistler waves on the plasma column and (2) the effects of heating on the plasma flow and the conversion efficiency of energy into thrust. In our model, whistler waves are excited by a helix wrapped around the plasma near the peak of the magnetic field. Because the field strength is nearly constant in this region, we neglected variations along the field and assumed that the plasma parameters were radially constant in the column when we analyzed the coupling. The helix lies close to the plasma surface, but there is a vacuum between the helix and the walls of the cylindrical waveguide.

We based our calculations on parameters that are characteristic of FY 1993 experiments planned with the National Aeronautics and Space Administration: a density of about 10^{18} m^{-3}, magnetic field of 0.2 T, and frequency of 0.9 GHz. We found that resonances in the coupling impedance occurred when the plasma fields at the edge of the column had the same structure as those of the whistler wave on the helix. At these resonances, we predict that the coupling will be highly efficient even at high density and the microwave power will be efficiently converted into whistler wave energy.

Heating Effects

Whistler wave heating strongly distorts the electron distribution function. In response, the plasma accelerates down the expanding magnetic field, reducing the energy flow up the field to a small fraction of that of a hot plasma without the microwaves. Figure 1 shows the resulting ion-flow velocity.

During FY 1993, our primary effort will be to study the separation of the plasma from the magnetic nozzle that imparts thrust to the vehicle. We will base our study on the results and tools we developed in FY 1992. ◆

Phase Dynamics in the Early Universe

C. R. Alcock, D. P. Bennett, G. J. Mathews, G. Fuller,* P. Lubin,† and S. H. Rhie‡

Phase transitions appear to be important in very early cosmic history. For instance, the quark-hadron transition occurred only about 10 μs after the big bang when a dense plasma of quarks, gluons, and hadrons recombined to create the elements that constitute our present universe. Our previous work shows that first-order quark-hadron phase transitions affect light-element nucleosynthesis—the process that created deuterium, helium, and lithium. During FY 1992, we investigated phase dynamics and their impact on primordial nucleosynthesis.

Some phase transitions are believed to have occurred much earlier when the universe was only 10^{-35} s old. The strong gravitational fields of topological relics such as cosmic strings, global monopoles, or global textures may be the seeds around which the smooth materials of the early universe coalesced to form galaxies. We are focusing on the relics' combined impact on present-day observables, which are the results for anisotropy in the cosmic background radiation found in the differential microwave experiment on the Cosmic Background Explorer satellite.

Nucleosynthesis Code

We analyzed the "neutrino inflation" that follows the cosmic quark-hadron phase transition. This process diminishes large-amplitude fluctuations in the baryon number density by transferring heat into the high-baryon-density regions. These regions then expand to reach mechanical equilibrium with their surroundings. Our dynamic models show that neutrino inflation diminishes all fluctuations to an amplitude of about 7500, independent of the initial amplitude. This information tells us how to set the starting point for our nucleosynthesis code. Our preliminary work shows that neutrino inflation has a significant effect on light-element yields.

Numerical Code for Phase Dynamics

In FY 1992, we developed the first numerical code to model the dynamic evolution of a universe containing either global monopoles or textures. Our preliminary work supports our theory that these relics may indeed be the seeds around which galaxies formed. We are studying the effect of these relics on cosmic microwave background radiation (CMBR). We will then be able to use observations of the CMBR to determine if these theories are correct, which in time will tell us how much we know about galaxy formation.

In FY 1993, we will finish studying the effect of first-order quark-hadron phase transition on light-element nucleosynthesis. We will complete the nucleosynthesis simulations for the period following neutrino inflation and for the analogous photon inflation that we discovered. The photon inflation occurs at the end of the nucleosynthesis epoch and might substantially alter the yield of lithium. We intend this work to be the definitive study on how light-element nucleosynthesis affected phase transitions.

**University of California at San Diego.*
†University of California at Santa Barbara.
‡University of California at Santa Cruz.

We will also complete the numerical investigation of the dynamic evolution of global monopoles and textures. We will simulate the development of anisotropies in the cosmic microwave background radiation and compare these anisotropies directly with the results from experimental determinations by the Cosmic Background Explorer satellite (Figure 1) and various ground-based measurements. In concluding, we plan to establish conclusively that either global monopoles or textures are the viable seed of galaxy formation. ◆

Figure 1. Simulation of fluctuations observed in the microwave background radiation by the Cosmic Background Explorer satellite.

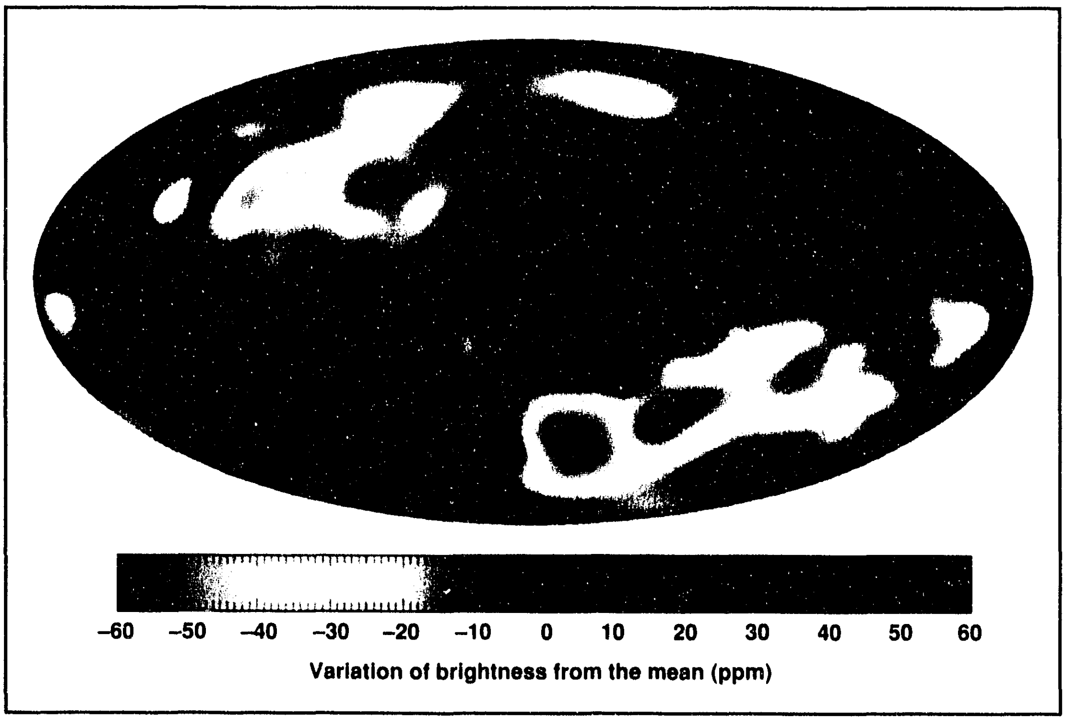

Publications and Author Index

Laboratory Directed Research
and Development FY 1992

Publications for FY 1992

Ables, E., et al. (1992) "Measurements of Optical Properties of Waveshifting Optical Fiber for Liquid Scintillator Hadron Calorimetry," *Nucl. Instrum. Methods Phys. Res. A* **313**, 142–150.

Ables, E., et al. (1991), *Muon Drift Chamber Physics and Engineering R&D Activities for the L* and GEM Detectors in FY 1991*, Lawrence Livermore National Laboratory, Livermore, CA, UCRL-ID-108489.

Ables, E., et al. (1992), "Muon Drift Chamber Wire Bond Failure Analysis," *Nucl. Instrum. Methods Phys. Res. A* **317**, 523–530.

Ables, E., et al. (1992), "Observation of Drift Chamber Signals Using a Mach–Zehnder Electro-Optic Modulator," *Nucl. Instrum. Methods Phys. Res. A* **316**, 452–456.

Altenbach, T., and A. Lamont (1992), *The Energy Economics Modeling Project and the Lawrence Laboratories Energy Model*, Lawrence Livermore National Laboratory, Livermore, CA, UCRL-ID-112336.

Amendt, P., D. C. Eder, R. A. London, and M. D. Rosen (1992), *Plasma Dispersion in Ultra-Short-Pulse X-Ray Lasers*, Lawrence Livermore National Laboratory, Livermore, CA, UCRL-JC-109987.

Amendt, P., R. A. London, and M. Strauss (1991), "Extended Modal Analysis of Steady-State X-Ray Laser Coherence," *Phys. Rev. A* **44**, 7478.

Amendt, P., R. A. London, and M. Strauss (1991), "Modal Study of Refractive Effects on X-Ray Laser Coherence," in *OSA Proc. on Short-Wavelength Coherent Radiation: Generation and Applications*, P. H. Bucksbaum and N. M. Ceglio, Eds. (Optical Society of America, Washington, DC), vol. 11, p. 91.

Amendt, P., R. A. London, and M. Strauss (1992), *Optimization of Single-Stage X-Ray Laser Coherence*, Lawrence Livermore National Laboratory, Livermore, CA, UCRL-JC-110900.

Amendt, P., R. A. London, and M. Strauss (1992), *Optimization Study of X-Ray Laser Coherence in Ni-Like Ta*, Lawrence Livermore National Laboratory, Livermore, CA, UCRL-JC-110084.

Ammon, C. J., and G. Zandt (in press), "Receiver Structure beneath the Southern Mojave Block, California," *Bull. Seism. Soc. Am.*

Barnard, J. J., H. D. Shay, S. S. Yu, A. Friedman, and D. P. Grote (1992), *Emittance Growth in Heavy Ion Recirculators*, Lawrence Livermore National Laboratory, Livermore, CA, UCRL-JC-110292.

Barton, J. J., and L. J. Terminello (in press), "Source Wave Angular Momentum Alters Electron Angular Distributions from Surfaces," *Phys. Rev. B*.

Baum, S. A., T. M. Heckman, and W. J. M. van Breugel (1991), "Spectroscopy of Emission Line Nebulae in Powerful Radio Galaxies: Interpretation," *Astrophys. J.* **389**, 208.

Becker, J. A., E. A. Henry, S. W. Yates, T. F. Wang, A. Kuhnert, M. J. Brinkman, J. A. Cizewski, R. M. Diamond, M. A. Deleplanque, F. S. Stephens, and J. E. Draper (1992), "Level Spin for Superdeformed Nuclei near A = 194," *Phys. Rev. C* **46**, 889.

Bell, J. B., and D. L. Marcus (1992), "A Second-Order Projection Method for Variable Density Flows," *J. Comp. Phys.* **101**, 334.

Benz, H. M., and G. Zandt (in press), "Teleseismic Tomography: Lithospheric Structure of the San Andreas Fault System," in *Seismic Tomography: Theory and Practice*, H. M. Iyer, Ed. (Chapman and Hall).

Benz, H. M., G. Zandt, and D. H. Oppenheimer (1992), "Lithospheric Structure of Northern California from Teleseismic Images of the Upper Mantle," *J. Geophys. Res.* **97**, 4791–4801.

Boercker, D. B. (1991), "Constant-Pressure Simulation of Carbon in the BC8 Structure," *Phys. Rev. B* **44**, 11592.

Bogen, K. T. (1992), *Reassessment of Human Peripheral T-Lymphocyte Lifespan Deduced from Cytogenetic and Cytotoxic Effects of Radiation*, Lawrence Livermore National Laboratory, Livermore, CA, UCRL-JC-111762.

Bogen, K. T. (1992), *RiskQ: An Interactive Approach to Probability, Uncertainty, and Statistics for Use with Mathematica (Reference Manual)*, Lawrence Livermore National Laboratory, Livermore, CA, UCRL-MA-110232.

Candy, J. V., D. R. Manatt, F. L. Barnes, J. A. Becker, E. A. Henry, and M. J. Brinkman (1991), "Rotational Band Identification: A Model-Based Detection and Estimation Approach," *Int. J. Imaging Systems Technol.* **3**, 1.

Cann, D. (1992), *Sisal 1.2: A Brief Introduction and Tutorial*, Lawrence Livermore National Laboratory, Livermore, CA, UCRL-MA-110620.

Cann, D. (1992), *The Optimizing Sisal Compiler: Version 12.0*, Lawrence Livermore National Laboratory, Livermore, CA, UCRL-MA-110080.

Chang, B., P. R. Bolton, and D. N. Fittinghoff (1992), *Closed Form Solutions for the Production of Ions in Collisionless Ionization of Gases by Intense Lasers*, Lawrence Livermore National Laboratory, Livermore, CA, UCRL-JC-108001.

Charatis, G., N. D. Delamater, G. E. Busch, R. A. Bosch, G. G. Ganger, J. L. Thomburg, D. Sullivan, H. A. Neal, Jr., R. L. Shephard, C. J. Keane, A. L. Osterheld, D. C. Eder, and D. L. Matthews (1992), "Evidence for Population Inversions in Al and Mg by Laser Irradiation at 20-ps Pulse Lengths," *Opt. Soc. Am. B* **9**, 1–5.

Chinn, C. R., J. F. Berger, D. M. Gogny, and M. S. Weiss (1992), "Limits on the Lifetime of the Shape Isomer of ^{238}U," *Phys. Rev. C* **45**, 1700.

Chuang, C. C., and J. E. Penner (1992), "Effects of Anthropogenic Sulfur Aerosols on Climate," in *Nucleation and Atmospheric Aerosols*, N. Fukuta and P. E. Wagner, Eds. (Deepak Publishing, Hampton, VA), pp. 501–504.

Chuang, C. C., J. E. Penner, and L. L. Edwards (1992), "Drop Size Distributions and the Efficiency of Nucleation Scavenging over the Hardiman Fire," in *Precipitation Scavenging and Atmosphere-Surface Exchange Processes*, S. E. Schwartz and W. G. N. Slinn, Eds. (Hemisphere Publishing, Washington, DC), pp. 563–573.

Chuang, C. C., J. E. Penner, and L. L. Edwards (1992), "Nucleation Scavenging of Smoke Particles and Simulated Droplet Size Distributions over Large Fires," *J. Atmos. Sci.* **49**, 1264.

Cohen, B. I., and T. J. Williams (1992), *Implementation of a Semi-Implicit Orbit-Averaged Gyrokinetic Particle Code*, Lawrence Livermore National Laboratory, Livermore, CA, UCRL-JC-109803.

Cohen, B. I., and T. J. Williams (1991), "Semi-Implicit Particle Simulation of Kinetic Plasma Phenomena," *J. Comput. Phys.* **97**, 224.

Cohen, B. I., et al. (1992), *Gyrokinetic Simulations of Poloidal Velocity-Shear Effects on Ion-Temperature-Gradient Modes*, Lawrence Livermore National Laboratory, Livermore, CA, UCRL-JC-112577.

Cook, G. O., Jr. (1992), "Code Generation in ALPAL Using Symbolic Techniques," in *Proc. 1992 Int. Symp. Symbolic and Algebraic Computation*, Lawrence Livermore National Laboratory, Livermore, CA, UCRL-JC-108973.

Cook, G. O., Jr., and J. F. Painter (1992), "ALPAL: A Tool to Generate Simulation Codes from Natural Descriptions," in *Expert Systems for Scientific Computing*, J. Rice, E. Houstis, and R. Vichnevetsky, Eds. (Elsevier, North Holland, Amsterdam), pp. 401–420.

Cook, G. O., Jr., and J. F. Painter (1991), "Construction of Large-Scale Simulation Codes with ALPAL," in *Proc. IMACS World Congress*, Lawrence Livermore National Laboratory, Livermore, CA, UCRL-JC-106562.

Cook, G. O., Jr., and J. F. Painter (1992), "Construction of Large-Scale Simulation Codes Using ALPAL: Generation of a Hydrodynamics Code Module," in *Artificial Intelligence, Expert Systems, and Symbolic Computing*, E. N. Houstis, J. R. Rice, and R. Vichnevetsky, Eds. (Elsevier, North Holland, Amsterdam), pp. 82–88.

Cook, G. O., Jr., J. F. Painter, and S. A. Brown (1991), "How Symbolic Computation Boosts Productivity in the Simulation of Partial Differential Equations," *J. Sci. Comput.* **6**, 193–210.

Covey, C. (1991), "Ocean Uncertainty," *Nature* **235**, 309.

Cowan, T. E., B. R. Beck, J. H. Hartley, R. H. Howell, R. R. Rohatgi, J. Fajans, and R. Gopalan (1992), *Development of a Pure Cryogenic Positron Plasma Using a Linac Positron Source*, Lawrence Livermore National Laboratory, Livermore, CA, UCRL-JC-113157.

Cowan, T. E., M. W. Clark, J. H. Hartley, J. L. McDonald, J. W. McDonald, R. R. Rohatgi, D. H. G. Schneider, R. L. Watson, V. Horvat, and W. H. Trazaska (1991), *Search for Correlated Positron–Electron Peaks in Xe + Au Collisions*, Lawrence Livermore National Laboratory, Livermore, CA, UCRL-JC-110841.

Cowan, T. E., J. Hartley, R. H. Howell, J. L. McDonald, R. R. Rohatgi, and J. Fajans (1992), "Search for Resonant States in Positron–Electron Scattering," *Mater. Sci. Forum* **105–110**, 529.

Cowan, T. E., M. W. Clark, J. H. Hartley, J. L. McDonald, D. H. G. Schneider, R. L. Watson, and V. Horvat (1992), "Systematic Investigations of Correlated Positron–Electron Peaks in Heavy-Ion Collisions," in *Cyclotron-Based Nuclear Science* (Texas A&M University, College Station, TX).

Crutchfield, W. Y., and J. B. Bell (1991), *Instabilities of the Skyrme Model*, Lawrence Livermore National Laboratory, Livermore, CA, UCRL-JC-107427.

Crutchfield, W. Y., N. J. Snyderman, and V. R. Brown (1992), "Deuteron in the Skyrme Model," *Phys. Rev. Lett.* **68**, 1660.

Dannevik, W. (1992), "Massively Parallel Computing and Large Eddy Simulation in Geophysical Fluid Dynamics," in *Large Eddy Simulation of Complex Engineering and Geophysical Flows*, B. Galperin and S. Orszag, Eds. (Cambridge University Press, New York, NY).

Dannevik, W. P., P. G. Eltgroth, M. G. McCoy, A. A. Mirin, and M. F. Wehner (1992), "Development of a Portable Parallel Atmospheric General Circulation Model," in *The 1992 MPCI Yearly Report: Harnessing the Killer Micros*, E. D. Brooks III, Ed., Lawrence Livermore National Laboratory, Livermore, CA, UCRL-ID-107022-92.

Da Silva, L. B., J. E. Trebes, R. Balhorn, S. Mrowka, E. Anderson, D. T. Attwood, T. W. Barbee, Jr., J. Brase, M. Corzett, J. Gray, J. A. Koch, C. Lee, D. Kern, R. A. London, B. J. MacGowan, D. L. Matthews, and G. Stone (1992), "X-Ray Laser Microscopy of Rat Sperm Nuclei," *Science* **258**, 269.

Da Silva, L. B., J. E. Trebes, S. Mrowka, T. W. Barbee, Jr., J. Brase, J. A. Koch, R. A. London, B. J. MacGowan, D. L. Matthews, D. Minyard, G. Stone, T. Yorkey, E. Anderson, D. T. Attwood, and D. Kern (1992), "Demonstration of X-Ray Imaging with an X Ray Operating near the Carbon K-Edge," *Opt. Lett.* **17**, 1.

DeFord, J. F., G. D. Craig, G. Kamin, and L. Walling (1992), *Computation of Wakefields in Structures Containing Dispersive Materials,* Lawrence Livermore National Laboratory, Livermore, CA, UCRL-JC-110200.

Diaz de la Rubia, T., A. Caro, and M. Spaczer (1992), *The Kinetics of Radiation-Induced Disordering of A_3B Intermetallic Compounds: A Molecular Dynamics Simulation Study,* Lawrence Livermore National Laboratory, Livermore, CA, UCRL-JC-111642.

Diaz de la Rubia, T., A. Caro, M. Spaczer, G. A. Janaway, M. W. Guinan, and M. Victoria (in press), "Radiation-Induced Disordering and Defect Production in Cu_3Au and Ni_3Al Studied by Molecular Dynamics Simulation," *Nucl. Intrum. Methods B.*

Dignon, J., C. S. Atherton, J. E. Penner, and J. J. Walton (1991), "NO_x Pollution from Biomass Burning: A Global Study," in *Proc. 11th Conf. on Fire and Forest Meteorology,* P. L. Andrews and D. F. Potts, Eds. (Society of American Foresters, Bethesda, MD), pp. 430–437.

Dignon, J., and J. E. Penner (1991), "Biomass Burning: A Source of Nitrogen Oxides in the Atmosphere," in *Global Biomass Burning,* J. Levine, Ed. (MIT Press, Cambridge, MA), pp. 370–375.

Dignon, J., J. E. Penner, C. S. Atherton, and J. J. Walton (1992), *Atmospheric Reactive Nitrogen: A Model Study of Natural and Anthropogenic Sources and the Role of Microbial Soil Emissions,* Lawrence Livermore National Laboratory, Livermore, CA, UCRL-JC-107393.

Dimits, A. M., and B. I. Cohen (1992), *Simulation Models for Tokamak Plasmas,* Lawrence Livermore National Laboratory, Livermore, CA, UCRL-JC-109895.

Dowla, F. U., T. F. Hauk, and J. B. Rundle (1992), "Earthquake Forecasting Using Neural Networks," *Seismol. Res. Lett.* **63**, 63.

Eder, D. C., and P. Amendt (1992), *Table-Top X-Ray Lasing Based on Optical-Field-Induced Ionization,* Lawrence Livermore National Laboratory, Livermore, CA, UCRL-JC-110043.

Eder, D. C., P. Amendt, M. D. Rosen, J. K. Nash, and S. C. Wilks (1991), "Saturation and Kinetic Issues for Optical-Field–Ionized Plasma X-Ray Lasers," in *OSA Proc. Short-Wavelength Coherent Radiation: Generation and Applications,* P. H. Bucksbaum and N. M. Ceglio, Eds. (Optical Society of America, Washington, DC), vol. 11, p. 96.

Eder, D. C., P. Amendt, and S. C. Wilks (1992), "Optical-Field–Ionized X-Ray Lasers," *Phys. Rev. A* **45**, 6761.

Eder, D. C., S. Maxon, R. A. London, and B. J. MacGowan (1992), "Cavity Issues for Ni-Like Ta X-Ray Laser," in *Ultrashort-Wavelength Lasers,* S. Suckewer, Ed. (Society of Photo-Optical Instrumentation Engineers, Bellingham, WA; *Proc. SPIE* **1551**), pp. 143–149.

Eder, D. C., H. A. Scott, S. Maxon, and R. A. London (1992), "Photon Trapping Models for X-Ray Lasers," *Appl. Opt.* **31**, 4962.

Ermak, D. L. (1992), *Dense-Gas Dispersion Advection-Diffusion Model,* Lawrence Livermore National Laboratory, Livermore, CA, UCRL-JC-109697.

Esser, B. K., and S. Niemeyer (in press), "Absolute Re–Os Ages of IAB, IIE, and IIIA Iron Meteorites," *Geochim. Cosmochim. Acta.*

Falabella, S., and D. M. Sanders (1992), "Comparison of Two Filtered Cathodic Arc Sources," *J. Vac. Sci. A* **10**, 394.

Feo, J., Ed. (1992), *Proceedings of the Second Sisal User Conference,* Lawrence Livermore National Laboratory, Livermore, CA, UCRL-JC-112593.

Feo, J., Ed. (1992), "Sisal," in *A Comparative Study of Parallel Programming Languages: The Salishan Problems* (Elsevier, North Holland, Amsterdam).

Fittinghoff, D. N., P. R. Bolton, B. Chang, and K. C. Kulander (1992), "Observation of Nonsequential Double Ionization of Helium with Optical Tunneling," *Phys. Rev. Lett.* **69**, *2642.*

Fittinghoff, D. N., P. R. Bolton, B. Chang, L. D. Van Woerkum, and W. E. White (1991), "Ion Yields from Strong Field Ionization Experiments Using 100-Femtosecond Laser Pulses," in *Short-Pulse High-Intensity Lasers and Applications* (Society of Photo-Optical Instrumentation Engineers, Bellingham, WA; *Proc. SPIE* **1413**), p. 81.

Friedman, A., and R. O. Bangerter (1992), *Inertial Fusion Energy (IFE) Using Heavy-Ion Drivers,* Lawrence Livermore National Laboratory, Livermore, CA, UCRL-JC-111595.

Friedman, A., J. J. Barnard, D. A. Callahan, J. F. DeFord, W. M. Fawley, D. P. Grote, I. Haber, K. D. Hahn, E. Henestroza, D. W. Hewett, D. D.-M. Ho, A. B. Langdon, C. C. Shang, W. M. Sharp, and S. S. Yu (1992), *Simulation of Heavy-Ion Fusion Beams,* Lawrence Livermore National Laboratory, Livermore, CA, UCRL-JC-110193.

Friedman, A., D. A. Callahan, D. P. Grote, I. Haber, and A. B. Langdon (1992), *3D and r,z Particle Simulations of Heavy-Ion Fusion Beams,* Lawrence Livermore National Laboratory, Livermore, CA, UCRL-JC-110201.

Friedman, A., D. P. Grote, and I. Haber (1992), "Three-Dimensional Particle Simulation of Heavy-Ion Fusion Beams," *Phys. Fluids B* **4**, 2203.

Fu, C. Y., B. Law, and G. Chapline (1992), *Customizable VLSI Artificial Neural Network Chips Based on a Novel Technology*, Lawrence Livermore National Laboratory, Livermore, CA, UCRL-JC-110366.

Fu, C. Y., B. Law, G. Chapline, and D. Swenson (1992), *A Novel Technology for Fabricating Customizable VLSI Artificial Neural Network Chips*, Lawrence Livermore National Laboratory, Livermore, CA, UCRL-JC-109597.

Fu, C. Y., L. Petrich, and B. Law (1992), *A Novel Process Monitoring and Control System Based on a Neural Manufacturing Concept*, Lawrence Livermore National Laboratory, Livermore, CA, UCRL-JC-110367.

Fuller, G. M., R. W. Mayle, B. S. Meyer, and J. R. Wilson (1992), "Can a Closure Mass Neutrino Solve the Shock Re-Heating Problem?" *Astrophys. J.* **339**, 517.

Ghan, S. J., C. C. Chuang, and J. E. Penner (1992), *A Parameterization of Cloud Droplet Nucleation, Part I: Single Aerosol Types*, Lawrence Livermore National Laboratory, Livermore, CA, UCRL-JC-112011, pt. 1.

Gold, D. M., H. Nathel, P. R. Bolton, W. E. White, and L. D. Van Woerkum (1991), "Prepulse Suppression Using a Self-Induced, Ultrashort-Pulse Plasma Mirror," in *Short-Pulse High-Intensity Lasers and Applications* (Society of Photo-Optical Instrumentation Engineers, Bellingham, WA; *Proc. SPIE* **1413**), p. 41.

Heckman, T. M., M. D. Lehnert, G. K. Miley, and W. J. M. van Breugel (1991), "Spectroscopy of Spatially Extended Material around High-Redshift Quasars," *Astrophys. J.* **381**, 373.

Hewett, D. W., D. J. Larson, and S. Doss (1992), "Solution of Simultaneous Partial Differential Equations Using Dynamic ADI: Solution of the Streamlined Darwin Field Equations," *J. Comput. Phys.* **101**, 11.

Hooper, E. B., B. W. Stallard, M. A. Makowski, S. W. Ferguson, J. A. Crotinger, and R. H. Cohen (1992), "Plasma Thruster/Rocket Based on ECRH Using Whistler Waves," *Bull. Am. Phys. Soc.* **37**, 1450.

Hooper, E. B., B. W. Stallard, and M. A. Makowski (in press), "Whistler Wave-Driven Plasma Thruster," in *Proc. Tenth Symp. Space Nuclear Power and Propulsion*," (American Institute of Physics, New York, NY).

Howell, R. H., C. Berger, F. Solal, Y. Calvayrac, and P. E. A Turchi (1992), "Structural Features in Icosahedral $Al_{63}Cu_{25}Fe_{12}$," *Mater. Sci. Forum* **105–110**, 651–654.

Huang, C. P., M. T. Asaki, S. Backus, M. M. Murnane, H. C. Kapteyn, and H. Nathel (1992), "17-fs Pulses from a Self-Mode Ti:Sapphire Laser," *Opt. Lett.* **17**, 1289.

Kautz, D. D., J. S. Sze, E. P. Dragon, and R. S. Hargrove (1991), "Preliminary Cutting and Drilling Studies with High-Power, High-Radiance Lasers," in *The Laser and the Electron Beam in Welding, Cutting, and Surface Treatment State of the Art 1991* (Bakish Materials Corporation, Englewood, NJ), pp. 302–306.

Kautz, D. D., J. S. Sze, E. P. Dragon, and R. S. Hargrove (1991), "Preliminary Cutting and Drilling Studies with High-Power, High-Radiance Lasers," in *Proc. Int. Conf. Lasers '91* (STS Press, McLean, VA), pp. 501–505.

Kirbie, H. C., G. J. Caporaso, M. A. Newton, and S. S. Yu (1992), *Evolution of High-Repetition-Rate Induction Accelerators through Advancements in Switching*, Lawrence Livermore National Laboratory, Livermore, CA, UCRL-JC-110213.

Klepeis, J. E., K. J. Schafer, T. W. Barbee III, and M. Ross (1991), "Hydrogen–Helium Mixtures at Megabar Pressures: Implications for Jupiter and Saturn," *Science* **254**, 986.

Knauss, K. G., and S. A. Copenhaver (1993), *The Effect of Malonate Dicarboxylic-Acid Anion on the Dissolution Kinetics of Quartz, Alkali Feldspar (Microcline) and Plagioclase Feldspar (Albite) as a Function of pH at 70°C*, Lawrence Livermore National Laboratory, Livermore, CA, UCRL-JC-112461.

Knauss, K. G., S. A. Copenhaver, R. L. Braun, and A. K. Burnham (1992), "Hydrous Pyrolysis of New Albany and Phosphoria Shales: Effects of Temperature and Pressure on the Kinetics of Production of Carboxylic Acids and Light Hydrocarbons," *Am. Chem. Soc. Preprints* 37, 16216.

Knauss, K. G., S. N. Nguyen, and H. C. Weed (1993), "Diopside Dissolution Kinetics as a Function of pH, CO_2, Temperature, and Time," *Geochim. Cosmochim. Acta* **57**, 285.

Krause, J. L., B. H. Lengsfield, K. C. Kulander, and A. E. Orel (1992), *Wave Packet Studies of the Predissociation of H_3*, Lawrence Livermore National Laboratory, Livermore, CA, UCRL-JC-110486.

Kresin, V. (1992), "Analysis of Collective Resonances in Clusters: Metals and Carbon," *Mater. Res. Soc. Symp. Proc.* **272**, 177.

Kresin, V. (1992), "Collective Resonances and Photoabsorption in Metal Clusters," *Phys. Rep.* **220**, 1.

Kresin, V. (1992), "Electron Distribution and Collective Resonances in Nonspherical Metal Clusters," *Phys. Rev. B* **45**, 14321.

Kresin, V. (1992), "Electron Scattering and Electromagnetic Response Properties of Metal Clusters," in *Nuclear Physics Concepts in the Study of Atomic Cluster Physics*, R. Schmidt, Ed. (Springer-Verlag Publishing, Berlin), p. 214.

Kresin, V., and E. Lipparini (1992), "Photodisintegration Sum Rule and Electron Distribution in Metal Clusters," *Phys. Rev. B* **46**, 9812.

Krieger, S. J., P. Bonche, M. S. Weiss, J. Meyer, H. Flocard, and P. H. Heenen (1992), "Super Deformation and Shape Isomerism: Mapping the Isthmus," *Nucl. Phys. A* **542**, 43.

Kuhnert, A., M. A. Stoyer, J. A. Becker, E. A. Henry, S. W. Yates, F. F. Wang, M. J. Brinkman, J. A. Cizewski, F. S. Stephens, M. A. Deleplanque, R. M. Diamond, A. O. Macchiavelli, J. E. Draper, F. Azaiez, W. H. Kelly, and W. Korten (1992), "Oblate Collectivity in ^{197}Pb," *Phys. Rev. C* **46**, 133.

Kulander, K. C., J. L. Krause, K. J. Schafer, S. W. Allendorf, J. K. Crane, K. S. Budil, and M. D. Perry (1992), *Time-Dependent Dynamics of an Atom in an Intense Laser Field*, Lawrence Livermore National Laboratory, Livermore, CA, UCRL-JC-110145.

Lamont, A. (1992), *A Demonstration of the Network Approach to Energy Economics Modeling Using the ProtoNet Modeling System*, Lawrence Livermore National Laboratory, Livermore, CA, UCRL-ID-110643.

Lawrence, T. W. (1992), *The Search for Anyon Superconductivity: Do High-Temperature Superconductors Exhibit a Spontaneous T, Violating Circular Dichroism?*, Ph.D. dissertation, Stanford University, Palo Alto, CA.

Lawrence, T. W., A. Szöke, and R. B. Laughlin (1992), "The Absence of Circular Dichroism in High-Temperature Superconductors," *Phys. Rev. Lett.* **69**, 1439.

Lee, R. L. (1992), *A Finite Element/Finite Difference Approach for Modeling Three-Dimensional Flow and Pollutant Dispersion around Structures*, Lawrence Livermore National Laboratory, Livermore, CA, UCRL-JC-107758, Rev. 1.

London, R. A., P. Amendt, M. R. Carter, M. D. Feit, J. A. Fleck, D. L. Matthews, S. Mason, R. E. Stewart, J. E. Trebes, and M. Strauss (1991), "Designs for Coherent X-Ray Lasers," in *OSA Proc. Short-Wavelength Coherent Radiation: Generation and Applications*, P. H. Bucksbaum and N. M. Ceglio, Eds. (Optical Society of America, Washington, DC), vol. 11, p. 116.

Mailhiot, C., L. H. Yang, and A. K. McMahan (1992), "Polymeric Nitrogen," *Phys. Rev. B* **46**, 14419.

Makowski, M. A., E. B. Hooper, and B. W. Stallard, 1992, "Whistler Wave Dispersion Relation for Plasma Thruster Geometries," *Bull. Am. Phys. Soc.* **37**, 1450.

Mangino, S. G., G. Zandt, and C. J. Ammon (in press), "The Receiver Structure beneath Mina, Nevada," *Bull. Seism. Soc. Am.*

Marcus, D. L., and J. B. Bell (1992), "Evolution and Structure of the Temperature and Vorticity Fields in Thermals," *Theor. Comput. Fluid Dynamics* **3**, 327.

Marcus, D. L., and J. B. Bell (1991), "Numerical Simulation of a Viscous Vortex Ring Interaction with a Density Interface," in *Proc. 22nd Annu. Conf. Fluid Dynamics, Plasma Dynamics, and Lasers* (American Institute of Aeronautics and Astronautics, Honolulu, HI), AIAA-91-1817.

Marcus, D. L., E. G. Puckett, J. B. Bell, and J. Saltzman (1991), "Numerical Simulation of Accelerated Interfaces," in *Proc. Third Int. Workshop Physics of Compressible Turbulent Mixing* (Abbey of Royaumont, France).

McCammon, K., et al. (1992), "High-Sensitivity External Modulator Data Link for High-Energy Particle Detector Diagnostics," in *Proc. SPIE OE/Fibers '92 Conf.* (Society of Photo-Optical Instrumentation Engineers, Bellingham, WA; *Proc. SPIE* **1790**).

Miley, G. K., K. C. Chambers, W. J. M. van Breugel, and D. Macchetto (in press), "HST Imaging of Distant Galaxies: 4C 41.17 at z = 3.8," *Astrophys. J.*

Moran, M. J. (1992), "X-Ray Production by the Smith–Purcell Effect," *Phys. Rev. Lett.* **69**, 2523.

Newton, M. A., H. C. Kirbie, H. D. Shay, and S. S. Yu (1992), *Development of Advanced Modulators for Recirculating Heavy-Ion Accelerators*, Lawrence Livermore National Laboratory, Livermore, CA, UCRL-JC-108513.

O'Dea, C., S. A. Baum, C. Stanghellini, A. Dey, W. J. M. van Breugel, S. E. Duestua, and E. P. Smith (1992), "Radio and Optical Observations of 0218 + 357: The Smallest Einstein Ring?" *Astrophys. J.* **104**, 1320.

Oliveira, J. S., G. O. Cook, Jr., and M. R. Purtill (1991), *New Algorithms for the "Minimal Form" Problem*, Lawrence Livermore National Laboratory, Livermore, CA, UCRL-JC-109225.

Osterheld, A. L., B. K. F. Young, R. S. Walling, R. Shepard, W. H. Goldstein, J. H. Schofield, M. H. Chen, C. Cerjan, S. Maxon, R. London, M. D. Rosen, and R. E. Steward (1992), *Atomic Physics Modeling of X-Ray–Laser Plasmas*, Lawrence Livermore National Laboratory, Livermore, CA, UCRL-JC-109854.

Pagoria, P. F., C. L. Coon, A. R. Mitchell, and R. L. Simpson (in press), "The Synthesis, Scale-Up, and Characterization of 3-amino-5-nitro-1,2,4-triazole (ANTA)," *J. Propel. Expl. Pyrotech.*

Painter, J. F. (1992), *Index Mappings for Interactive Editing of Symbolic Matrices*, Lawrence Livermore National Laboratory, Livermore, CA, UCRL-JC-110700.

Painter, J. F. (1992), *The Matrix Editor for Symbolic Jacobians in ALPAL*, Lawrence Livermore National Laboratory, Livermore, CA, UCRL-JC-109266.

Pekala, R. W., C. T. Alviso, F. M. Kong, and S. S. Hulsey (1992), "Aerogels Derived from Multifunctional Organic Monomers," *J. Non-Cryst. Solids* **145**, 90.

Penner, J. E. (1992), "The Role of Human Activity and Land Use Change in Atmospheric Chemistry and Air Quality, in *Proc. 1991 Global Change Institute on Global Land Use/Cover Change*, B. Turner, Ed. (Global Change Institute, Snowmass, CO).

Penner, J. E., M. M. Bradley, C. C. Chuang, L. L. Edwards, and L. F. Radke (1991), "A Numerical Simulation of the Aerosol–Cloud Interactions and Atmospheric Dynamics of the Hardiman Township, Ontario Prescribed Burn," in *Global Biomass Burning*, J. Levine, Ed. (MIT Press, Cambridge, MA), pp. 420–426.

Portnoff, M. R. (in press), "An Efficient Method for Transposing Large Matrices and Its Application to Separable Processing of Two-Dimensional Signals," *IEEE Trans. Image Processing* **2**.

Procassini, R., J. Bolstad, and W. Dannevik (1991), *A Distributed-Memory Implementation of the Shallow-Water Equations on a MIMD Parallel Computer*, Lawrence Livermore National Laboratory, Livermore, CA, UCRL-JC-107384.

Purtill, M. R., J. S. Oliveira, and G. O. Cook, Jr. (1991), *A New Algebra Core for the "Minimal Form" Problem*, Lawrence Livermore National Laboratory, Livermore, CA, UCRL-JC-109226.

Ratowsky, R. P., R. S. Craxton, M. D. Feit, R. A. London, R. S. Walling, A. L. Osterheld, G. M. Shimkaveg, and M. R. Carter (1992), *Two-Dimensional Time-Dependent Hydrodynamic/Radiation Transport Modeling of X-Ray Emission from Line Focus Laser Plasmas*, Lawrence Livermore National Laboratory, Livermore, CA, UCRL-JC-110000.

Reinhard, L., and P. E. A. Turchi (1992), *Monte-Carlo Simulations and Cluster Variation Method Studies of Phase Decomposition in FeCr*, Lawrence Livermore National Laboratory, Livermore, CA, UCRL-JC-109006 abs.

Reinhard, L., J. L. Robertson, S. C. Moss, G. E. Ice, P. Zschack, and C. J. Sparks (1992), "Anomalous X-Ray Scattering Study of Local Order in bcc $Fe_{0.53}Cr_{0.47}$," in *Proc. TMS Symp. Kinetics of Ordering Transformations in Metals*, H. Chen and V. K. Vasudevan, Eds. (TMS Publications, Warrendale, PA), pp. 37–52.

Reinhard, L., J. L. Robertson, S. C. Moss, G. E. Ice, P. Zschack, and C. J. Sparks (1992), "Anomalous X-Ray Scattering Study of Local Order in bcc $Fe_{0.53}Cr_{0.47}$," *Phys. Rev. B* **45**, 2662–2676.

Robertson, J. L., D. A. Neumann, S. C. Moss, and L. Reinhard (in press), "Inelastic Neutron Scattering Study of Phonon Dispersion in FeCr near the σ-Phase Transformation," *Acta Metall.*

Rogers, L. (1992), *Optimal Groundwater Remediation Using Neural Networks and the Genetic Algorithm*, Ph.D. dissertation, Stanford University, Palo Alto, CA.

Rogers, L., and F. U. Dowla (1992), *Optimal Groundwater Remediation Using Artificial Neural Networks with Parallel Solute Transport Modeling*, Lawrence Livermore National Laboratory, Livermore, CA, UCRL-JC-109016.

Rogers, R. D. (1991), "Relativistic Enhancement of the Compton-Reflected Component in Active Galactic Nuclei," *Astrophys. J.* **383**, 550.

Rogers, R. D., and G. B. Field (1991), "A Compton Reflection Model for the Cosmic X-Ray and Gamma-Ray Backgrounds," *Astrophys. J. Lett.* **378**, L–17.

Rosen, M. D. (1991), "Future Directions of Laboratory X-Ray–Laser Research," in *OSA Proc. Short-Wavelength Coherent Radiation: Generation and Applications*, P. H. Bucksbaum and N. M. Ceglio, Eds. (Optical Society of America, Washington, DC), vol. 11, p. 73.

Runge, J. J., M. P. Surh, C. Mailhiot, and E. L. Pollock (1992), "Path Integral Monte Carlo Calculations of Orientational Ordering in Compressed H_2," *Phys. Rev. Lett.* **69**, 3527.

Schmitt, R. G., P. B. Butler, N. E. Bergan, W. J. Pitz, and C. K. Westbrook (1991), *Destruction of Hazardous Waste in Supercritical Water. Part II: A Study of High-Pressure Methanol Oxidation Kinetics*, Lawrence Livermore National Laboratory, Livermore, CA, UCRL-JC-108654, pt. II.

Sharp, W. M., and J. J. Barnard (1992), *Steering Algorithms for a Heavy-Ion Recirculating Accelerator*, Lawrence Livermore National Laboratory, Livermore, CA, UCRL-JC-110868.

Sharp, W. M., J. J. Barnard, and S. S. Yu (1992), *Pulse Shaping in an Accelerator for Heavy-Ion Fusion*, Lawrence Livermore National Laboratory, Livermore, CA, UCRL-JC-110221.

Sharp, W. M., J. J. Barnard, and S. S. Yu (1992), *Transverse Beam Dynamics in Recirculating Accelerators for Heavy-Ion Fusion*, Lawrence Livermore National Laboratory, Livermore, CA, UCRL-JC-108512.

Shepherd, R., W. White, D. Price, and H. Nathel (1992), "Interaction of Ultrahigh Intensity Lasers with Solid Targets," in *OSA Annual Meeting Technical Digest* (Optical Society of America, Washington, DC), vol. 13, p. 20

Shimkaveg, G. M., M. R. Carter, R. S. Walling, J. M. Ticehurst, J. A. Koch, S. Mrowka, J. E. Trebes, B. J. MacGowan, L. B. Da Silva, D. L. Matthews, R. A. London, and R. E. Stewart (1992), *X-Ray–Laser Coherence Experiments in Neon-Like Yttrium*, Lawrence Livermore National Laboratory, Livermore, CA, UCRL-JC-107745.

Sims, J. M., R. Lee, R. McCallen, B. Lawver, J. Clark, D. Rueppel, and T. Sullivan (1992), *Advances in Real-Time Technology Assessment and Emergency Response: Close-In Atmospheric Dispersion Modeling and Exposure Estimation*, Lawrence Livermore National Laboratory, Livermore, CA, UCRL-JC-111095.

Snyderman, N. J. (1992), "Soliton Dynamics of the $B = 2$ Sector of the Skyrme Model," in *Baryons as Skyrme Solitons 1992*, G. Holzwarth, Ed. (World Scientific Publishing, Singapore).

Stoyer, M. A., E. A. Henry, Y. A. Akovali, J. A. Becker, C. R. Bingham, J. Breitenbach, H. K. Carter, R. W. Hoff, M. Jario, P. Joshi, J. Kormicki, A. Kuhnert, P. F. Mantica, T. F. Wang, J. L. Wood, and M. Zhang (1992), *Search for Population of Superdeformed States in ^{194}Pb Using ^{194}Bi β^+-Decay*, Lawrence Livermore National Laboratory, Livermore, CA, UCRL-JC-111336.

Terminello, L. J., J. J. Barton, and D. A. Lapiano-Smith (in press), "Holographic Imaging of Atoms Using Multiple-Wavenumber Electron Angular Distribution Patterns," *Phys. Rev. Lett.*

Terminello, L. J., J. J. Barton, and D. A. Lapiano-Smith (1992), "Near-Surface Atom Imaging Using Multiple-Energy Photoelectron Holography," *J. Vac. Sci. Technol. B* **10**, 2088.

Terminello, L. J., J. J. Barton, and D. A. Lapiano-Smith (1992), *Surface and Near-Surface Atom Imaging with Photoelectron Holography*, Lawrence Livermore National Laboratory, Livermore, CA, UCRL-JC-111627.

Terminello, L. J., G. D. Waddill, and J. G. Tobin (1992), "High-Resolution Photoabsorption and Circular Polarization Measurements on the University of California/National Laboratory Spherical Grating Monochromator Beamline," *Nucl. Instrum. Methods A* **319**, 271.

Tobin, J. G., G. D. Waddill, and D. P. Pappas (1992), "Giant X-Ray Absorption Circular Dichroism in Magnetic Ultrathin Films of Fe/Cu(001)," *Phys. Rev. Lett.* **68**, 3642.

Tobin, J. G., M. K. Wagner, X. Q. Guo, and S. Y. Tong (1991), "Photoelectron Diffraction of Magnetic Ultrathin Films: Fe/Cu(001)," *Mater. Res. Soc. Symp. Proc.* **208**, 283.

Trebes, J. E., K. A. Nugent, S. Mrowka, R. A. London, T. W. Barbee, M. R. Carter, J. A. Koch, B. J. MacGowan, D. L. Matthews, L. B. Da Silva, G. F. Stone, and M. D. Feit (1992), "Measurement of the Spatial Coherence of a Soft-X-Ray Laser," *Phys. Rev. Lett.* **68**, 588.

Turchi, P. E. A., and A. Finel (1992), "Ordering Phenomena in A15-Based Alloys," *Phys. Rev. B* **46**, 702–722.

Turchi, P. E. A., L. Reinhard, M. Sluiter, and G. M. Stocks (in press), "First-Principles Study of Local Order in bcc-Based FeV and FeCr Alloys," *Phys. Rev. B*.

Turchi, P. E. A., L. T. Reinhard, and M. Sluiter (1992), *First-Principles Approach to Alloy Phase Stability*, Lawrence Livermore National Laboratory, Livermore, CA, UCRL-JC-110724.

Turchi, P. E. A., and M. Sluiter (1992), *Electronic Structure Theory of Alloy Phase Stability*, Lawrence Livermore National Laboratory, Livermore, CA, UCRL-JC-109658.

Turchi, P. E. A., and M. Sluiter (1992), "Real-Space Multiple Scattering Description of Phase Stability in Alloys," *Mater. Res. Soc. Symp. Proc.* **253**, 227–242.

Turchi, P. E. A., M. Sluiter, F. J. Pinski, D. D. Johnson, D. M. Nicholson, G. M. Stocks, and J. B. Staunton (1991), "First-Principles Study of Phase Stability in Cu–Zn Substitutional Alloys," *Phys. Rev. Lett.* **67**, 1779–1782, Erratum, *Phys. Rev. Lett.* **68**, 418.

Turchi, P. E. A., M. Sluiter, and G. M. Stocks (1991), "A Comparative Study of Short Range Order in Fe–Cr and Fe–V Alloys around Equiatomic Composition," *Mater. Res. Soc. Symp. Proc.* **213**, 75–80.

Turchi, P. E. A., M. Sluiter, and G. M. Stocks (1992), "First-Principles Prediction of Alloy Phase Stability," *J. Phase Equilibria* **13**, 391–399.

Turteltaub, K. W., J. S. Vogel, and J. S. Felton (in press) "Low-Level Biological Dosimetry of Heterocyclic Amine Carcinogens Isolated from Cooked Food," *Environmental Health Perspectives*.

Turteltaub, K. W., J. S. Vogel, C. E. Frantz, and E. Fultz (1992), *Studies on DNA Adduction with Heterocyclic Amines by Accelerator Mass Spectrometry (AMS): A New Technique for Tracing Isotope-Labeled DNA Adduction*, Lawrence Livermore National Laboratory, Livermore, CA, UCRL-JC-111534.

Turteltaub, K. W., J. S. Vogel, C. E. Frantz, and N. H. Shen (1992), "Fate and Distribution of 2-amino-1-methyl-6-phenylimidazo[4,5-b]pyridine (PhIP) in Mice at a Human Dietary Equivalent Dose," *Cancer Res.* **52**, 4682–4687.

van Bibber, K., et al. (1993), "A Next-Generation Cavity Microwave Experiment to Search for Dark-Matter Axions," *Proc. Dark Matter Workshop*, R. Field, Ed. (World Scientific Publishing Co., Singapore).

van Breugel, W. J. M. (in press), "Radio Galaxies and Their Environment," in *Proc. Schloss Ringberg II Conf. Jets in Extragalactic Radio Sources, Lecture Notes in Physics*, H. J. Roeser and K. Meisenheimer, Eds. (Springer-Verlag, Berlin).

van Breugel, W. J. M., and A. Dey (in press), "Induced Star Formation in a Lobe of the Radio Galaxy 3C 285?" *Astrophys. J.*

van Breugel, W. J. M., C. Fanti, R. Fanti, C. Stanghellini, T. Schillizi, and R. Spencer (1992), "3CR Compact Steep Spectrum Radio Sources, VLA Observations at 1.5, 15, and 22 GHz," *Astron. Astrophys.* **256**, 56.

Vitello, P. A., B. M. Penetrante, and J. N. Bardsley (1992), "Multi-Dimensional Modeling of the Dynamic Morphology of Streamer Coronas," in *NATO Advanced Research Workshop on Non-Thermal Plasma Techniques for Pollution Control, Cambridge University, England, September 21–25, 1992.*

Vogel, J. S. (in press), "Rapid Production of Graphite without Contamination for Biomedical AMS," *Radiocarbon* **34**.

Vogel, J. S., and K. W. Turteltaub (1992), "Biomolecular Tracing through Accelerator Mass Spectrometry," *Trends Analytical Chem.* **11**, 142–149.

Vogtlin, G. E. (1992), "Pulsed Coronal Discharge for Combined Removal of SO_2, NO_x, and Fly Ash from Flue Gas," in *NATO Advanced Research Workshop on Non-Thermal Plasma Techniques for Pollution Control, Cambridge University, England, September 21–25, 1992.*

Waddill, G. D., J. G. Tobin, and D. P. Pappas (1992), "Magnetic Dichroism in Core-Level Photoemission from fcc Fe/Cu(001) Films," *Phys. Rev. B* **46**, 552.

Wang, T. F., E. A. Henry, J. A. Becker, A. Kuhnert, M. A. Stoyer, S. W. Yates, M. J. Brinkman, J. A. Cizewski, A. O. Macchiavelli, F. S. Stephens, M. A. Deleplanque, R. M. Diamond, J. E. Draper, F. Azaiez, W. H. Kelly, W. Korten, E. Rubel, and Y. A. Akovali (1992), "First Lifetime Measurement of Dipole Collective Bands in Neutron-Deficient Lead Nuclei," *Phys. Rev. Lett.* **69**, 1737.

Warner, B. E., H. W. Friedman, R. P. Hackel, R. S. Hargrove, and J. A. Paisner (1992), "Applications of High-Average-Power, Visible Lasers at Lawrence Livermore National Laboratory to Commercial and Scientific Problems," *Int. Quantum Electron. Tech. Digest* **9**, 68.

Westbrook, C., and W. J. Pitz (1991), *Numerical Modeling of Chemical Kinetics of Oxidation of Chlorinated Hydrocarbons* (American Institute of Chemical Engineers, Los Angeles, CA).

White, W. E., T. Donelly, J. P. Hunter, D. F. Price, R. L. Shepherd, and L. Van Woerkum (1992), "Amplification of 100-fs Laser Pulses to TW Peak Power Levels," in *OSA Annual Meeting Technical Digest* (Optical Society of America, Washington, DC), vol. 23, p. 162.

White, W. E., J. P. Hunter, L. D. Van Woerkum, J. Ditmire, and M. D. Perry (1992), "120-fs TW Ti:Al_2O_3/Cr:$LiSrAlF_6$ Laser System," *Opt. Lett.* **17**, 15.

Widgoff, M., et al. (1992), *Resistive Plate Counter Technology Review*, Superconducting Super Collider Laboratory, Dallas, TX, GEM Technical Memorandum SSCL/ GEM-TN-92-206.

Williams, T. J., and Y. Matsuda (1992), "3D Gyrokinetic Particle-In-Cell Codes on the TC2000 and CM2," in *The 1992 MPCI Yearly Report: Harnessing the Killer Micros*, E. D. Brooks III, Ed., Lawrence Livermore National Laboratory, Livermore, CA, UCRL-ID-107022-92, pp. 303–311.

Wuest, C. (1992), *TART Calculations of Neutron Attenuation and Neutron-Induced Photons on 5% and 20% Borated Polyethylene Slabs*, Superconducting Super Collider Laboratory, Dallas, TX, GEM Technical Memorandum SSCL/GEM-TN-92-172.

Wuest, C., and G. J. Mauger (1992), *Effects of Light Exposure on Irradiated Barium Fluoride Crystals*, Superconducting Super Collider Laboratory, Dallas, TX, GEM Technical Memorandum SSCL/GEM-TN-92-182.

Wuest, C., B. Fuchs, and W. Kway (1992), *Barium Fluoride Research and Development at Lawrence Livermore National Laboratory*, Superconducting Super Collider Laboratory, Dallas, TX, GEM Technical Memorandum SSCL/ GEM-TN-92-163.

Yang, L. H., E. D. Brooks III, and J. Belak (1992), "A Linked-Cell Domain Decomposition Method for Molecular-Dynamics Simulation on a Scalable Multiprocessor," in *1992 MPCI Yearly Report: Harnessing the Killer Micros*, Lawrence Livermore National Laboratory, Livermore, CA, UCRL-ID-107022-92, p. 290.

Yoo, C. S., N. C. Holmes, M. Ross, D. Webb, and C. Pike (1992), *Shock Temperatures, Melting, and Phase Diagrams of Iron at Earth Core Conditions*, Lawrence Livermore National Laboratory, Livermore, CA, UCRL-JC-112242.

Yoo, C. S., N. C. Holmes, and E. See (1992), "Shock-Induced Optical Changes in Al_2O_3 at 200 GPa," in *Shock Waves in Condensed Matter—1991*, S. C. Schmidt, R. D. Dick, J. W. Forbes, and D. G. Tasker, Eds. (Elsevier, North Holland, Amsterdam), p. 733.

Young, K., et al. (1992), "Measurements of the Radiation and Chemical Stability of Plastic Waveshifting Optical Fibers," *J. Rad. Chem. Phys.* **41**, 215–219.

Author Index

END

DATE FILMED

10/6/93